2D Heterostructured Photocatalytic Materials for Water Treatment and Disinfection

Anukriti Singh

B.Tech, M.Tech (Nanotechnology)

Faculty of Computing, Engineering and the Built Environment

Ulster University

Thesis submitted for the degree of Doctor of Philosophy

July 2020

I confirm that the word count of this thesis is less than 100,000 words

Contents

Chapter 3. Materials, Methods and Equipment 58

Acknowledgements

First and foremost, I would like to thank Professor James McLaughlin for giving me the opportunity to work on this project in NIBEC at Ulster University. I would also like to acknowledge the Ulster University Doctoral College for providing me the financial support through the Vice Chancellor’s Research Scholarship.

I would like to express my sincere gratitude and appreciation to the chair of my supervisory team, Professor Tony Byrne, for his constant motivation, guidance and support that encouraged me to accomplish this research project. I am also immensely grateful to my other supervisory team members Dr Pilar Fernandez and Dr Patrick Dunlop, for their support, guidance and inspiration throughout the PhD.

I would like to thank Dr Jeremy Hamilton for his assistance, training and support with fruitful discussions throughout the PhD. I would like to thank Dr Preetam Sharma for his assistance with TEM and SEM analysis and initial training taken as part of this research. I would also like to acknowledge Professor Andrew Mills and Dr Dilidaer Yusufu for their assistance with photoluminescence measurements carried out at Queens University Belfast.

Thank you to Mrs Ann Blair, Ms Ruth Holman, Mr Damien McDonald and Mr Brian McGrath for their administrative and technical support. I would also like to thank all the fellow PhDs and staff in NIBEC for their help and support provided during this research.

Thank you to all my friends in Northern Ireland, and to the ones in India and Germany for their unconditional support and encouragement. Especially during the anxious days of my PhD journey.

Finally, I would like to dedicate this work to my family. To my parents Mr Shailendra Singh and Mrs Sangeeta Singh, for their unconditional love and support that has brought me here. For believing in me and being the two pillars of my strength to accomplish this work. To my brother Prakhar and sister in law Kajal for their infinite moral support and guidance. Thank you to all of you for being the sounding boards in this journey.

Anukriti Singh

Note on access to contents

"I hereby declare that with the effect from the date on which the thesis is deposited in the Library of the Ulster University, I permit

1. the Librarian of the University to allow the thesis to be copied in the whole or in part without reference to me on the understanding that such authority applies to the provision of single copies made for study purposes or for the inclusion within the stock of another library.

2. the thesis to be made available through the Ulster Institutional Respiratory and/or EThOS under the terms of the Ulster eThesis Deposit Agreement which I have signed.

IT IS A CONDITION OF USE OF THIS THESIS THAT ANYONE WHO CONSULTS IT MUST RECOGNISE THAT THE COPYRIGHT RESTS WITH THE AUTHOR AND THAT NO QUOTATION FROM THE THESIS AND NO INFORMATION DERIVED FROM IT MAY BE PUBLISHED UNLESS THE SOURCE IS PROPERLY ACKNOWLEDGED."

Anukriti Singh

July 2020

Publications and Presentations

Book Chapter

1. Fernandez-Ibañez, P., Byrne, J.A., **Singh, A**., McMichael, S., Singhal, A., Polo-Lopez M.I. (2020), Photocatalytic inactivation of microorganisms in water (chapter 8). In *'Nanostructured Photocatalysts: Materials and Applications'*, Elsevier, Editors: Rabah Boukherroub, Satish Ogale and Neil Robertson.
   ISBN: 9780128178362

Publications

1. Bougarrani, S.; Sharma, P.K.; Hamilton, J.W.J.; **Singh, A**.; Canle, M.; El Azzouzi, M.; Byrne, J.A.,"Enhanced Photocatalytic Degradation of the Imidazolinone Herbicide Imazapyr upon UV/Vis Irradiation in the Presence of Ca_xMnO_y-TiO_2 Hetero-Nanostructures: Degradation Pathways and Reaction Intermediates", *Nanomaterials* 2020, **10**, 896.
2. Waso, M.; Khan, S.; **Singh, A**.; McMichael, S.; Ahmed, W.; Fernandez-Ibañez, P.; Byrne, J. A.; Khan, W., "Predatory bacteria in combination with solar disinfection and solar photocatalysis for the treatment of rainwater", *Water Research*, 2020, **169**, 115281.
3. Kumaravel, V.; Rhatigan, S.; Mathew, S.; Bartlett, J.; Nolan, M.; Hinder, S.J.; Sharma, P.K.; **Singh, A**.; Byrne, J.A.; Harrison, J.; Pillai, S.C., "Indium-Doped TiO_2 Photocatalysts with High-Temperature Anatase Stability", *The Journal of Physical Chemistry C* 2019, **123**, 21083-21096.

Presentations (Chronological order)

1. **A. Singh**, P. Fernandez-Ibañez, P.S.M. Dunlop, J.A. Byrne, "Electrochemically assisted photocatalytic disinfection of water using 2D WO_3/g-C_3N_4 heterostructures", at *International conference on Photo-irradiation and adsorption based novel innovations for water treatment* (PANIWATER), March 2020, Goa, India (poster).
2. **A. Singh,** J.W.J Hamilton, P.S.M. Dunlop, P. Fernandez- Ibañez, J.A. Byrne "Investigating the electron transfer process in WO_3/g-C_3N_4 heterostructures for photocatalysis", at *Royal Society of Chemistry, Chemical Nanoscience and Nanotechnology Annual Symposium-2019*, July 2019, University of East Anglia, England (oral).
3. **A. Singh,** J.W.J. Hamilton, P.K. Sharma, P.S.M. Dunlop, P. Fernandez- Ibañez, J.A. Byrne "Investigating the electron transfer process in WO_3/g-C_3N_4 heterostructures for photocatalysis", at *European Materials Research Society Spring Meeting-2019*, May 2019, Nice, France (oral).
4. **A. Singh,** P.K. Sharma, J.W.J. Hamilton, P.S.M. Dunlop, P. Fernandez- Ibañez, J.A. Byrne "2D materials for solar photocatalytic disinfection of water", at *2018 Joint UK & Ireland Semiconductor Photochemistry Network meeting*, September 2018, Gran Canaria, Spain (oral).
5. **A. Singh**, P.K. Sharma, J.W.J. Hamilton, P.S.M. Dunlop, P. Fernandez- Ibañez, J.A. Byrne, "2D WO_3/C_3N_4 composites for enhanced solar photocatalytic disinfection of water", at *International Workshop for Safewater*, June 2018, NIBEC, Ulster University, UK (oral).
6. **A. Singh**, P.K. Sharma, Y. Han, J.W.J. Hamilton, P.S.M. Dunlop, P. Fernandez-Ibañez, J.A. Byrne, "Visible light active photocatalytic materials for solar water purification", at *2nd Summer school on Environmental applications of Advanced Oxidation Processes(AOPs)*, July 2017, Porto, Portugal (poster).

List of Abbreviations

AM	Air Mass
BE	Binding energy
CB	Conduction band
CFU	Colony-forming units
EAP	Electrochemically assisted photocatalysis
EDX	Energy-dispersive X-ray analysis
E_f	Fermi energy level
E_{fb}	Flat band potential
E_g	Bandgap
eV	Electron volts
HOMO	Highest occupied molecular orbital
IPCE	Incident photon-to-current conversion efficiency
ITO	Indium tin oxide
J	Current density
LSV	Linear sweep voltammetry
LUMO	Lowest unoccupied molecular orbital
NHE	Normal hydrogen electrode
PL	Photoluminescence
ROS	Reactive oxygen species
SCE	Saturated calomel electrode
SEM	Scanning electron microscopy
TEM	Transmission electron microscopy
UVA	Ultraviolet A (320-400 nm)
UVB	Ultraviolet B (280-320 nm)
UV-Vis	Ultraviolet-visible
VB	Valence band
XPS	X-ray photoelectron spectroscopy
XRD	X-ray diffraction

List of Figures

List of Tables

Abstract

It is estimated that nearly 2 billion people commonly drink water that is not safe. There is a real and urgent need to develop technologies that can disinfect water at the point of use for household based water treatment in developing countries. Solar disinfection can be used to inactivate pathogenic microorganisms in water. However, some organisms are more resistant to solar photo-inactivation. The efficiency of solar disinfection may be improved using heterogeneous photocatalysis. The identification, design and development of semiconductors with band gap energies between 2-3 eV with band potentials suitable for the generation of reactive oxygen species (ROS) is critical to improving the solar efficiency of photocatalysis for environmental applications. The overall aim of this research was to join two narrow bandgap semiconductors in a z-scheme with complementary band edge potentials suitable for ROS generation and test for the solar driven photocatalytic disinfection of water.

Two-dimensional nanostructures of tungsten trioxide (WO_3) and graphitic carbon nitride (g-C_3N_4) were fabricated as individual and heterostructures to study their performance for photocatalyst degradation of organic pollutants (formic acid and phenol) and inactivation of *Escherichia. coli* under simulated solar irradiation. Contrary to the published literature, the photocatalytic efficiency of the 2D heterostructures was poor compared to a standard benchmark photocatalyst P25-TiO_2 (*Evonik Aeroxide*). The detailed physicochemical properties of the heterostructures were investigated to elucidate the reasons for the poor performance. Chemical probe studies indicated that the 2D heterostructures could work for photocatalytic oxidation reaction and generate hydroxyl radicals, but only with the presence of an electron scavenger. This suggested that the rate limiting step for the photocatalytic activity was the reduction of oxygen. Further investigations showed that WO_3, g-C_3N_4 and the heterostructures were unable to photocatalytically reduce methyl viologen that was easily achieved with TiO_2 under UV-Vis irradiation. XPS analysis indicated a structural defect in g-C_3N_4 with reducing nitrogen (N1s) atomic percentage after heterostructure formation. A surface defect arising from NH_2 groups of g-C_3N_4 was associated with limited photocatalytic reduction. A photocurrent switching from anodic to cathodic was observed for g-C_3N_4 on sweeping potential from +1.0 to -1.0 V (SCE) through linear sweep voltammetry. The Mott-Schottky analysis in the dark and under UV-Vis irradiation suggested an

electron trap between +0.5 to +0.8 V (SCE) for the g-C_3N_4. The M-S analysis also indicated the presence of the electron trapping state in the WO_3/g-C_3N_4 heterostructure. This suggests that photoexcited conduction band electrons in the WO_3 are transferred to the g-C_3N_4 but trapped in the defect state. The trapped electrons cannot be passed on to reduce molecular oxygen and thus this reaction is rate limiting.

From photoelectrochemical studies, an increased photocurrent density of 12.14 µA.cm^{-2} under a fixed potential of +1.0 V for WCN91 heterostructure electrode was observed compared to 1.82 µA.cm^{-2} for WO_3 electrode, due to the improved electron-hole pair separation. The heterostructure electrode was tested as photoanode for the electrochemically assisted photocatalytic disinfection (EAP) of water and showed a 6-log reduction of *E. coli* (10^6 CFU.mL^{-1}) in 150 min of UV-Vis irradiation as compared to a 5-log reduction with WO_3 electrode in 240 min. The increased rate of EAP inactivation of *E. coli* with the 2D heterostructure electrode was encouraging as compared to the poor activity observed with the suspended photocatalytic system.

Chapter 1. Introduction

1.1 Global water crisis

Water is the core aspect of every individual's daily life. It serves a crucial connection between maintaining a healthy ecosystem and for socio-economic development. A necessity for survival, water is a fundamental human right; however, with increasing global population and adverse climate changes, there is an alarming increase in demand for freshwater resources, with many regions of the world facing a threat of absolute water scarcity. Recent studies estimate annually, 4 billion people (nearly two-thirds) of the global population live in severe water scarcity for at least 1 month [1], out of which 500 million live in water-scarce regions all year round. Mekonnen and Hoekstra assessed a monthly global blue water scarcity for a decade (1996-2005), as shown in figure 1.1, wherein blue water is the fresh surface water or ground water [1].

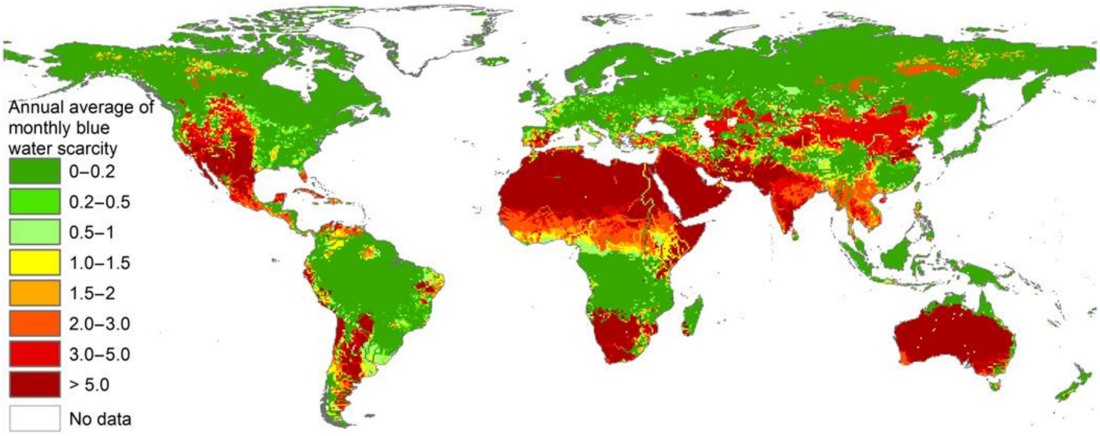

Figure 1.1 Global blue water scarcity map at 30 × 30 arc min resolution with average months. Reproduced from Mekonnen, and Hoekstra, Science Advances, (2016) [1].

As can be seen, from the global water scarcity map, regions of sub-Saharan Africa, South Asia and Australia are the worst affected with problems of water scarcity all year round. Due to the existing climate changes taking place, the world is facing a threat of absolute water scarcity, and 50% of the global population fears to be living in the highly water-stressed area by 2025 [2, 3].

Besides, its limited availability for human use; the pollution of water with hazardous and faecal waste decreases the availability of safe fresh water resources. The World Health Organization (WHO) estimates that globally nearly 2.2 billion people lack access to a safe source of drinking water at home[4, 5]. Many people are forced to rely on microbiologically contaminated sources that increase the risk of contracting waterborne diseases leading to diarrhoea. In 2019 WHO published statistics on diarrhoeal deaths, that revealed, 35% of the total 829 000 diarrheal deaths occurring annually were due to contaminated sources of drinking water. An 8% global child mortality rate was associated with diarrhoeal cases among children below the age of five years [6]. It is mostly the least developed and low-middle-income countries (LMICs), where people are likely to be affected by the consumption of unsafe drinking water, contributing to 60% global diarrhoeal deaths. A good illustration of the affected population can be seen in figure 1.2, where the people from rural areas are dependent more on the surface and unimproved sources of water.

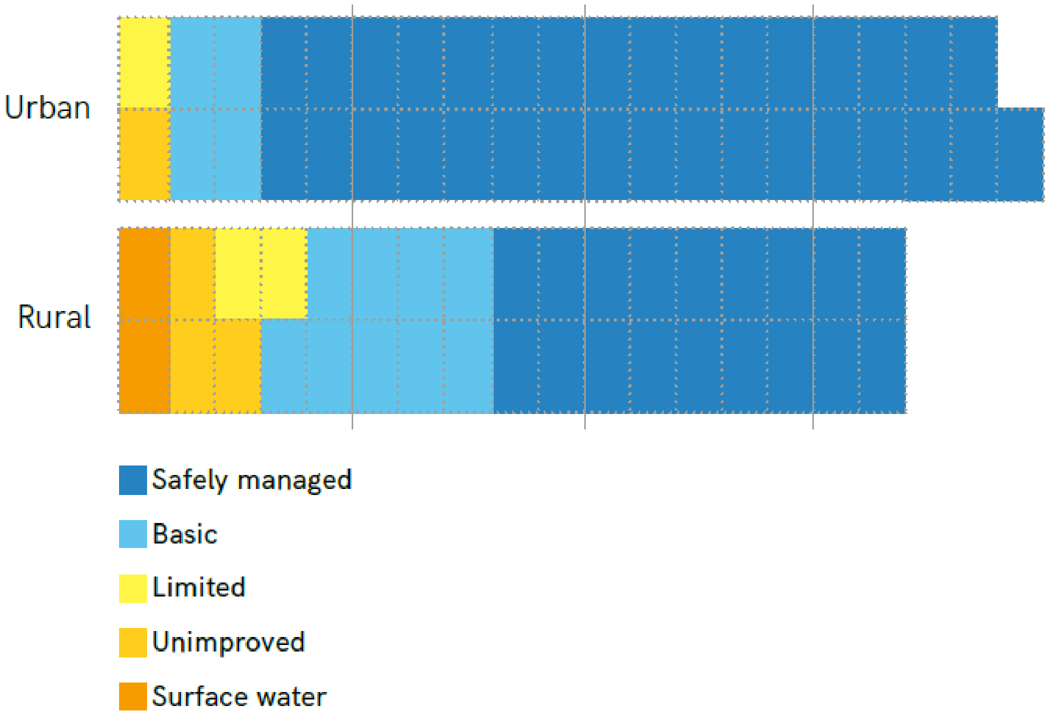

Figure 1.2 Urban and rural population in 2015 using different levels of drinking water services. (A row represents the population using different levels of service and each unit in a row is equivalent to 100 million people). Reproduced from Joint Monitoring Programme (JMP) report on Progress in drinking water, sanitation and hygiene: 2017 updates and Sustainable Developments Goals (SDG) baselines [5].

Contamination of groundwater resources with heavy metals ions like arsenic, lead, or increased level of fluoride in drinking water are additional threats to public health [7-9]. To overcome the problem of water scarcity and improve access to safe drinking water, the United Nations launched the Sustainable Developments Goals (SDGs) to be achieved by 2030. Under the SDGs, the sustainable development goal 6 is targeted to ensure availability of safe and clean drinking water for all [10]. The SDG-6 takes account of the accessibility, availability and good quality services of safely managed drinking water, which can be achieved by water-free from faecal contamination. The World Health Organization (WHO) publishes and updates comprehensive Guidelines for drinking-water quality [11]. *Escherichia coli (E. coli)* or thermotolerant coliforms are the model choice of indicator organism set by WHO, to detect the faecal contamination in drinking water sample of 100 mL tested at the time of collection [11].

For those without access to safely managed drinking water, simple household water treatment and storage (HWTS) interventions may be adopted. Appropriate HWT include boiling, filtration, chemical disinfection (chlorination), solar disinfection, UVC disinfection and flocculation[12]. Although these WHO-recommended methods are not long term solutions, they provide safer drinking water to people who lack access to piped water sources. Nevertheless, the safety of the treated potable water is compromised sometimes by using unclean water tanks/containers, which may lead to recontamination. Chemical disinfection methods using chlorine are cost-effective and simple for disinfecting water tanks for storage. However, the use of chlorination leads to the formation of toxic disinfection by-products such as trihalomethanes (THMs) that are carcinogenic [13]. Furthermore, some pathogenic microorganism, such as protozoa may be resistant to chlorination [14]. Solar disinfection can be easily practiced in regions of the world where the sunshine is available all year round.

1.2 Solar disinfection

Solar disinfection of water is a low-cost, simple technique that provides some level of disinfection. It is a potentially free technology in which the ultraviolet (UV), visible (Vis) and infrared (IR) radiations from the sun lead to the inactivation of microorganisms. The total solar spectrum consists of UV, Vis and IR radiations. However, UVC photons (200-280 nm) from the sun are absorbed by the ozone layer and blocked from reaching the earth's surface. Therefore, at sea level, only a fraction of UVB (280-320 nm) and UVA (320-400 nm) radiations reach the earth with a total around 4-6% of the solar spectrum; this is referred to as the solar UV spectrum. A total of ~47 $W.m^{-2}$ solar UV dose is present in 1 sun's spectrum at air mass 1.5 global irradiance [15]. The UV energy from the solar spectrum combined with thermal heating (>45°C) cause a synergistic effect and attack directly on the pathogens by generating reactive oxygen species (ROS) in the presence of water. These ROS react with the microorganisms and inactivate them [16].

The technology of solar disinfection is exploited by the SODIS protocol, that uses sunlight (solar energy that is free and found in abundance all over the world) and plastic polyethylene terephthalate (PET) bottles (similar to coke bottles) that can be easily found and recycled. A typical SODIS protocol involves 4 simple steps to get a clean and safer water, which are illustrated in figure 1.3[17]. One needs clear 2 L plastic (PET) bottles that are UV transparent and fill it with the contaminated/raw water and close the cap and leave to be exposed in the direct sunlight for nearly 6-48 hours.

The SODIS protocol is effective against the removal of pathogenic micro-organisms present in water. *Escherichia coli* (*E. coli)* is a gram negative bacteria and a human pathogen found in the gastrointestinal tracts. *E. coli* easily survive inside the body at temperature up to 37°C and in humid and dark conditions. However, once they are released in water sources, as faecal waste, their removal by UV radiation is possible as the UVA irradiation directly interact with cell DNA, and destruct the cellular structure and cause cell death, or the UV irraditions interact with dissolved oxygen in water to generate ROS that attack the bacterial cells. Either way, the cells do not have a strong defense mechanism against UV radiation leading to their inactivation. However, *E. coli* are typically resistant to SODIS, because of their survival upto 37-44 °C. Therefore, a synergistic process of thermal water temperature of 50-60°C along with UVA radiation is required to give total inactivation of 99.99% (4 log) in 6 h by solar disinfection. *E.coli* is considered as the model indicator organism for faecal contamination in water based on WHO recommendations. Currently, 5 million people at household, health centres and school level follow SODIS protocol to get safe and clean drinking water, mainly in sub-Saharan Africa, South America and Asia [18].

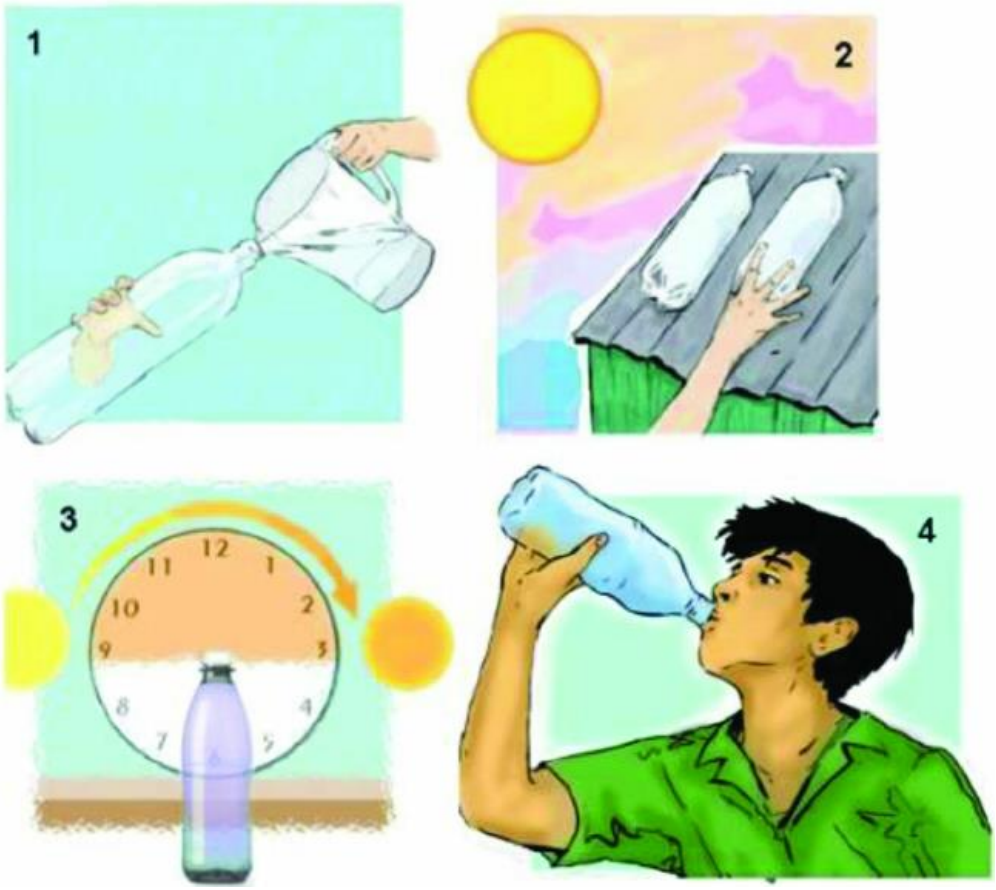

Figure 1.3 SODIS protocol. Reproduced from McGuigan et al.(2012), Journal of Hazardous Materials, 235-236, 29-46, (2012)[17].

A Cochrane review published by Clasen et al.(2006) [19], analysed the interventions to improve the drinking water quality in order to prevent increasing diarrhoeal cases. According to the published review, household interventions were said to be more effective to prevent diarrhoea as compared to the public/community water sources. A year later, Clasen et al.(2007) [20], compared the cost effectiveness of various household interventions utilised to improve the drinking water quality. According to the published data in this review and later in a report by WHO in 2008 [21], solar disinfection was slightly less cost-effective intervention to chlorination. The daily cost of both the interventions was roughly identical ~US$ 0.63-0.66. Even though solar disinfection is widely promoted, it does face many challenges making it a less cost-effective intervention as compared to chlorination, mainly due to its limitation of treating large volumes of clean water in a short period. Besides, it is most effective under direct sunlight, and the production and treatment of safe drinking water can be compromised in cloudy and rainy days, requiring longer treatment times. Also, if the water is turbid, with turbidity higher than 30 Nephelometric Turbidity Units (NTU), it requires a pre-filtration step before being exposed to sunlight. Other disadvantages are that solar disinfection does not improve the chemical quality of the water and has a potential risk of recontamination of the treated water beyond its shelf life of 24 h [22]. The risk of recontamination potentially is due to an incomplete inactivation process of microorganisms. The incomplete treatment could be a reason of short irradiation/time. The storage of this incomplete treated water at temperature of 37°C beyond 24 h, will lead to regrowth/repair of any bacterial cells present.

1.3 Heterogeneous photocatalysis for enhancing the efficiency of solar disinfection

The solar disinfection process can be improved by several methods, for example, using specific designs of solar reactors[23], by increasing the overall solar dose[24] or by use of heterogeneous photocatalysis[25-27]. Effective use of solar energy using photocatalysis can accelerate the disinfection of water[28]. The quality of water is also affected by natural organic matter, and organic compounds that are from anthropogenic activities, including agriculture and industrial processes [29]. Photocatalysis is an advanced oxidation process that can degrade organic pollutants in water [30-32]. Photocatalysis is a potential “green” technology for water purification, utilising sunlight to activate semiconductors that act as photocatalysts to drive the redox processes in water. The photo-excited semiconductor photocatalyst generates charge carriers that react with water to produce reactive oxygen species (ROS) that can degrade refractory organic contaminants and inactivate harmful microorganisms. However, while photocatalysis is a very active area for research, there are few examples of large-scale water treatment using solar photocatalysis. Limitations such as designing of photocatalytic reactors for large-scale treatment, longevity and mass production of catalyst and availability of more solar light absorbing semiconductors, reduce the effectiveness of using photocatalysis as a large-scale water treatment technology.

To obtain higher photocatalytic activity, selective determination of materials based on the application of interest is necessary. For instance, in solar photocatalytic disinfection, the photocatalyst should be able to produce ROS under solar irradiation. Therefore, understanding the fundamental mechanism of heterogeneous photocatalysis for solar disinfection of water is essential.

1.3.1 Fundamental mechanism of heterogeneous photocatalysis

The IUPAC "Gold Book" defines photocatalysis;

> "*As the change in the rate of a chemical reaction or its initiation under the action of ultraviolet, visible or infrared radiation in the presence of a substance-the photocatalyst-that absorbs light and is involved in the chemical transformation of the reaction partners.*"

IUPAC, Compendium of Chemical Terminology, 2nd ed. (the "Gold Book"),1997 [33].

These photocatalysts facilitate chemical reactions without being consumed or transformed. Photocatalysis can be either homogeneous or heterogeneous. Use of semiconductors in photocatalysis is a class of heterogeneous photocatalysis. It utilises a semiconductor material that acts as a photocatalyst that is excited by electromagnetic irradiation with photon energy equal to or greater than the bandgap energy ($E_{h\nu} \geq E_g$.) [26]. Because of this irradiation, an electron is promoted from the valence band (VB) to the conduction band (CB), leaving behind a positively charged hole in the valence band. Thus, an electron-hole pair (e^--h^+) is generated. These electrons and holes can either recombine or transfer to the particle surface [26]. The conduction band electrons then pass to an electron acceptor (reduction reaction), provided the conduction band edge potential is more negative than the corresponding reduction potential of the electron acceptor. Whereas, the holes may accept electrons from the electron-donating species (oxidation reaction) if the valence band edge is slightly more positive than the corresponding reduction potential of the electron donor. For wide bandgap oxide semiconductors, such as TiO_2, the holes can oxidise water to generate hydroxyl radicals ($^\bullet OH$) which are powerful oxidising agents and electrons in the conduction band can reduce molecular oxygen (O_2) to form superoxide radical anion ($O_2^{\bullet -}$), hydroperoxyl radicals ($^\bullet OOH$), hydrogen peroxide (H_2O_2) and even hydroxyl radical ($^\bullet OH$) through subsequent reduction reactions. These reactive oxygen species (ROS) can inactivate microorganisms or degrade organic pollutants. The product in the case of complete organic pollutant degradation is CO_2 and H_2O, along with inorganic acids or salts. A schematic illustration of the mechanism of photocatalytic disinfection is demonstrated in figure 1.4.

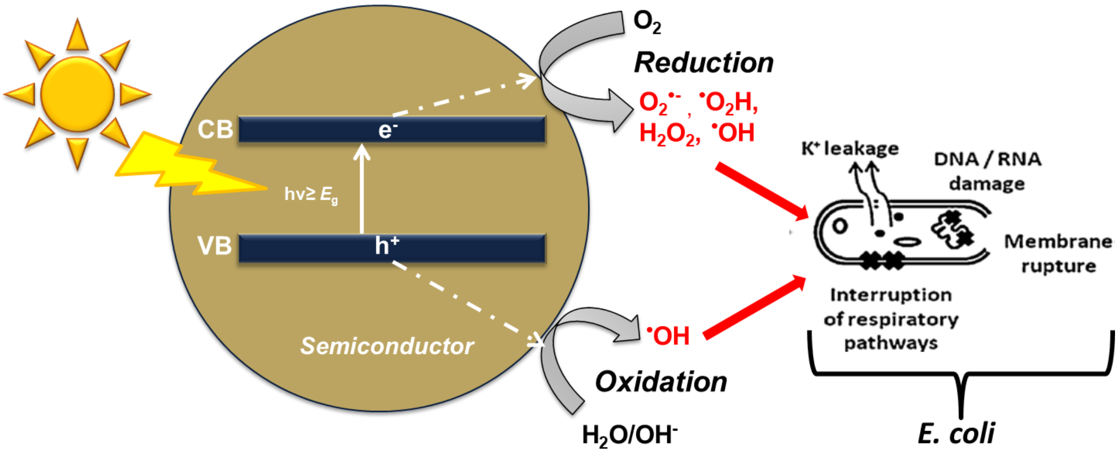

Figure 1.4 Mechanism of photocatalytic disinfection, including ROS generation and inactivation of a bacterial cell.Adapted from Rengifo-Herrera and Pulgarin, Sol. Energy, 84 (2010) 37–43[34].

1.3.2 Reactive oxygen species in solar photocatalytic disinfection

Reactive oxygen species are relatively short-lived species and have half-lives ($t_{1/2}$) in the aqueous environment from nanoseconds to hours. Burn et al.(2012) published a review that focused in-depth on the various analytical and detection methods of ROS generated in surface water and aquatic environment [35]. The reactive oxygen species (ROS) generated during heterogeneous photocatalysis have been reported to cause damage to the DNA or proteins of the microorganisms. For example, ROS attack and damage the cell wall of the bacterial cells. The ROS cause an oxidative attack on the cell membrane leading to lipopolysaccharide oxidation. The cellular respiration provided as an attachment site to the bacterial cell membrane gets damaged and stops. This combination of damage to the cell membrane and oxidative attack on the intercellular components leads to the cell inactivation [36]. In photocatalytic disinfection, potassium ion leakage provides an important evidence of cell damage and membrane disruption.

For metal oxide semiconductors such as TiO_2, the valence band potential is positive enough to generate hydroxyl radical (E^0 $^{\bullet}OH_{free}$ = +2.73 V (NHE) at pH 0) [37]. Apart, from microbial disinfection $^{\bullet}OH$ radicals are also primary oxidants in degrading organic contaminants, particularly weak adsorbing alcohols and aromatic compounds [38].

While hydroxyl radical is the primary oxidising agent in photocatalytic disinfection, other ROS formed from the reduction of molecular oxygen are also involved in the photocatalytic disinfection. Superoxide anion radical ($^{\bullet}O_2^-$)[39], hydrogen peroxide (H_2O_2)[40], and singlet oxygen ($^1O_2$) [40, 41] have been reported to be involved in photocatalytic disinfection. Table 1.1, shows the reaction pathway for ROS formation as per equations 1.1 to 1.7 against their corresponding potential E^0 (vs NHE at pH0). Previously at Ulster, P25-TiO_2 and TiO_2-rGO as photocatalyst were used for mechanistic investigation of photocatalytic inactivation of *E.coli* under both UV-visible and visible only irradiation [40]. The modified catalyst TiO_2-rGO showed a better disinfection activity over unmodified TiO_2. A 6-log reduction of *E. coli* (10^6 CFU.mL^{-1}) was reported in 90 min for TiO_2-rGO in UV-vis irradiation as compared to total inactivation in 120 min for P25-TiO_2. ROS detection studies performed by the authors show H_2O_2, $^{\bullet}OH$ and $^1O_2$ to be the main species involved in the disinfection under UV-visible irradiation with both P25-TiO_2 and TiO_2-rGO photocatalyst. However, only $^1O_2$ was detected as the ROS under visible only irradiation using P25-TiO_2 and TiO_2-rGO photocatalyst.

Table 1.1 Oxygen reduction reactions with the corresponding potential vs NHE [42, 43]

Oxygen reduction reactions	**Potential E^0 (NHE)**	**Eq.**
$O_2 + e^- \rightarrow O_2^{\bullet-}$	-0.16 V	1.1
$O_2 + e^- + H^+ \rightarrow HOO^\bullet$	+0.12 V	1.2
$HOO^\bullet + e^- + H^+ \rightarrow H_2O_2$	+1.47 V	1.3
$H_2O_2 + e^- + H^+ \rightarrow HO^\bullet + H_2O$	+0.80 V	1.4
$O_2 + 4H^+ + 4e^- \rightarrow 2H_2O$	+1.23 V	1.5
$HO^\bullet + H^+ + e^- \rightarrow H_2O$	+2.73 V	1.6
$O_2^1 + e^- \rightarrow O_2^{\bullet-}$	+0.81 V	1.7

1.4 Nanostructured photocatalysts

Photocatalytic disinfection faces many challenges for low inactivation rate. Some of these challenges include the rapid recombination of electron-hole pair generated upon irradiation of photocatalyst, insufficient band potentials to perform photocatalytic reduction or oxidation reactions and to generate ROS. The recombination can be avoided by fabricating nanostructured photocatalysts with the desired band edge potentials for the generation of ROS. The bandgap energy and the corresponding band positions are essential criteria for selecting active photocatalysts. A photocatalyst that has bandgap narrow enough (2-3 eV) to effectively utilise the solar spectrum (UV and visible) and with a wide enough potential window to drive the necessary redox reactions (or more significant overpotential of at least 1.0 V) to generate ROS ($E^0_{H2O/\bullet OH}$ = +2.73 V (NHE) and $E^0_{O2/O2\bullet-}$ = -0.16 V (NHE)) for photocatalytic disinfection is desired.

Titanium dioxide (TiO_2) is by far the most investigated photocatalyst used in water disinfection and treatment with extensive reviews published in literature [25-27, 44-48]. Some of the previous studies on photocatalytic disinfection at Ulster University used *Evonik Aeroxide* (formerly Degussa) P25-TiO_2 as the photocatalyst in suspension [40], immobilised on glass tubes [23], or borosilicate glass plates[49], or on titanium foil[50]. Any novel photocatalysts should be evaluated for its efficiency against a known standard such as P25-TiO_2. The continuous search for alternatives of TiO_2 as novel photocatalytic materials has been going over decades to increase the overall photonic efficiency under UV-vis irradiation. Other semiconductors such as $BiVO_4$, Fe_2O_3, WO_3 or Cu_2O are also reported to show visible light activity. Amongst them, WO_3 is the prominent alternative to TiO_2 due to its positive valence band edge (3.1 V (NHE)) for photocatalytic oxidation reactions [51].

Nanostructuring of bulk semiconductors has been reported to give improvements in photocatalytic activity. For instance, a faster kinetic rate degradation for formic acid was observed with hydrothermally synthesized titania nanotubes when compared to P25-TiO_2 nanoparticles by Wadhwa et al.(2011) [52]. The photocatalytic activity correlated to an increase in the specific surface area obtained for 1D nanotubes (401 $m^2.g^{-1}$), compared to 50 $m^2.g^{-1}$ for P25-TiO_2. Changes in the energy band structure of the bulk materials may be observed through size quantization[53]. The effect comes into consideration when the size of the particle is within few nanometer regimes and becomes comparable to the de Broglie wavelength of the charge carriers or is smaller than the Bohr's radius [54].

A nanomaterial is classified as a material with one of the dimensions being confined to less than 100 nm [55]. With this classification, it can be 0D with all dimensions less than 100 nm (nanoparticles) or smaller (quantum dots), 1D having only one dimension greater than 100 nm (nanorods, nanotubes, nanowires,) or 2D with two dimensions in macroscale or greater than 100 nm (nanosheets, nanoplates). 3D or bulk materials have all dimensions greater than 100 nm [56-58]. A coherent relationship between different classes of nanomaterials in 3D space is illustrated in figure 1.5.

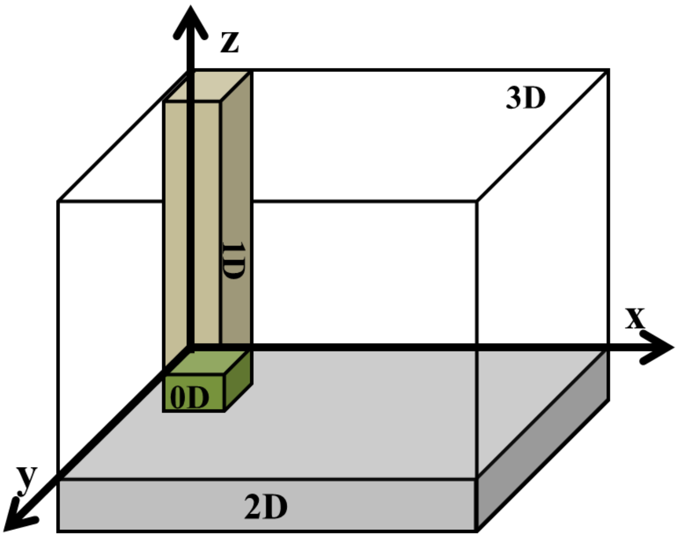

Figure 1.5 Classification of 0D, 1D, 2D nanomaterials in three dimensional space where x, y and z axis represent dimensions less than 100 nm. Reproduced from Ashby et al.(2009) Nanomaterials, Nanotechnologies and Design, (2009)[59].

When moving from bulk materials (3D) to 0D, 1D or 2D nanomaterials, the bandgap of the semiconductor is increased by observing a blue shift in the absorption spectrum. In 0D nanomaterials, no delocalization of electrons takes place, and all electrons are confined in all 3 dimensions, therefore a larger amount of energy is required to excite an electron from the VB to CB of a 0D semiconductor. On the contrary, in a 1D and 2D nanomaterial both delocalization and electron confinement take place together. In 2D materials, the electrons are confined across the nanometer dimension i.e. the thickness. But they are delocalized and free to move in the planar direction. Therefore, under such electron confinement conditions, a semiconductor can be easily modulated for its physical, chemical or structural properties, which is useful to develop novel semiconductor photocatalysts.

The development of two-dimensional nanomaterials (2D) as photocatalysts is more advantageous due to two of the intrinsic characteristic they possess. First is a high specific surface area, increasing the availability of active catalytic sites. And second, the 2D structure of the photocatalyst decreases the migration distance for charge carriers to reach the semiconductor/solution interface. This potentially reduces charge recombination and improves the photocatalytic efficiency of the material. A good overview of the use of 2D materials for photocatalytic applications was covered by Singh et al.(2015) [60]. The authors performed a computational screening of all the existing and potential 2D materials from literature and studied the structural and electronic changes occurring in 2D materials using DFT studies. The majority of the materials covered in this review were potentially used for solar photocatalytic water splitting. Two-dimensional metal oxides such as WO_3 [61], Bi_2WO_6[62] and transitional metal chalcogenides such as MoS_2[63], have been investigated as photocatalysts for different applications. 2D materials and their heterostructures investigated for photocatalytic water disinfection are reviewed in chapter 2.

The layering of two different 2D materials as heterostructured photocatalysts can be expected to improve the limitations of a poor performing photocatalyst with wide bandgap or insufficient band edge potentials. Materials with a high surface area such as graphene, reduced graphene oxide (rGO) or graphene oxide (GO) prove to have superior conductivity, leading to interfacial charge transfer from one semiconductor to another and may reduce charge carrier recombination [40, 41]. Another class of metal-free 2D photocatalyst is graphitic carbon nitride (g-C_3N_4). Recently, this polymeric semiconductor has gained interest in evaluating its photocatalytic efficiency as a single photocatalyst and in the form of heterostructures with other inorganic metal oxide photocatalyst possibly forming 2D/2D heterostructured photocatalysts.

1.5 Electrochemically assisted photocatalytic disinfection of water

One approach to increasing the efficiency of photocatalysis with immobilised photocatalysts is to use electrochemically assisted photocatalysis (EAP) by applying an external electrical potential [64]. A comparison of the photoelectrochemical system to suspended photocatalytic system for water disinfection is shown in figure 1.6.

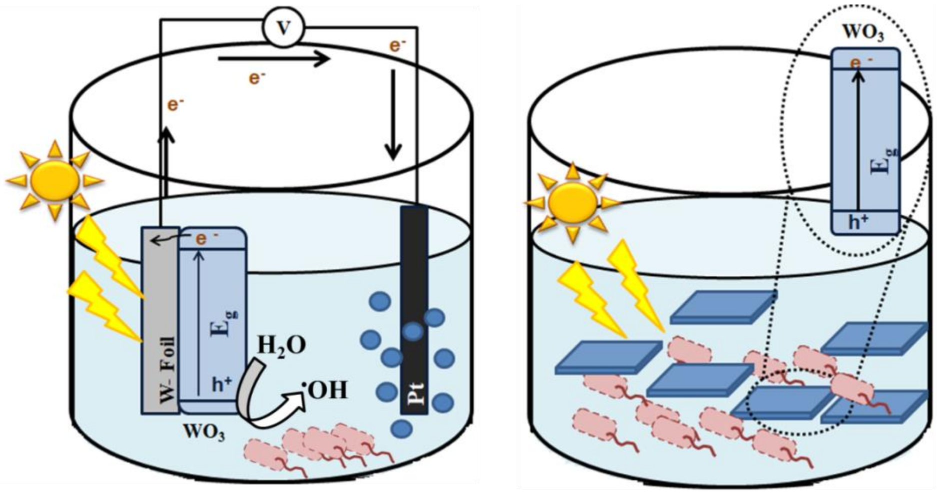

Photoelectrochemical system **Suspended photocatalytic system**

Figure 1.6 Schematic representation of photoelectrochemical vs suspended photocatalytic inactivation of microorganism in water.

Some earlier studies at Ulster University reported the successful use of TiO_2 as photoelectrode for electrochemically assisted photocatalytic inactivation of *E. coli* under externally applied potential. In two separate works, TiO_2 nanoparticles electrodes[65] and electrochemically anodised titania nanotubes along with N-doped titania nanotubes[50] were proven to show *E. coli* inactivation under electrochemically assisted photocatalytic (EAP) conditions with +1.0 V (SCE) as the externally applied potential in UV-Vis irradiation. More recently, materials such as WO_3 have also come under consideration to be used as photo(electro)catalyst for *E. coli* inactivation [66] and also for photoelectrocatalytic pollutant degradation under visible light irradiation [67]. Photoelectrocatalytic water splitting using WO_3 has been studied extensively, but EAP disinfection using WO_3 is relatively unexplored. Therefore, the latter part of this thesis has been in exploring the electrochemical properties of 2D heterostructures for electrochemically assisted photocatalytic disinfection. Considering the new morphology and electronic properties they possess, 2D/2D heterostructures provide an exciting area for research into materials for photocatalytic applications.

1.6 Aim and Objectives of the thesis

1.6.1 Aim

The overall aim of this work was to investigate the use of 2D materials as photocatalysts and to combine narrow bandgap semiconductors in heterostructures which could effectively utilise solar energy for the photocatalytic disinfection of water.

1.6.2 Objectives

i. To undertake a detailed literature review on existing 2D materials for photocatalytic water treatment, including the challenges faced during heterostructure formation
ii. To synthesise 2D nanostructures of tungsten trioxide (WO_3) and graphitic carbon nitride ($g\text{-}C_3N_4$) and to combine these as heterostructured photocatalysts
iii. To study the photocatalytic performance of 2D $WO_3/g\text{-}C_3N_4$ heterostructures for the degradation of organic pollutants and inactivation of *Escherichia coli* K12 under simulated solar irradiation.
iv. To compare the photocatalytic efficiency of the 2D photocatalyst with a known research standard, i.e. *Evonik Aeroxide* P25-$TiO_{2.}$
v. To investigate the photocatalytic charge transfer mechanism taking place between $WO_3/g\text{-}C_3N_4$ heterostructures.
vi. To determine the photoelectrochemical properties of WO_3 and $g\text{-}C_3N_4$ as photoanodes and determine the incident photon to current conversion efficiency.
vii. To test the efficacy of 2D/2D heterostructured WO_3 & $g\text{-}C_3N_4$ as electrodes for the electrochemically assisted photocatalytic inactivation of *E. coli*.

1.7 Thesis structure

Chapter 2 describes a detailed literature review relevant to the thesis title. It starts with an introduction to the use of heterogeneous photocatalysis in water remediation issues, covering the fundamental mechanism of the photocatalytic materials in degrading the organic pollutants, contaminants of emerging concern and inactivation of micro-organisms. The various ideal parameters required for a potential semiconductor photocatalyst have been taken into consideration. An illustration of the energy band diagram with respect to target pollutants reduction/oxidation potential is presented in this chapter. Different possible formations of heterostructures have been discussed and reviewed here correlating the photocatalytic charge transfer mechanism. A significant part of this review focuses on the two-dimensional heterostructured photocatalyst, current challenges and possible solutions. The later section of the report focuses on the 2D materials for photocatalytic disinfection. It ends with the current state of the art research on modification of the efficiency of the heterostructure of 2D WO_3 and g-C_3N_4 on applying an electric potential and considering the photoelectrocatalytic activity of the materials.

Chapter 3 discusses the experimental techniques, materials and methods. All the synthesis methods, analytical methods and calibrations are presented in detail.

Chapter 4 investigates the physicochemical and photocatalytic properties for a range of WO_3 and g-C_3N_4 heterostructures synthesized. The morphological characteristics were studied using TEM, SEM, XRD and specific surface area analysis. The as-synthesized heterostructures were analysed for their photocatalytic efficiency under simulated solar irradiation for degradation of phenol and formic acid as model pollutants. Their photocatalytic disinfection capability was also assessed using photocatalytic inactivation of *E. coli* K12 in water under simulated solar irradiation.

Chapter 5 investigates the reasons for the limited photocatalytic activity of the WO_3/g-C_3N_4 heterostructures, by performing chemical probe studies on the parent 2D WO_3 and g-C_3N_4 photocatalysts. It also includes the analysis of the chemical and optical properties of the materials and to determine their effect on the charge transfer process. This chapter finally, provides some electrochemical evidence of trapped electronic states below the expected band edges and is concluded with giving a summary of the potentials of the traps identified and its effect in photocatalytic performance.

Chapter 6 studies the photoelectrochemical properties of the synthesized WO_3 and g-C_3N_4 nanomaterials. The nanomaterials were fabricated on a range of substrate to be used as photoelectrodes, and their photoelectrochemical response was analysed by linear sweep voltammetry and current at fixed potential. The fabricated photoelectrodes were used as potential photoanodes for investigating the electrochemically assisted photocatalytic disinfection of water under simulated solar irradiation. A comparative investigation of EAP water disinfection using WO_3/g-C_3N_4 and WO_3 photoelectrodes was done with previous reports on P25-TiO_2 and titania nanotube electrodes analysed under same EAP conditions at Ulster University.

Chapter 7 discusses the overall conclusion of the thesis and research conducted with key discussions on the potential charge transfer mechanism of the heterostructure formation in photocatalysis and electrochemically assisted photocatalysis. Recommendations and summary of the future work have also been presented here.

Chapter 2. Literature review

2.1 Introduction

In 2019, WHO released statistics on the current drinking water quality and management services [68]. According to the statistics, 785 million people globally still lack access to basic drinking water services. This was further classified into 3 categories:

- A population of 206 million were relying on improved sources of water by collection from limited sources located more than 30 min away from their household,
- Another, 435 million were depending on water from unimproved sources such as spring and unprotected wells and,
- And 144 million people were relying on untreated surface water directly coming from lakes, rivers, streams and ponds.

Consumption of water from these limited, unimproved and unsafe sources, has cost nearly 485 000 diarrhoeal deaths globally every year. To reduce the number of preventable deaths caused by drinking water contaminated with pathogens, household water treatment interventions and safe storage (HWTS) were established by WHO in coordination with UNICEF. The HWTS were implemented to manage drinking water safely at the point of use and collection [21]. A straightforward water treatment intervention is solar water disinfection. It is referred to as a treatment in which inactivation of pathogens present in water takes place as a result of irradiation by sunlight leading to some direct and indirect attack on the functioning mechanisms of pathogens. The protocol based on solar water disinfection is often referred to as SODIS. A good understanding and overview of the protocol and technology of solar water disinfection have been described in the SODIS manual by Luzi et al.(2016) [22]. SODIS protocol following the solar disinfection intervention works well as an immediate treatment. However, its implication is affected by several other facts such as dependency on a specific amount of solar intensity, use of clear PET bottles for maximum penetration of light, the effect of water turbidity, (requires a pre-filtration step for turbidity > 30 NTU), ineffective against few resistant pathogenic micro-organisms, relatively slower and time-consuming process to generate large volumes of safe drinkable water and includes the risk of recontamination and unsafe storage after treatment[22].

The shortcomings of solar disinfection can be overcome by the potential use of advanced oxidation processes (AOPs), which are processes based on the generation of reactive oxygen species (ROS) in the form of radicals or anions, helpful for inactivation of microbial contaminants in drinking water. Heterogeneous photocatalysis is one such technology that works well for the production of ROS. Heterogeneous photocatalysis (or semiconductor photocatalysis) is a potential approach for disinfection of drinking water in lower and middle-income countries such as Africa [69] and Asia or the tertiary treatment of wastewater for re-use[70, 71]. It is employed in the treatment of water using a semiconductor. It allows the possibility of a breakdown of persistent organic pollutants and micro-organisms present in water under artificial or solar irradiation. The primary reactions involved in semiconductor photocatalysis are the electrochemical reduction and oxidation reaction (redox reactions) utilising the electron and hole pair generated during the process as depicted in figure 2.1.

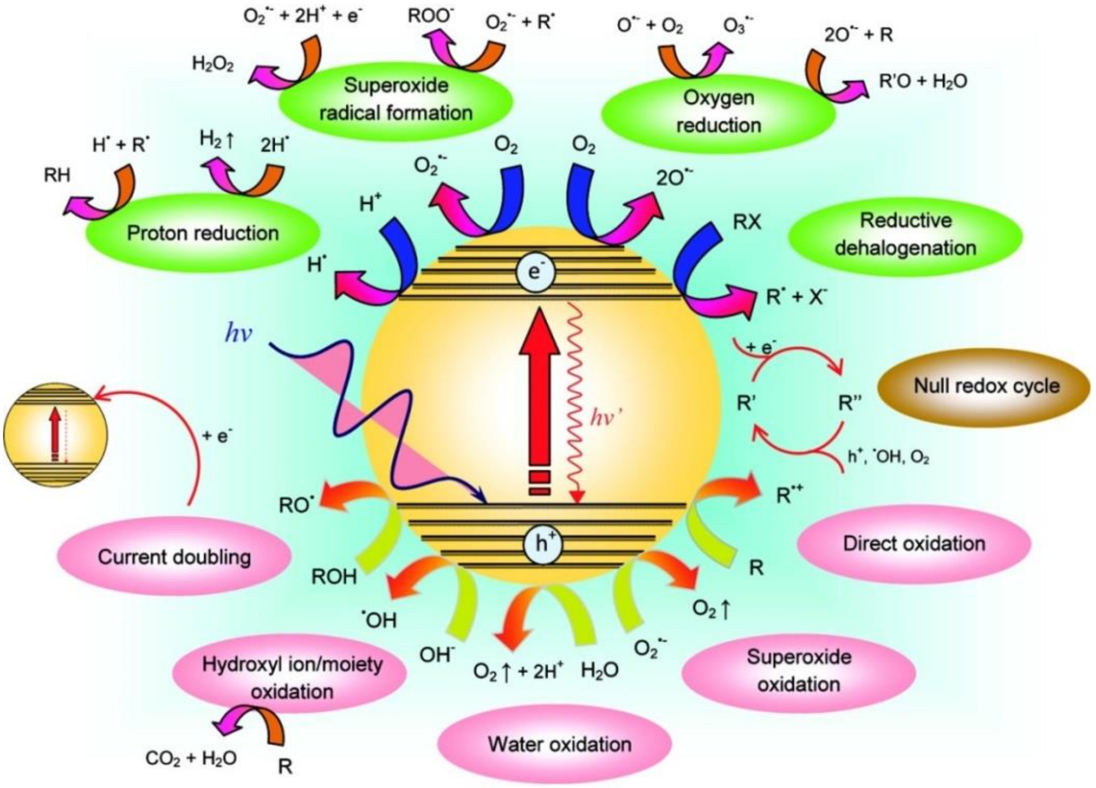

Figure 2.1 Possible reaction pathways arising from the excitation of photocatalysts, R denotes the general organic electron donor molecule. Reproduced from Amal et al.(2012), The Journal of Physical Chemistry Letters, 3 629-639(2012)[72] .

Photocatalysis has been proposed for a wide range of environmental applications, including air remediation and the oxidation of NO [73, 74], or the conversion of CO_2 to fuels (artificial photosynthesis)[75]. Research into photocatalysis has been ongoing for at least 5 decades. The first report on photoelectrolytic water splitting was published in 1972 by Fujishima and Honda on TiO_2 semiconductor electrodes under UV irradiation [76]. Many researchers have investigated the environmental remediation applications with heterogeneous photocatalysis including Fox and Dulay [77] Hoffmann and Bahnemann [27], Mills [25, 44], Kamat [78], Eggins and Byrne[31, 79, 80], and Amal[54].

There are five basic working steps of heterogeneous photocatalysis taking place (Figure 2.2). First, the semiconductor surface is irradiated with electromagnetic irradiation with energy equal to or greater than the bandgap energy (E_{bg}) of the material (step-1). As a result, an electron-hole pair (e^--h^+) is generated (step-2). The excitation of an electron from the filled valence band (VB) to the empty conduction band (CB) takes place, leaving behind a positively charged hole in the valence band (step-3). These electrons and holes can either recombine and emit energy in the form of heat or light (step-4), or transfer to the particle surface (step-5). Now, at the particle surface, the electrons in the conduction band (CB) edge can pass to an electron acceptor having a more positive reduction potential as compared to the semiconductor’s CB. Simultaneously, the positive holes in the valence band (VB) can accept electrons from the electron-donating species that have a more negative reduction potential than the VB. The overall reaction taking place here is the reduction of the electron accepter and the simultaneous oxidation of the electron donor. This electrochemical redox process is driven by the potential difference generated in the semiconductor by the absorption of the photon energy. This overall potential difference is equivalent to the semiconductor’s bandgap energy.

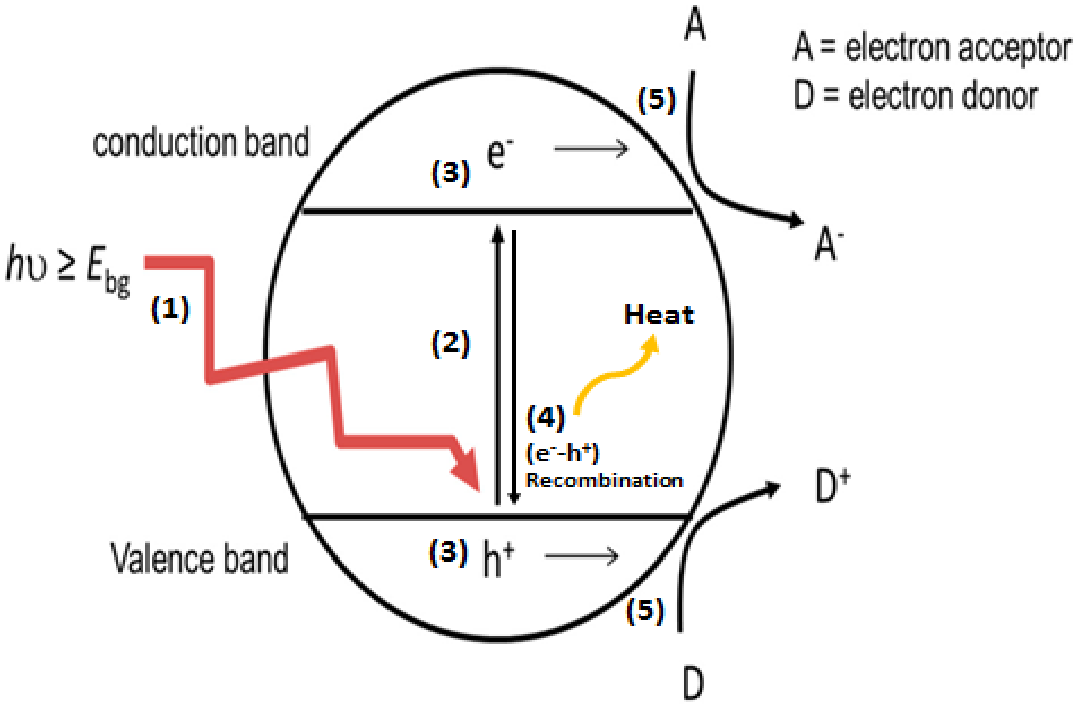

Figure 2.2 Mechanism of heterogeneous photocatalysis. Adapted from Byrne et al.(2015), Molecules 20, 5574-5615 (2015) [26].

While semiconductor photocatalysis is a very interesting phenomenon, there are several challenges to overcome to achieve higher quantum efficiencies; these include improving the separation and lifetime of charge carriers, and matching the band edge potentials to the half-cell reactions of interest, enhancing the use of the solar spectrum to include the visible photons. Nano-photocatalytic materials provide a greater surface area to volume ratio for the adsorption of pollutants, short diffusion lengths for charge carriers to reach the semiconductor air/water interface. In some cases, size quantisation may be observed, leading to an increase in the absorption coefficient for certain photon wavelengths (but with a blue shift in the absorbance spectrum).

2.1.1 Photocatalytic materials

The most employed semiconductor materials considered for photocatalytic applications are transition metal oxides (TMOs) and transitional metal chalcogenides (TMCs) [81-83]. For a material to be a good photocatalyst for water treatment and disinfection, it should possess some of the following characteristics:

i. Narrow bandgap (for utilisation of solar energy) and suitable positions of the conduction band and valence band with respect to the reduction and oxidation potentials for the generation of reactive oxygen species
ii. Good charge separation and good charge carrier diffusion lengths
iii. Large surface area
iv. Available and low cost
v. Photochemically, chemically and thermally stable
vi. Non-toxicity.

Figure 2.3 shows some examples of n- and p-type semiconductors with their respective band edge potentials used as photocatalysts. For photocatalytic disinfection, the photocatalyst should possess suitable band edge potentials to reduce molecular O_2 to generate superoxide ($^{-}O_2^{\bullet}$) (E^0 = -0.16 V (NHE)) and to oxidise water (H_2O) or hydroxide ions (^{-}OH) to produce hydroxyl radicals ($^{\bullet}OH$) (E^0 = +2.73 V (NHE)).

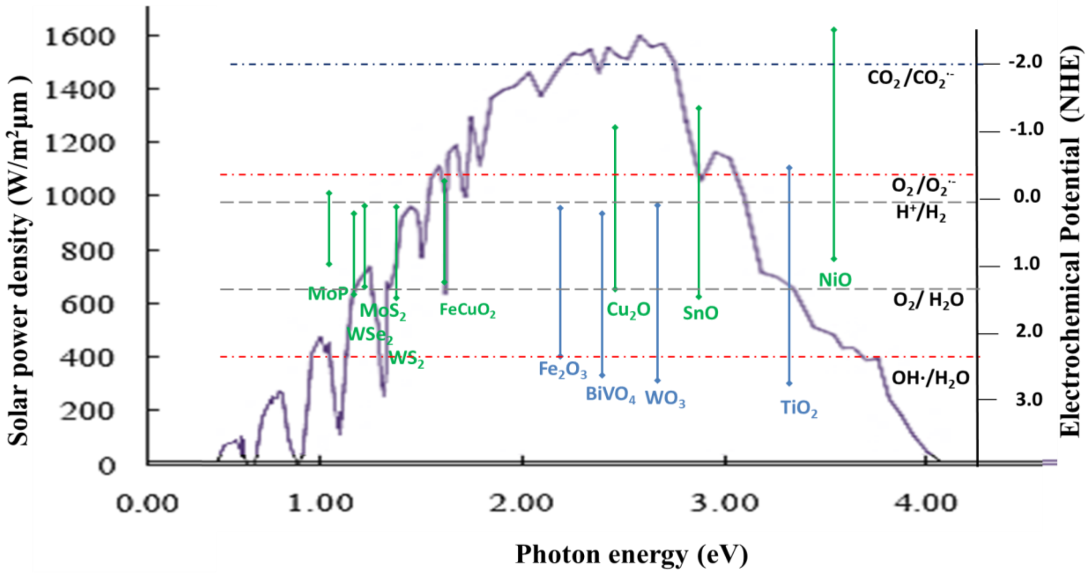

Figure 2.3 Semiconductor photocatalysts with their bandgap and band edge potentials with *E* (NHE, pH 0) with redox potentials and solar power density. p-type (green) and n-type (blue). Adapted from the solar power density vs photon energy diagram of Z.B. Van, Principles of semiconductor devices, (2011) [84].

As shown in figure 2.3, TiO_2 is the only metal-oxide semiconductor that satisfies this criterion, other examples not included in the figure but meet the criteria are ZnO and $SrTiO_3$. However, its wide bandgap limits its efficiency for solar applications. Other semiconductors (SCs) can also absorb the UV and some visible photons and have the necessary potential to oxidise water, e.g. WO_3 [85], $BiVO_4$ [86] and Fe_2O_3[87] but their CB edge is not sufficiently negative to driven the one-electron reduction of O_2. Similarly, p-type materials like Cu_2O [88], SnO show some potential for photocatalytic reduction due to their negative CB potential. However, p-type semiconductors are typically unstable in aqueous environments and undergo photo-corrosion. Not all semiconductor materials are suitable as photocatalysts (for water related applications) mainly due to their inappropriate band edge positions and instability in aqueous environments. There is some opportunity to combine two (or more) narrow band SCs to create heterostructures which can utilise more than one photon provided they have the necessary CB and VB potentials to drive the formation of ROS [89].

2.1.2 Heterostructure formation

In physics, a heterostructure is defined as a semiconductor structure in which chemical composition can change with the position [90]. The simplest heterostructure is a single heterojunction. Whereas a heterojunction is defined as the semiconductor crystal’s interface across which the chemical composition of the semiconductor has been changed. Heterostructures can be classified in 3 basic types based on their alignment of band positions, i.e. Type-I, Type-II and Type-III (Figure 2.4).

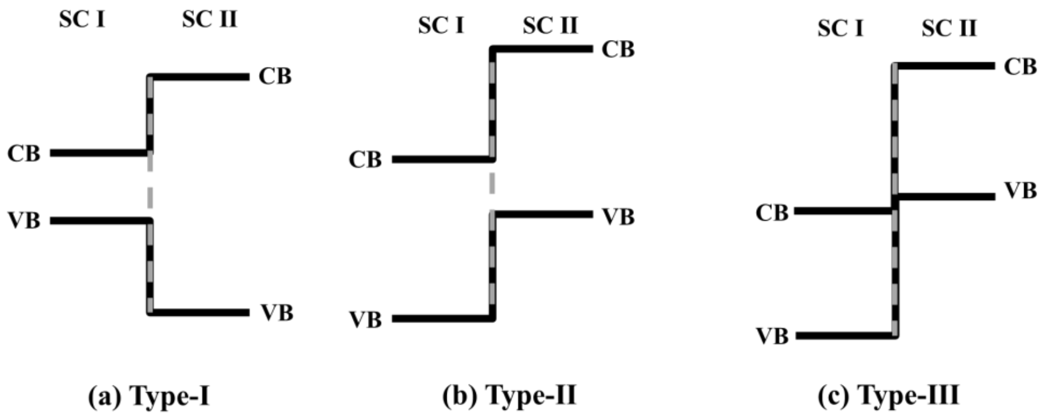

Figure 2.4 Different type of heterostructures (a) Type-I straddling gap; (b) Type-II staggered gap and (c) Type-III broken gap. ----The grey dotted line is the heterojunction interface.

Type I (straddling): A type-I heterostructure is one where the bandgap of one semiconductor (SC I) is entirely overlapped with the bandgap of the other semiconductor (SC II) (Figure 2.4a). It is often referred to as the straddling type, where SC I is entirely situated within the SC II. An example to include is GaAlAs-GaAs. Such heterostructures are unsuitable for photocatalytic applications due to rapid recombination of charges and low redox potential to promote the photocatalytic reduction or oxidation reactions, which are entirely, based on SC I.

Type II (staggered): These heterostructures are the staggered type, where charge transfer takes place via band to band. The CB and VB of SC I are positioned at a lower potential than that of SC II (Figure 2.4b). Also, the bandgap of SC I is not entirely necessary to be smaller than SC II. A typical example of type-II heterostructure is InP-InSb. In terms of photocatalysis, under irradiation the photogenerated electron in type-II heterostructures transfer downhill from more negative CB of SC II to CB of SC I, where the photocatalytic half reduction reactions take place. On the other hand, the hole transfer is from more positive VB of SC I to VB of SC II, where oxidation reactions take place in VB of SC II. Although type II heterostructures have effective charge separation with the electron in CB of SC I and hole in VB of SC II, the overall potential window to drive the photocatalytic redox reactions is reduced in this case too.

Type III (broken gap): Type-III heterostructures are the category wherein both SC I and SC II in heterojunction have broken gap between their band positions. In this type, the bandgap of SC I and SC II do not overlap with each other. However, the charge transfer upon irradiation is similar to type-II heterostructures (Figure 2.4c).

The two-photon excitation mechanism in semiconductor photocatalysis is analogous to the natural photosynthesis process in green plants. This phenomenon was initially compared by Bard in 1979, where a dual n-type semiconductor photoelectrosynthesis system was compared to the biological photosynthesis [91]. In photosynthesis, the CO_2 reduction and water oxidation take place at the two different chlorophyll-protein complex photosystems referred to as photosystem I and photosystem II (Figure 2.5a). Likewise, a type-II heterostructure can follow two-photon excitation mechanism in two processes, i.e. a traditional band to band charge transfer (Figure 2.5b) or via z-scheme (Figure 2.5c). In a z scheme charge transfer mechanism, upon irradiation of the heterostructure with dual photon energy (hν), the generation of electron-hole pairs take place in both SC I and SC II with electron transfer from the CB of SC I into the VB of SC II. At this point, some recombination might take place between the electrons from SC I and holes of SC II. However, the photoexcited electrons in SC II will be free to perform reduction reactions and photogenerated holes left behind in SC I will be taking part in the oxidation reactions. The photocatalytic oxidation and reduction take place at different semiconductors, i.e. semiconductor I (SC I) acting as oxidation photocatalyst and semiconductor II (SC II) acting as reduction photocatalyst. No significant loss of overpotential during the electron transfer takes place via z scheme mechanism making it more advantageous over the traditional band to band transfer type-II heterostructures. A much larger potential window is achieved to drive overall photocatalytic reactions. Type-II and z-scheme photocatalysis that have been investigated for heterostructure combinations of WO_3/g-C_3N_4 [92-102] WO_3/TiO_2 [103], g-C_3N_4/TiO_2 [104, 105] for photocatalytic water treatment and gas phase applications are discussed in later sections.

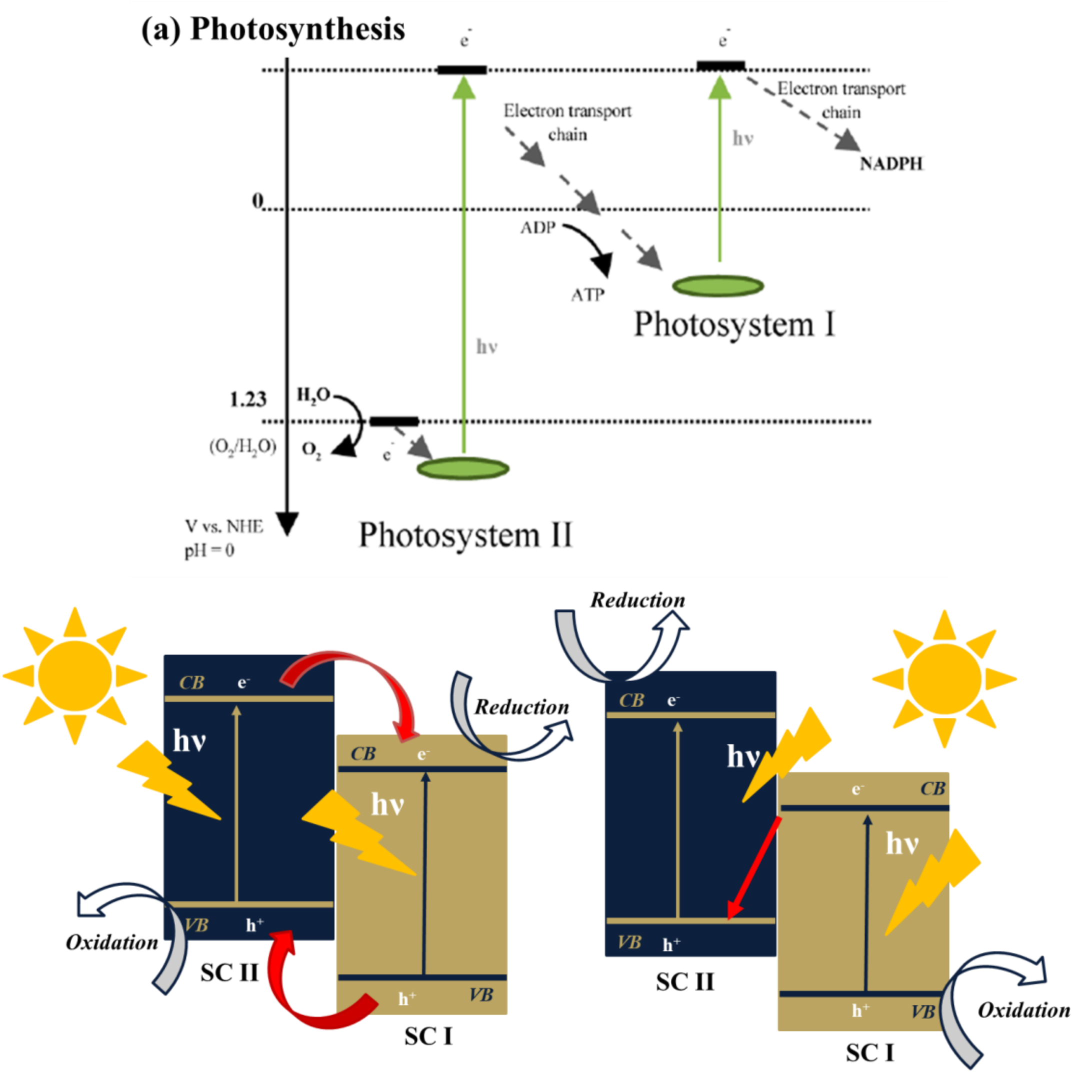

(b) Band to band transfer **(c) Z-scheme**

Figure 2.5 Mechanism of two-photon irradiation in (a) photosynthesis; and type-II heterostructured photocatalysts with charge-transfer (b) via band to band and (c) z-scheme. Figure (a) adapted from Martin et al. (2014), J. Am. Chem. Soc. 136, 36, 12568-12571 (2014)[106].

Solid-state z schemes have become more attractive recently. For example, a combination WO_3 as the oxidation half and g-C_3N_4 for the reduction half-reaction will be a suitable choice for a z-scheme photocatalytic system. WO_3 does not have a negative enough CB edge (+0.42 V, NHE) to reduce H^+ or O_2. However, the VB edge(+3.1 V, NHE) is capable of oxidising water to produce O_2(+1.23V, NHE) [107] or $^{\bullet}OH$ radicals(+2.73 V, NHE) [108] under visible light irradiation. Similarly, g-C_3N_4's CB potential (-1.13 V,NHE)is negative enough to reduce H^+ to produce H_2 (0 V,NHE) [109] or produce other reactive oxygen species such as $^{\bullet}O_2^-$ (-0.16 V,NHE) [110], H_2O_2 (+0.695 V, NHE) [111] or by multiple electron reduction of O_2 to $^{\bullet}OH$ radicals [112]. The reported examples of z-scheme of WO_3/g-C_3N_4 for visible light photocatalytic applications will be discussed in detail in later sections.

2.2 Two Dimensional (2D) nanomaterials as photocatalysts

After the successful isolation of free-standing monolayer of graphene from bulk graphite in 2004 by Giem and Novoselov, a path for the development of new two dimensional (2D) materials had been paved [113]. Functionalisation of 2D materials in layered combination with another 2D material is referred to as 2D/2D heterostructures. Such materials offer opportunities in developing technologies such as optoelectronic devices, photovoltaics or energy transformation and automobiles. With increasing or decreasing the number of layers during heterostructure formation, engineering of the bandgap is possible, with each layer inducing large electric field. Often 2D heterostructures are based on the van der Waals interactions taking place between the layers and are called van der Waals heterostructures [114-116]. The unique electronic and optical properties that these 2D heterostructures offer have made them fascinating candidates in heterogeneous catalysis too [115]. A wide classification of available 2D materials in literature has been presented in figure 2.6. Some of these materials have been already investigated in heterogeneous catalysis, while other materials are yet to be investigated. For example, materials like MoO_3, WO_3 and CuO are potentially stable in air; therefore, use of these materials as heterogeneous catalyst is a probable choice.

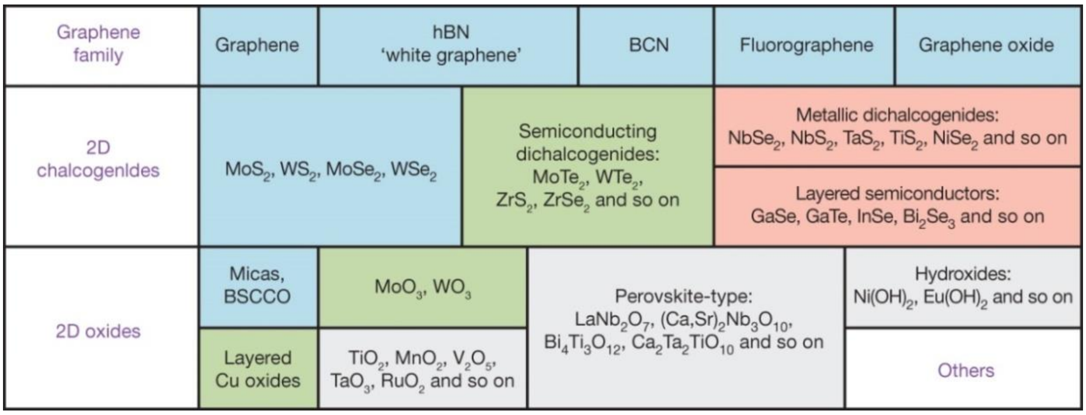

<table>
<tr><td>Graphene family</td><td>Graphene</td><td colspan="3">hBN
'white graphene'</td><td>BCN</td><td colspan="2">Fluorographene</td><td>Graphene oxide</td></tr>
<tr><td rowspan="2">2D chalcogenides</td><td colspan="2" rowspan="2">MoS_2, WS_2, $MoSe_2$, WSe_2</td><td colspan="3" rowspan="2">Semiconducting dichalcogenides:
$MoTe_2$, WTe_2,
ZrS_2, $ZrSe_2$ and so on</td><td colspan="3">Metallic dichalcogenides:
$NbSe_2$, NbS_2, TaS_2, TiS_2, $NiSe_2$ and so on</td></tr>
<tr><td colspan="3">Layered semiconductors:
GaSe, GaTe, InSe, Bi_2Se_3 and so on</td></tr>
<tr><td rowspan="2">2D oxides</td><td>Micas,
BSCCO</td><td colspan="2">MoO_3, WO_3</td><td colspan="3" rowspan="2">Perovskite-type:
$LaNb_2O_7$, $(Ca,Sr)_2Nb_3O_{10}$,
$Bi_4Ti_3O_{12}$, $Ca_2Ta_2TiO_{10}$ and so on</td><td colspan="2">Hydroxides:
$Ni(OH)_2$, $Eu(OH)_2$ and so on</td></tr>
<tr><td>Layered
Cu oxides</td><td colspan="2">TiO_2, MnO_2, V_2O_5,
TaO_3, RuO_2 and so on</td><td colspan="2">Others</td></tr>
</table>

Figure 2.6 2D materials reported in the literature against their stability under ambient condition. 🟦 Materials proved to be stable under ambient room temperature + air; 🟩 Materials potentially stable in the air; 🟥 Materials unstable in air, but stable in an inert atmosphere; ⬛ 3D materials exfoliated from monolayers with limited information on stability; other includes 2D material based on nitrides, borides and carbides. Reproduced from Geim & Grigorieva, Nature 499, 419-425 (2013) [116].

2D materials as photocatalysts stand out as being more advantageous over their counterparts 0D and 1D nanomaterial, because of their properties that potentially improve the overall photocatalytic efficiency. Due to a 2D configuration, the specific surface area of such materials is enhanced as compared to 0D and 1D materials, and hence they offer increased active sites for photocatalytic reactions. The migration distance for the photogenerated electrons and holes to reach the semiconductor/solution interface is also reduced in 2D material photocatalysts, provided the e^--h^+ transfer does not take place at the edge planes of the 2D materials. However in some exceptional cases, the electron transfer at the edge plane is important, e.g. graphene which is a zero bandgap semiconductor. Therefore, a slower electron-hole pair recombination rate is expected.

Few of the critical parameters required for a 2D material photocatalyst for solar water splitting reactions were listed by Singh et al.(2015) in their review. A 2D photocatalyst in addition to the critical parameters required for an ideal photocatalyst mentioned earlier in section 2.2.1, should also have properties such as low formation energy, low backward reaction rate, ability to absorb solar photons, insolubility in water, passivated edges, and should form a stable suspension in water [60]. Passivation of edge or corners of the 2D photocatalyst is crucial to minimise the undesired chemical reactions such as the attack of ions present in the solution. Low formation energy in 2D material relative to its bulk counterpart is required, such that single layer or flakes can be extracted and suspended easily in solution. Theoretical studies and computational screening of 2D materials with density functional calculation can help in establishing the bandgap and band edge potentials of novel 2D materials in an absolute vacuum. The band edge potentials of materials of interest should straddle across the redox potentials of desired photocatalytic reactions for ROS generation. An insight into the true nature of 2D photocatalyst through such computational screening potentially will help differentiate novel photocatalysts suitable for solar water disinfection from applications like solar photocatalytic water splitting.

In this review, a list of available 2D photocatalysts investigated for photocatalytic disinfection of water has been outlined. Photocatalytic disinfection using 2D material as photocatalyst has gained a progressive interest. Many researchers have attempted to fabricate 2D morphologies of existing semiconductor photocatalysts such as TiO_2, WO_3, Bi_2WO_6, MoS_2, and more recently antibacterial activities using 2D morphology of CuO and VS_2 have also been reported. These 2D materials were studied as either single or in heterojunction with another 2D material for their photocatalytic disinfection activity by the inactivation of microorganisms present in water. Carbon-based 2D materials such as graphene, rGO have also been reported to show promising results for the photocatalytic inactivation of microorganisms.

2.2.1 2D-Metal oxides as photocatalysts for water disinfection

Metal oxide semiconductors have been the first choice for photocatalytic applications. Materials like TiO_2, WO_3, ZnO, SnO_2, etc. were fabricated in 2D morphologies to test their photocatalytic performance. Metal oxide 2D nanosheets were successfully obtained in the past using top-down strategies such as exfoliation of layered metal oxides into a monolayer of atom thickness or vice versa by applying the bottom-up approach, via controlling the reaction parameters such as pH, temperature, time, solvent etc., leading to nucleation of smaller particles to obtain 2D sheets. Research on TiO_2 morphologies other than 2D has been published for water disinfection using nanoparticles, nanotubes, nanorods and so on. However, 2D-TiO_2 is relatively unexplored for photocatalytic disinfection. The photocatalytic performance of TiO_2 largely depends on its crystal structure and exposed facets. To increase the absorption of TiO_2 in visible region, use of metal dopant or changes in its crystal structure have been performed in the past via controlling the growth in specific facet/orientations. The use of metal dopants improve the photocatalytic activity of the 2D titania sheets under visible light irradiation is most commonly reported. For instance, 2D-TiO_2 nanosheets with dominant crystal facet (001) were fabricated by introducing dopants such as carbon [117], nitrogen [118], boron and fluorine [119] in the crystal lattice of anatase-TiO_2 and the photocatalytic performance was evaluated under visible light irradiation. However, only Wang et al.(2013) investigated the efficiency of TiO_2 nanosheets with co-dopants boron and fluorine for photocatalytic disinfection with *E. coli* as the model microorganism [119]. They reported 100% inactivation of *E. coli* using B, F doped TiO_2 nanosheets in 15 min under visible light irradiation. However, Wang et al.(2013) offered no explanations of the basic reaction conditions such as start concentration of *E. coli* used, the volume of the total photocatalytic-*E. coli* suspension, or the photocatalytic reactor cell dimensions. In another case, ultra-thin 2D-TiO_2 nanofilms were reported to show antibacterial activity in the dark towards *E. coli* and *E. faecalis* [120]. They reported that the 2D- TiO_2 nanosheets were pre-irradiated with UV light, and the photogenerated electrons were stored as memory in the TiO_2 films, which were later released in dark catalysis to generate ROS and inactivate the microorganisms. This study used photo-excitation as a pre-step for the generation of electrons and used 2D-TiO_2 nanosheets as antibacterial memory film for disinfection to occur. The use of Ag nanoparticle to improve the photocatalytic performance of 2D-TiO_2 nanoporous layers was also reported for antibacterial activity [121]. Two-dimensional heterostructures of TiO_2-Bi_2WO_6 prepared by a two-step hydrothermal method in the study of Jia et al.(2016) displayed a total reduction (10^7 CFU.mL^{-1}) of *E. coli* in 1.5 h visible irradiation. The photocatalytic disinfection mechanism was correlated to the generation of radical species detected by a spin trapping method [62].

Similarly, Ma et al.(2015) investigated heterostructures of 2D/2D TiO_2-Fe_3O_4 for photocatalytic destruction of *E. coli* and *S aureus*. The VB h^+ and H_2O_2 were presented as the primary ROS towards photocatalytic disinfection in their report [122]. Bismuth based photocatalyst materials can be fabricated with 2D morphology and have been reported to show visible light activity. Due to their narrow bandgap, materials like Bi_2WO_6, Bi_2MoO_6, Bi-oxyhalides (BiOBr, BiOCl, BiOI) have been explored for their photocatalytic performance by researchers for inactivation of microorganisms present in water. These materials are explored in detail in later sections.

2.2.1.1 Tungsten oxide (WO_3) as a 2D metal oxide photocatalyst

Use of materials with extended absorption spectrum into the visible region of the solar spectrum can potentially improve the photocatalytic yields for solar and ambient lighting applications. One such material is tungsten trioxide (WO_3), which is capable of utilising approximately 12% of the solar spectrum with an absorption band extended up to 460 nm. Previously at Ulster University, the potential use of nanocrystalline thin films of WO_3 as visible light active photocatalyst for water oxidation was examined by Hamilton et al.(2008) [123]. The WO_3 thin films prepared by different tungsten precursor were investigated for their photoelectrochemical performance in comparison to a sol-gel synthesized TiO_2 thin film under simulated solar irradiation. The outcome of their investigations was that both WO_3 and TiO_2 thin films were reported to exhibit comparable efficiency (IPCE %) of 7% UV-Vis irradiation but at different peak wavelengths, i.e. TiO_2 at 355 nm and WO_3 at 380 nm, with the WO_3 showing some visible IPCE. These findings were one of the initial reports that prompted the use of WO_3 over TiO_2 as photocatalyst under visible light irradiation.

WO_3 is an n-type transition metal oxide (TMO) semiconductor which is of interest due to its narrow bandgap (E_g) of ~2.7 eV. It is an attractive candidate due to its non-toxicity, photochemically and thermally stable nature, and good stability in acidic solutions. It exists in six different polymorphs by sharing corners and edges that are: monoclinic I (γ-WO_3), monoclinic II (ε-WO_3), triclinic (δ-WO_3), tetragonal (α-WO_3), orthorhombic (β-WO_3), and cubic WO_3 [124]. The phase transition of WO_3 crystals takes place during the annealing and cooling process from temperatures as low as -43°C to 740°C. The phase transformation in bulk form occurs due to changing temperatures in the following sequence: monoclinic II (<−43°C) → triclinic (−43°C to 17°C) → monoclinic I (17°C to 330°C) → orthorhombic (330°C to 740°C) → tetragonal (> 740°C). In all the phase transitions of WO_3, monoclinic I (γ-WO_3) has been reported as the most stable phase of bulk-WO_3 at room temperature. WO_3 is generally referred to as γ-WO_3 in most of the research studies. A complete structural representation of the WO_3 is given in figure 2.7.

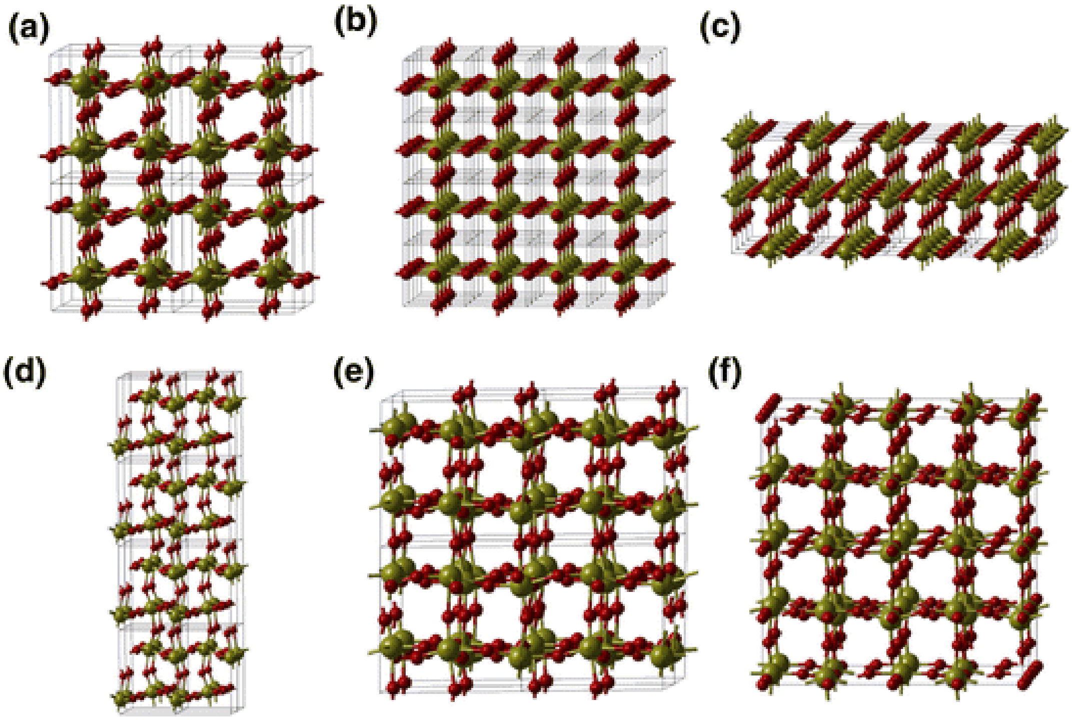

Figure 2.7 The structural models of various phases of WO_3: (a) room temperature monoclinic; (b) simple cubic; (c) tetragonal; (d) low temperature monoclinic; (e) triclinic and (f) orthorhombic structures. The large green and small red spheres represent W and O atoms, respectively. All the models shown contain 256 atoms. Reproduced from Valentin et al.(2013), Catalysis, 56 1404-1419 (2013) [124].

Other forms exist including hexagonal-WO_3 (h-WO_3) that is stable at room temperature, but changes to γ-WO_3 on annealing at temperature > 400°C. The transition of phases in nano-WO_3 is comparatively lower than the bulk WO_3. This is mainly due to the morphological structure of WO_3, which is affected during the synthesis process and also depends on the initial precursors. Even though limited research has been taken on the influence of crystal structure on the photocatalytic activity, it is proposed that γ-WO_3 is more suitable for photocatalytic applications than h-WO_3.

However, just like other semiconducting photocatalysts, WO_3 has disadvantages including slow hole migration kinetics, slow interfacial charge transfer at the semiconductor/electrolyte interface, and therefore faster charge carrier recombination rate. Despite having a suitable narrow bandgap of ~2.7 eV, the conduction band potential of WO_3 (+0.42 V, NHE) is more positive than proton reduction potential (0.0 V, NHE) or oxygen reduction potential (-0.16 V, NHE) leading to poor photocatalytic reduction reactions. Therefore, it is unable to liberate hydrogen gas by the reduction of

H^+ or form ROS through reduction of molecular oxygen. However its valence band potential (+3.1 V, NHE) is more positive than the water oxidation potential (O_2/H_2O (+1.23 V, NHE)), making it favourable to perform photocatalytic oxidation reactions such as oxidation of water to yield oxygen or photocatalytic oxidation of organic pollutants via $^{\bullet}OH$ radical formation (+2.73V, NHE). Different strategies have been adopted to improve the photocatalytic activity of WO_3, by improving the charge transfer rate and charge separation, by controlling the morphology of the material through size quantisation or by elemental doping/co-catalyst loading and also by the construction of heterojunctions with other semiconducting materials.

2D-WO_3 as photocatalyst by size quantisation: Waller and co-workers fabricated single crystal WO_3 nanosheets by exfoliating layers of $Bi_2W_2O_9$ [107]. A size quantisation effect was reported by the authors. The bandgap (E_g) shifts from 2.68 eV (bulk-WO_3) to 2.81 eV in $Bi_2W_2O_9$ consisting of W_2O_6 layers with 0.75 nm thickness. Further, the exfoliation of $Bi_2W_2O_9$ to WO_3 nanosheets shifts the bandgap to 2.88 eV with changes in the crystal structure, i.e. formation of monoclinic WO_3 from tetragonal $Bi_2W_2O_9$. The prepared WO_3 nanosheets and bulk-WO_3 were used with aq. $AgNO_3$ and $(NH_4)_2Ce(NO_3)_6$ solutions to observe the photochemical oxygen formation in visible only irradiation and under the full solar spectrum. They reported bulk-WO_3 gave the maximum O_2 evolution rate of 69.7 μmol.h^{-1} with $AgNO_3$ (aq.) as compared to the WO_3 nanosheets (+ $AgNO_3$) that had 35.5 μmol.h^{-1} under the solar spectrum. The O_2 evolution rate was reduced by 1.8 times in bulk-WO_3 and 6.8 times in WO_3 nanosheets in visible light irradiation. However, Waller et al.(2012) reported the O_2 evolution rate and quantum efficiency yields to change under monochromatic irradiation at 375 nm using a LED light source. WO_3 nanosheets observed a higher quantum efficiency of 1.55% than bulk-WO_3 with 1.43% under 375 nm LED irradiation in the presence of $AgNO_3$. The improved quantum efficiency and O_2 evolution rate in WO_3 nanosheets (3.2 μmol.h^{-1}) over bulk WO_3(2.5 μmol.h^{-1}) in the monochromatic irradiation as compared to full solar spectrum was attributed to the absorption of low energy photons by WO_3 nanosheets in full solar irradiation, that was avoided under 375 nm irradiation. From the onset potential for anodic photocurrent, the conduction band edge was determined to be at +0.11 V for nano-WO_3, and +0.23 V for bulk-WO_3 i.e. a blue shift in the onset anodic potential was observed from bulk to 2D-WO_3.

WO_3 nanosheets show excellent optical properties and possess suitable bandgap A change in sheet thickness drastically alters the optical absorption of these 2D crystals. For instance, a change in colour of the 2D-WO_3 was observed from blue to red by Zadeh et al.(2010) when the thickness of the sheets was increased from 15 to 150 nm [125]. Likewise, Chen et al.(2012) synthesized ultrathin WO_3 nanosheets with clear evidence of a blue shift in the UV-vis spectrum due to size quantization in the 2D structure [126]. These WO_3 nanosheets were compared to commercial WO_3 powder, and their band edges observed a shift from 2.63 eV (commercial WO_3) to 2.79 eV (WO_3 nanosheets). The fabricated 2D WO_3 were reportedly able to reduce CO_2 to CH_4 (-0.24 V (NHE)). The commercial WO_3 had CB of +0.05 V (NHE) and did not reduce CO_2. Apart from the thickness and high crystalline structure of 2D-WO_3, charge carrier migration and a short transition distance of charge carrier also contribute towards a slower recombination rate and thus improved photocatalytic properties. Reactant molecules, when combined to generate electron-hole pairs, can easily lead to separation and transfer of the charge carriers. This was proven by Chen et al.(2008) in their work, who fabricated 2D-WO_3 nanobelts with an inorganic-organic tungstate precursor using a topochemical conversion [61]. This synthetic method was a topochemical conversion of inorganic-organic hybrid lamellar precursors to low-dimensional inorganic 2D nanocrystals, with controlled morphology. These WO_3 nanoplates had a high specific surface area of magnitude 180 $m^2.g^{-1}$ in comparison to commercial powder that had 32 $m^2.g^{-1,}$ and the average thickness of the plates was 10-30 nm and with side length dimensions in the range of 200-500 nm. These prepared plates were tested against commercial WO_3 powder for photocatalytic oxidation of water for the evolution of O_2 using Ag^+ as electron acceptor sacrificial agent in visible light. The WO_3 nanoplates were reported to generate O_2 ~100 µmol.g^{-1} in 3 h, which was of 1 order magnitude higher than commercial WO_3 powder. This can be attributed to the high specific surface area of WO_3 nanoplates and an increase in charge transfer rates at the interface. γ-WO_3 nanoplates were also synthesized by Zhang et al.(2014) using a template-free hydrothermal method and tested for the photocatalytic degradation of Rhodamine B under visible light irradiation [127]. The γ-WO_3 nanoplates reported exhibiting high crystallinity and a good BET surface area, as compared to the commercial WO_3 powder. The photocatalytic response was observed to be 4.7 times higher than the commercial WO_3.

It should be noted that the use of dyes to determine visible light activity in photocatalysts is not recommended. However in another study, Gao et al.(2013) also reported the synthesis of triclinic-WO_3 square nanoplates by p-aminobenzoic acid to be efficient photocatalyst for MB degradation [128]. These WO_3 nanoplates synthesized were also investigated to show specific gas sensing properties and a high response towards detection of cyclohexane, i.e. 1000 ppm of cyclohexane; Ra/Rg = 140.

2D-WO_3 photocatalyst with oxygen vacancies: The oxygen vacancies present in the 2D-WO_3 structure mainly serve as shallow donors and eventually enhance the donor density and electrical conductivity of the material. An example of introducing oxygen vacancies in 2D-WO_3 was demonstrated by Gong et al.(2015), who synthesized single crystal nanosheets of WO_3 by exfoliating layers of tungstic acid and subsequently introducing oxygen vacancies through hydrogen or vacuum treatment [129]. This synergistic effect from the 2D-WO_3 and oxygen vacancies present on the surface promoted the multichannel light-harvesting performance of the WO_3. The hydrogen treated WO_3 exhibited the maximum quantum efficiency of 9.3% at 420 nm and gave the highest O_2 evolution rate as compared to vacuum treated-WO_3 and pristine WO_3. Under AM1.5 simulated solar irradiation, WO_3 prepared by hydrogen treatment exhibited the highest O_2 evolution rate of 1593 $\mu mol.h^{-1}g_{cat}^{-1}$ which was nearly 20% higher than vacuum treated WO_3 and over 2.5 times more than pristine WO_3 nanosheets. Modified 2D-WO_3 nanoflakes were also fabricated by Li et al.(2014) using a simultaneous post-growth method of etching and reducing in a weak acid [130]. The post-growth modification treatment gave a rough surface area to WO_3 nanoflakes by introducing oxygen vacancies. These flakes show optimal photoelectrochemical response and obtain a photocurrent density of ~1.10 $mA.cm^{-2}$ at +1.0 V (Ag/AgCl) (+1.23 V vs reversible hydrogen electrode), which was two times higher than pristine WO_3 nanoflakes. The dual etched/reduced flakes showed a band edge decrease of 0.1 eV, i.e. a blue shift as compared to 2.6 eV of pristine WO_3 nanoflakes. The simultaneous etching and reducing of the nanoflakes mainly increases the charge carrier density due to a synergistic effect taking place.

2D-WO_3 photocatalyst with crystal facet engineering: Crystal facet engineering has been employed for WO_3 to obtain nanostructures with specified exposed facets and hierarchy. Monoclinic WO_3 (γ-WO_3) can be synthesized through hydrothermal method with dominating exposed facets for 0D, 1D, 2D and 3D structures. The monoclinic phase of WO_3 with (002) exposed facet is an interesting aspect considered for photocatalysis. Xie et al.(2012) investigated the different crystal facets of WO_3 as photocatalyst for CO_2 photoreduction to CH_4 in the presence of H_2O vapour and O_2 evolution using $AgNO_3$ as electron acceptor [131]. Crystal facet engineering of WO_3 was performed controlling the acidic hydrolysis of W precursor. The resultant output was 2D rectangular sheet morphology of monoclinic WO_3 with predominant facet (002). Another quasi cubic 3D crystal of cubic WO_3 with equivalent facets (002), (020), (200) was also synthesized. A blue shift of 10 nm in the bandgap of the materials was also reported with bandgap extending from 2.71 eV (quasi cubic-WO_3) to 2.79 eV (rectangular WO_3 nanosheets). The blue shift in bandgap was attributed by the authors, due to a crystal facet orientation in the WO_3 structure and not size quantisation effect in WO_3. The author reported the rectangular WO_3 nanosheets to promote CO_2 reduction to CH_4 with a rate of 0.34 $\mu mol.h^{-1}.g^{-1}$ as compared null by cubic WO_3. However, on examining the photocatalytic O_2 evolution rates, a normalised rate of 5.9 $\mu mol.h^{-1}$ was obtained with quasi cubic WO_3 as compared to 0.7 $\mu mol.h^{-1}$ with rectangular WO_3 nanosheets. A deep VB edge of 2.14 eV was obtained for cubic-WO_3 as compared to 1.92 eV of rectangular WO_3. The results of VB XPS and bandgap energy presented by the authors were explanatory of an elevated CB minimum for WO_3 nanosheets promoting the reduction of CO_2 to CH_4. Likewise, the deep VB edge of cubic WO_3 was assigned as the reason for improved O_2 evolution in cubic WO_3. Organic acid assisted synthesis of 2D WO_3 has been explored widely to obtain stable WO_3 nanoplates. For example, Su et al.(2010) used tartic acid and citric acid as capping agents to fabricate 2D square nanoplate of WO_3 using the hydrothermal method [132]. Hydrochloric acid was used as the structure-directing agent in their process. It was reported that when tartic acid was used as the capping molecule, hexagonal phases of WO_3 were obtained, whereas when citric acid was used as the capping molecule orthorhombic-WO_3 was observed. This confirmed that even using different capping molecules, the crystallinity of the material can be easily tuned from one phase to another under hydrothermal conditions. However, these synthesise 2D plates were not investigated for any photocatalytic applications.

2D-WO_3 photocatalyst with co-catalyst doping: A comparative study of bare WO_3 nanosheets and platinum doped WO_3 nanosheets (Pt-WO_3) was investigated by Zhang and co-workers [133]. Bare WO_3 nanosheets proved to show better photocatalytic activity in degradation of tetracycline as compared to bulk-WO_3. But, the photocatalytic activity enhanced nearly 4 times, when the WO_3 nanosheets were doped with 2% platinum as co-catalyst. Tetracycline degradation was achieved within 1 h of irradiation, and the amount of degradation was as follows for commercially available WO_3, bare WO_3 nanosheets and 2% Pt-WO_3 are 2.86%, 19.69% and 72.82% respectively. Along with predominating exposed facets in a crystal lattice, a large specific surface area of the 2D materials also enhances the photocatalytic activity. Also, molybdenum was used as a dopant for improving the photocatalytic efficiency of 2D-WO_3 in one of the studies of Li et al.(2015) [134]. The Mo-doped WO_3 nanosheets synthesized by a simple hydrothermal process tend to show good photocatalytic activity for rhodamine B degradation. However, one should avoid the use of dyes for the determination of the visible light activity of semiconductors as a dye-sensitised mechanism may be in operation. The authors chose Mo as a dopant due to the equivalent ionic radius of Mo and W, 0.59 Å and 0.60 Å respectively, which easily allows Mo incorporation in the W lattice further enhancing the photocatalytic properties in the visible irradiation. Introducing ion dopants in the crystal lattice have proved to be an effective means to construct stable and active functionalized photocatalysts. Similarly, a comparative study of pristine WO_3 nanosheets and 2D-WO_3 nanosheets doped with other Ti [135] was reported in the literature to investigate photocatalytic efficiency in visible light irradiation. Ni-doped WO_3 nanoplate arrays were also constructed by Zhang et al.(2017) that were reported to show effective photoelectrochemical water splitting[136].

However, photocatalytic disinfection using 2D-WO_3 remains a relatively unexplored area. The only investigations reported to date of using 2D-WO_3 are with the help of Ag nanoparticles as co-catalyst. For example, the photocatalytic disinfection activity of WO_3 nanoplates was investigated using Ag nanoparticles as dopants by Yan et al.(2016) [137]. In their work, they deposited Ag nanoparticles on the surface of WO_3 using a photodeposition method, where under light irradiation Ag^+ ions photo reduce to Ag^0 at reduction potential +0.779 V (NHE). This is achievable due to a much more negative CB potential of WO_3 that is capable of transferring electron in a downhill process. The Ag-WO_3 nanoplates displayed 10^8 CFU.mL^{-1} reduction of *E. coli* in 2 h i.e. complete (100%) inactivation in 2 h. However, when photocatalytic activity of only WO_3 nanoplates was assessed, less than 2-log reduction of initial concentration (10^8

CFU.mL^{-1}) was observed in 2 h, which means the WO_3 nanoplates were inactive. Another study reports the use of Ag/AgBr with WO_3 plates for photocatalytic destruction of *E. coli* under visible light irradiation [138]. In this case, AgBr particles were reduced to Ag nanoparticles in situ in the presence of $Ag_8W_4O_{16}$ as the precursor for WO_3 and HBr as the structure-directing agent. The in situ grown Ag/AgBr/$WO_3.H_2O$ plates were visible light active due to the surface plasmon effect of Ag nanoparticles. The complex 2D structure of Ag/AgBr/$WO_3.H_2O$ showed photocatalytic inactivation of 10^7 CFU.mL^{-1} of *E. coli* within 20 min and no measurable destruction of *E. coli* were observed using pure materials, i.e. $WO_3.H_2O$ and Ag/AgBr. Surprisingly, the Ag nanoparticle formed in their research did not show any antibacterial/photocatalytic properties against *E. coli* colonies for 30 min irradiation. A good overview of the role of sacrificial agents in photocatalytic applications was published by Schneider and Bahnemann in 2013 [139].

2.2.2 Carbon based 2D photocatalyst for water disinfection

Graphene is a 2D material with a monolayer sp^2 bonded carbon atom configuration. It shows remarkable electronic properties and often is a desirable 2D intrinsic support catalyst with a 0 eV energy bandgap for photocatalytic water purification [140]. Combination of graphene or one of its derivatives with semiconductors has been reported mostly to increase the activity by reducing the electron-hole recombination. However, unlike pure graphene, its oxide form, i.e. graphene oxide undergoes a significant loss of conductivity, which can be improved to some extent by the partial reduction of its functional groups to form reduced graphene oxide. For example, graphene sheets coupled with plasmonic particles such as Ag/AgX(X= Cl, Br, I) as visible light photocatalyst for *E. coli* inactivation investigated by Xia et al.(2016) displayed complete inactivation in 8 min for ~10^7 CFU.mL^{-1} of *E. coli* [141]. The authors reported the inactivation as a result of Ag^+ ions and formation of H_2O_2 as the ROS as a synergetic effect. Another study by Khadgi et al.(2017) reported H_2O_2 as the main ROS generated from a composite of $ZnFe_2O_4$/Ag/rGO as the photocatalyst showing 7.2-log inactivation of *E. coli* in 1 h of visible light irradiation [142]. GO, or rGO with TiO_2 as a semiconductor photocatalyst has been widely reported for photocatalytic disinfection [23, 40, 41]. In collaboration with the Ulster photocatalysis group, Fernandez-Ibáñez et al.(2015) studied the photocatalytic activity of TiO_2

nanoparticles modified by reduced graphene oxide prepared by photocatalytic reduction of GO in the presence of methanol as hole scavenger [41]. The efficiency of P25-TiO_2-rGO was tested in real sun conditions for the inactivation of *E. coli* and *F. solani* spores. The authors also report the production of single oxygen $^1O_2$ in the visible light irradiation using P25-TiO_2-rGO as photocatalyst as a reactive oxygen species for *E. coli* inactivation. A further continuation of this study at Ulster was performed by Cruz-Ortiz et al.(2017) in identifying the photocatalytic charge transfer mechanism between TiO_2-rGO composites towards photocatalytic disinfection in both UV as well as visible only irradiation [40]. Chemical probe studies were performed in the work of Cruz-Ortiz et al.(2017) to detect the ROS generated. The detection and use of ROS generated were further confirmed by using scavengers to identify the primary ROS in photocatalytic disinfection. In UV-visible irradiation, •OH, H_2O_2 and $^1O_2$ were identified as the primary ROS, this was in agreement to their previous report of Fernandez et al.(2015) were single oxygen was identified in visible only irradiation using the same photocatalyst. However, the singlet oxygen production was found to be increased in the presence of chloride ions that can react with H_2O_2 in visible only irradiation. The use of dye sensitizers in hybrid photocatalysts systems has also been explored for photocatalytic disinfection. For instance, porphyrin dye sensitizer was used the electron promoter in TiO_2-graphene composites as visible light active photocatalyst for *E. coli* inactivation [143].

Apart from graphene-TiO_2 combination, continuous research has been performed with other materials like CdS-GO [144], ZnO-GO[145, 146], TiO_2-rGO-WO_3 [147], g-C_3N_4-GO [148, 149] etc. towards photocatalytic water disinfection.

The next section explores another more recent 2D carbon-based material as photocatalyst ca. graphitic-carbon nitride for water disinfection. The use of a π-conjugated system such as graphene, GO, rGO or even g-C_3N_4 possibly promote the electron transport in semiconductor photocatalysis yielding to higher electron mobility. These materials generally act as deep electron traps/sink leading to a slower charge recombination rate. Moreover, the interaction of photocatalytic materials with carbon layers because of surface modification contributes towards enhanced light absorption capabilities.

2.2.2.1 Graphitic carbon nitride (g-C_3N_4)

Graphitic carbon nitride (g-C_3N_4) has a two-dimensional laminar structure that has been widely reported in the past decade for its photocatalytic applications. It consists of a planar amino (NH_2) group in the edge of a triazine unit or connecting three triazine units referred to as tri-s-triazine or heptazine units as shown figure 2.8(a) and (b). The layered sheets of g-C_3N_4 are held together by weak van der Waals forces that can be broken down to single nanosheets by chemical or mechanical exfoliation from the bulk form [150]. As an organic semiconductor, the energy difference between its highest occupied molecular level (HOMO) and lowest unoccupied molecular level (LUMO) is termed as the H-L gap. The LUMO of g-C_3N_4 is mainly contributed by C1s and few N1s atoms, while the HOMO is mostly occupied by N1s atoms as can been seen from figure 2.8(c), through the DFT calculated partial density of states (PDOS) for g-C_3N_4 [151]. A gap of 2.7 eV was first reported as the bandgap of g-C_3N_4 by Wang et al. (2008) for photocatalytic H_2 production under visible light irradiation [109].

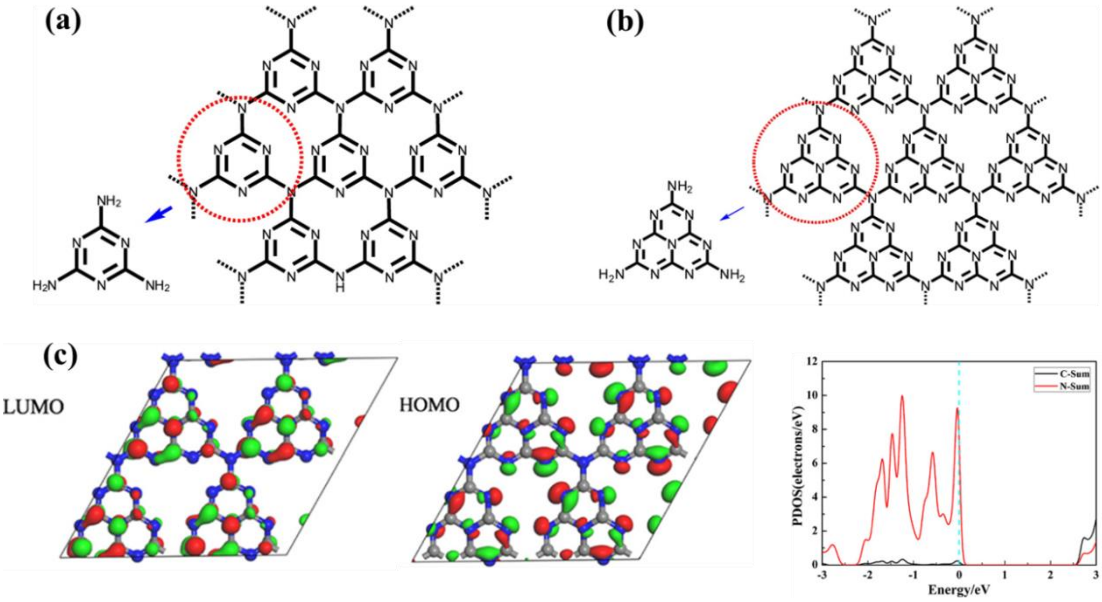

Figure 2.8 Structural representation of g-C_3N_4 based on tectonic units,(a) s-triazine and (b) tri-s-triazine (or heptazine); (c) DFT calculated LUMO and HOMO of heptazine based g-C_3N_4 with corresponding partial density of states (PDOS). The blue and gray balls represent C- and N- atoms respectively. Figure (a) and (b) reproduced from Antonietti et al.(2012), ACS Catal. (2012), 2, 8, 1596-1606 [152] and (c) from Su et al.(2018), J. Phys. Chem. C 2018, 122, 14, 7712–7719 [151].

The bandgap has been determined to be 2.7 eV in agreement to theoretical approximation [151, 153] and reported band edge potentials are -1.13 V (NHE) at pH 7 for LUMO and +1.57 V (NHE) at pH 7 for HUMO. g-C_3N_4 has been reported to show visible light activity in photocatalytic applications by effectively absorbing up to 460 nm, i.e. nearly 12% of the solar spectrum [109, 150, 154, 155]. Theoretically, the LUMO of g-C_3N_4 is more negative than the oxygen reduction potential to produce superoxide anion ($^{-}O_2^{\bullet}$), $E_{=}$ -0.16 V (NHE). Therefore in the presence of oxygen, it is capable of accepting electrons to produce reactive oxygen species (ROS) such as superoxide anion and H_2O_2 and $^{\bullet}OH$ through the subsequent reduction of molecular oxygen via hydroperoxyl radicals. However, the photocatalytic inactivation of microorganisms using g-C_3N_4 is only reported by few researchers for inactivation of *E. coli* and MS2 virus present in water [39, 110, 149, 156, 157]. A metal-free heterostructure of graphene/g-C_3N_4 with cyclo-octasulfur crystal was reported in 2013 for photocatalytic inactivation of *E. coli* under visible light irradiation [149]. This was the preliminary report on using g-C_3N_4 as the metal-free photocatalyst for water disinfection. However, in this study, the authors used two different approaches to wrapping sequence of rGO and g-C_3N_4 around α-S_8 rings. The wrapping of individual 2D material and in heterojunction with each other around the cyclic ring of sulfur showed significant improvement in photocatalytic inactivation process as compared to particular materials, g-C_3N_4 or rGO. Wrapping of graphene around α-S_8 was more active due to excellent electron conduction properties of graphene.

The photocatalytic inactivation of *E. coli* using pristine g-C_3N_4 has also been reported. A mesoporous g-C_3N_4 prepared by self-condensation of cyanamide and silica as a hard template was reported towards an effective photocatalytic inactivation rate as compared to bulk g-C_3N_4. By tuning the weight ratio of silica and cyanamide precursor, the mesoporous g-C_3N_4 with the maximum surface area of 230 $m^2.g^{-1}$ reportedly gave 6-log reduction in *E. coli* in 4 h visible light irradiation [156]. Also, exfoliation of g-C_3N_4 to an atom thick single layer sheet to improve the surface area and photocatalytic disinfection activity was investigated by Zhao et al.(2014)[157]. Thermal etching and ultrasonic exfoliation of bulk and nanosheets of g-C_3N_4 in isopropanol were performed respectively to form a 0.5 nm thick single layer g-C_3N_4 that showed a low charge transfer resistance and an effective charge separation to understand the photocatalytic disinfection mechanism. They reported a 7-log reduction of *E. coli* in 4 h. The reducing thickness of the sheet was concluded to improve the photocatalytic efficiency of g-C_3N_4 due to higher surface area and more active sites. Similar studies on preparing a porous g-C_3N_4 nanosheets by a two-step hydrothermal treatment and thermal etching for enhanced photocatalytic inactivation of *E. coli* was reported by Wang et al.(2017) [39]. They reported a total kill of *E. coli* (5×10^6 $CFU.mL^{-1}$) in 4 h using porous g-C_3N_4 sheets as compared to the bulk g-C_3N_4 that could only kill 77.1% of *E. coli* cells (initial conc. = 5×10^6 $CFU.mL^{-1}$) in 4 h [39]. Apart from bacterial disinfection, there is only a single report to date regarding the use of g-C_3N_4 as photocatalyst for removal virus MS2 phage by Li et al.(2016) [110]. The authors report after five repeated tests, complete removal of MS2 (10^8 $PFU.mL^{-1}$) using g-C_3N_4 in 6 h of visible light irradiation. The inactivation could be confirmed as the distorted shape, and ruptured capsid cells observed through electron microscopic images after the photocatalytic reaction took place. Few other studies on heterojunctions of g-C_3N_4 with other semiconductor photocatalysts such as AgBr[158], or using Ag[159] as co-catalyst have been considered too for photocatalytic disinfection.

2.2.3 Heterostructure photocatalysts of 2D/2D WO_3/g-C_3N_4

2D-2D layered heterostructures can be a solid construction just like to 0D-2D or 1D-2D combinations [160]. This is achievable mainly due to higher surface area and a large number of active surface sites available between the sheets, possibly leading to highly stable 2D layered heterostructures. The large contact surface area also provides a good interfacial charge transfer, and thus higher photocatalytic activities from the 2D-2D heterostructure can be expected. One of the practical approaches to have a slower recombination rate in potential photocatalyst like 2D-WO_3 is by constructing a 2D-2D heterostructure of WO_3 with another 2D material. The positive CB edge of WO_3 is unsuitable for the photocatalytic generation of ROS by the one-electron reduction of molecular oxygen. Combining 2D-WO_3 with other 2D photocatalysts such as g-C_3N_4 with more negative CB edge (or LUMO) possibly can lead to higher negative reduction potential by the construction of a z-scheme, as explained in section 2.1.2.

The photocatalytic activity of WO_3/g-C_3N_4 heterostructures with a z-scheme charge transfer mechanism has been studied previously for applications such as photocatalytic water splitting [106](O_2 evolution and H_2 evolution [92, 161]), dye degradation [94, 95, 162-164], CO_2 reduction [98], organic pollutant degradation [102, 165] and degradation of contaminants of emerging concern; few examples are antibiotics, anti-inflammatory drugs, cyanotoxins and personal care products[166].

2.2.3.1 2D/2D WO_3/g-C_3N_4 heterostructures in photocatalytic water splitting

Metal oxide-carbon photocatalytic heterojunctions for photocatalytic water splitting in a redox-mediated charge transfer mechanism were reported by Martin et al.(2014) [106]. In their work, WO_3 and $BiVO_4$ were used as the inorganic semiconductor photocatalyst in conjugation with g-C_3N_4, which is a 2D organic semiconductor. Although only g-C_3N_4 was the only 2D photocatalyst present in their study, the authors demonstrated photocatalytic splitting of water using WO_3/g-C_3N_4 yielding to O_2 and H_2 evolution under visible light irradiation. In the presence of a soluble redox mediator such as I^-/IO_3, 21.2 μmol.h^{-1}.g^{-1} of H_2 and 11.0 μmol.h^{-1}.g^{-1} of O_2 was produced by WO_3/g-C_3N_4 photocatalyst in visible light irradiation of over 24 h. However, in their study, 0.5 wt% of Pt with WO_3 and 3 wt% of Pt with g-C_3N_4 was used as a sacrificial electron acceptor. Pt-g-C_3N_4, as a sole photocatalyst, did not show any water splitting to either produce H_2 or O_2 without the redox mediator. However, when 5 mM NaI as used as a mediator, 5 μmol.h^{-1}.g^{-1} of H_2 was produced but no O_2 evolution was observed. Therefore, it was not true photocatalytic water splitting.

A 2D heterostructure of WO_3/g-C_3N_4 as photocatalyst with nanosheets morphology for visible-light-driven H_2 production was reported by Liu et al.(2019)[161]. The WO_3 nanoplates were prepared under hydrogen treatment, and Pt was photo deposited as a co-catalyst of g-C_3N_4 sheets. An average H_2 production rate of 843 μmol.h^{-1} was obtained by the 2D hybrid heterostructures in four consecutive runs of 5 h each. Another report by Fu et al.(2019) reported photocatalytic H_2 production using 2D/2D z-scheme based heterostructures of WO_3/g-C_3N_4 albeit with hole sacrificial agent such as 20 wt% lactic acid and photodeposited 2 wt% Pt as co-catalyst under UV-Vis irradiation [92]. The authors report an electrostatic interaction taking place between the heterostructure formation of 2D WO_3 and 2D g-C_3N_4 at pH 4 in a z-scheme. A 15 wt% of WO_3 in g-C_3N_4 as 2D heterostructure was evaluated for H_2 production against pure g-C_3N_4 and WO_3 nanosheets. The H_2 production rate for 15% WO_3/g-C_3N_4 photocatalyst was 982 μmol.h^{-1}.g^{-1} against 583 μmol.h^{-1}.g^{-1} for pure g-C_3N_4, but in the presence of Pt and lactic acid as the sacrificial agents. No activity was observed WO_3 nanosheets even in the presence of sacrificial agents by Fu et al.(2019). Similarly, Han et al.(2018) report the use of 10 v% of triethanolamine (TEOA) as a sacrificial agent for visible light production of H_2 using 2D WO_3/g-C_3N_4 photocatalyst [93]. Again in their case too, Pt was photodeposited on the heterostructure as a co-catalyst. TEOA is a sacrificial electron donor and undergoes oxidation by photogenerated holes. Therefore, when the WO_3/g-C_3N_4 is irradiated, the oxidation of TEOA takes place at the VB of WO_3 instead of water oxidation. Similarly, in the presence of Pt nanoparticles the photoexcited electrons in CB of g-C_3N_4, migrate to Pt which is a noble metal and due to very negative potential; it facilitates the reduction of H^+ to produce H_2 at an enhanced rate. Therefore, in reality, both the reduction and oxidation reactions in water splitting in the examples above are only achievable with the help of sacrificial agents, and this is not true water splitting.

2.2.3.2 2D/2D WO_3/g-C_3N_4 heterostructures for photocatalytic dye degradation

A layered sheet on sheet z-scheme based heterostructure of WO_3/g-C_3N_4 prepared via calcination route was reported by Chen et al.(2019). They tested the photocatalytic degradation of rhodamine dye under simulated solar irradiation [164]. The authors made different ratios of in situ 2D-WO_3 in exfoliated g-C_3N_4 powder, suspended in acidic solution and calcined at 450°C. The WO_3/g-C_3N_4 composites displayed photocatalytic degradation of rhodamine with degradation rate 6.5 times higher to pure WO_3 and 3 times higher to g-C_3N_4. An investigation into reactive oxygen species generation and scavenger studies to assess the charge transfer mechanism revealed superoxide ($^{\bullet}O_2^-$) and hydroxyl radicals ($^{\bullet}OH$) as the dominant radical species involved in the photocatalytic degradation.

Similarly, a comparison of photocatalytic activity of WO_3/g-C_3N_4 heterostructures in z-scheme, as well as Type-II band to band charge transfer, was performed by Chen et al.(2014) towards photocatalytic degradation of methylene blue and fuchsin dye [95]. The authors prepared different ratios of WO_3 and g-C_3N_4 composites by ball milling and thermal treatment. Although the morphology of WO_3, in this case, was nanoparticles and not 2D but Chen et al.(2014) reported the difference in photocatalytic activity when the content of WO_3 in the mixture was reversed. According to them, when g-C_3N_4 was the primary part of the heterostructure, a photocatalytic z-scheme mechanism was followed by the heterostructures with the migration of electrons from WO_3 into g-C_3N_4. However, when the mixture ratio was reversed with WO_3 as the major part of the

WO_3/g-C_3N_4 heterostructures, a Type-II band to band charge transfer mechanism was obeyed. The type-II heterostructure was formed with a maximum WO_3 content and surface of g-C_3N_4 was observed to be covered by WO_3, prohibiting any reaction takin place from g-C_3N_4, a lower rate of photocatalytic degradation was achieved for both methylene blue and fuchsin in visible light irradiation. Photocatalytic degradation with other dyes such as methyl orange (MO) has been previously reported using WO_3/g-C_3N_4 heterostructures [163, 167].

2.2.3.3 2D/2D WO_3/g-C_3N_4 heterostructures for photocatalytic organic pollutant degradation

Recently, the role of the Fermi level of the metallic interconnects used in combined photocatalytic systems of WO_3 and g-C_3N_4 was evaluated by Li et al.(2016)[165]. The Fermi level of noble metals Au, Ag and Cu used as interconnects was measured with respect to vacuum level and to corresponding electrochemical potential. The efficacy of 2D WO_3/g-C_3N_4 photocatalysts with metal these interconnects was tested for degradation of 4-nonylphenol (4-NP) under visible light irradiation of 100 $mW.cm^{-2}$. A degradation rate of 0.066 h^{-1} for 4-NP was observed for WO_3/g-C_3N_4 without any interconnect. The rate was shown to improve only to a fraction with Ag and Au, i.e. 0.0834 h^{-1} for WO_3/Ag/g-C_3N_4 and 0.0792 h^{-1} for WO_3/Au/g-C_3N_4 considering their Fermi levels were reportedly above and below the respective Fermi levels of g-C_3N_4 and WO_3. However, when Cu was with a Fermi level situated in between the Fermi levels of WO_3 and g-C_3N_4, a degradation rate 11.6 times higher to original heterostructures WO_3/g-C_3N_4 was observed, i.e. 0.7776 h^{-1}. The reported enhancement in photocatalytic degradation rate was also confirmed with improved •OH generation studied by photoluminescence technique with terephthalic acid as the fluorescent probe. Their study justified the rationale designing of photocatalytic systems by using a metal interconnect with a Fermi level matching to that of the parent materials. However, use of redox mediator/metal interconnect for the charge transfer does not make it a true z-scheme as the mediator/metal connect itself can take part in the reaction by absorption of photons and reduce the actual efficiency of the heterostructure. Also, an interesting point to note here was the energy difference between the Fermi level and CB of g-C_3N_4 was roughly 1 eV, suggestive of intrinsic semiconductor behaviour of g-C_3N_4.

2.2.3.4 $WO_3/g\text{-}C_3N_4$ heterostructures for other photocatalytic applications

Heterostructures of WO_3 and g-C_3N_4 as z scheme photocatalysts have also been explored for some other applications such as the degradation of contaminants of emerging concern or gas-phase photocatalytic oxidation or reduction (Table 2.1). Some photocatalytic type-II heterostructures of $WO_3/g\text{-}C_3N_4$ are reported too; however, in such cases, the photocatalytic activity is limited due to insufficient overpotential to drive the redox reactions. Such reactions mostly show the potential use of these heterostructures as photoanodes [99-101], to improve the photocatalytic performance under applied potential and will be discussed separately in section 2.5.

Table 2.1 Summary of other major applications of $WO_3/g\text{-}C_3N_4$ heterostructures

Photocatalyst	Photocatalytic Applications	Mechanism	Ref.
g-C_3N_4/WO_3	Acetaldehyde gas degradation	Type-II	[96]
WO_3/g-C_3N_4	Selective photooxidation of 5-HMF to 2,5-DFF	Z-scheme	[97]
g-C_3N_4/WO_3	CO_2 reduction	Z-scheme	[98]
WO_3/Ag/g-C_3N_4	Tetracycline degradation	Z-scheme	[102]
WO_3/g-C_3N_4	Tetracycline hydrochloride (TC-HCl) ceftiofur sodium (CFS) degradation	Z-scheme	[166]
g-C_3N_4/WO_3	Acetaldehyde oxidation	Z-scheme	[168]
WO_3/g-C_3N_4	Sulfamethoxazole (SMX) degradation	Z-scheme	[169]

2.2.4 Other 2D materials in photocatalysis disinfection

Metal oxyhalides based 2D structures such as BiOX (X = I, Br or Cl) have also been investigated for photocatalytic disinfection. For example, a comparison of hydrothermally synthesized 2D-BiOBr nanosheets with specific orientations of (001) and (010) were investigated for photocatalytic inactivation of *E. coli* by Wang et al.(2015) [170]. The BiOBr nanosheets with exposed (001) facet showed superior photocatalytic activity by giving a complete 10^7 CFU.mL^{-1} inactivation of *E. coli* in 120 min of visible light irradiation over its counterpart B010 BiOBr nanosheets showing only 1-log reduction in 2 h. The progressive output of 2D BiOBr towards photocatalytic inactivation lead the authors to further study on inducing dopants and increasing the photocatalytic efficiency of BiOBr nanosheets by doping with boron to fabricate Bo-doped BiOBr sheets of the different molar ratio of B: Bi. A 7-log reduction in *E. coli* was observed with an optimised ratio of 0.75 (B/Bi) in visible light radiation of 30 min in 3 repeated runs [171]. In another report, Bi_2O_4 formation by a post-treatment of BiOBr in alkaline solution was investigated to fabricate a composite of BiOBr-Bi_2O_4 for microbial disinfection [172]. Surprisingly a 15 min irradiation time was reported for a 7- log reduction of *E. coli* by the authors. A reason for the rapid inactivation can be the extended absorption range of Bi_2O_4 upto near-infrared region.

Just like 2D metal oxyhalides, interest in using transition metal chalcogenides (TMCs) as photocatalysts for water disinfection is increasing too. The advantages of having a narrow bandgap, makes the TMC photocatalyst a probable choice for visible light active photocatalysis, especially as p-type materials in the heterojunction and photocatalytic reduction reactions. The use of TMCs in photocatalytic water remediation is still in its developing stage, and not many materials have been investigated to date.

Molybdenum sulphide (MoS_2), a 2D layered TMC has been reported for its photocatalytic activity due to a direct bandgap of 1.9 eV and an indirect bandgap of 1.29 eV. With such a low bandgap, it allows MoS_2 to absorb a broader range of solar spectrum and promote an effective electron-hole pair separation by increasing the active surface sites. Recently, 2D-MoS_2 pyramid-shaped photocatalysts were potentially tested for *E. coli* inactivation with a minimal photocatalytic concentration of 0.7 mg.L^{-1} by Cheng et al.(2018), that demonstrated an 81.3% kill in 40 min of simulated visible light irradiation [173]. However, the authors went ahead in improving the photocatalytic performance of MoS_2 performance to 100% kill in 40 min using ultrathin Ag nanofilms. Considering, Ag is a good conductor of electrons and is a good sacrificial agent for electron-hole pair separation, an important point that was overlooked in this work was Ag is also a source of the antibacterial activity itself. A similar report was published by Liu et al.(2016) in which few-layered vertically aligned MoS_2 nanosheets under visible light irradiation gave a 5-log reduction of *E. coli* cells in over 120 min [63]. Again with the incorporation of metal ions such as Cu or Au, the disinfection rate profoundly increased to a total kill within 20 and 60 min respectively; also the best performance shown by Cu-MoS_2 was because of the good electrical conductivity of Cu, causing an interaction with the gram-negative *E. coli* cells.

Other 2D TMCs such as VS_4 [174], WS_2 [175, 176]and WSe_2 [176] have also shown some antibacterial activity in previous reports by wrapping around the viable cells and causing oxidative stress by the generation of reactive oxygen species. Still, their potential use as a photocatalytic disinfectant is yet to be considered. Therefore, these finding may promote tungsten-based chalcogenide materials to be used as possible 2D photocatalytic material for bacterial inactivation in future. Though transitional metal chalcogenides have a much narrow bandgap compared to other semiconductors, their application in photocatalytic disinfection of water is minimal due to their unstable behaviour in aqueous solution, due to photo-corrosion. They may be effective p-type materials to be used in 2D/2D heterojunction photo (or electro) catalyst for solar water disinfection.

Recently black phosphorous (BP) was reported as a robust 2D photocatalyst with a direct bandgap of 0.3 eV for a monolayer. Hybrid photocatalyst of BP-TiO_2 under visible light irradiation was tested for *E. coli* and *S. aureus* inactivation [177]. A 5-log inactivation of both microbial contaminants was reported in 70 min using black phosphor-hybrid TiO_2 semiconductor photocatalyst. The activity of BP-TiO_2 was compared against standard P25-TiO_2 and only BP, demonstrated a faster rate constant of 2.48 h^{-1} for *E. coli* and 2.06 h^{-1} for *S. aureus*. The rate constants reported for only BP were 0.01 h^{-1} *(E. coli)* and 0.02 h^{-1} *(S. aureus)* against P25-TiO_2 as 0.24 h^{-1} *(E. coli)* and 0.29 h^{-1} *(S. aureus)*. This particular study suggests the use of black phosphor as a practical alternative to graphene for electron transport and improved photocatalytic reactions.

2.3 Electrochemically assisted photocatalysis with 2D materials

Electrochemically assisted photocatalysis (EAP) is referred as the photocatalysis with an externally applied potential. EAP uses a minimum applied potential to separate the electron-hole pair during irradiation of a semiconductor photocatalyst, and hence reduce the rate of recombination [64, 178]. With the externally applied potential, the electrons are removed from the semiconductor and passed to a counter electrode as photocurrent. Simultaneously, the photogenerated holes can be used for photoelectrocatalytic water oxidation to degrade organics or other contaminants. In photoelectrochemical cells, the sites for oxidation and reduction are spatially separate, and the external electrical bias can be adjusted to enhance the rate of disinfection or improve the efficiency for water splitting [60]. Figure 2.9 shows EAP systems with n-type, p-type and heterostructured photoelectrodes.

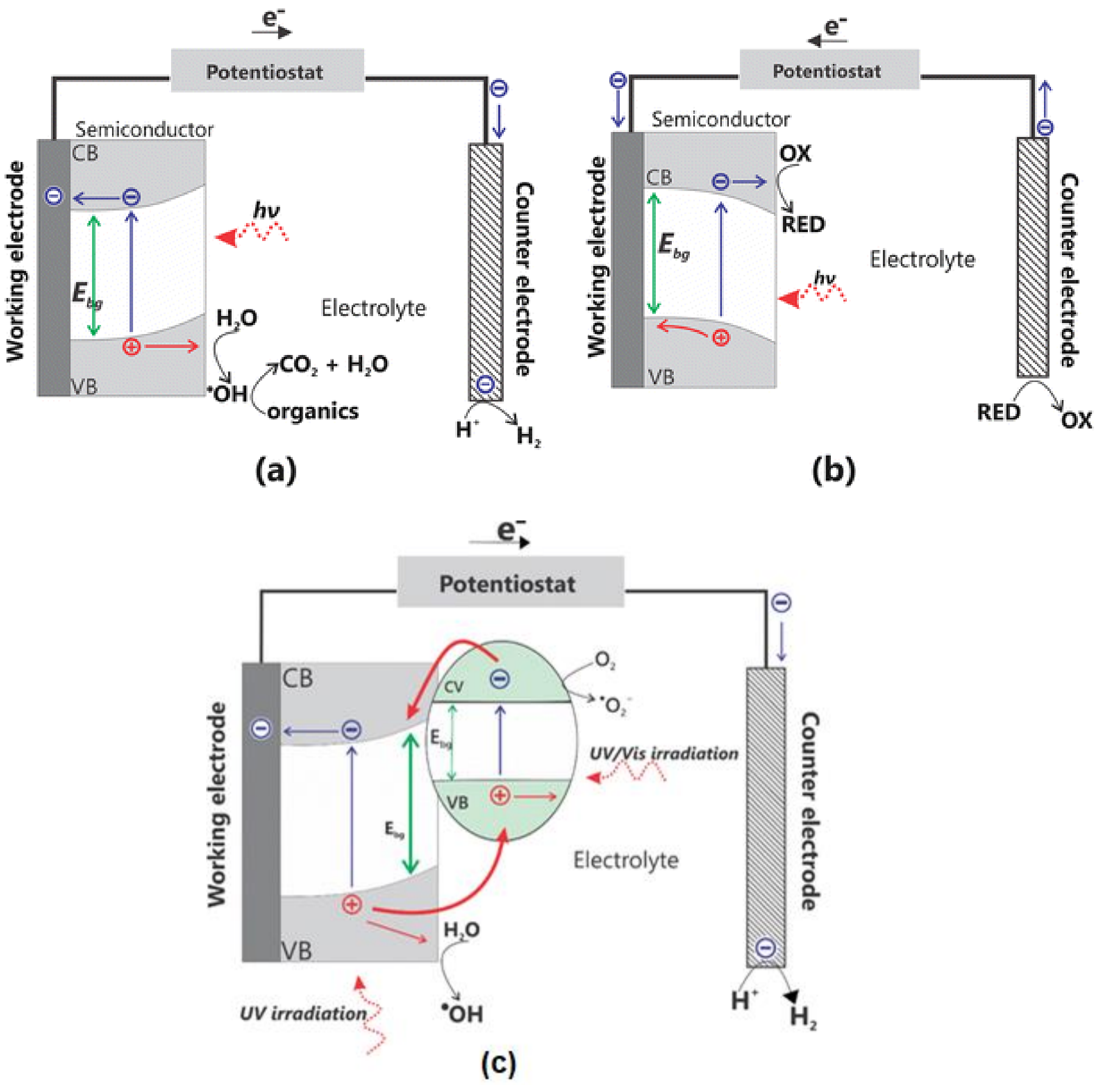

Figure 2.9 EAP mechanism for (a) n-type semiconductor electrode; (b) p-type semiconductor electrode and (c) Type-II heterostructured electrode. Reproduced from Bessegato et al.(2015), Electrocatalysis 6, 415–441 (2015) [64] .

Many materials such as TiO_2, WO_3, and g-C_3N_4 were investigated for their photo electrocatalytic performance for different applications. TiO_2 has been reported as photoelectrocatalyst for water treatment and disinfection. At Ulster University, various forms of TiO_2 as photoelectrodes have been explored for its use in photoelectrocatalysis

[50, 65, 179, 180]. For instance, Byrne et al.(2002) studied the electrochemically assisted photocatalytic degradation of formic acid using P25-TiO_2 electrodes prepared by electrophoretic deposition of Degussa P25 on conductive SnO_2: glass substrate [179]. The EAP activity of TiO_2 electrodes was compared in anaerobic (OFN purging) and aerobic conditions (air purging). Later using a similar electrophoretic deposition method for TiO_2 electrodes, Dunlop et al.(2002) compared two types of commercial TiO_2 (Aldrich and Degussa P25; currently known as *Evonik aeroxide* P25) as photoanodes for electrochemically assisted photocatalytic disinfection under UV-vis irradiation [65]. The efficiency of TiO_2 electrodes was assessed against *E. coli* present in drinking water in photocatalytic open circuit conditions and photocatalysis with +1.0 V (SCE) as applied potential, i.e. electrochemically assisted photocatalysis. In both the cases, Degussa P25-TiO_2 electrode (anatase(70%): rutile(30%) mixture) was reported to perform better over Aldrich electrode (pure anatase) by giving a faster inactivation rate of total bacterial cells (5×10^5 $CFU.mL^{-1}$) within 60 min. More recently, the EAP disinfection efficiency of TiO_2 was also examined by formation of 1D titania nanotubes by Pablos et al.(2017) [50]. In this particular work, vertically aligned titania nanotubes (TiO_2-NT) were prepared by electrochemical anodization of Ti foil in a fluoride-based electrolyte. To extend the absorption range of titania nanotubes towards visible region, nitrogen doping was also performed to obtain N-doped titania nanotubes (N-TiO_2-NT). The use of 1D nanotubes (TiO_2-NT and N-TiO_2-NT) in comparison to electrophoretic deposited P25-TiO_2 electrodes was investigated for *E. coli* inactivation under externally applied potential +1.0 V (SCE) in both UV-visible and visible only irradiation. As reported by the authors, N-TiO_2-NT were the fastest to achieve a total 5-log reduction of *E. coli* in 60 min, followed by undoped titania nanotubes that showed a 5- log reduction in 120 min of UV-vis irradiation. However, only 4-log reduction was reported for P25-TiO_2 electrode in 240 min of UV-Vis irradiation. Although the authors reported some observable photocurrent response for titania nanotubes (3 µA for N doped titania nanotubes and 0.5 µA for undoped nanotubes) in +1.0 V fixed potential under visible light irradiation, no EAP inactivation of *E. coli* was observed from the same electrodes under visible light irradiation.

Considering the progressive enhancement of efficiency from 0D to 1D TiO_2 electrodes. The research interest recently has moved to explore the use of 2D materials as photoelectrocatalyst. Therefore presented here are some of the examples from the literature of potential 2D photoelectrocatalytic materials like WO_3 and g-C_3N_4 as a single photoanode or as heterostructured electrodes.

2.3.1 2D WO_3 as photoanode

WO_3 as a semiconductor photoanode for photoelectrochemical conversion was first investigated by Hodes et al.(1976) [181]. WO_3 has an intrinsic property of reversible switching from $W^{6+} \leftrightarrow W^{5+}$ valence state. The formation of WO_3 anodes was a result of heat treatment of bare tungsten metal at 500°C in air. Hamilton et al.(2008) have synthesized electrodeposited tungsten oxide nanostructure electrodes using different peroxo-tungsten precursors [123]. The group studied comparison of the photoelectrochemical performance of electrodes towards to oxidation of water in visible light. Different synthesis techniques have been explored for preparation of 2D-WO_3 photoelectrodes for photoelectrocatalytic application such as hydrothermal [130, 136, 182], electrochemical anodisation [183], sputtering, spray coating of preformed nanostructures of WO_3 on conductive supports of FTO or ITO, direct heat treatment etc. Different morphologies of WO_3 as photoanode have been reported from nanoplates, nanosheets, nanoparticles or direct growth of thin films of $WO_{3.}$ Since the scope of this review was limited to 2D materials, therefore, only 2D WO_3 photoanodes have been taken into account here. Two dimensional photoelectrodes show good prospects of being used as photoanodes by facilitating separation of electron and holes under applied potential. Therefore reports have been already published using 2D-WO_3 electrodes for enhanced photocatalytic activities in water-splitting reactions such as oxidation of water for O_2 evolution [107, 130, 136, 184], EAP degradation of organic pollutants[67, 183], and more recently EAP water disinfection [66].

For instance, Xiao et al.(2017) have reported the use of nickel doped WO_3 nanoplates as stable photoelectrocatalyst for photoelectrochemical water splitting under visible light irradiation [136]. They report the formation of Ni-O-W bonds by replacement of W^{6+} in the monoclinic lattice of WO_3 with Ni^{2+} in the Ni-WO_3 nanoplates array, because of which a 1.74 times higher photocurrent response (0.80 $mA.cm^{-2}$) was obtained for 3 wt% Ni-doped WO_3 in comparison to undoped WO_3 nanoplates (0.46 $mA.cm^{-2}$) at +1.0

V (Ag/AgCl). The electrochemically active surface area of the prepared electrodes was also tested and was two-fold larger in Ni-doped WO_3 than undoped WO_3. According to the authors, it was assumed that the increased electroactive surface area was an indication of the potential of Ni-doped WO_3 photoanodes to be better photoelectrodes as compared to undoped WO_3 for photoelectrochemical water splitting. Direct growth of hydrated WO_3 nanoplatelets on FTO as thin-film photoelectrodes in the presence of capping agents have been reported to show enhanced photoelectrochemical performance [182]. The authors obtained nanoplatelet thin films of WO_3 using ammonium acetate as the capping agent and studied the response towards hydrogen production through photoelectrochemical water splitting in 1 M H_2SO_4 electrolyte. A 0.3% of an incident solar photon to hydrogen production efficiency (PCE %) was reported by them at an applied potential of 0.65 V, with a photocurrent density of ~0.5 $mA.cm^{-2}$. They also report the WO_3 nanoplatelet electrodes promoted the photoelectrocatalytic oxidation of methanol by achieving a maximum anodic photocurrent of 1.15 $mA.cm^{-2}$ under similar light irradiation conditions i.e. 100 $mW.cm^{-2}$ of simulated solar light.

WO_3 nanoplate photoanodes prepared by microwave irradiation have also been investigated for O_2 evolution by Hilaire et al.(2014) [184]. The authors activated the surface of the WO_3 photoanodes using a short cathodic polarization in the dark and analysed the effect of polarization on the photoelectrochemical performance of the electrodes. An IPCE of 45% was obtained for polarized electrodes in the visible range, which was 1.8 times higher to the unpolarised electrodes. However, when they assessed the use of the polarized WO_3 photoanodes for O_2 evolution, a substantial decrease in the O_2 evolution rate was recorded. Despite improved photocurrent obtained by cathodic polarization, no water oxidation to O_2 was observed in their case, suggestive that photocurrent measurements should not be considered the only criteria for reporting the capabilities of novel photoelectrodes towards water oxidation/water splitting reactions. Therefore, if higher photocurrent is achieved for novel photoelectrocatalyst, evidence of their photoelectrocatalytic performance for water splitting reactions towards O_2 or H_2 evolution should be also be reported.

The potential use of WO_3 photoanodes for photoelectrocatalytic water treatment by removal of persistent organic pollutants or disinfection has started gaining interest of scientists. Studies on use of 2D-WO_3 nanostructures as photoelectrodes for atrazine degradation in a photoelectrocatalytic system was reported by Garcia et al.(2018)[183]. A three-electrode quartz photoelectrochemical cell was used as the photo electrocatalytic reactor to assess the atrazine degradation at an applied potential of 1.0 V (Ag/AgCl) (3M KCl) as reference and Pt wire as the counter electrode. The authors using WO_3 photoanode under EAP conditions reported complete degradation of atrazine (20 mg.L^{-1}) in 3 h. Their study on intermediate species reveals 2-hydroxyatrazine as the primary intermediate achieved by rupturing of the heterocyclic ring of atrazine. The studies showed some interesting evidence of using visible light photoelectrodes such as WO_3 over conventional TiO_2 electrodes in the near future.

A photoelectrocatalytic(PEC) fuel cell configuration using WO_3 electrodes as the photoanodes for removal of 2,4-dichlorophenol was examined by Macphee et al.(2012) [67]. Instead of using a conventional photoelectrochemical cell, they fabricated a five-layer photoelectrocatalytic fuel cell similar to proton exchange membrane fuel cell to assess the photoelectrocatalytic efficiency of WO_3. The authors used a five-layer membrane exchange assembly in between separating cathode from the anode in the configuration: Pt ring as cathodic contact, a gas diffusion layer, nafion as the proton exchange membrane, WO_3 as the photoanode, a cathode layer and last a carbon-teflon current collector grid. The pollutant water was allowed to flow through the inlet and outlet in circulation, and the degradation of dichlorophenol was tested for 24 h. The authors report a 74% degradation of dichlorophenol using their PEC assembly that also includes a 20% adsorption of pollutant on the photoanode. Although the results in terms of photoelectrocatalytic degradation were not so promising due to a prolonged degradation, the initial attempt of fabricating a PEC fuel cell was the exciting part of their research, showing the potential of different reactor configurations that can be considered in increasing the photocatalytic efficiency of $WO_{3.}$

The EAP inactivation of *E. coli* under visible light radiation using WO_3 photoelectrodes was recently reported by Choi et al.(2019) through investigation of reactive chlorine species generated during the process [66]. Using WO_3/FTO as the photoanode under EAP conditions of +0.5 V (Ag/AgCl) and visible light irradiation, they observed oxidation of chloride to form chlorate ions in UV irradiation, which were held accountable for the EAP degradation of some contaminants of emerging concern and inactivation of *E. coli* in water. According to their report, no EAP activity was observed in the absence of chloride ions for any of the target contaminants, microorganism and even no H_2 production was observed. Their studies reported first time the inactivation of *E. coli* in photocatalysis as a result of reactive chlorine species generated instead of reactive oxygen species.

2.3.2 2D g-C_3N_4 as photoanode

Compared to the numerous reports on the photocatalytic performance g-C_3N_4, its photoelectrochemical performance or photoelectrocatalytic activity is very limited in the literature. Shortly, after the breakthrough of its promising photocatalytic activity towards water splitting to produce H_2, the research on the incorporation of g-C_3N_4 as electrodes in photovoltaic devices was presented by Zhang et al.(2010) [155]. The authors followed different protocols for preparation of electrodes using polymeric binders such as PEDOT: PSS or Nafion solution to deposit uniform films of protonated g-C_3N_4, deprotonated g-C_3N_4, mesoporous g-C_3N_4 and regenerated g-C_3N_4 to measure photocurrent response of each in visible light irradiation. In the preliminary attempt towards photocurrent generation of g-C_3N_4, a photocurrent of 150 $\mu A.cm^{-2}$ was obtained with an IPCE on 3% at 420 nm. A dual photocurrent was observed for g-C_3N_4 depicting its bipolar nature for the first time. Recently, the dual photocurrent response of g-C_3N_4 was again highlighted by Jing et al.(2019) in their study while assessing the photoelectrochemical properties of g-C_3N_4 [185]. The results shown in this work, suggest the Fermi level for g-C_3N_4 to be situated approximately in the middle of the bandgap, which could be easily modulated on the application of external potential. A further modification in the dual amphoteric nature of g-C_3N_4 was carried out by the authors through ionic doping with potassium (K^+) and iodide (I^-) ions to make an n-type g-C_3N_4. Nevertheless, no photoelectrocatalytic applications for g-C_3N_4 photoanodes were reported in the work of both Zhang et al.(2010)[155] and Jing et al.(2019)[185].

Recently, g-C_3N_4 with metal dopants Ag and Pd as the potential photoanode materials for photoelectrocatalytic water oxidation were reported by Nazarabad et al.(2019) to show enhanced photocurrent [186]. The authors compared the photoelectrocatalytic performance of g-C_3N_4 photoanode for O_2 evolution with the metal-doped g-C_3N_4 thin-film electrodes. At 1.23 V (RHE), the authors report photocurrent density for g-C_3N_4 thin film electrode as 24.8 $\mu A.cm^{-2}$, whereas with 2% Ag-g-C_3N_4 a photocurrent density of 41.86 µA.cm^{-2} was reported. When 2% Pd was used as the metal-doped, an enhancement of photocurrent density of 78.83 µA.cm^{-2} was achieved. The authors report the increase in photocurrent as an efficient electron-hole separation in g-C_3N_4 and confirmed that the photocurrent enhancement could lead to electrocatalytic water oxidation to generate O_2. However, the practical application of g-C_3N_4 photoanodes in photoelectrocatalytic O_2 evolution was missing in their report.

The practical usage of g-C_3N_4 photoanode remains an unexplored field, and so does the use of 2D materials as photocathodes for photoelectrocatalytic reduction or oxidation of water. g-C_3N_4 owing to its π-conjugated 2D structure and carbon configuration was tested for its cathodic response by Zhang et al.(2013) [187]. g-C_3N_4 was modified by incorporation of biopolymers such as alginate (Alg) and gelatine (Gel) to display cathodic response as compared to pure g-C_3N_4. The photoelectrochemical measurements of the biopolymer active g-$C_3N_{4,}$ i.e. Alg-5-CN, was assessed as a photocathode material against Pt counter electrode and Ag/AgCl as the reference electrode. The alginate coated g-C_3N_4 displayed an IPCE 3.1 times the pristine g-C_3N_4 at 440 nm on applying a potential of -0.2 V. The increased IPCE and photocurrent was attributed to a synergistic effect between carbon nitride and self-organized alginate that increased the porosity of the materials also observed through BET surface area measurements.

2.3.3 2D/2D WO_3/g-C_3N_4 as photoanodes

Coupling of two semiconductors together as a compound photoelectrodes is an alternative to improve the photocatalytic efficiency of the materials like WO_3 and g-C_3N_4. Two-dimensional heterostructures in electrochemically assisted photocatalysis have also been reviewed here. Mostly the heterostructures in EAP applications have seen to follow a type-II heterostructure mechanism, i.e. the electron transfer is via band to band. In type-II heterostructures, the overpotential to drive photocatalytic reaction is limited. In such cases, applying an external potential to the electrodes will improve the flow of electrons out of the semiconductor surface to the counter electrode for the desired reduction reaction to occur. Simultaneously, the holes will be free to react with the semiconductor-electrolyte interface to perform oxidation. For instance, 2D/2D heterostructures of WO_3/g-C_3N_4 as photoanodes have been fabricated by Li et al.(2016), to test their performance in the photoelectrochemical splitting of natural seawater [101]. The electrodes were prepared by direct hydrothermal grown 2D nanosheets of WO_3 on FTO and g-C_3N_4 deposited by subsequent dipping and annealing at 400°C. The hybrid 2D heterojunction of WO_3/gC_3N_4 reported exhibiting a photocurrent density of 0.73 mA.cm^{-2} under AM 1.5G irradiation (100 mW.cm^{-2}) at 1.23 V (RHE), which were comparatively two-fold higher than pristine WO_3 nanosheet arrays. The electrodes showed potential stability against photo-corrosion and improved electrochemical performance. The improved photocurrent density obtained in the hybrid was regarded as an accelerated electron transfer from g-C_3N_4 to WO_3 in downhill reaction, then through the external circuit on the application of positive bias. However, photocurrent measurements for alone g-C_3N_4 as photoanode in comparison were not reported by the authors.

Another example of 2D WO_3/g-C_3N_4 heterojunction nanoplate array for photoelectrochemical performance was performed by Zhan et al.(2015) [99]. The IPCE reportedly increased from 25.1% with WO_3 nanoplate as the photoanode to 53.1% in the heterostructure with g-C_3N_4 deposition. The heterostructure electrodes showed promising photoelectrocatalytic activity through photocurrent and impedance measurements, but the practical application of the electrodes was not examined.

In the work of Feng et al.(2014), a hybrid heterostructure of 2D-WO_3 nanosheet array was fabricated with layered g-C_3N_4 and CoO_x nanoparticles [100]. This system was a 3D structure of WO_3NSA/C_3N_4/CoO_xNps and was tested for its photoelectrochemical activity. It was reported to produce 5.76 mA.cm^{-2} photocurrent density as compared to the bare WO_3 array with a photocurrent density of 3.07 mA.cm^{-2}. Cobalt oxide nanoparticles were used as electrocatalyst for water oxidation to provide improved surface active sites and suppress any undesirable photo-corrosion of electrodes in reaction to the ions present in the solution. The evolution of O_2 with fabricated hybrid electrodes was evaluated by inverting the electrolyte filled graduated cylinder on top of photoanodes, rather than a proper laboratory gas detection technique.

Nevertheless, a faradic efficiency of 82.8% was calculated by the authors using this technique for WO_3NSA/C_3N_4/CoOxNps photoanode against an ideal expected 100%. The IPCE% for the hybrid at a maximum peak wavelength of 350 nm was 42.3%, 1.15 times higher than WO_3 nanoplate array electrodes with IPCE of 36.7%. The authors report the enhanced performance of heterojunction as a window effect that leads to improved light absorption. WO_3/g-C_3N_4 heterostructures as potential photoelectrocatalytic for hydrogen production in simulated solar irradiation were also reported by Nazarabad et al.(2017) through improved photoelectrochemical properties observed as compared to parent materials [188]. Overall 2D/2D WO_3/g-C_3N_4 through the previous reports show a potential to be used as the next generation photoelectrocatalyst for solar photoelectrocatalytic application mainly water splitting and water disinfection due to a suitable matching of band positions for both the materials as discussed in the start of this review.

2.4 Summary

Two-dimensional heterostructures as solar active photocatalysts still require a lot more investigation towards applications such as water disinfection. This literature review presents a detailed list of all the 2D materials that have been investigated thus far for the photocatalytic disinfection of water. For fabrication of active photocatalytic heterostructures, the correct choice of materials is crucial. The critical criteria, as discussed in the review, should be the band edge potentials of individual material suitable enough to drive photocatalytic reduction and oxidation reactions. With the current state of the art of using 2D heterostructures for visible-light activity, this research will explore the potential use of 2D/2D WO_3/g-C_3N_4 heterostructures as photocatalyst for solar water disinfection following z scheme charge transfer mechanism. To date, there are no significant reports on 2D/2D WO_3/g-C_3N_4 heterostructures in z scheme for the solar-driven photocatalytic/photoelectrocatalytic disinfection of water.

Chapter 3. Materials, Methods and Equipment

This chapter presents the materials, methods and equipment used throughout this research. The synthesis methods of all the photocatalytic materials used have been discussed in detail. The material characterisation techniques with specific conditions have been explained in brief. The photocatalytic and photoelectrocatalytic reactor design and operating conditions are also presented along with the analytical methods. All the experiments were performed in NIBEC by the author unless otherwise stated. The contribution of others has been explicitly mentioned in the acknowledgements.

3.1 Materials

3.1.1 List of reagents, materials, source and purity

All reagents used during the experimental research were of analytical grade, and no further purification was performed before the synthesis. A detail list of reagents and materials used throughout the research is given below in table 3.1

Table 3.1 List of reagents with chemical formula, their source and purity

Name	*Chemical Formula*	*Supplier*	*Purity*
Absolute ethanol	C_2H_5OH	Sigma-Aldrich	≥99.5%
Agar	$(C_{12}H_{18}O_9)n$	Sigma-Aldrich	For microbiology
1,4-benzoquinone	$C_6H_4O_2$	Sigma-Aldrich	≥99.5%
Catechol	$C_6H_6O_2$	Aldrich	≥99.0%
Citric acid monohydrate	$C_6H_8O_7.H_2O$	Sigma-Aldrich	99.5-100.5%
Conductive Epoxy CW 2400	-	Circuit works	-
Decon 90	-	Decon Laboratories Ltd	-
De-ionized water	Millipore H_2O	ELGA Pure Lab	15MΩ.cm^{-1}
Distilled water	H_2O	In-house	-
Durapore Membrane Filter	PVDF	Merck millipore	Hydrophilic, 0.22μm,

Name	***Chemical Formula***	***Supplier***	***Purity***
			25 mm
Formic acid	CH_2O_2	Merck	98-100%
Hydrochloric acid	HCl	Merck	37% (0.001ppm)
Hydroquinone	$C_6H_6O_2$	Aldrich	≥ 99.0%
Indium tin oxide glass	ITO	Diamond coatings	15-30 Ohms.Sq^{-1}
Isopropanol	$(CH_3)_2CHOH$	Sigma-Aldrich	≥99.5%
Melamine	$C_3H_6N_6$	Sigma-Aldrich	99.0%
Methanol anhydrous	CH_4O	Sigma-Aldrich	99.8%
Methanol for HPLC	CH_3OH	Sigma-Aldrich	≥99.9%
Methylviologen dichloride hydrate	$C_{12}H_{14}Cl_2N_2.xH_2O$	Sigma-Aldrich	98%
Nitric acid	HNO_3	Sigma-Aldrich	≥65%
Nitrogen (oxygen-free)	OFN	BOC	≥ 99.99%
N,*N*-Dimethyl-4-nitrosoaniline	$ONC_6H_4N(CH_3)_2$	Sigma-Aldrich	97%
Perchloric acid	$HClO_4$	Sigma-Aldrich	99.999%
Phenol	C_6H_6O	VWR, BDH, PROLAB	AnalaR Normapur
Poly(3,4-ethylenedioxythiophene)-poly(styrenesulfonate)	PEDOT: PSS	Sigma-Aldrich	3.0-4.0% in H_2O, high conductivity grade
Potassium chloride	KCl	Sigma Aldrich	≥99.0%
Potassium iodide	KI	BDH	99.0-100.5%

Name	***Chemical Formula***	***Supplier***	***Purity***
Ringer’s solution ¼ strength tablets	-	Fluka Analytical	For microbiology
Scotch magic tape 810	-	Scotch	Heat resistant ≤ 150°C
Silver nitrate	$AgNO_3$	Riedel-de Haen	≥99.8%
Sodium chloride	NaCl	Sigma-Aldrich	≥99.8%
Sodium citrate dihydrate	$HOC(COONa)(CH_2COONa)_2.2H_2O$	Sigma-Aldrich	≥99.0%
Sodium Hydroxide	NaOH	Sigma-Aldrich	≥98.0%
Sodium tungstate dihydrate	$Na_2WO_4.2H_2O$	Sigma-Aldrich	≥99.0%
SU8 photoresist	-	MicroChem	-
Titanium dioxide (P25)	TiO_2	Evonik aeroxide	≥ 99.5%
Tryptone (vegetable)	-	Fulka-analytical	For microbiology
Tungsten foil	W	Sigma-Aldrich	≥99.9%
Tungsten(VI) oxide	WO_3	Sigma-Aldrich	99.9%
Yeast Extract	-	Sigma-Aldrich	For microbiology

3.2 Methods

3.2.1 Hydrothermal synthesis

Hydrothermal synthesis of nanomaterials is a heterogeneous reaction that takes place at high temperatures and under self-generated pressure. Usually, the reaction temperature is above 100°C. The precursor solution is an aqueous media that on applying specific temperature and pressure leads to the dissolution and crystallisation of the bulk materials. The hydrothermal reactions are always conducted in enclosed autoclavable vessels because the vessel is resistant to corrosion on applying high temperature and is rated to elevated pressure. In most cases, the hydrothermal reactor consist of a stainless steel vessel with a teflon container inside that holds the reactant solution to be treated [189] (See figure 3.1).

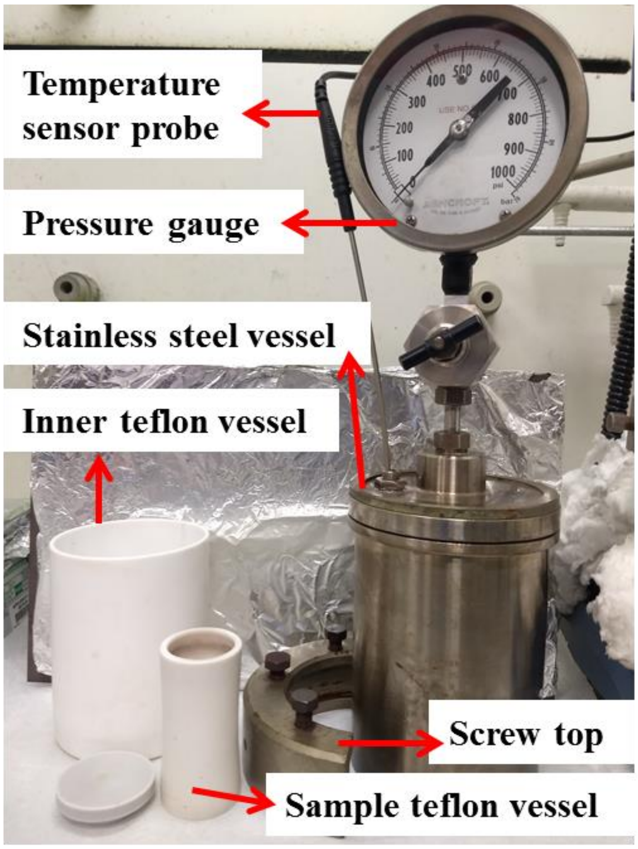

Figure 3.1 Hydrothermal Parr reactor (Parr Instruments) used for WO_3 synthesis.

Beyond the boiling point of water, when the reaction reaches specific elevated temperatures, the insoluble precursor crystallises and dissolves in the solution. This leads to the transformation of bulk material into nanomaterials, which can be 0D (quantum dots), 1D (nanorods, fibres) or 2D (sheets, plates,) in morphology [190]. The structural morphology of the nanomaterials can be tuned by the hydrothermal method. However, it depends on various reaction parameters such as (i) precursor type, (ii) reaction temperature, (iii) pH of the solution, (iv) addition of a stabiliser, (v) washing, centrifugation, drying steps, (vi) post-annealing treatment [191]. Hydrothermal synthesis is a relatively simple and easy process, which usually gives high quality and yield of nanomaterials and therefore is often considered appropriate for scale-up.

3.2.1.1 Tungsten oxide nanoplates synthesis

Tungsten trioxide nanostructures were synthesized by a modified hydrothermal method, similar to one reported by Zhang et al.(2014) [133]. The typical synthesis for WO_3 was as follows: At first 10 mL of 65% purity nitric acid (HNO_3) was slowly diluted into 40 mL of distilled water drop by drop under continuous stirring for 15 min. In a separate step, 1.0 g of the precursor sodium tungstate dihydrate ($Na_2WO_4.2H_2O$) was homogeneously dissolved in 20 mL of distilled water to form a transparent precursor solution. The tungsten precursor solution was next added very slowly drop by drop to the above acidic solution under constant stirring. With the addition of each drop of precursor, the colour of the suspension gradually changed from white to yellow. After 1 h of stirring, the above suspension was transferred to a teflon-lined sample container (with a volume of ~80 mL) within the hydrothermal stainless steel Parr reactor. The Parr reactor was sealed and allowed to heat at 180ºC for 3 h increasing the pressure to 10 bar. After 3 h of reaction, the final yellow precipitate was obtained and allowed to cool down naturally to room temperature and the obtained products were collected by centrifugation at 7500 rpm and washed with distilled water several times to remove any undissolved acidic residues, until the pH of the solution was neutral. A final rinse with ethanol was given, and the samples were dried overnight in a vacuum oven at 60ºC.

For structural characterization, a few milligrams (~10 mg) of dried WO_3 powder was dispersed in ethanol for 15 min, followed by drop-casting of ~10 μL of a solution on silicon (Si) substrate (1 cm^2) or TEM grids and the drop casted samples were left for drying under IR lamp for few hours. For crystallographic analysis and surface area measurements, the dried powder was weighed directly and analysed as it is.

3.2.2 Thermal polymerisation

Thermal polymerisation refers to a process in which a monomer is chemically converted to a polymer in a chain or step reaction by application of thermal energy. The formation of graphitic carbon nitride is a process of thermal polymerisation of nitrogen-rich precursors consisting of core C-N bonds. In brief, the thermal polymerisation of melamine to graphitic-C_3N_4 is a polycondensation process, which leads to the elimination of ammonia (NH_3) above 390°C. A detailed reaction pathway of g-C_3N_4 formation is discussed in chapter 4.

3.2.2.1 Graphitic carbon nitride synthesis

Graphitic carbon nitride, which is a layered two-dimensional nanomaterial, was prepared by direct thermal polymerisation of the precursor melamine. In a typical process adapted from Igor et al.(2017)[192], bulk graphitic carbon nitride was synthesized by heating 10 g of melamine in a closed cap ceramic crucible at a temperature of 520°C for 2 h in an air muffle furnace. The first cycle was allowed to cool down to room temperature with a ramp down rate of $2°C.min^{-1}$. The bulk graphitic carbon nitride sample prepared from melamine in cycle-I was further grounded to a fine powder for about 20 min, and yield obtained in this cycle was ~4-4.5 g every time on repeated synthesis. The finely ground sample was spread evenly in a large ceramic crucible with a diameter of 14 cm and reheated this time without a lid (uncovered) at 500°C for 4 h with the ramp-up rate of $3°C.min^{-1}$. After the heating cycle was over, it was allowed to cool down with a ramp down rate of $2°C.min^{-1}$. The second cycle product was named as graphitic carbon nitride nanosheets (g-C_3N_4); a yellow powder of 3 g was obtained. A final yield of ~41 % was obtained every time at the end of the reaction.

3.2.2.2 Chemical exfoliation of g-C_3N_4 layers into single sheets

Based on a method adapted from Ajayan et al.(2013) [193], liquid-phase exfoliation of the prepared g-C_3N_4 nanosheet layers was done in a polar protic solvent such as isopropanol (IPA). In brief, 300 mg of g-C_3N_4 layers were ultrasonicated in 100 mL IPA for 10 h using a probe ultrasonicator (Misonix Sonicator 3000) with power = 12 W at a pulse ON time = 0.5 s and pulse OFF time = 1.0 s. The exfoliated solution was centrifuged at 3000 rpm for 10 min to extract the suspended nanosheets and dried overnight in air.

3.2.3 Preparation of WO_3/g-C_3N_4 Heterostructures

The WO_3/g-C_3N_4 heterostructures were prepared following several approaches as described below.

3.2.3.1 Ultrasonic exfoliation in polar protic solvents

Using distilled water (H_2O) as the solvent: A method for construction of ultrasonic exfoliation was adapted and modified from the reports of Yang et al.(2014)[194]. The WO_3/g-C_3N_4 heterostructures were synthesized by ultrasonic exfoliation of WO_3 nanoplates and g-C_3N_4 layers in 1:1 ratio. In brief, 150 mg of the prepared WO_3 nanoplates were dispersed in 6 mL of distilled water by ultrasonication for 30 min. In a separate tube, 150 mg of g-C_3N_4 was dispersed in 6 mL distilled water by ultrasonication for 30 min. The two solutions were mixed using a magnetic stirrer for 10 min. Additional 3 mL distilled water was added and the suspension was mixed with ultrasound for another 30 min. The solids were recovered by centrifugation at 7500 rpm. The final product was dried in air. This sample was named as **WCN (1:1).**

Using isopropyl alcohol (IPA) as the solvent: In a synthesis of WO_3/g-C_3N_4 heterostructure, IPA was used as the protic solvent for chemical exfoliation using a modified method adapted from Li et al.(2016)[101]. The exfoliated g-C_3N_4 of concentration (30 $mg.L^{-1}$) prepared was dispersed with 50 mg of WO_3 nanoplates in IPA and sonicated for 1 h and then stirred for 30 min to form a heterostructure. The dispersion was dried at 50°C overnight to evaporate the IPA and annealed at 400°C for 1 h. The prepared sample was named as **Ex.WCN (1:1).**

3.2.3.2 Calcination

The synthesis of WO_3/g-C_3N_4 heterostructures based on physical mixing and calcination was also investigated. A one-step calcination method was followed wherein WO_3 nanoplates and g-C_3N_4 layers in weight % ratio of WO_3: C_3N_4, 05:95, 10:90 and 90:10 were mixed and finely ground in an agate mortar for 20 min and calcined at 400°C for 1 h in an air muffle furnace. The samples were named thereafter as **WCN595, WCN19** and **WCN91** respectively.

3.2.3.3 In-situ hydrothermal synthesis

In-situ hydrothermal synthesis of WO_3 nanoplates in a dispersion containing g-C_3N_4 was also carried out by modifying the method reported by Zhou et al.(2017)[169]. Briefly, 100 mg of synthesized g-C_3N_4 were dispersed in 50 mL distilled water under sonication for 1 h. The concentration of dispersed g-C_3N_4 was 2 $g.L^{-1}$. Then 1 g $Na_2WO_4.2H_2O$ was completely dissolved in 20 mL g-C_3N_4 dispersion under continuous stirring. In a separate beaker, 10 mL of HNO_3 was dissolved in 40 mL distilled water under vigorous stirring, and the tungsten-C_3N_4 dispersion was added dropwise to the acidic solution and stirred for 1 h. The W precursor-C_3N_4 solution was hydrothermally treated in the Parr reactor at 180°C for 3 h. The powder was collected by centrifugation, followed by washing with distilled water and ethanol several times and then dried overnight at 60°C. This sample was designated as **WCN2**, based on the concentration of g-C_3N_4 used during the synthesis.

3.2.3.4 Dispersion in citrate buffer

Heterostructure formation between WO_3 and g-C_3N_4 based on electrostatic attraction between the materials has been reported previously in the literature[92]. A similar method was adapted and modified to study the electrostatic interaction of WO_3 and g-C_3N_4 in a range of pH based 100 mM citrate buffer solution. Initially, a buffer range from pH 2.0-6.5 was investigated for individual samples of WO_3 and g-C_3N_4 to determine their point of zero charge value (pzc) to identify the pH range where both materials would hold the opposite zeta potential, e.g. WO_3 is negatively charged, and g-C_3N_4 is positively charged. At pH 2.25, the parent materials possessed opposite zeta potential. Therefore, 100 mg of WO_3 nanoplates were dispersed in 10 mL citrate buffer (pH 2.25) and 400 mg of g-C_3N_4 was dispersed in 40 mL citrate buffer via ultrasonication. The two exfoliated solutions were mixed for 1 h under vigorous magnetic stirring and final pH of the solution was pH 2.25. After stirring, the precipitate was collected by centrifugation and dried overnight to obtain the powder. Hence, the WO_3/g-C_3N_4 composite was obtained in the weight ratio of 1:4 (WO_3: g-C_3N_4) in pH 2.25. This sample was named as **WCN(1:4)pH2.25.**

3.2.4 Electrode preparation

The nanomaterials including the synthesized tungsten oxide (WO_3) nanoplates, graphitic carbon nitride (g-C_3N_4) and all heterostructures of WO_3/g-C_3N_4 were coated on electrically conducting supports to form electrodes and to test their photoelectrochemical properties.

3.2.4.1 Pre-cleaning of the substrate

For electrode preparation, tungsten foil (0.127 mm thick) cut into coupons of 30×10 mm^2 and indium tin oxide (ITO) coated coverslips (22×26 mm^2) were used as the electrically conducting support. The substrates were cleaned by ultrasonication in 5% solution of Decon 90 surfactant for 15 min, followed by sequential washes with distilled water and absolute ethanol to remove any leftover surfactant. The cleaned W foils and ITO glass were dried under oxygen-free nitrogen (OFN; BOC purity ≥ 99.99%) stream.

3.2.4.2 Spray coating method

The prepared samples of WO_3, g-C_3N_4 and their heterostructures were immobilised on W-foil by a spray coating method. The W foils were used as the electrically conducting support for the electrodes and masked using a scotch tape (Scotch Magic Tape 810; with heat resistant up to 150°C), to leave an exposed area of 20×10 mm^2 for spray coating. A suspension (1 wt. %) of each material was sonicated in methanol for 30 min and uniformly spray-coated on the exposed area of W foil using a lab spray gun. Each spray-coated sample was dried on a hot plate for 5 min between subsequent coats to get a thick film. In this way, an optimal catalyst loading of 1 ± 0.15 $mg.cm^{-2}$ was determined by weighing all dried nanomaterial coated W foils before annealing. The spray-coated foils were annealed at 400°C in the muffle furnace (Lenton Furnace) for 1 h (Ramp up $2°C.min^{-1}$; Ramp down $2°C.min^{-1}$) to sinter particles and improve adhesion of the sample to the foil.

3.2.4.3 Doctor Blading method

With some materials, e.g. g-C_3N_4, it was difficult to spray coat as the dispersion of the powders in methanol or water was not effective. Therefore, a different electrode preparation recipe was followed based on one published by Zhang et al.(2010) by traditional doctor blading and sintering treatment on ITO coated glass substrates with poly(3,4-ethylenedioxythiophene)-poly(styrenesulfonate) (PEDOT:PSS) as the conductive polymer blend[155]. PEDOT:PSS is used as an organic binder with carbon nanomaterials to form a hydrated colloidal solution which is easy to coat. Briefly following the method of Zhang et al.(2010), 10 mg of the nanomaterial samples were mixed with 20 μL of PEDOT:PSS (1.5-2%) in 100 μL distilled water and grounded in an agate mortar to form a uniform slurry paste. The ITO glass (with the conductive side facing up) were masked using a scotch tape (Scotch Magic Tape 810; with heat resistant up to 150°C) to leave a working area of 20 × 20 mm^2 for coating. The slurry paste was then doctor bladed in the form of a homogenous thin film on the conducting side of the ITO glass using a glass rod following a simple protocol reported by Smestad and Grätzel [195]. The coated films were allowed to dry in air at room temperature, and the loading of coated materials was optimised to 2.5 ± 0.1 $mg.cm^{-2}$ before the annealing step. Finally, the dried films were annealed at 150°C for 30 min in an air oven. In this way, the samples were named as nanomaterial/PEDOT/ITO electrodes.

3.2.4.4 Electrical contact preparation

Electrical contact to the conductive supports (coated W foil and ITO glass) was made with a Cu wire. The end of the Cu wire was pre-cleaned using abrasive paper and connected on the back of the W foil and to an uncoated area of ITO on the ITO glass using conductive silver epoxy (CircuitWorks CW2400). The connection was allowed to dry at room temperature, followed by curing at 120°C for 30 min. The contact and any remaining area on the electrodes that were not coated were insulated with negative SU8 photoresist (MicroChem) twice, leaving the photoactive area. The photoresist coated electrodes were then exposed to UVB irradiation (2 Philips PL-S 9W/01/2P) for 5 min on both sides followed by hard baking at 160°C for 30 min. The UV exposure step was repeated two times to ensure proper curing of the photoresist.

3.3 Materials characterization

The nanomaterials synthesized were characterized for their physicochemical properties using techniques including transmission electron microscopy (TEM) and scanning electron microscopy (SEM). The crystalline properties of the nanomaterials were investigated by the X-ray diffraction pattern. The elemental analyses of the samples were performed by X-ray photoelectron spectroscopy (XPS) and valence band XPS for determination of valence band position of the semiconductor nanomaterials. Ultraviolet-visible spectroscopy and photoluminescence spectroscopy were used for the optical measurements on the samples. The specific surface area of the samples was analysed by gas adsorption.

3.3.1 Transmission electron microscopy

The TEM measurements on the synthesized nanostructures were performed using a JEOL JEM-2100F system consisting of a field emission gun operating at 200 kV. The samples for TEM analysis were prepared by ultra-sonication of ~ 10 mg of the nanomaterial powders in absolute ethanol for 15 min, then drop-casted 10 μL of the solution on the holey carbon grid (Agar Scientific). Afterwards, the TEM grid was allowed to dry under the IR lamp for few hours. The TEM images were recorded using a charge-coupled device (CCD) detector camera controlled by Gatan Digital Micrograph software. The High-resolution images (HRTEM) were also obtained to study the morphology of the WO_3 nanoplates and g-C_3N_4 nanosheet layers. The HRTEM system equipped with selected area electron diffraction (SAED) was also performed to determine the lattice fringes and crystalline phase of the nanomaterials.

3.3.2 Scanning electron microscopy

The scanning electron microscopy was performed on the samples to determine their surface morphology and thickness of the layers. SEM analysis was carried out on Hitachi SU5000 FE-SEM that operated in an accelerating voltage of 10 kV, the high vacuum pressure of ~10^{-8} bar and at a working distance of 10 mm. The SEM was also equipped with a dispersive energy X-ray (EDX/EDS) analyser and used to determine the elemental composition of the samples under low vacuum pressure of ~10^{-4} bar. The images were recorded using a backscattered secondary electron detector, and EDS analysis was done using the Aztec software provided with the instrument.

3.3.3 X-ray diffraction analysis

The XRD analysis was performed on Bruker D8 discover Diffractometer equipped with a Cu Kα X-ray source (λ = 1.54 Å). The analysis scan was performed from range 10-70° (2θ) with an increment step potential of 0.03. The scan speed was 25 $s.step^{-1}$. The applied voltage of the tube was 40 kV, with a current of 40 mA. For powder samples, the scan type was always kept in locked couple mode. The experimentally obtained diffraction patterns of the individual nanomaterials were compared to the standard JCPDS files available in the published inorganic crystal structure database (ICSD).

3.3.4 X-ray photoelectron spectroscopy

X-ray photoelectron spectroscopy (XPS) is employed to determine the elemental composition of a specific material, and it also informs about the chemical and electronic states present from different elements within the materials. A Kratos Axis Ultra instrument having AlKα as X-ray source with photon energy $h\nu$ = 1486.7 eV was used for all XPS measurements. The wide energy survey scans (WESS) were analysed for all samples in the binding energy range of 0-1250 eV with a pass energy of 160 kV. High resolution (HR) scans of each target element (tungsten W4f; carbon 1s; oxygen 1s and nitrogen 1s) were studied at slow scan speeds and 14.2 kV pass energy. The XPS peak fitting was done using CasaXPS software with reference to adventitious carbon (C1s) peak at 284.8 eV. The high-resolution scan peaks were quantified using Gaussian-Lorentzian (GL) function with Shirley background correction done before quantification. The fitting constraints for all elements were obtained from XPSfitting.com[196] and previously published work[197, 198].

3.3.5 Specific surface area analysis

The specific surface area analysis for materials was analysed using a Quantachrome Autosorb-1 system. The Brunauer-Emmett-Teller (BET) surface area and N_2 gas adsorption were performed to measure the surface area. For analysis, the specific weight of each sample was outgassed at 250°C for 3 h to remove any moisture from the sample. A 12 mm OD sample cell without rod was used for all measurements.

3.3.6 Ultraviolet-visible spectroscopy and diffuse reflectance analysis

The UV-Vis absorption spectrum for all photocatalytic nanomaterial samples was recorded using a Perkin Elmer Lambda 35 UV-Vis spectrophotometer. The absorption spectrum for all samples was taken in the wavelength range of 200-700 nm. The aqueous suspensions of the powder samples were prepared in different concentrations, and the absorbance was measured in the spectrum mode. The wavelength with maximum absorbance peak of each sample was considered to calculate the optimal catalyst loading of the materials using Beer Lambert’s law.

The optical band gap measurements were performed using the diffuse reflectance accessory (Labsphere RSA-PE-20) equipped with UV-visible spectrophotometer. Samples were made in pellet form or spray-coated on glass slides and the transmittance of each sample was analysed in wavelength 250- 800 nm with a Spectralon disk as the reference standard. The optical bandgap (E_g) of the material was calculated using the Kubelka-Munk function.

3.3.7 Photoluminescence spectroscopy

The photoluminescence intensity of the prepared samples was investigated in aqueous solutions by a Perkin Elmer LS55 Fluorescence Spectrometer. The excitation wavelength used for measurements was 330 nm and corresponding emission peaks where recorded between 300-600 nm for all the samples. The photoluminescence study was performed in the School of Chemistry and Chemical Engineering at Queen’s University, Belfast.

3.3.8 Zeta potential measurement

The zeta potential for tungsten oxide (WO_3) and graphitic carbon nitride (g-C_3N_4) was performed using the Malvern zetasizer Nano Zs series. The zeta potential measurements tell us about the point of zero charge (pzc) for a material at a particular pH. The zeta potential of the material suspended in a solvent is measured as a function of pH at room temperature (25°C). The cuvette cells used for zeta potential measurements were folded capillary cells (DTS 1061).

3.4 Photocatalysis experiments

3.4.1 Stirred Tank reactor

The photocatalytic reactor used in all experiments throughout this research was a customized stirred tank reactor, as shown in figure 3.2, and has been reported previously[199].

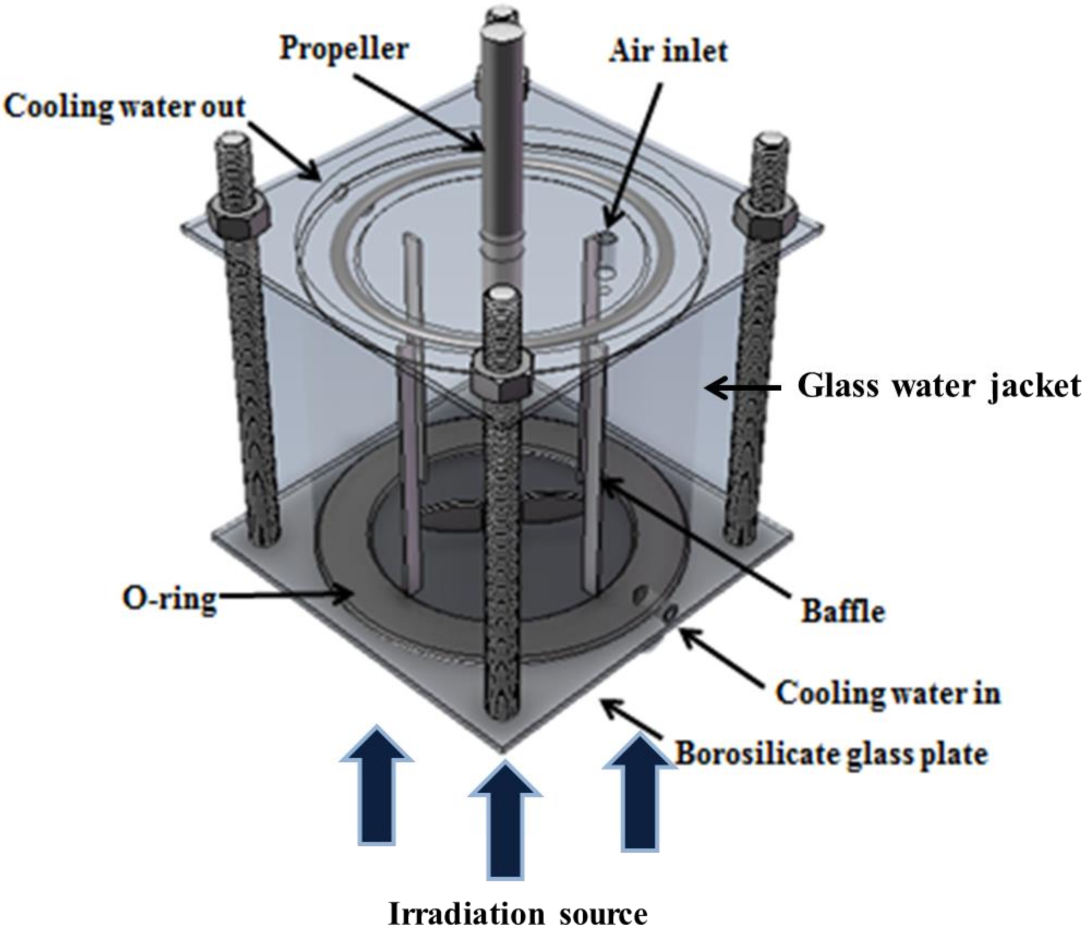

Figure 3.2 Schematic 3D representation of stir tank reactor

The main part of the system was a glass water jacket vessel with a total volume of approximately 350 mL. The reactor was built with an outer water jacket for circulation of water and to keep the reaction temperature constant through the experiments (20 ± 2°C) controlled with a thermostatic water bath. A working volume of 200 mL of the suspension (pollutant or bacteria + photocatalyst) was stirred at a rotation speed of 500 rpm using a stainless steel propeller (IKA Eurostar digital, homogenator motor) and baffle inside the reactor to provide efficient mixing and mass transfer. The reactor was irradiated from the bottom with the base of reactor being a 2 mm thick borosilicate glass plate (110 × 110 mm). Air sparging was provided into the suspension at least 15 min before the experiments and during the total time of experiments using an aquarium pump with a constant flow rate of 900 cc.min^{-1} to maintain the dissolved oxygen. A 1000 W xenon arc lamp (ss1000 Spear Robinson) with filters was used as the light source for solar simulated irradiation experiments with an output similar to the Air Mass 1.5 Global irradiation spectrum of sun (ASTM NREL data -ASTM G-173-0) [15]. The details on spectral intensity optimisation to simulate solar irradiation are given in chapter 4. At the beginning of each experiment, the lamp was shielded and allowed to stabilise for at least 30 min before irradiation of the reactor. The photocatalytic reactor assembly as a whole set up is shown in figure 3.3.

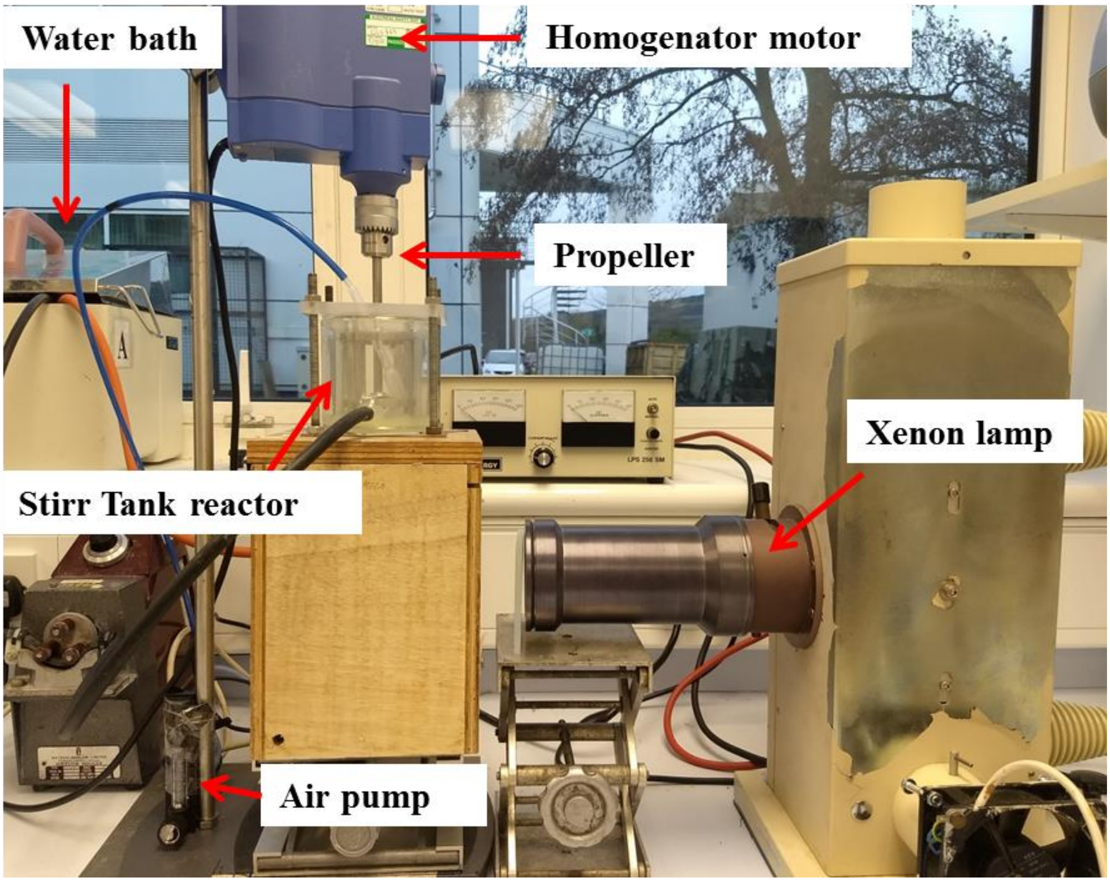

Figure 3.3 Photocatalytic reactor assembly used in experiments

3.4.2 Photocatalytic experiments

For photocatalytic degradation of pollutants, a stock solution of 1×10^{-2} mol.L^{-1} formic acid (Sigma-Aldrich, UK) and 1×10^{-3} mol.L^{-1} phenol (BDH, Poole Germany) in distilled water was prepared. The photocatalytic powder with the estimated optimal loading of 30 mg.L^{-1} was added to the 200 mL solution of the target pollutant. Details of the determination of the estimated optimal loading are discussed in chapter 4. During all experiments, a sample of 3 mL was taken at time t = 0 s and the suspension was irradiated with the lamp. The samples were taken every 30 min of irradiation during the experiment and filtered using 0.22 µm PVDF (Merck Millipore) filter to separate the photocatalyst powder before analysis.

3.4.2.1 Analytical methods for detection of the pollutants

UV-visible spectroscopy: The calibration of UV-visible spectrophotometer and the limit of detection of formic acid were determined by measuring the absorption of known concentration of formic acid (figure 3.4). In replicates of 3 set of experiments, 3 mL each of different standard solution of formic acid, i.e. 1,2,4,6,8,10 mM was poured into a quartz cuvette and analysed by noting the UV absorbance at a peak wavelength of λ = 210 nm. The molar absorption coefficient was determined for formic acid by drawing a calibration curve and fitting a trend line to the experimental data sets. A linear trend line where R^2 value was close to 1, was established and slope of the line of best fit was used as the molar absorption coefficient, details for which are specified in chapter 4.

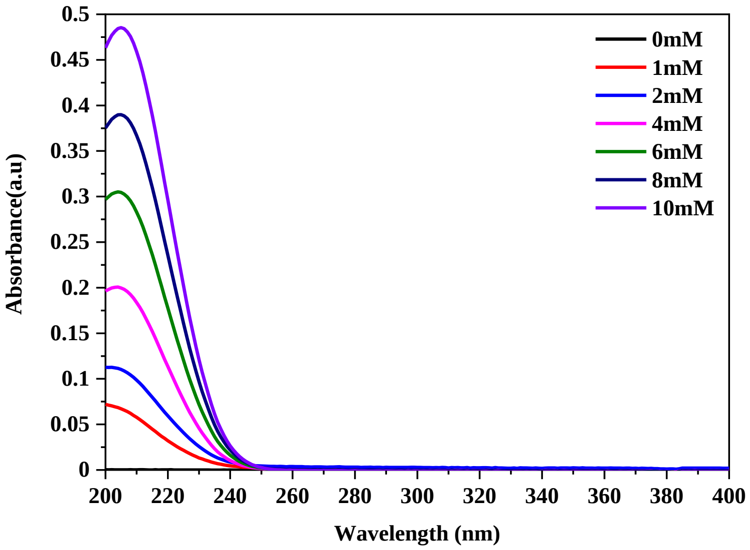

Figure 3.4 UV-Vis spectra for different formic acid concentrations to determine peak absorbance vs corresponding wavelength (nm).

High-performance liquid chromatography (HPLC): HPLC was used to determine the concentration of phenol during photocatalytic experiments. The samples were analysed using an Agilent 1200 series High-performance liquid chromatography (HPLC) system equipped with a UV detector. A reverse-phase supelco IL (250.0 mm × 4.6 mm, 5 μm) was used as the separation column along with a C18 phenomenox guard column (22.0 mm × 4.0 mm, 5μm). The mobile phase used for analysis was a mixed ratio of 40:60 HPLC grade methanol: formic acid + deionized H_2O (pH 3.2) (15MΩ.cm^{-1}, ELGA PURE Lab) with isocratic elution at a flow rate of 1 mL.min^{-1}. The sample injection volume for photocatalytic treated phenol samples was 30 μL, analysed at a UV detection wavelength of 270 nm. The wavelength of 270 nm for detection was considered as per the UV-Vis spectrum obtained for phenol (1 mM) as shown in figure 3.5. The pump pressure was constant at 200 bar for all the measurements. The column temperature was maintained at room temperature throughout the analysis.

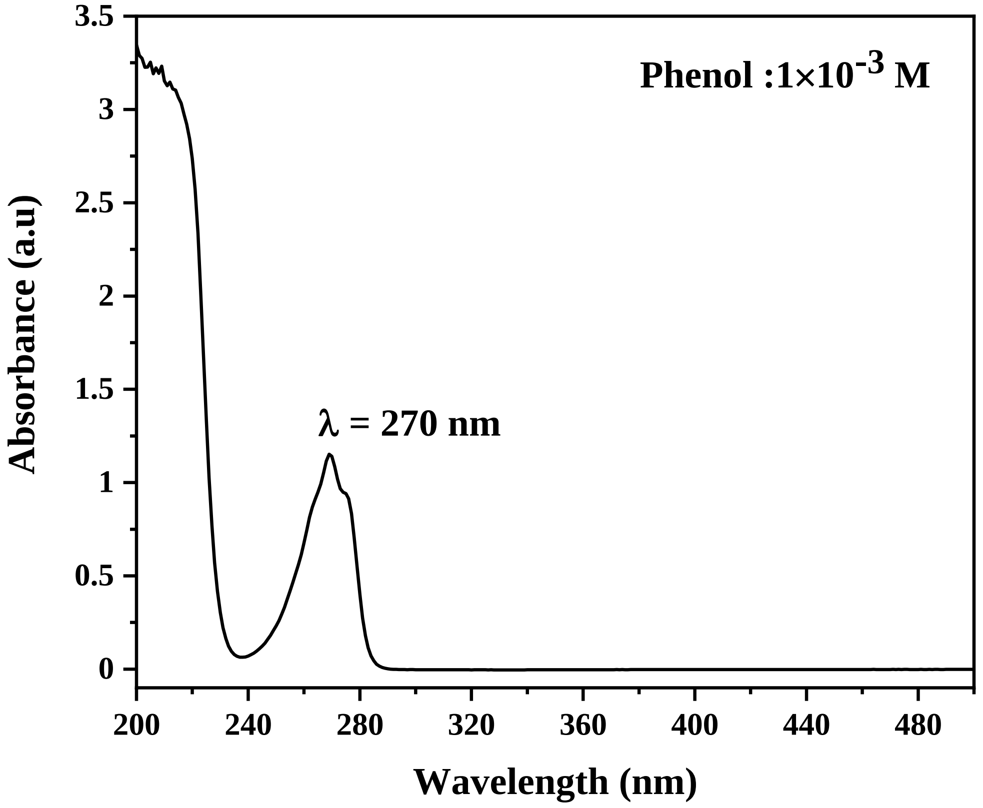

Figure 3.5 UV-Vis spectrum for 1 mM phenol to determine absorbance vs peak wavelength.

The HPLC system was calibrated by injection of different standard solutions of phenol and its intermediates benzoquinone (BQ), hydroquinone (HQ) and catechol (COH), i.e. 0.1, 0.3, 0.5, 1.0 mM. Each of the standard solutions was filled into the HPLC vials for analysis, and three replicates per sample were analysed. A 30 μL of each sample was automatically injected into the HPLC system from the vial and analysed at UV absorbance wavelength λ = 270 nm. The individual as well as overlaid chromatograms for each sample at varying concentration to determine the retention time are shown in figure 3.6 and figure 3.7. The details of the peak area versus phenol + intermediate concentrations are described in chapter 4.

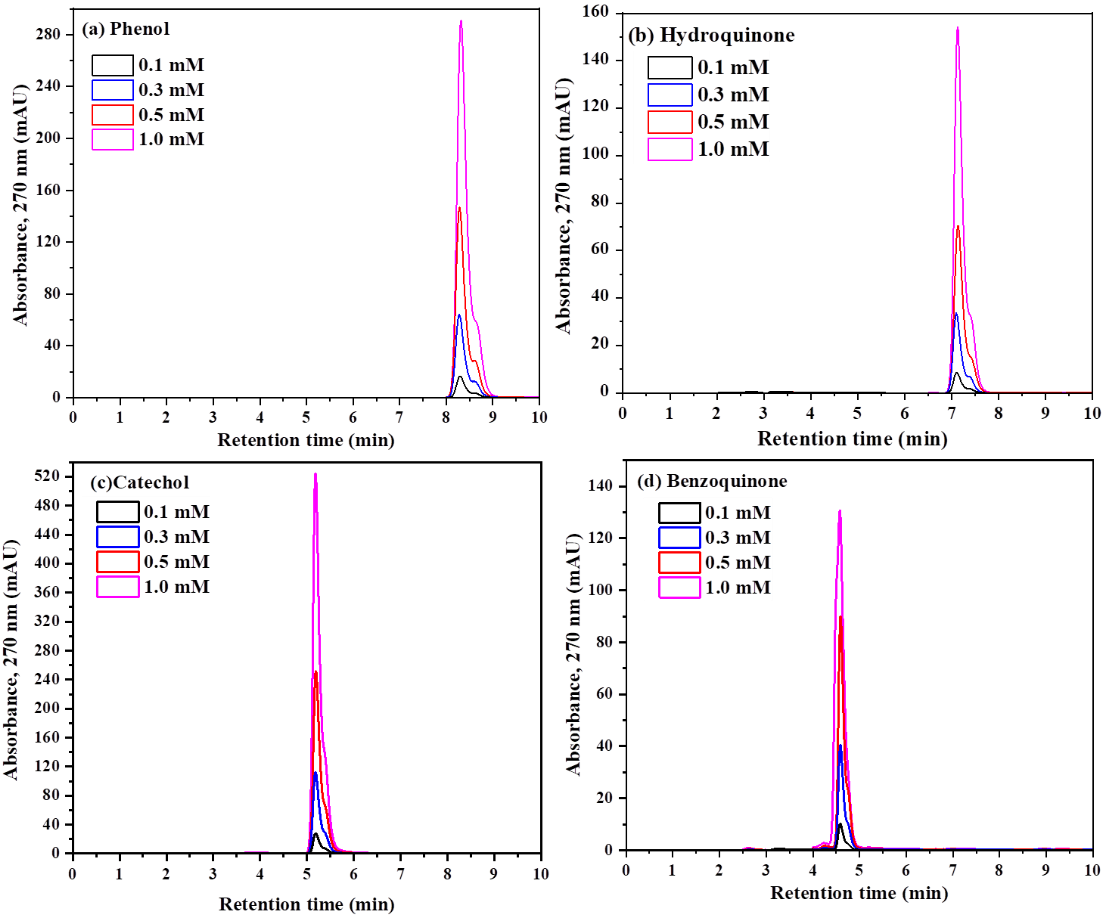

Figure 3.6 Individual HPLC chromatogram for (a) phenol, (b) hydroquinone (c) catechol and (d) benzoquinone at varying concentrations.

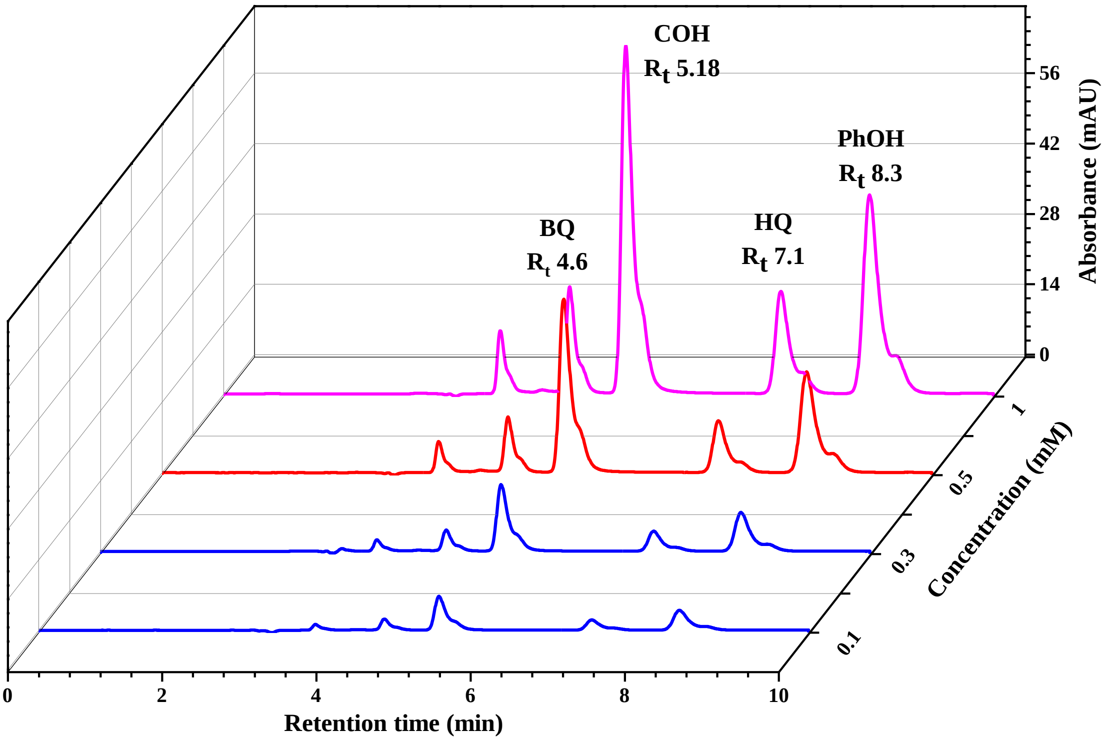

Figure 3.7 Overlaid 3D HPLC chromatogram for phenol + intermediates at varying concentrations.

3.4.2.2 Bacterial culture and quantification

Escherichia coli K12 (CTEC 4624) was chosen as the model indicator organism to study the inactivation kinetics following the WHO guidelines for drinking water quality. Fresh *E. coli* stocks were cultured overnight in Luria Bertani broth(tryptone 10 $g.L^{-1}$, NaCl 10 $g.L^{-1}$ and yeast extract 5 $g.L^{-1}$, Sigma Aldrich) and incubated at 37°C under constant agitation of 120 rpm in orbital rotary shaker in aerobic conditions. The bacterial suspension was collected after 21 h of incubation with a concentration of ~10^9 $CFU.mL^{-1}$. The cell density of the bacterial culture was analysed before the experiments by measuring the absorbance at 590 nm to predict the initial bacterial concentration.

For photocatalytic disinfection experiments, a 200 μL of stock (5×10^8 $CFU.mL^{-1}$) *E. coli* K12 were spiked into the 200 mL of 9 $g.L^{-1}$ NaCl solution with photocatalyst powder inside the reactor to get an initial concentration of *E. coli* of ~10^6 $CFU.mL^{-1}$.

During all photocatalytic disinfection experiments, samples were taken every 30 minutes and plated as it is without any removal of photocatalytic powder. The negative control in each experiment was plated in a separate agar dish, and no biocidal effect of nanomaterials on *E. coli* cells was observed. The colonies forming units were enumerated using a standard plate count method by serial 10-fold dilution in quarter strength (1/4) of Ringer's solution. In every experiment, 6 drops of each 10 µL volume were plated on Luria-Bertani agar (LB agar) plates and colony-forming units (CFUs) were counted after 24 h incubation at 37°C. In higher irradiation time, 100 µL samples were taken from the working suspension and spread over LB agar plates to decrease the detection limit down to 2 CFU.mL^{-1}. The control experiments performed in all cases were (i) under irradiation and absence of a catalyst, i.e. light control and (ii) the absence of light and presence of a catalyst, i.e. dark control.

3.4.3 GInaFIT modelling tool

To thoroughly understand the disinfection process taking place, it is essential to model the disinfection kinetics using appropriate fitting models. Given that the disinfection kinetics follow a mixture of phases, e.g. lag phase, log phase and tail phase, a suitable kinetic model was developed by Geeraerd *et al* [200]. The disinfection experiments kinetics can be assessed using the Gerraerd and Van Impe Inactivation model Fitting Tool, i.e. GInaFIT v1.6. GInaFIT is open-source free software and is used as an add-in tool in Microsoft Excel to predict the disinfection kinetics and microorganism survivability rate using 8 different models, as shown in figure 3.8. The users can apply different models to compare the statistical parameters obtained on each data set to determine the best fitting. On applying each model to experimental data, statistical parameters are calculated automatically by modelling. These parameters include identified values of microbial survivability ($Log_{10}N_0$), root mean sum of squared errors (RMSE), the coefficient of determination (or regression values) R^2, and in some cases the residual log of microbial concentration after the end of experiment, i.e. $Log_{10}N_{res.}$

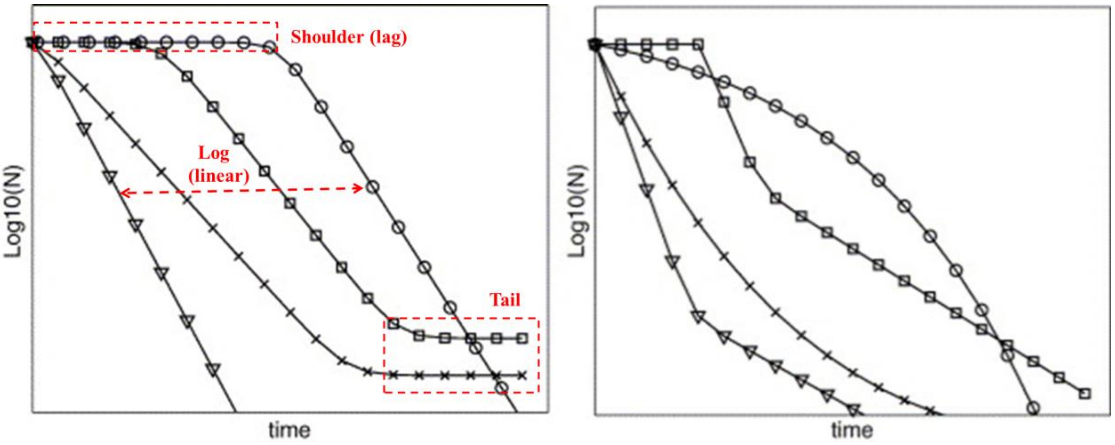

Figure 3.8 Eight basic types of inactivation curves in GInaFIT software. **Left**: log-linear regression (▽), log-linear with tail (×), log-linear with shoulder and tail (□) and log-linear with shoulder (○); representing different phases of inactivation. **Right:** biphasic (▽), concave with p< 1 (×), biphasic + shoulder (□) and convex with p>1 (○). Adapted from Geeraerd et al.(2005) International Journal of Food Microbiology, **102**,95-105 (2005) [200].

This model has been previously used for fitting kinetic data in solar disinfection [201, 202] and photocatalytic disinfection experiments [40, 41, 203]. Different models were applied for comparison on each data set to determine the best fit. The best-fitted model was based on the lowest possible root mean sum of squared errors (RMSE) (RMSE close to 0) obtained for each data and a maximum regression (or the coefficient of determination) close to unity, i.e. $R^2 = 1$ and noting the $Log_{10}N_{res}$ value at the end of the experiment.

3.4.4 Chemical probe studies

3.4.4.1 Photocatalytic RNO degradation

The hydroxyl ($^\bullet$OH) radical detection test was performed by photocatalytic degradation of p-nitrosodimethylaniline (RNO) as the chemical probe. RNO quantification was done by measuring the absorbance values for the standard concentration of RNO, i.e. 0, 5, 10, 15, 20, 30 and 50 $\times 10^{-6}$ M at wavelength 440 nm. For each concentration, 3 mL sample was analysed in 3 replicates, and a line of best fit was determined (details are discussed in chapter 4). For $^\bullet$OH detection, a 200 mL stock RNO solution of 22×10^{-6} M was used as the start concentration with suspended photocatalyst in the stirred tank reactor under the same photocatalytic experimental conditions as discussed in section 3.4.1. The photocatalytic degradation of RNO was assessed by sampling every 10 min and measuring the optical absorbance at 440 nm through UV-visible spectrophotometer. Control experiment of photolytic bleaching of RNO was also performed under the same conditions. The degradation of RNO was further assessed in the presence of an electron scavenger (2×10^{-4} M $AgNO_3$) to determine the rate and pathway for $^\bullet$OH detection using all the materials.

3.4.4.2 Photocatalytic methyl viologen dichloride reduction

To study the electron transfer via reduction pathway in photocatalysts, methyl viologen dichloride (MV^{2+}) was used as the chemical probe, following a method adapted from Roy et al.(1995) [204]. Fresh stock solutions (1×10^{-6} M) of MV^{2+} were prepared in distilled water having pH 6.5. The individual photocatalyst powder (50 mg) was dispersed in 100 mL of MV^{2+} stock solution by ultrasonication. The suspension was deoxygenated for 1 h by oxygen-free nitrogen (OFN) purging before and during the experiment under continuous stirring. The pH of the degassed suspension was adjusted by addition of either 0.1 M NaOH or 0.1 N HCl to observe the blue colour change at some specific pH for MV^{2+} to $MV^{\bullet+}$ transition (E^0 = -0.445 V,NHE). A combined glass pH electrode (HANNA INSTRUMENTS pH meter 8417) was used to monitor the pH of the suspension. The degassed suspension was irradiated with 1000 W Xe lamp to observe any colour change. pH was increased from low to high pH scale and any color change was noted. Since the amount of NaOH or HCl added between the measurements was generally low, only small deoxygenation of 5 min with OFN was necessary between the pH changes.

3.5 Photoelectrochemical measurements

3.5.1 Photoelectrochemical cell

The photoelectrochemical activity for all the photocatalyst was investigated in a single compartment PTFE cell with a quartz window. The set up was a three-electrode cell with the test sample as the working electrode, a platinum mesh paddle (5.9 cm^2) as the counter electrode and saturated calomel electrode (Gamry instruments) as the reference electrode. The cell was connected to a PC controlled electrochemical workstation (AUTOLAB PGSTAT 30) and irradiated through the quartz window by a 450 W xenon lamp (Horiba Jobin Yvon FL-1039/40) equipped with an IR water filter as the light source. The light intensity of the 450 W Xe lamp was measured at a distance of 4 cm away from the electrochemical cell using a spectral radiometer (FLAME-S-UV-VIS-ES, Ocean Optics B.V, Netherlands). The incident light intensity on the reactor window was 185 $W.m^{-2}$ in the UV-visible region (280-800 nm). The spectral emission of the light source is shown in figure 3.9. An optical shutter (Uniblitz, WMM-T1 by Vincent associates, Rochester, NY, USA) was used for chopped irradiation experiments, and grating output was set at 1200 $groove.mm^{-1.}$ The intensity output was measured at every 10 nm interval in the range of 250-500 nm, as shown in figure 3.10.

For photoelectrochemical measurements, 0.1M perchloric acid ($HClO_4$) was used as the electrolyte, unless stated otherwise. All potentials were referenced against the saturated calomel electrode (SCE) (unless stated otherwise). General Purpose Electrochemical Software (GPES) provided with AUTOLAB workstation was utilised for measuring the potential and current values.

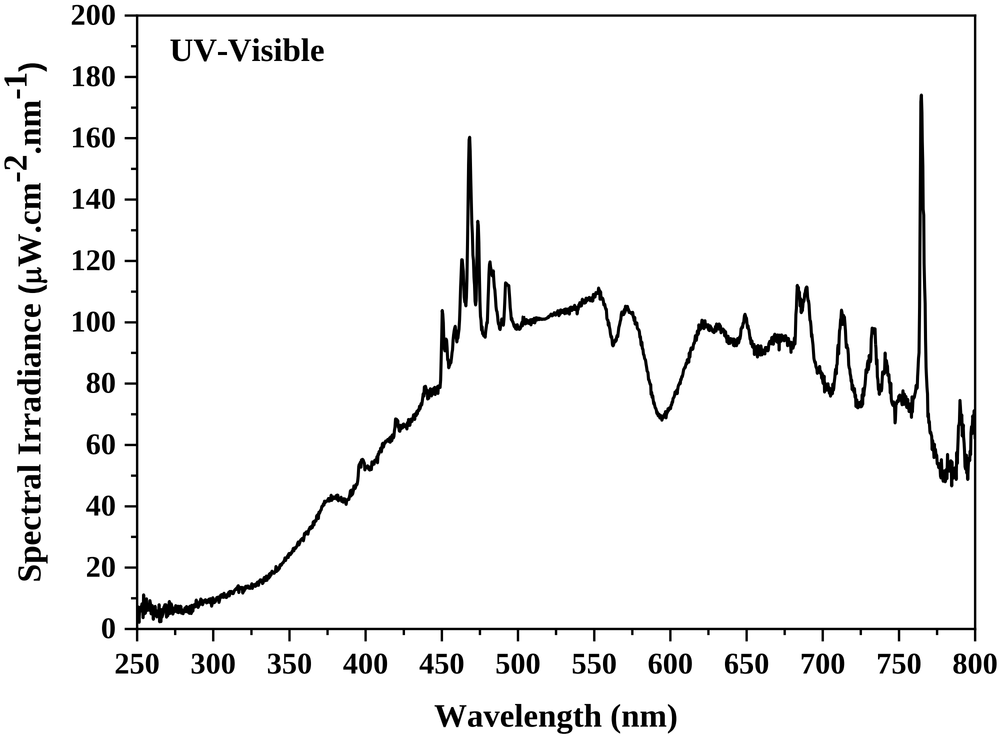

Figure 3.9 Spectral irradiance for the 450 W Xe lamp for UV-Vis irradiation.

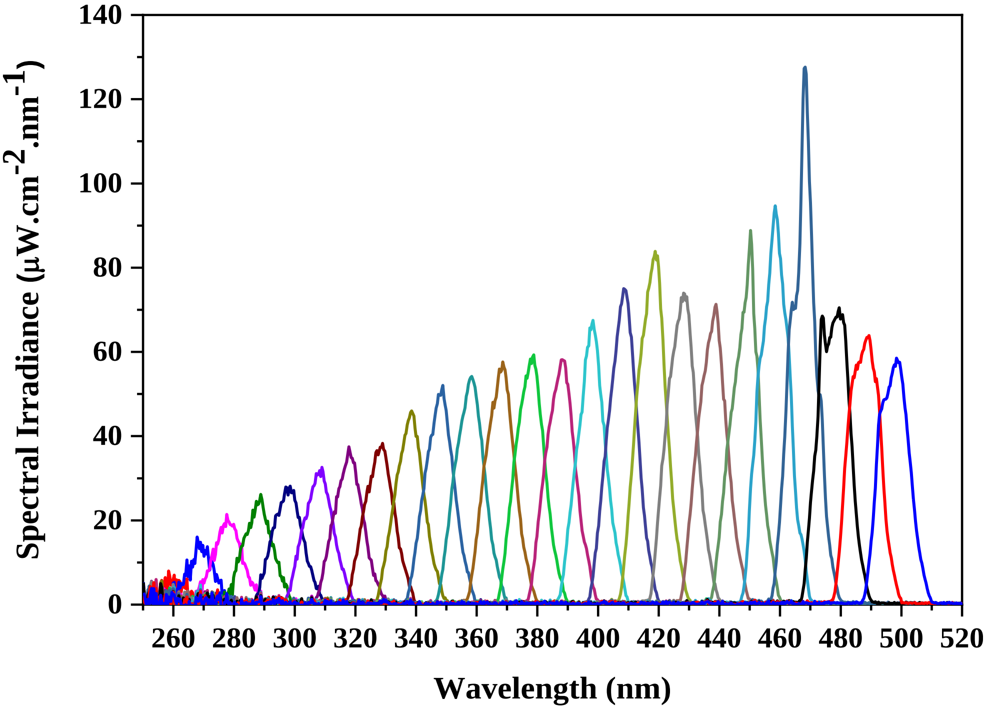

Figure 3.10 Monochromatic spectral intensity for 450 W Xe lamp from 250-500 nm at 10 nm intervals.

3.5.2 Photoelectrochemical methods

3.5.2.1 Linear sweep voltammetry

Linear sweep voltammetry is a method in which on sweeping potential from a range E_1 to E_2 at a constant scan rate, the corresponding current is recorded by the system and the output is represented as a *J*-V curve i.e. current density vs potential applied. The LSV measurements under irradiation determine the photocurrent response of the material across an applied potential range. Typical, LSV measurements were performed in this research from +1.0 V to 0.0 V and +1.0 V to -1.0 V at a constant scan rate of 5 $mV.s^{-1}$. The measurements were recorded under chopped irradiation, with light ON and OFF at every 10 s interval. The difference between the dark and light current is referred to as the photocurrent. The photoactive area of all electrodes was controlled for a suitable comparison between each measurement.

3.5.2.2 Current-time response at fixed potential

The current-time response was measured at a fixed potential of +1.0 V vs saturated calomel (SCE) as the reference electrode under chopped irradiation. To determine the onset potential (for anodic or cathodic current) the current was measured at different fixed potentials under chopped irradiation.

3.5.2.3 Spectral photocurrent response

The spectral photocurrent response was determined by measuring the current at +1.0 V (SCE) with monochromatic irradiation at 10 nm intervals from 250-500 nm. The spectral wavelength versus photocurrent obtained for each electrode was used to determine the incident photon to current efficiency (IPCE) (equation 3.1 and 3.2) [180, 205].

$$\mathrm{IPCE} = \frac{\text{n (Number of charge carriers generated)}}{\text{N (Number of incident photons)}} \qquad 3.1$$

$$\text{Or,} \quad \mathrm{IPCE}(\%) = \frac{hc}{e}\left(\frac{j_{ph}(\lambda)}{\lambda P(\lambda)}\right) \times 100 \qquad 3.2$$

Where h (Plank's constant) = 6.63×10^{-34} J.s; c (speed of light) = 3×10^{8} $m.s^{-1}$; e^- (charge of 1 electron) = 1.6×10^{-19} C, J_{ph} (λ) is the photocurrent density ($A.cm^{-2}$) at every monochromatic wavelength (nm) and P (λ) = incident spectral intensity ($W.cm^{-2}$) of the 450 W Xe light monochromatic source at every monochromatic wavelength.

3.5.3. Electrochemical impedance spectroscopy

Electrochemical impedance spectroscopy (EIS) was used to measure the charge transfer properties at the semiconductor electrolyte interface with the Autolab PGSTAT 30. It was conducted using AC amplitude of 10 mV in the frequency range of 0.01 Hz to 100 kHz, at a logarithmic frequency step and wave type single sine. The Nyquist and Bode plots were studied by fitting the data to an electrochemical equivalent circuit using the fit model tool. Nova version 1.16 was used to analyse the electrochemical impedance measurements. The electrochemical impedance measurements were performed in dark conditions.

3.5.3.1 Mott Schottky analysis

The Mott-Schottky (M-S) analysis is used to determine the flat band potential of a semiconductor electrode. Mott-Schottky plots were obtained based on the electrochemical fitted data from impedance spectroscopy. A potential range of -1.0 to +1.0 V and 0.0 to +1.0 V was applied in potential scan with step potential of 0.1 V to obtained the M-S plots in frequency range from 0.01 Hz to 100 kHz, with single sinusoidal AC voltage and 10 mV as the root mean square (RMS) value. The Rs-Cp/Rp M-S plots were analysed to determine the flat band potential at x-intercept of applied potential range.

3.5.4 Electrochemically assisted photocatalytic (EAP) disinfection

For electrochemically assisted photocatalytic disinfection experiments, a quartz water jacket reactor of total capacity 35 mL was used as the photoreactor (Figure 3.11). A plastic cap was used with groves for 3 electrodes (WE, CE and RE) and 1 grove for air sparging. The working volume of the reactor for all experiments was 15 mL, and air sparging was done using a Pasteur pipette before and during the reaction through an aquarium pump. The temperature of the reactor was maintained at 20 ± 2°C using a water circulation pump. The initial concentration of *E. coli* in the EAP experiments used was 10^6 CFU.mL^{-1}. Therefore, 15 µL of *E. coli* (10^6 CFU.mL^{-1}) was spiked in 15 mL of quarter (1/4) strength of Ringer's solution (pH 7 ± 0.2) used as the working electrolyte and also to maintain the osmotic balance for the microorganism survival at the start. For all EAP experiments, a fixed potential of +1.0 V was applied to the working electrode, which was irradiated on the front face. The photocurrent was recorded at every sampling interval of 30 min and through the experiment continuously.

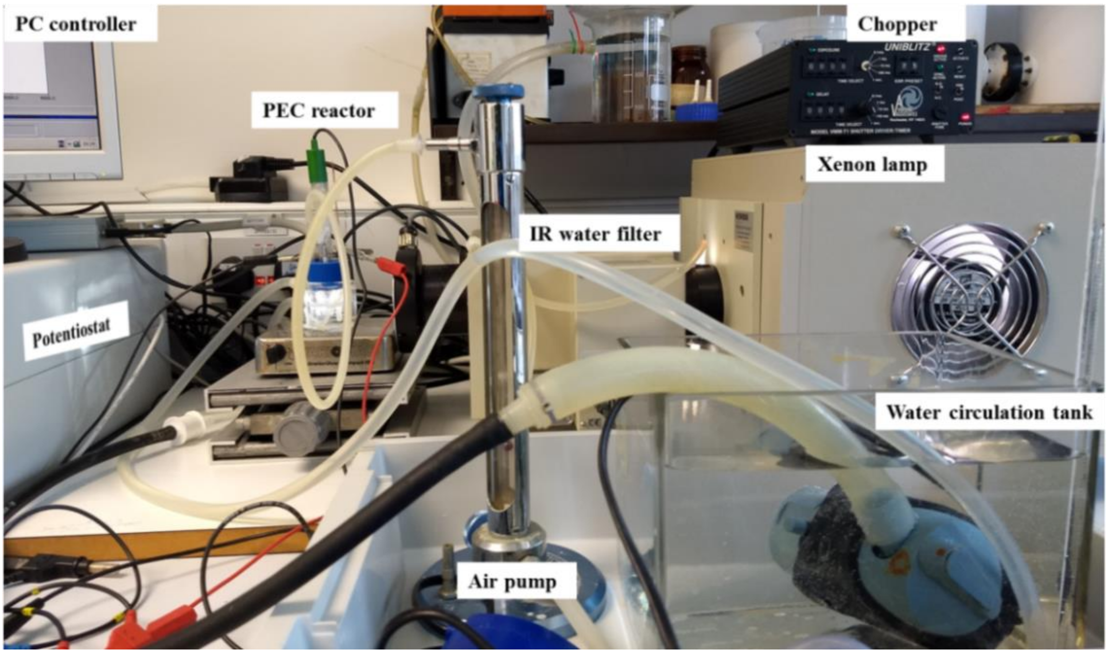

Figure 3.11 Electrochemically assisted photocatalytic reactor set up

Chapter 4. Physicochemical characterisation and photocatalytic activity of WO_3/g-C_3N_4 heterostructures

4.1 Aim and Objectives

4.1.1 Aim

This chapter aims to study the physicochemical characterisation and photocatalytic activity of the two-dimensional nanostructures of tungsten trioxide (WO_3) and graphitic-carbon nitride (g-C_3N_4) as individual photocatalytic materials and combined in heterostructured materials for the degradation of organic pollutants and inactivation of *Escherichia coli* K12 under simulated solar irradiation.

4.1.2 Objectives

i. To synthesise 2D-tungsten trioxide (WO_3) using a hydrothermal method and graphitic carbon nitride (g-C_3N_4) using a thermal polymerisation route.
ii. To study the characteristic properties of WO_3 nanoplates and g-C_3N_4 by advanced analytical techniques such as SEM, HRTEM for morphology and crystal phase by XRD patterns.
iii. To perform specific surface area analysis for determining the surface area of the materials.
iv. To perform control experiments with the stirred tank reactor and estimate an optimal photocatalyst loading (from UV transmission and empirical tests) for photocatalytic experiments using P25-TiO_2 as reference.
v. To study the photocatalytic activity of WO_3 and g-C_3N_4 using formic acid and phenol as model organic pollutants.
vi. To investigate the photocatalytic activity of WO_3/g-C_3N_4 heterostructures for the photocatalytic inactivation of *Escherichia coli (E. coli)* under simulated solar irradiation.

4.2 Introduction

Titanium dioxide (TiO_2) is the most popular semiconductor in the field of photocatalysis [27, 44, 47]. There are challenges as TiO_2 has a wide bandgap (3.2 eV) restricting its ability to absorb only in the UV region (~ up to 4% of solar spectrum). For solar applications of photocatalysis, alternatives to TiO_2 must be considered that can utilise both the UV and visible spectrum [206]. Tungsten oxide ($WO_{3)}$ is a metal oxide with a bandgap extending into the visible region. It is an n-type semiconductor having a narrow bandgap range between 2.6-2.8 eV [207, 208]. The valence band (VB) of WO_3 is formed by filled O *2p* orbitals and empty W $5d^0$ orbitals form the conduction band of WO_3 (CB). The narrow bandgap of WO_3, non-toxicity, stability in acidic solutions and a positive valence band edge (+3.1 V (NHE) at pH 0), make it a possible material for solar light-driven photocatalysis for water purification (organic pollutant degradation) [108, 133, 134] and water oxidation (O_2 evolution) [61, 129, 131, 209]. However, the conduction band edge of WO_3 is not negative enough (+0.4 V (NHE) at pH 0) for reduction reactions such as H_2 production ($E_{H2/H2O}$ = 0 V (NHE)) or the one electron reduction of oxygen ($E_{O2/\bullet O2}^{-}$ = -0.16 V (NHE)). Combination of WO_3 with another semiconductor (potentially with a negative CB edge to drive photocatalytic reduction reaction) as a z-scheme photocatalyst for an overall photocatalysis is possible [102, 103, 165, 166, 210].

The photocatalytic efficiency and good electron-hole separation in WO_3 can be achieved by nanostructuring of WO_3 into two-dimensional structures (2D). Two dimensional (2D) nanostructured photocatalysts have been frequently employed, mainly due to their advantages of having higher specific surface area compared to 0D, 1D or 3D (bulk) materials producing more catalytic active sites for photocatalysis [61, 125, 131]. The crystallite size of WO_3 has a direct effect on the optical absorption of the material. The bandgap of bulk-WO_3 has been reported to increase as a result of decreasing crystallite size, causing a blue shift in the optical absorption. The blue shift in the optical absorption is a result of size quantisation due to the quantum confinement (QC) effect, which can be either strong or weak. If the crystallite size is smaller than Bohr’s radius for WO_3 (~ 3 nm), strong QC effect takes place. Otherwise, a weak QC effect is observed when the crystal size is greater than Bohr’s radius. However, Gullapalli et al.(2010) reported a linear inverse relationship between the growth temperature, crystallite size and bandgap of WO_3 films prepared by RF sputtering [211]. In their case, a weak QC effect observed in WO_3 was accountable for the shift of bandgap by 0.58 eV (from 3.25 eV to 2.92 eV) with increasing crystal size from 9-50 nm. Therefore, a weak quantum confinement effect introduced in the nanostructures of WO_3 can induce a higher absorption coefficient.

Synthesis of 2D-WO_3 nanomaterials has been achieved using wet chemical routes. A method that is cost-effective, facile and leads to user-friendly controlled morphology on repeated synthesis is the most desirable for large scale production of 2D nanomaterials. The hydrothermal method is one such liquid phase method, most commonly used for achieving controlled 2D-WO_3. The chemical synthesis of 2D nanomaterials by a hydrothermal method depends on different parameters such as precursor type, reaction temperature, pH of the solution, the addition of a surfactant or not, centrifugation and post-annealing treatment. By careful consideration of these parameters, one can achieve a potential 2D nanomaterial with good functional yield. Hydrothermal synthesis of 2D-WO_3 in the form of nanoplates or nanosheets is reported at variable high temperature and under strong acidic environments [131, 209]. A fundamental process of formation of 2D-WO_3 nanosheets is shown in figure 4.1.

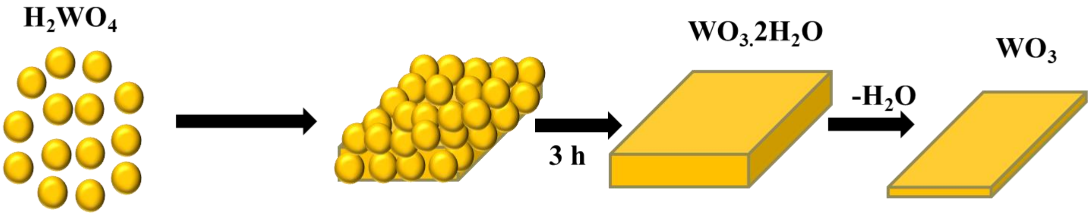

Figure 4.1 Formation of WO_3 nanosheets by hydrothermal method. Adapted from Zhang et al.(2014), Ind. Eng. Chem. Res. (2014) [133].

The hydrothermal synthesis of 2D-WO_3 structures, involves the dissolution of the tungstate precursor in a strongly acidic environment to form a yellow colloid of tungstic acid (H_2WO_4) at ambient temperature. The colloidal yellow particles self-agglomerate and integrate to form thicker sheets. The final step is the hydrothermal treatment of the multilayer sheets into specific orientation attachment and nucleation under applied temperature to form thin sheet/platelet like structures. The in-situ hydrothermal phase transformation leads to the formation of sharp-edged corners of WO_3 nanosheets that are generally rectangular shaped [133].

Two-dimensional WO_3 as photocatalyst in the presence of metal co-catalyst (Mo, Pt) has been investigated for photocatalytic oxidation reactions under visible irradiation [108, 133, 134]. In addition, the use of the electron acceptor (Ag^+) with WO_3 photocatalyst to drive the electron-hole pair separation for photocatalytic oxidation reactions has been studied. The associated reduction reacton in such case is the reduction of the electron acceptor. For instance, photocatalytic oxygen evolution reported using 2D-WO_3 nanoplates/flakes/sheets involves the reduction of a sacrificial electron acceptor, e.g. Ag^+ to Ag^0 [61, 107, 129, 131, 209]. Photocatalytic oxidation reactions using WO_3 are possible but taking into consideration the positive CB edge of WO_3, the practical implication of using 2D-WO_3 as an efficient photocatalyst without any sacrificial agent or metal co-catalyst for overall solar photocatalysis is still limited. Rational designing of multifunctional photocatalysts for utilising solar energy with suitable band edge potentials (CB and VB) is needed. The photocatalytic efficiency of 2D-WO_3 might be improved by coupling it with another 2D semiconductor in the form of heterostructure to achieve the desired photocatalytic application. The main criteria in designing of these multifunctional heterostructure photocatalysts are the correct position of the respective band edge potentials, where one material with a very negative CB edge is responsible for reduction reactions, and another with a very positive VB edge is responsible for oxidation reactions [89]. There are definite advantages of using such heterostructures over single semiconductor, that include the use of two solar photons, increased overall voltage window to drive reactions, and possible improvements in charge carrier lifetimes and transport distances. Multifunctional photocatalysts as heterostructures are n-n, n-p or n/p-organic semiconductor type. The latter being a relatively recent formation where an inorganic semiconductor typically n-type or p-type is combined with an organic semiconductor rich in carbon atoms such as graphene, rGO or graphitic carbon nitride. Organic semiconductors such as graphitic carbon nitride consist of a π conjugated structure with extending the π-electron system in a linear chain and have a lone pair of electrons at the nitrogen atom. These conjugated structures can be useful in promoting the limited electron transfer or modifying the inorganic semiconductors for enhanced visible-light photocatalytic activity.

The formation of graphitic carbon nitride (g-C_3N_4) is a combination of the condensation of the molecular precursor and a linear polymerisation of melem molecules via tri-s-triazine units at a range of temperature between 350-600°C [150]. Starting with precursor rich in C- and N- atoms such as melamine ($C_3H_6N_6$), at 390°C formation of melam takes place that are the dimers of melamine. Both melem and melamine consist of a molecular structure made of strong covalent bonds. Presence of weak van der Waals interactions and H-bonds are responsible for holding the structure together in case of both melam and melamine. The condensation of melam to melem takes via the release of NH_3 molecules and polymerisation of melem to melon at a temperature around 520°C leads to the formation of a linear polymeric chain of tri-s-triazine units, potentially forming the g-C_3N_4 polymeric solid as shown in figure 4.2.

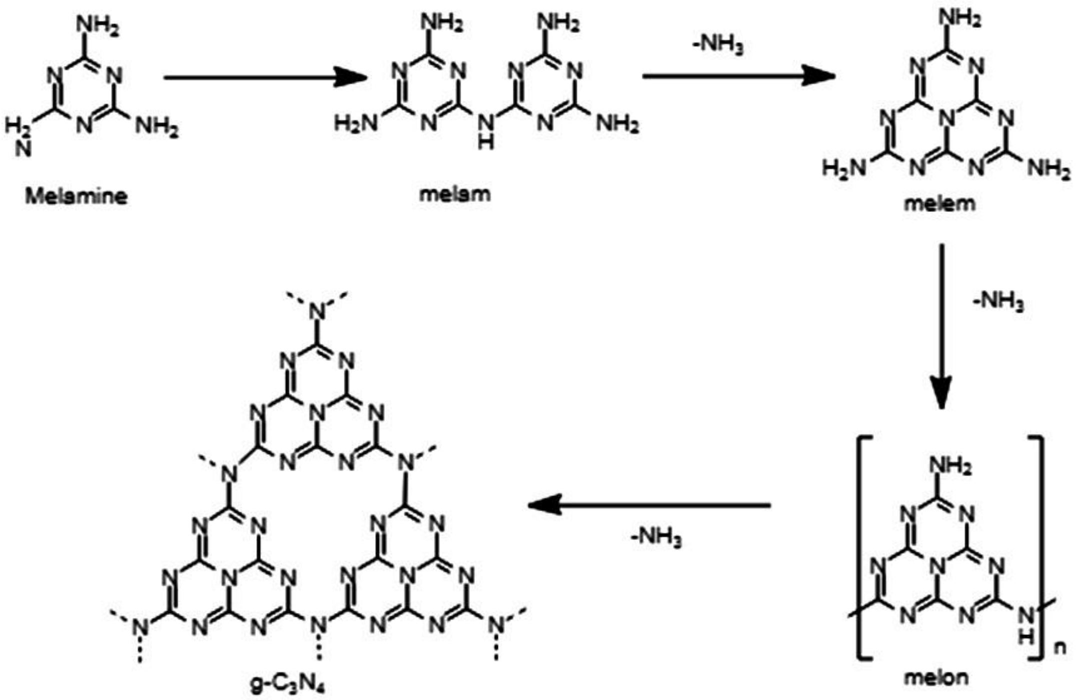

Figure 4.2 Pathway of g-C_3N_4 from precursor melamine. Adapted from Thomas et al.(2008) J. Mater. Chem., (2008) [150].

Studies on varying condensation temperatures to obtain an optimal C/N ratio for g-C_3N_4 have been reported. The change in temperature of synthesis affects the optical and electronic properties of g-C_3N_4. For instance, Antonetti et al.(2008) observed a decrease in the bandgap of g-C_3N_4 with increasing condensation temperatures. g-C_3N_4 has a narrow bandgap of 2.7 eV and absorption range extended up to 460 nm [109]. However, to be an ideal visible light absorbing photocatalyst, a material should also possess suitable conduction and valence band potentials to perform reduction and oxidation reaction. Being an organic polymeric solid, in g-C_3N_4, the electron transport levels are represented as the lowest unoccupied molecular orbital (LUMO) and hole transport level as the highest occupied molecular orbital level (HOMO). But often these levels are denoted as conduction band minima and valence band maxima in literature misrepresenting the critical difference between an organic and inorganic semiconductor. Figure 4.3 shows the basic difference between the energy levels of inorganic and organic semiconductors. (a) Represents the band energy levels of an inorganic semiconductor, where atoms within a solid are covalently bonded and obey the band theory of solids. The electrons are transferred from almost filled valence band to the empty conduction band. However, (b) shows the discrete energy levels of an organic semiconductor with a sp^2 configuration, where a valence p-orbital leads to delocalization of electrons because the molecular orbitals are not closely packed. During charge transfer in organic semiconductors, the hole transfer takes place in the HOMO, that overlaps with π-bonded molecular orbital and likewise electron transfer takes place in LUMO that overlaps with the π*(antibonding) orbital. The energy required to excite an electron from HOMO to LUMO is the HOMO-LUMO (H-L) gap, analogous to the bandgap (E_g) in inorganic semiconductors.

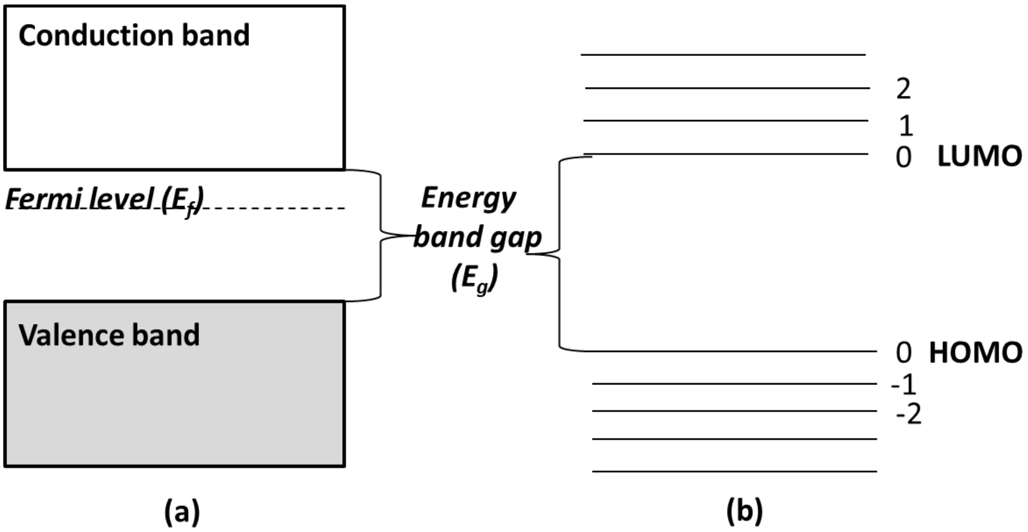

Figure 4.3 Energy band diagram (a) inorganic semiconductors and (b) organic semiconductors. Adapted from Dechun; Materials, Devices and Applications, (2013) [212].

There is extensive literature reporting on the positions of band edge potentials for g-C_3N_4 as CB_{edge} = -1.13 V (NHE) pH 7 and VB_{edge} = +1.75 V (NHE) pH 7 [155]. Considering these positions for g-C_3N_4, a greater overpotential for driving reduction reactions, including HER[155] and CO_2 reduction [198] is available. Still, the positive HOMO level (VB_{edge}) can only facilitate selective photocatalytic oxidation of species with relatively small positive redox potentials, e.g. alcohols present in water to convert to aldehydes [192, 213].

Therefore, coupling 2D-WO_3 and 2D g-C_3N_4 in a heterostructure might increase the overall photocatalytic efficiency. Both WO_3 and g-C_3N_4 have an equivalent bandgap of 2.7 eV and can easily absorb solar photons up to 460 nm when combined as heterostructures. Combination of WO_3/g-C_3N_4 in z-scheme as heterostructure photocatalyst has been reported for water splitting[101] (O_2 and/or H_2 production[92, 106]), for pollutant degradation[102, 163, 165] and CO_2 reduction[98], but the effectiveness of these heterostructured photocatalysts for water disinfection has not been investigated until now. The generation of reactive oxygen species (ROS) from photocatalytic disinfection initiated by single-electron reduction of molecular oxygen to superoxide ($^{\bullet}O_2^-$) radical (-0.16 V (NHE)) and oxidation of water to produce hydroxyl ($^{\bullet}OH$) radicals (+2.73 V (NHE)) using WO_3/g-C_3N_4 heterostructures has not been reported. Owing to its negative reduction potential and ability to perform selective oxidation reactions such as conversion of aromatic alcohol to aldehydes, only a few researchers have reported the use of g-C_3N_4 for the photocatalytic inactivation of *E. coli* [39, 110, 156, 157] and photocatalytic disinfection using only 2D-WO_3 has not been reported before.

The aim of this work was to determine the photocatalytic activity of 2D WO_3 and g-C_3N_4 and their z-scheme heterostructures. The prepared heterostructures of WO_3/g-C_3N_4 were characterised for their physicochemical properties to analyse the change in morphology and specific surface area. The photocatalytic activity of WO_3/g-C_3N_4 heterostructures along with the analogue WO_3 and g-C_3N_4 were investigated for organic pollutant degradation and inactivation of microorganism *E. coli* under simulated solar irradiations. The results of the photocatalytic tests obtained for WO_3/g-C_3N_4 were presented and compared against a standard commercial P25-TiO_2 as the reference photocatalyst.

4.3 Experimental Section

4.3.1 Photocatalyst preparation

Two-dimensional nanostructures of WO_3, g-C_3N_4 and their corresponding heterostructures were used as photocatalysts in this work. Tungsten oxide nanoplates (2D-WO_3) were synthesized by a modified hydrothermal method. The thermal polymerisation of graphitic carbon nitride (g-C_3N_4) was achieved using a two-step heat treatment. Heterostructures formation between 2D-WO_3 and 2D-g-C_3N_4 nanomaterials were synthesised following different approaches such as ultrasonic chemical exfoliation, calcination method, in-situ hydrothermal synthesis of WO_3 nanoplates in preformed g-C_3N_4 dispersions and by an electrostatic interaction technique by dispersion of WO_3 and g-C_3N_4 in a citrate buffer solution. The detailed synthesis procedure for all the 2D nanomaterials and their heterostructures are described from section 3.2.1 to 3.2.3.

A summarized list of all the 2D nanomaterials synthesised is shown in table 4.1 with their abbreviated names, method of preparation and the ratio of WO_3:g-C_3N_4 used in the heterostructure formation.

Table 4.1 Materials with their synthesis method and abbreviated names.

Sample	Abbreviation	Synthesis method
Tungsten trioxide	WO_3	Hydrothermal
g-carbon nitride	g-C_3N_4	Thermal polymerisation
WO_3/g-C_3N_4 (1: 1)	WCN(1:1)	Ultrasonication
WO_3/g-C_3N_4 (1: 1)	Ex.WCN(1:1)	Chemical exfoliation
WO_3/g-C_3N_4 (05: 95)	WCN595	Calcination
WO_3/g-C_3N_4 (10:90)	WCN19	Calcination
WO_3/g-C_3N_4 (90:10)	WCN91	Calcination
WO_3/g-C_3N_4	WCN2	In-situ hydrothermal
WO_3/g-C_3N_4	WCN(1:4)pH 2.25	Exfoliation in citrate buffer

4.3.2 Material characterisation

The synthesised WO_3 and g-C_3N_4 nanomaterials were characterised by transmission electron microscopy (TEM) and scanning electron microscopy (SEM). The crystallographic data were analysed by powder X-ray diffraction patterns. The specific surface area measurements of the samples were analysed by Quantachrome AUTOSORB-1 specific surface area analyser with outgassing at 250°C for 3 h.

4.3.3 Photocatalytic properties

4.3.3.1 Model Target pollutants

To study the photocatalytic properties of the synthesised nanostructures, it was necessary to choose the model pollutant with simple chemical structure, good water solubility, non-volatile, photochemically inactive and one that can be easily analysed for its photodegradation activity. Many complex organic pollutants form intermediate by-products, which are difficult to identify, remove, and also require sophisticated spectroscopic methods. An organic acid (formic acid, (HCOOH)) and a cyclic aromatic compound (phenol, C_6H_6O)) were used as model organic pollutants. Formic acid is the simplest carboxylic acid studied for photocatalytic activities due to its breakdown into CO_2 and H_2O [199, 214]. Its direct oxidation into CO_2 and H_2O often represents it as a final intermediate during the photodegradation of more complex compounds. Phenol, a persistent organic pollutant commonly found in water and wastewater at different sources, is resistant to biological and chemical treatments[215]. Both of these target pollutants are stable and soluble in aqueous solutions at room temperature. The stock concentrations of 1×10^{-2} mol.L^{-1} formic acid (Sigma-Aldrich, UK) and 1×10^{-3} mol.L^{-1} phenol (BDH, Poole Germany) prepared in distilled water, were used as the start concentrations for photocatalytic experiments.

4.3.3.2 Determination of formic acid using UV-visible spectroscopy

The UV-visible spectrophotometer was calibrated by injecting different standard solutions of formic acid, i.e. 1,2,4,6,8,10 mM. Each standard solution (3 mL) was poured into a quartz cuvette and absorbance analysed by taking 3 replicates of each solution. Formic acid showed a maximum absorption peak at 210 nm. The absorption values of the corresponding peak were plotted against formic acid concentration, and the line of best fit was determined, from the curve for formic acid concentration vs absorbance (Figure 4.4). The absorption coefficient for formic acid at wavelength 210 nm was calculated to be 0.0456 $mM^{-1}cm^{-1}$.

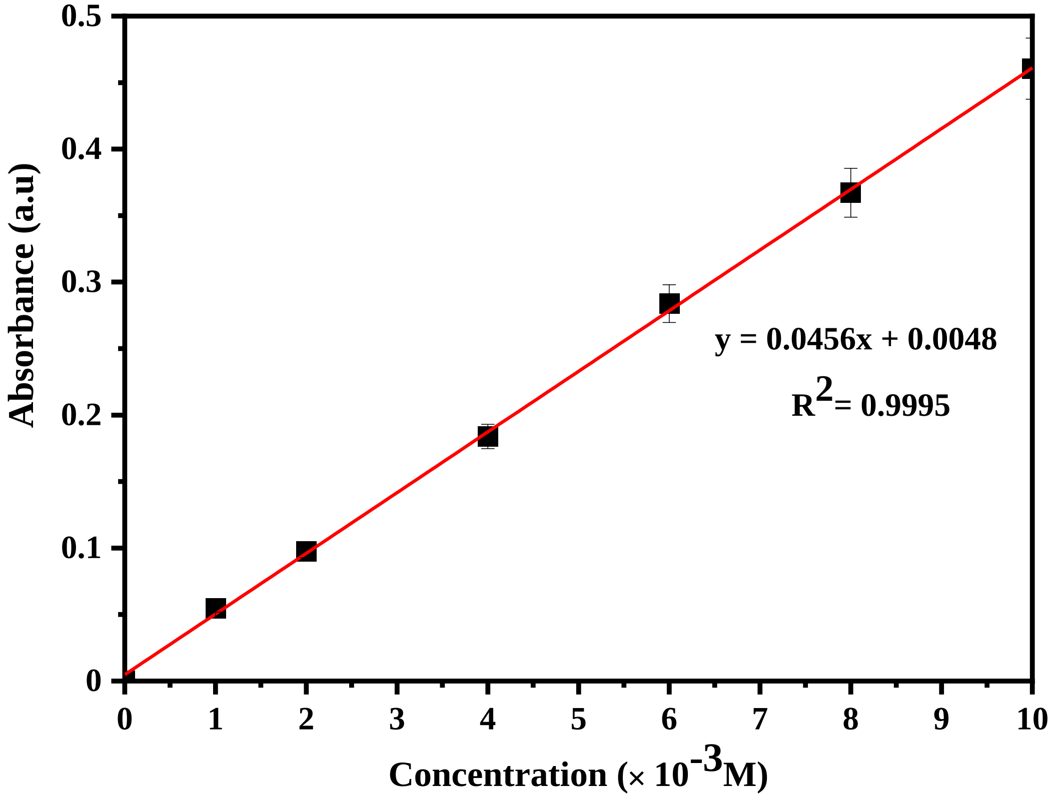

Figure 4.4 Formic acid determination by UV-Vis spectroscopy at λ = 210 nm.

4.3.3.3 Determination of phenol by HPLC

The concentration of phenol was determined by reverse-phase High-performance liquid chromatography (HPLC) using an Agilent 1200 series HPLC system equipped with a UV detector. The detailed specifications for HPLC are mentioned in chapter 3, section 3.4.2.1.

The HPLC system was calibrated by injection of different standard solutions of phenol and its intermediates: benzoquinone (BQ), hydroquinone (HQ) and catechol (COH), i.e. 0.1, 0.3, 0.5, 1.0 mM. Each of the standard solutions was filled into the HPLC vials for analysis, and 3 replicates per sample were analysed. The peak area absorbance versus concentration of phenol and its intermediate products is shown in figure 4.5. The retention time for each sample with the statistical parameters such as the slope of the line of best fit and coefficient of determination are presented in table 4.2.

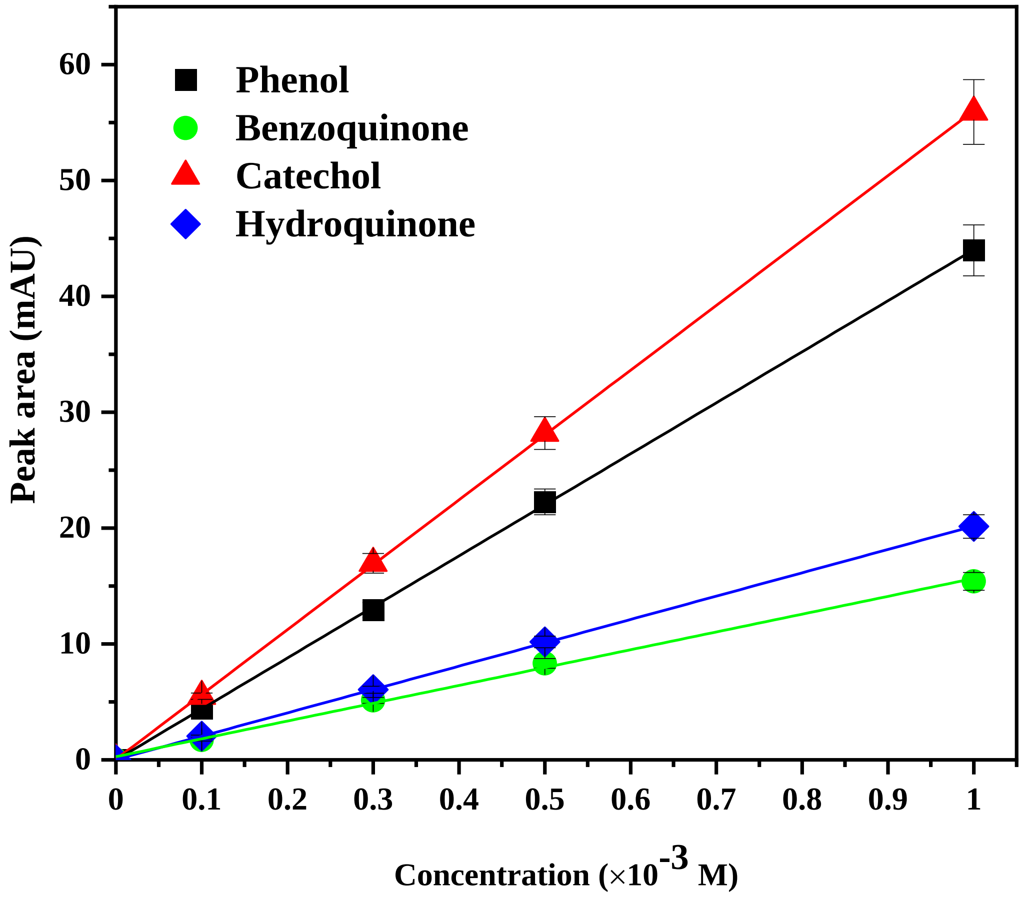

Figure 4.5 Determination of phenol (PhOH) + intermediate products (benzoquinone BQ, catechol COH, hydroquinone HQ) as a function of HPLC peak area vs concentration at detection wavelength (λ) = 270 nm.

Table 4.2 Statistical parameters for phenol and intermediate products

Sample	Retention time (min)	Slope (mAU^{-1}.mM^{-1})	Coefficient of determination (R^2)
Phenol	8.3	44.04	0.999
Benzoquinone	4.6	15.38	0.997
Catechol	5.2	55.97	0.999
Hydroquinone	7.1	20.15	0.999

4.3.3.4 Model indicator organism

To assess the photocatalytic disinfection activity of the prepared 2D photocatalyst, *Escherichia coli* K12 was used as the model microorganism. *E. coli* is the model choice of indicator organism set by WHO, to detect the faecal contamination in a drinking water sample where the standard is 0 CFU per 100 mL [216]. *E. coli* has been by far the most investigated microorganism in literature for photocatalytic water disinfection [217]. Fresh stocks of *E. coli* K12 (CTEC 4624) were cultured for experiments and details of the culture and quantification have been discussed previously in section 3.4.2.2. The initial start concentration of *E. coli* used for testing the photocatalytic disinfection activity was roughly 10^6 CFU.mL^{-1}.

4.3.3.5 GInaFIT model

The disinfection experiments were analysed by fitting different microbial survivability model using the GInAFIT tool. The kinetic parameters and different type of models used are described in section 3.4.3. Different models were applied for comparison on each data set to determine the best fit. The selection of the best fit model was made by comparing the lowest possible root mean sum of squared errors (RMSE) value (close to 0) and a maximum regression(or the coefficient of determination) close to unity, i.e. $R^2 = 1$ in different models for the single data set. Most of the data presented in this study had the best fit using Weibull, Weibull+ tail model or double Weibull model.

4.3.3.6 Photocatalytic reactor

A customised stirred tank reactor built to provide a proper mixing and efficient mass transfer was used as the photocatalytic reactor, with a working volume of 200 mL [199]. All photocatalysts used in this work were synthesised powders of WO_3, g-C_3N_4 and WO_3/g-C_3N_4 heterostructures. The optimal loading used for all materials has been discussed in later sections. The photocatalyst was suspended with the pollutant/microorganism solution under continuous stirring of 500 rpm using a stainless steel propeller. The rotation speed was selected based on a previous investigation of the group for photocatalytic disinfection (*E. coli* K12) using P25-TiO_2 and P25-rGO suspension with same stirred tank reactor, in which rotation speed of 500 rpm was shown to provide sufficient mixing and to avoid any mass transfer limitation [40]. McMurray et al.(2004) had already reported using the same reactor that the rate of degradation of organic pollutants (formic acid, oxalic acid) was not markedly dependent on the propeller rotation speed at rpm >500 [199]. The photocatalytic suspension was stirred for 1 h in the dark before irradiation for any adsorption to take place based on previous study performed at Ulster by Wadhwa et al.(2011) on the dark adsorption of pollutants; formic acid(1×10^{-2} M) and phenol(1×10^{-3} M) using TiO_2 photocatalysts. A dark adsorption of <15% of the initial concentration of formic acid was reported in 4 h by Wadhwa et al.(2011) [52]. In the present work, the reactor was irradiated with 1000 W Xe lamp from below with light intensity simulated to AM 1.5 global irradiation spectrum of the sun. For detailed experimental setup, please refer to section 3.4.1 and for bacterial culture and quantification to section 3.4.2.2.

4.3.3.7 Calibration of light intensity

In the solar spectrum at sea level, only 4-5% of the irradiation is in the UV domain. The calculated spectral dose is shown in table 4.3. A standard reference spectrum (ASTM NREL data -ASTM G-173-0), of air mass 1.5 was obtained from the American Society for Testing and Materials (ASTM) to simulate the in house 1000 W Xe light source according to AM1.5 global irradiance[15]. The reference spectrum table of Global Degree Tilt: ASTM G-173 consists of spectral wavelength (nm) vs total global spectral irradiance at a zenith angle of 37°. The AM1.5 global includes along with the direct, the scattered (blue sky) and diffused light, while the counterpart AM1.5 direct irradiation was the direct spectrum beam output of the sun with a circumsolar component of a disk of 2.5° around the sun.

The initial irradiance of 1000 Xe lamp was measured at a distance of 40 cm away from the photocatalytic reactor set up using a spectral radiometer (FLAME-S-UV-VIS-ES, Ocean Optics B.V, Netherlands) equipped with an integrating sphere. The unfiltered emission spectrum of the 1000 W Xe lamp measured had UVB intensity of 11.59 $W.m^{-2}$ (280-320 nm). This intensity was approximately 7 times of the UVB spectral intensity (1.63 $W.m^{-2}$) of the AM1.5 G standard. For photocatalytic disinfection experiments to be comparable to solar disinfection of water, it was essential to mimick the UVB dose equivalent to 1 sun’s output at AM1.5 G. Therefore, a 6 mm thick Pilkington K glass was placed in front of xenon lamp to filter the extra UVB component. Pilkington K glass has a reflective pyrolytic coating that allows most of the visible light to pass through and blocks 99% of UVB output emitted from the sun. The UVB output for the light source was reduced to 1.67 $W.m^{-2}$ (Table 4.3). The measured spectral intensity of the filtered 1000 W xenon light source is shown in figure 4.6 with the ASTM spectra standard of air mass 1.5 global and air mass 1.5 direct + circumsolar overlaid for reference.

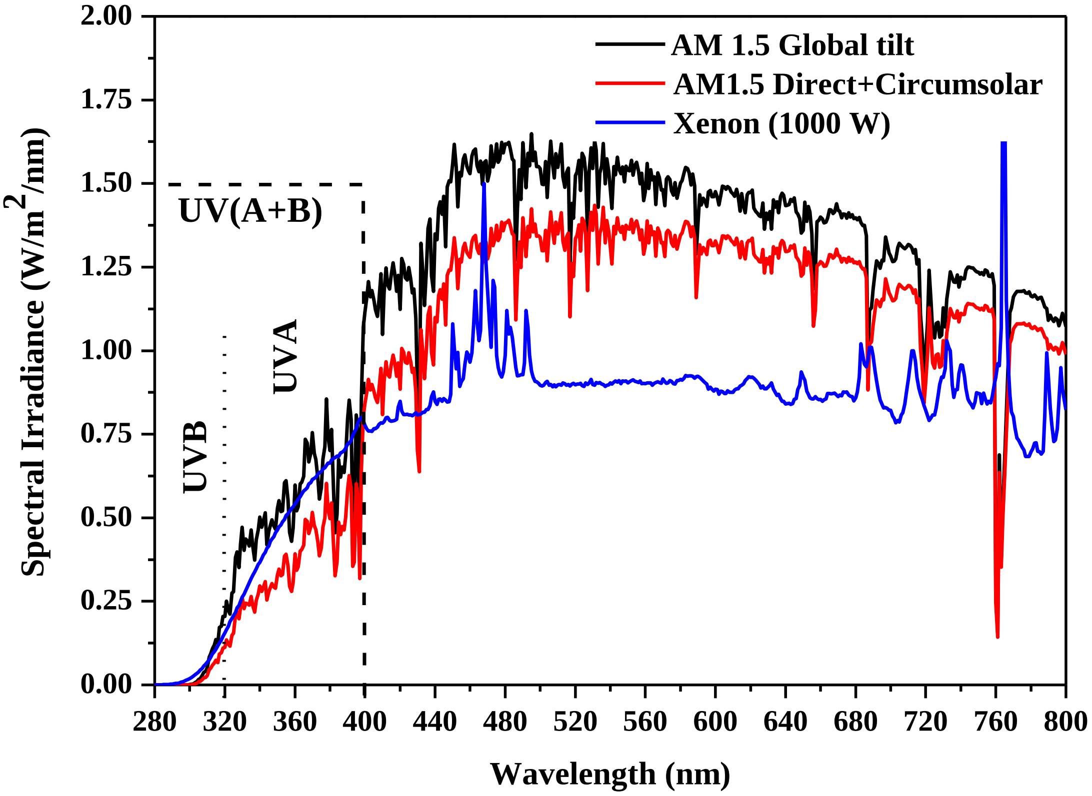

Figure 4.6 Spectral irradiance of 1000 W Xe lamp simulated to total UV output of air mass 1.5 global spectrum of the sun. The AM1.5 G and AM1.5 Direct spectra were obtained from the ASTM G-173 database provided by ASTM [15].

Table 4.3 The spectral output of the Xe lamp compared to the ASTM G-173 data [15].

Wavelength range (nm)	*Spectral output($W.m^{-2}$)*		
	Filtered Xe (1000 W)	**AM1.5(global)**	**AM1.5(direct)**
Total (280-4000)	-	1000.39	900.16
UV-Visible (280-800)	400.48	590.20	509.80
UVA+UVB (280-400)	44.35	47.23	31.38
UVB	1.67	1.63	0.89
UVA:UVB	27:1	28:1	34:1

4.4 Results and Discussion

4.4.1 Morphological characterisation of as-synthesised samples

The X-ray diffraction pattern of the synthesized WO_3 nanoplates is shown in figure 4.7. For comparison, the WO_3 nanoplates were overlaid with the XRD pattern for commercially bought WO_3 nanopowder (Sigma-Aldrich). The commercial WO_3 nanopowder is nanoparticles of size 100 nm or less (observed through TEM, as mentioned on specification sheet). The patterns for both synthesised WO_3 nanoplates and commercial WO_3 show diffraction peaks corresponding to the monoclinic phase (γ) of WO_3 and correlate with the JCPDS card no. 43-1035; a = 7.30 Å, b = 7.53 Å, c = 7.68 Å, where the dominant 2θ peaks at 23.1°, 23.6° and 24.3° are indexed to the crystalline planes (002), (020) and (200). The peak (200) in WO_3 nanoplates sample appears to be stronger than the other two peaks (002) and (020), which can be an indication of preferred crystallographic phase for facet oriented WO_3 [209]. The sample is a dehydrated form of WO_3, with no sign of any $WO_3.2H_2O$ peaks in the XRD patterns that usually appear around 16.5°.

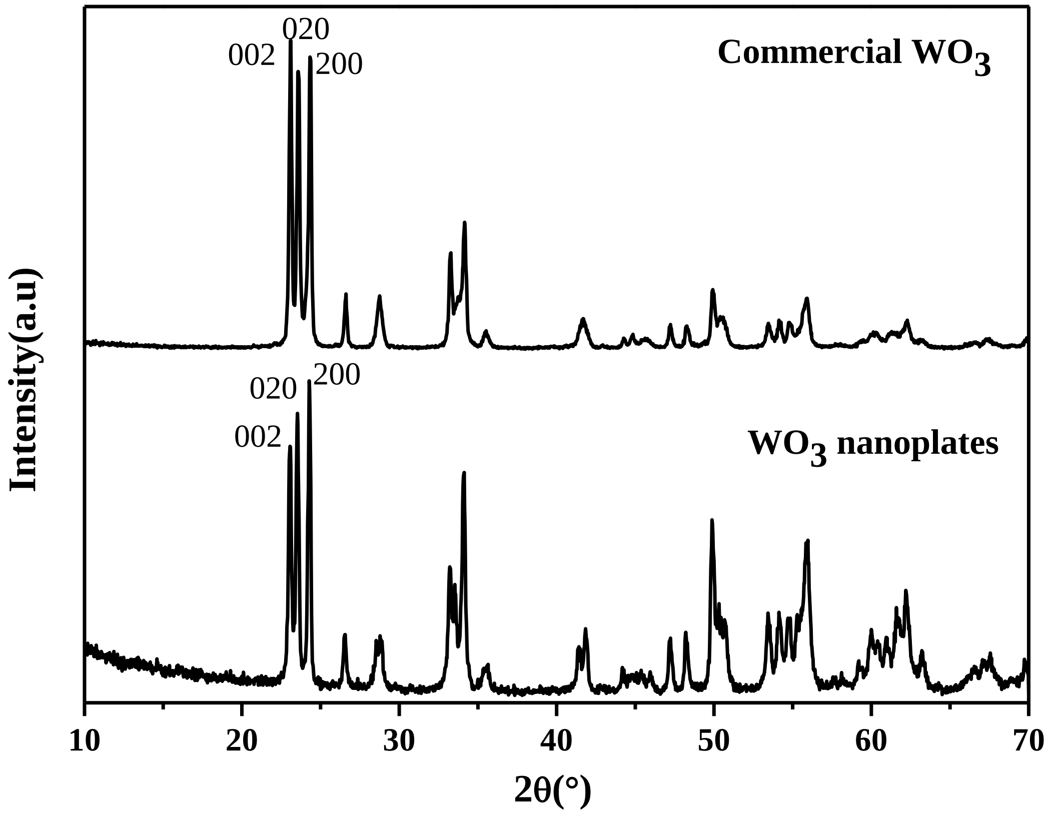

Figure 4.7 XRD patterns of commercial-WO_3 and synthesised WO_3 nanoplates.

The interplanar distance (d) or d-spacing was calculated using Bragg's law [218]:

$$n\lambda = 2d\sin\theta \qquad 4.1$$

Where n = 1 is a positive integer, λ is the wavelength of the incident X-ray beam (0.15406 nm), and θ is the incident angle.

In figure 4.8, the melamine derived g-C_3N_4 exhibits diffraction peaks at 13.2° and 27.5° that were attributed to (100) and (002) crystallographic planes of g-C_3N_4. These peaks observed were comparable to the literature reports on XRD patterns of a g-h-heptazine form of C_3N_4 [106, 109, 192, 219]. The weak intensity at 13.2° having a d-spacing (d) of 0.687 nm represents the structural heptazine (tri-s-triazine) unit of g-C_3N_4. Whereas the intense sharp peak at 27.2° (d = 0.326 nm) corresponds to the interlayer stacking of conjugated aromatic units of g-C_3N_4.

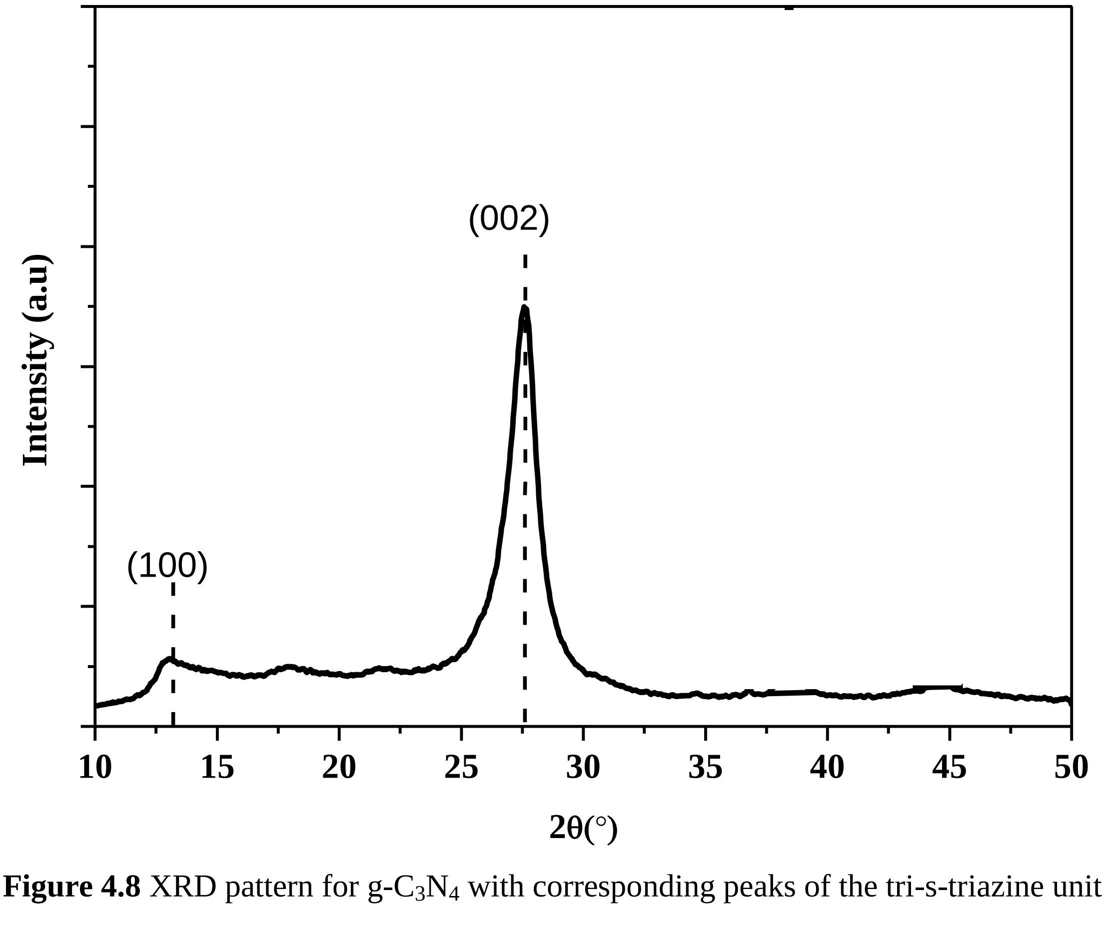

Figure 4.8 XRD pattern for g-C_3N_4 with corresponding peaks of the tri-s-triazine unit.

For WO_3/g-C_3N_4 heterostructure samples, the 3 dominating peaks for monoclinic-WO_3 were observed, as shown in figure 4.9. The intensity of the peaks differs with different composition and preparation method of the heterostructures, but no shift in the peak area was observed in any of the samples. It suggests that the crystallinity of WO_3

remains unaffected on the addition of g-C_3N_4. The distinct peaks of g-C_3N_4 were seen at 13.2° and 27.5°. The signal of 13.2° appears to be diminishing with decreasing concentration of g-C_3N_4 in the heterostructures, whereas the peak at 27.5° arising from the stacked layers of g-C_3N_4 was still observable in WCN19 and WCN(1:4)pH2.25 samples, but seems to have disappeared in WCN91, due to crystallinity of WO_3.

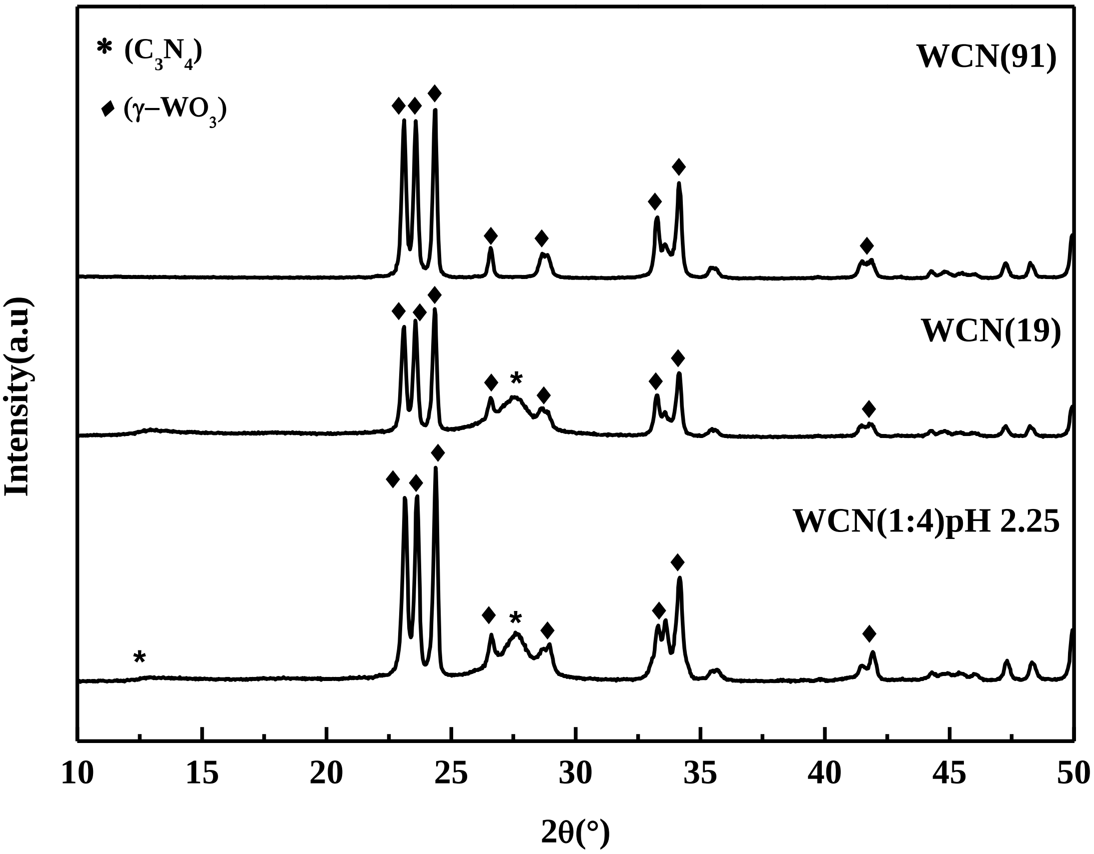

Figure 4.9 XRD patterns of WO_3/g-C_3N_4 heterostructures

The SEM images of the 2D-WO_3 nanoplates are shown in figure 4.10. The 2D-plate like morphology of WO_3 was clear from the microscopic images, most of which have sharp edges, but the orientations of the plates were random. Also, to note in figure 4.10(a) and (b), high concentrations of WO_3 nanoplates were found, that caused agglomeration and stacking of multiple plates together, which was not desirable to investigate the full dimensions of a single platelet. Therefore, a very dilute solution of WO_3 dispersed in H_2O (0.1 mg.mL^{-1}) was characterised to try to see a single platelet, as shown in figure 4.10 (c). The nanoplates exhibit sharp edges and planes, with nearly 4-5 plates adjoined together, but the dimensions of the plates are between 200-400 nm and thickness < 30 nm. A SEM image of the commercial WO_3 nanopowder bought from Sigma Aldrich has been shown in figure 4.10(d), with particle size less than 100 nm on a 500 nm scale image. The commercial WO_3 were nanoparticles with different morphology, more of a zero-dimensional (0D) particle, with multiple exposed facets.

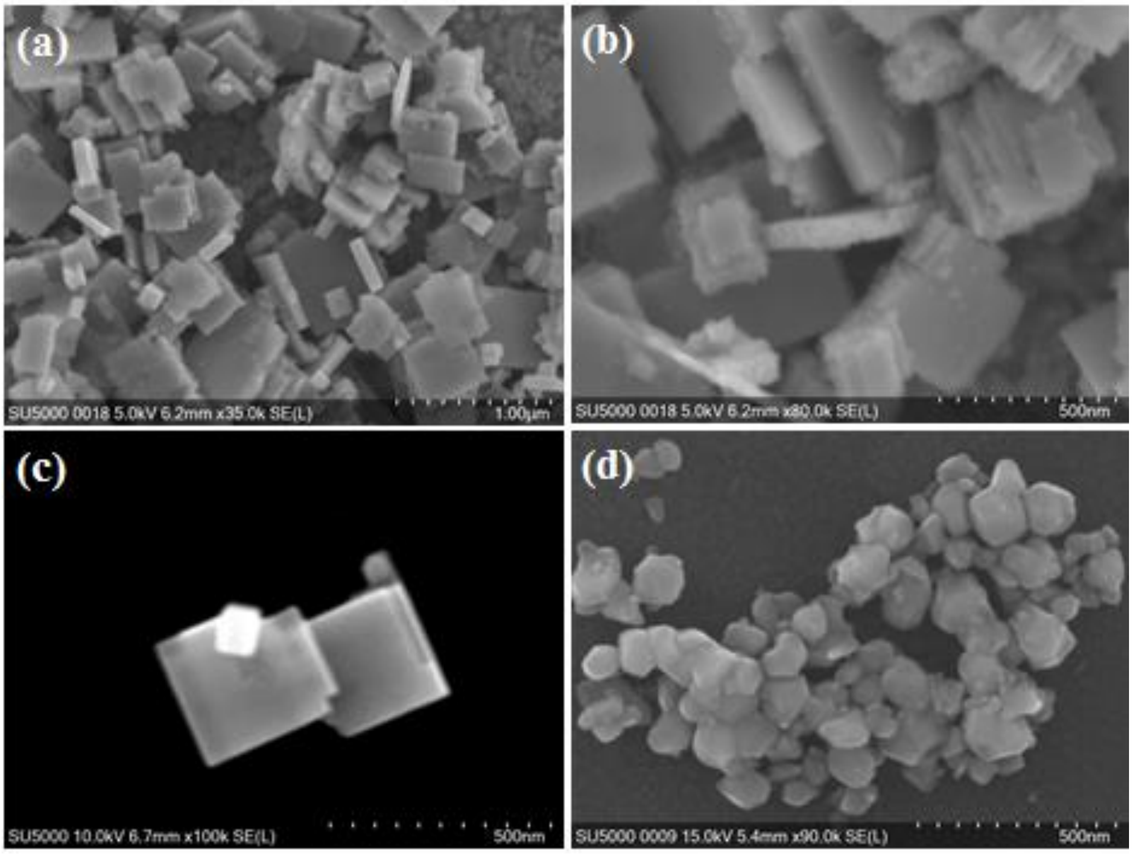

Figure 4.10 SEM images of (a)-(c) WO_3 nanoplates and (d) commercial-WO_3

The morphology of the synthesized graphitic carbon nitride flakes was also investigated by scanning electron microscopy (SEM). As shown in figure 4.11(a) g-C_3N_4 had a laminar structure with thin flake-like structure adjoined together to form the layered g-C_3N_4. In a higher resolution scan of 500 nm, individual flakes were also observed at the edges which were in lighter contrast to the bulky g-C_3N_4 (figure 4.11b), highlighted by white circles. The chemical exfoliation of g-C_3N_4 flakes into single fragments by ultrasonication in IPA was seen through SEM images in figure 4.11c and 4.11d. The liquid phase exfoliation breaks down the layered structure into smaller and thinner fragments of g-C_3N_4.

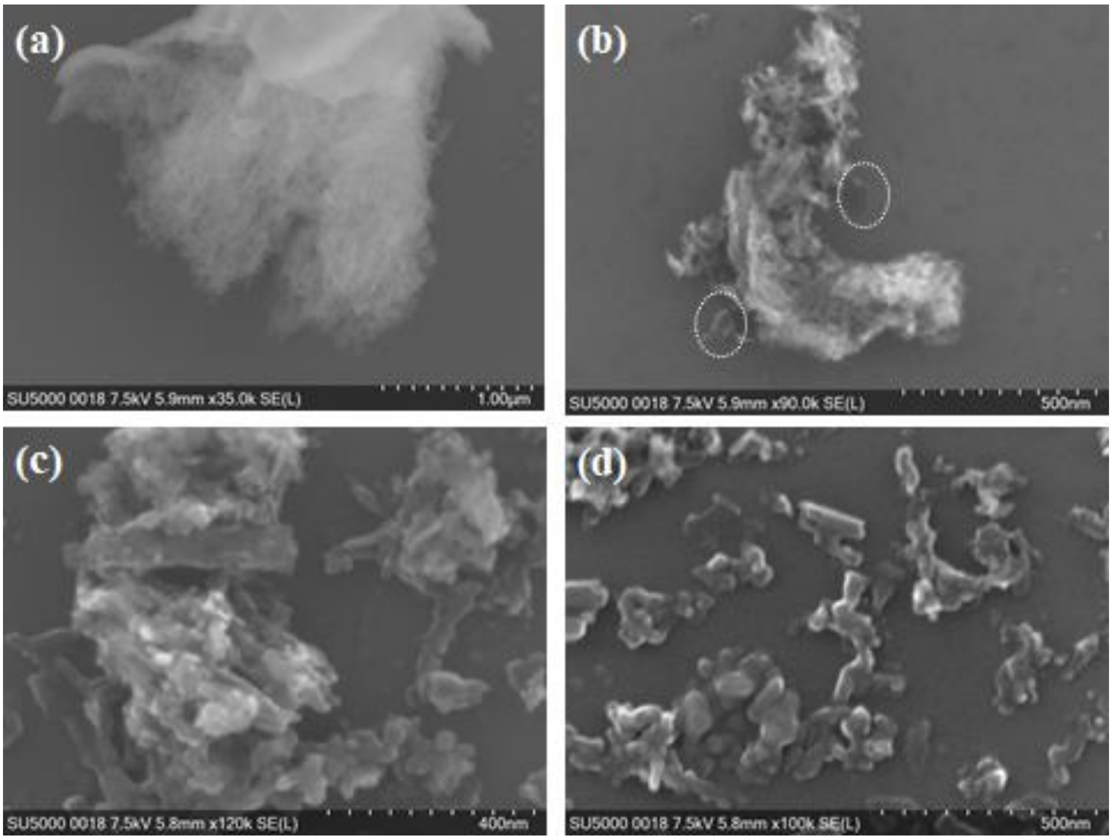

Figure 4.11 Typical SEM images of g-C_3N_4 before (a-b) and after exfoliation (c-d)

Figure 4.12(a) shows the TEM images for WO_3 nanoplates. The 2D rectangular plates of WO_3 were visible here. Although present in agglomerated form, the rectangular nanoplates of WO_3 had a thickness in the range of 20-25 nm. Figure 4.12(b) displays an HRTEM image of the WO_3, with the highlighted white region of a single nanoplate having dimensions of (length × breadth × height) 225 × 150 × 25 nm. The sharp edges and the perpendicular corner of the samples were presented in figure 4.12(c). Uniform lattice fringes were observed for WO_3 with interplanar spacing (d) of 0.377 nm and 0.365 nm measured in two different regions [61]. The d-spacing between the lattice fringes can determine the crystallinity of the materials. Therefore the d-spacing of 0.377 nm was assigned to (020) plane and 0.365 nm to the (200) plane of monoclinic (γ) WO_3. The brightest spots in the corresponding SAED pattern of WO_3 (inset figure 4.12(d)) were from the (020) plane. The separation angle between the two planes was 90°, comparable to the standard JCPDS card No. 43-1035 for γ-WO_3 and also confirmed by the XRD patterns observed for as-synthesized WO_3 nanoplates.

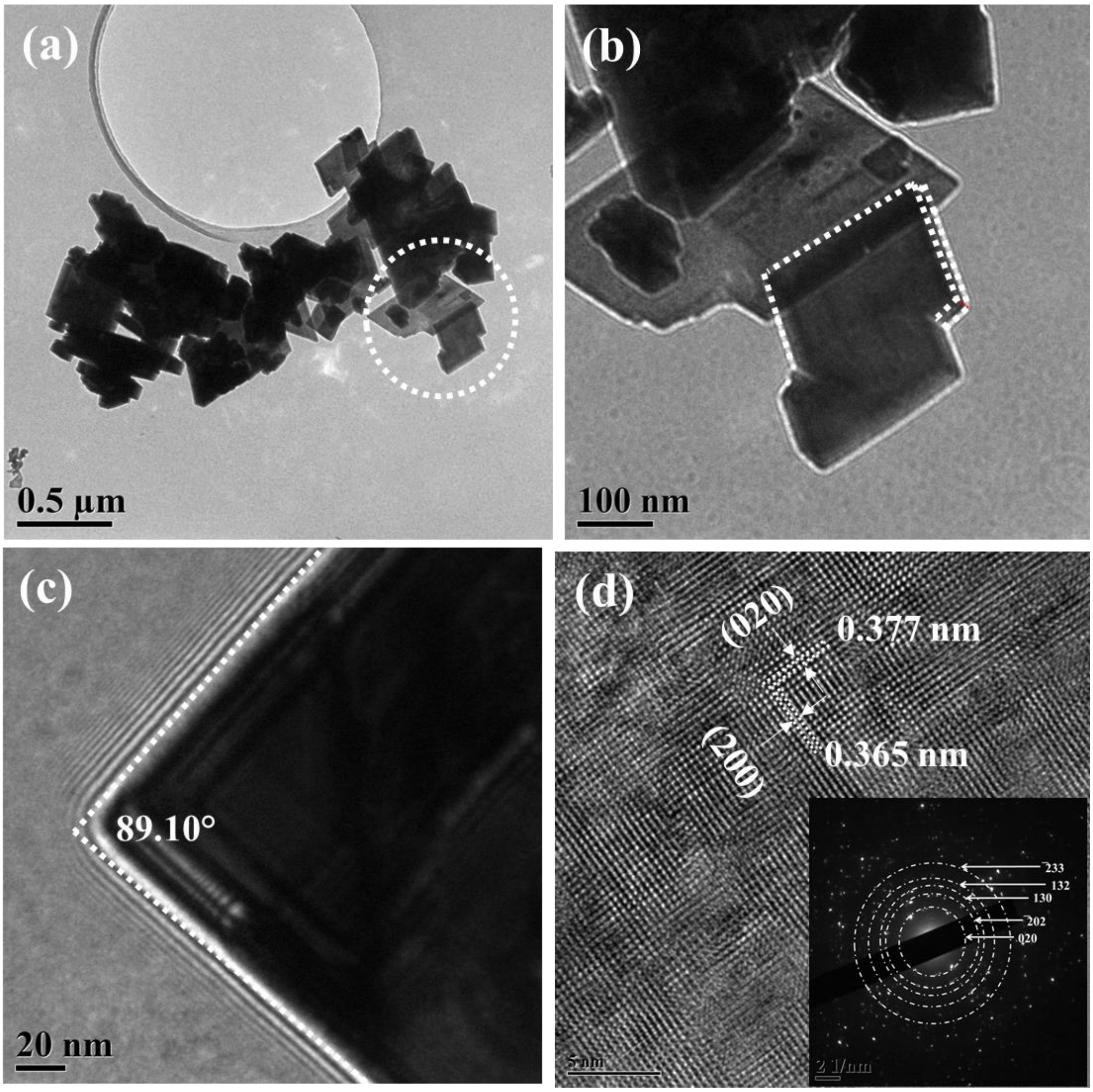

Figure 4.12 TEM images of synthesised WO_3 nanoplates (a) at 500 nm scale, circular region imaged at a higher resolution (HRTEM); (b) HRTEM of WO_3 nanoplates with 2D morphology; (c) HRTEM showing square corners (d) HRTEM images with observed fringes of WO_3. The inset demonstrates the corresponding SAED pattern of WO_3 nanoplates.

The high-resolution TEM images (HRTEM) of g-C_3N_4 were reported in figure 4.13 (a) showing a typical layered structure of large sheet-like flakes. A single layer of graphitic carbon nitride (g-C_3N_4) nanosheet was challenging to observe through high-resolution TEM, due to their transparency to electron beam (figure 4.13 (b)). There were possibilities of degrading the g-C_3N_4 layer under the influence of intense electron beam due to their thin-film structure, henceforth only in some cases the g-C_3N_4 was observed in dark contrast as demonstrated using HRTEM images in figure 4.13 (b)). A fringe pattern of (200) plane was observed for g-C_3N_4 in figure 4.13 (b)), attributed to the d-spacing of 0.322 nm, i.e. the interlayer distance, already confirmed through XRD patterns observed at 27.2° in figure 4.8.

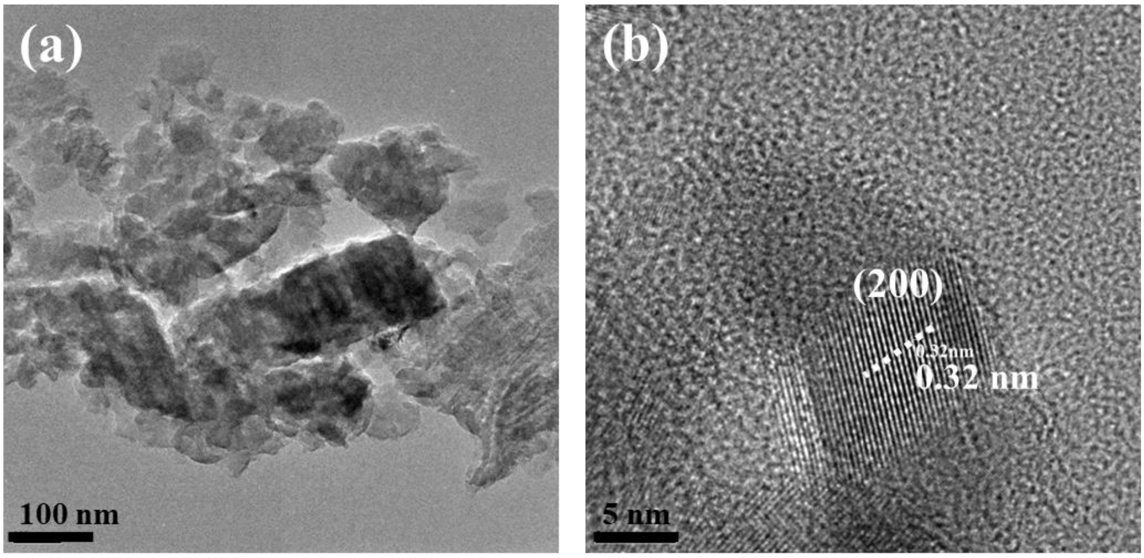

Figure 4.13 HR-TEM images of (a) g-C_3N_4 layers (b) fringe pattern observed of g-C_3N_4 representing the stacking of layers

Figure 4.14 represents the HRTEM images of WO_3/g-C_3N_4 heterostructures prepared by physical mixing and calcination at 400°C in the ratio of WO_3: g-C_3N_4 (1:9), i.e. WCN19 (figure 4.14(a)) and WO_3: g-C_3N_4 (9:1), i.e. WCN91 (figure 4.14((b)). For WCN19, the WO_3 nanoplates were embedded inside the layers of g-C_3N_4, indicating a contact or heterojunction formation between the g-C_3N_4 layers and WO_3 nanoplates. When the ratio of synthesis is opposite as in WCN91 heterostructure, the g-C_3N_4 was observed to be intimately coated on the surface of the WO_3 nanoplates forming a heterojunction on either of the facets of WO_3. The coating of g-C_3N_4 in a preferred orientation could be a possible reason why a diminishing signal was observed for the 27.2° peak of g-C_3N_4 in the XRD pattern of WCN91 sample (figure 4.9). The 27.2° peak of g-C_3N_4 indicated the multilayer stacking of g-C_3N_4, a thin coating of g-C_3N_4 onto the WO_3 facet, will reduce the peak’s intensity dramatically.

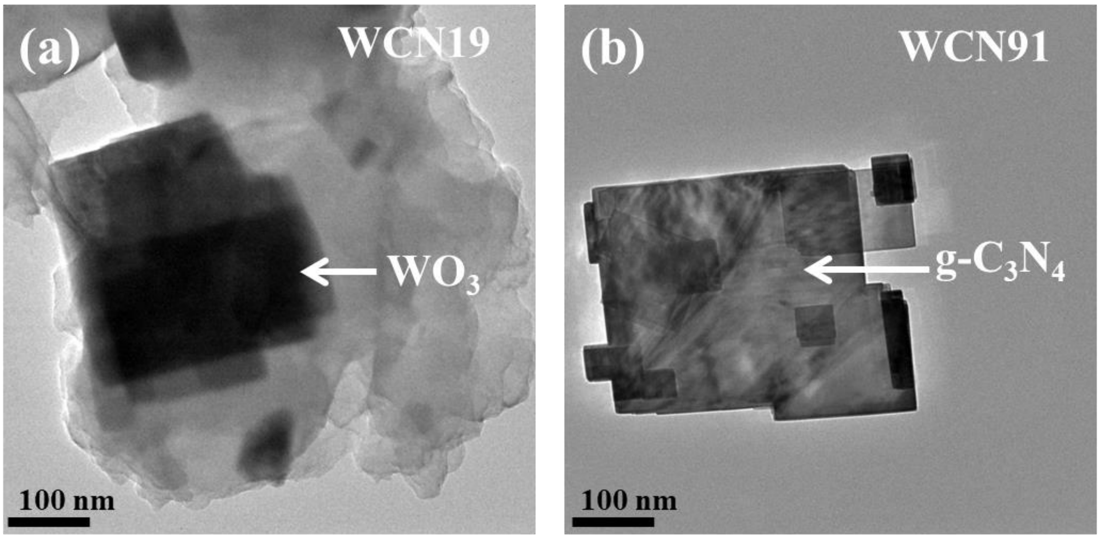

Figure 4.14 HR-TEM images of heterostructures (a) WCN19 with WO_3 nanoplates embedded in g-C_3N_4 layers ; (b) WCN91 with WO_3 nanoplates and possible thin g-C_3N_4 layer on the WO_3 surface.

The specific surface area measurements of WO_3 nanoplates and g-C_3N_4 samples were analysed using the N_2 adsorption-desorption isotherm process. Based on the IUPAC classification of the adsorption isotherm, all the samples obeyed a Type-IV isotherm representing mesoporous solids with an indicative pore size range of 2 nm<pore size<50 nm [220]. During the isotherm process, a hysteresis loop was formed on reaching saturation, with the desorption isotherm following an opposite trend as compared to adsorption. In figure 4.15, WO_3 nanoplates before and after annealing at 400°C demonstrated a type- H4 hysteresis loop, signifying uniform plate-like pores with regular size, in agreement with SEM and HRTEM investigations. A five-point BET method was used to calculate the specific surface area of 10.87 $m^2.g^{-1}$ before annealing and 25.59 $m^2.g^{-1}$ after annealing for the WO_3 nanoplates. The specific surface area of WO_3 increased ~2.5x times after the annealing process, favouring the improved number of active sites available for reaction.

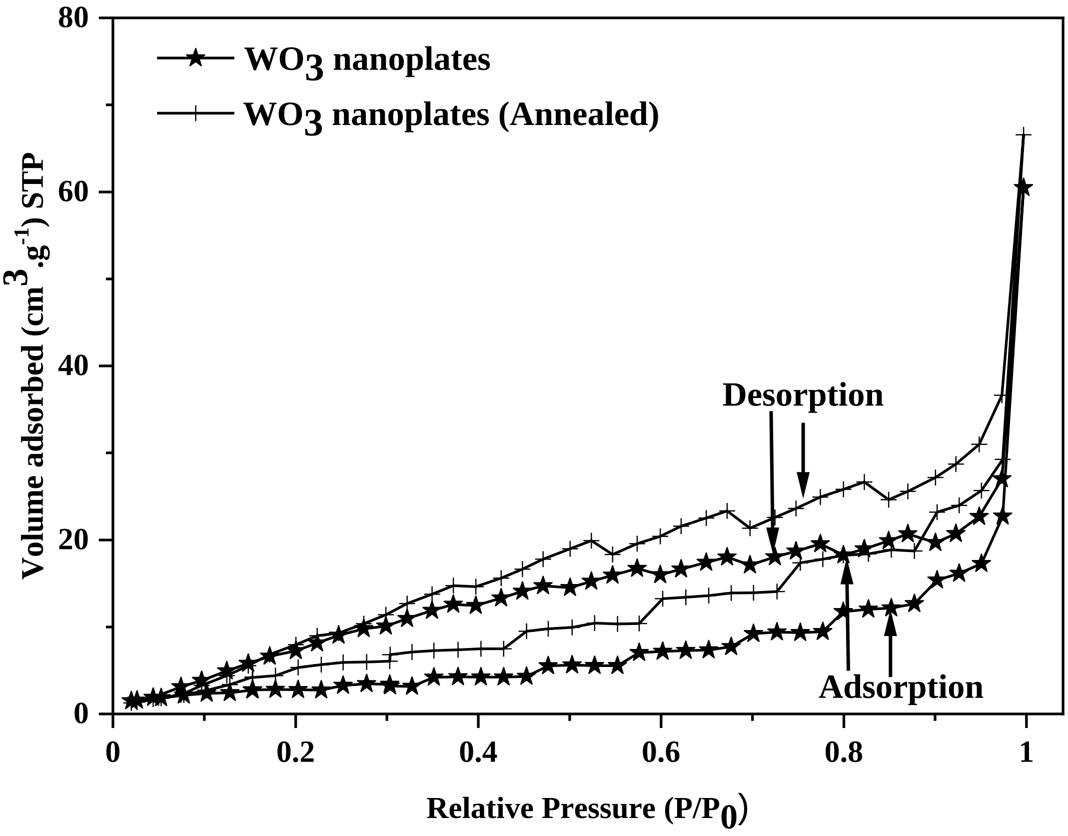

Figure 4.15 N_2 adsorption/desorption isotherm for WO_3 nanoplates before and after annealing at 400°C.

The adsorption isotherm of g-C_3N_4 obeyed a type-H3 hysteresis loop as a result of non-uniform agglomerated particles with slit pores. The specific surface area of the g-C_3N_4 was calculated in a two-step cyclic process, as depicted in figure 4.16. Cycle-1 treatment of melamine to form g-C_3N_4 gave a specific surface area of 8.25 m^2.g^{-1}, which could be a drawback for its use as a photocatalyst. On a second cycle, thermal treatment at 500°C for 4 the surface area increased to 91.27 m^2.g^{-1} for g-C_3N_4. A similar enhancement of the specific area obtained in two-cycle treatment to form porous g-C_3N_4 nanosheets was reported by Lopez et al.(2017) [192], where they compared the formation of g-C_3N_4 as a consequence two-cycle treatment of different precursors.

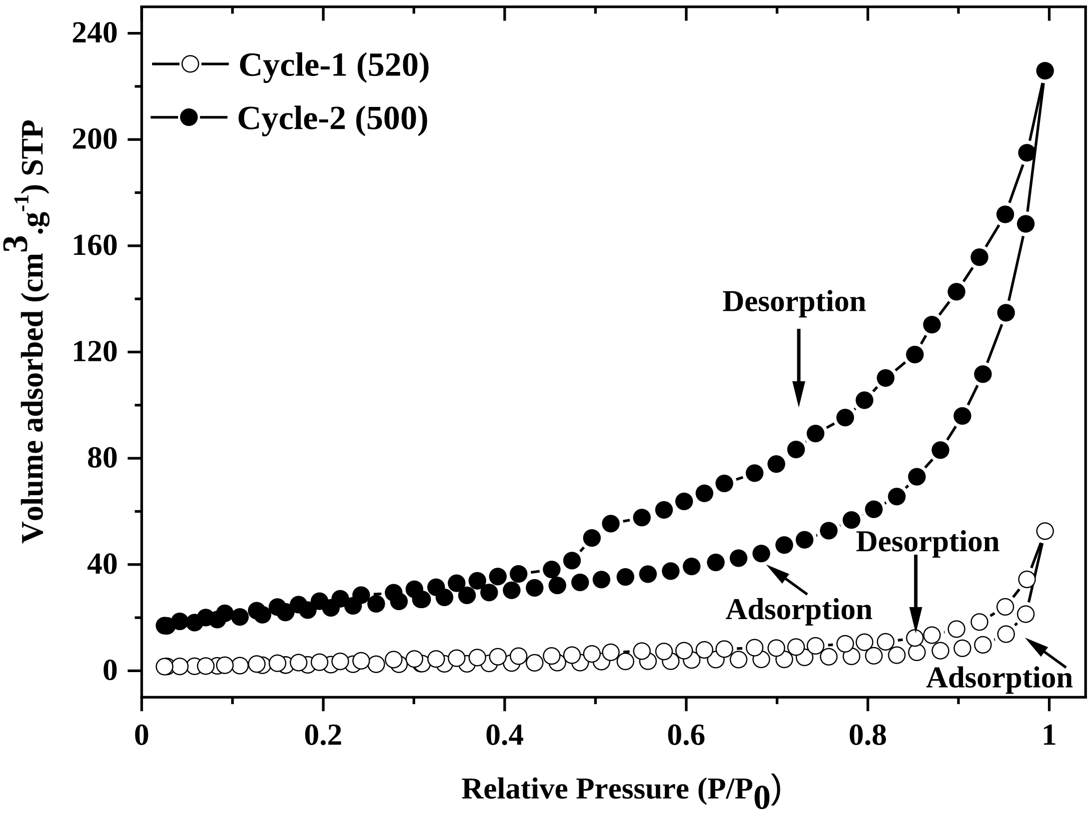

Figure 4.16 N_2 adsorption/desorption isotherm for g- C_3N_4 cycle-1 (520°C; 2 h) and cycle-2 (500°C; 4 h)

The adsorption-desorption isotherm for the heterostructure WCN91 is shown in figure 4.17, showing a hysteresis loop H4 similar to pure WO_3 nanoplates. The BET specific surface area calculated for WCN91 was 9.60 $m^2.g^{-1}$. A summarized report of the synthesis method of the nanostructured photocatalysts, with their specific surface area analysis, has been included in table 4.4.

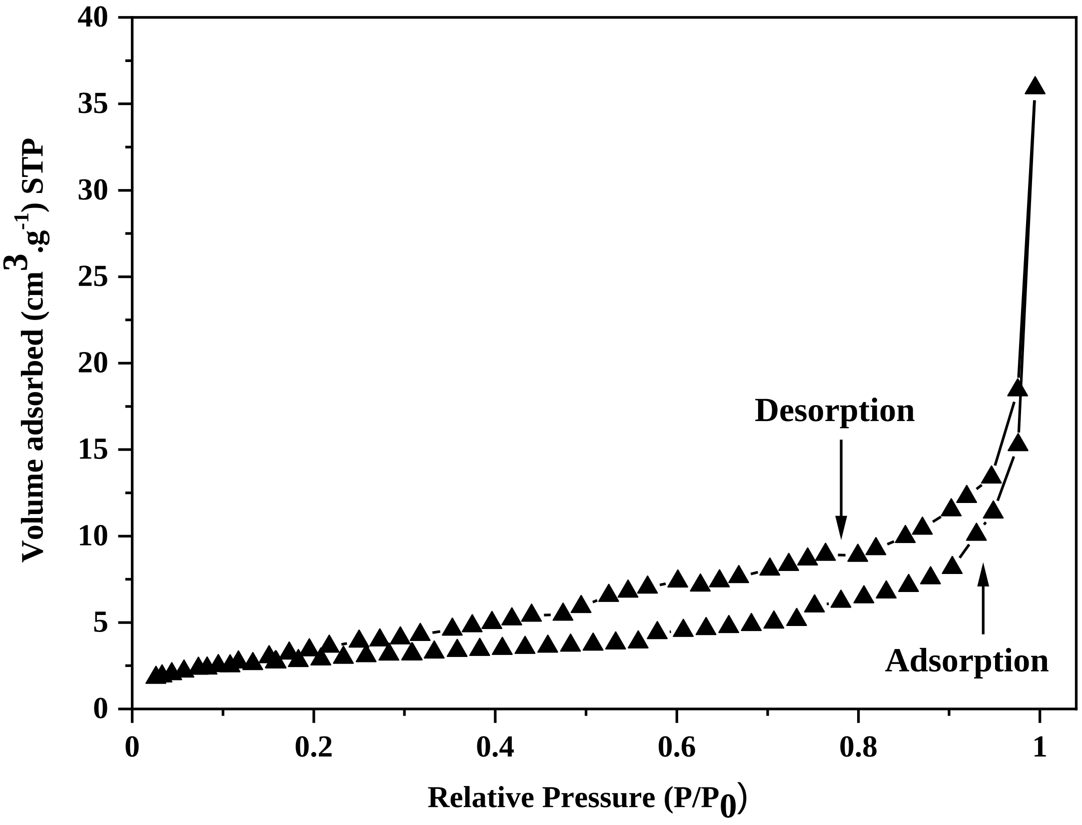

Figure 4.17 N_2 adsorption/desorption isotherm for WCN91 heterostructure prepared at 400°C for 1 h

Table 4.4 Specific surface area of the synthesised samples

Sample	**Key synthesis parameters**	**Weight after outgassing (g)**	**BET surface area (m^2.g^{-1})**
WO_3 nanoplates	Hydrothermal treatment at 180 °C;3 h	0.07	10.87
WO_3 nanoplates	Post annealing at 400°C;1 h	0.07	25.59
g-C_3N_4 (cycle-1)	Thermal treatment at 520°C; 2 h	0.27	8.25
g-C_3N_4 (cycle-2)	Thermal treatment at 500°C;4 h	0.27	91.27
WCN91	The physical mixture of (WO_3: C_3N_4) 9:1 annealed at 400 °C;1 h	0.46	9.60

4.4.2 Determination of optimal photocatalyst loading

The optimal loading for each material was determined by measuring the UV-visible absorbance spectrum of different concentrations of individual photocatalyst i.e. WO_3, g-C_3N_4 and P25-TiO_2. The absorption spectrum obtained in present case, also includes scattering of light at higher concentration of photocatalysts. The absorption spectrum obtained for each material at each concentration was superimposed on the 1000 W Xe lamp spectrum in the 280-500 nm range to calculate to the integrated absorbance A(λ) following equation 4.2;

$$A(\lambda) = \log\left(\frac{\int_{\lambda 1}^{\lambda 2} I_0}{\int_{\lambda 1}^{\lambda 2} I}\right) \qquad 4.2$$

Where λ_1 to λ_2 is the integrated wavelength range 280-500 nm, I_0 is calculated spectral irradiance of the 1000 Xe lamp from 280-500 nm i.e. the number of incident photons entering the photocatalytic reactor and I is the transmitted light (or number of transmitted photons in the range of 280-500 nm). For a detailed derivation of equation 4.2, please refer Appendix II. The integrated absorbance A(λ) vs concentration plot for individual photocatalyst is shown in figure 4.18(a-c). Using this plot, the molar extinction coefficient (ε) for each material was determined as the slope of the line of best fit. The Beer-Lambert like law (equation 4.3 and 4.4) was imposed to determine the optimal concentration (C) of each photocatalyst by transmittance of 1% photons at a calculated optical path length (L) = 6 cm for the 200 mL suspension volume inside the photocatalytic reactor i.e.

$$A = \varepsilon \times L \times C \qquad 4.3$$

$$C = A \div (\varepsilon \times L) \qquad 4.4$$

Following equation 4.4, at absorbance (A) = 2 and optical path length (L) = 6 cm and ε = molar extinction coefficient (i.e. slope of (A(λ) vs concentration plot)), the optimal concentration (C) was determined for WO_3, g-C_3N_4 and P25-TiO_2 and is presented in table 4.5 along with other statistical parameters. The optimal photocatalyst loading is inversely proportional to the molar absorption coefficient (ε). The inverse relation between photocatalyst loading (C) and ε is visible for WO_3 and P25-TiO_2 due to an R^2 between 0.99-1.0. However, the same could not be justified for g-C_3N_4 due to a low R^2

= 0.982. The standard deviation between the 3 replicates for absorbance was also calculated and is presented in table 4.5.

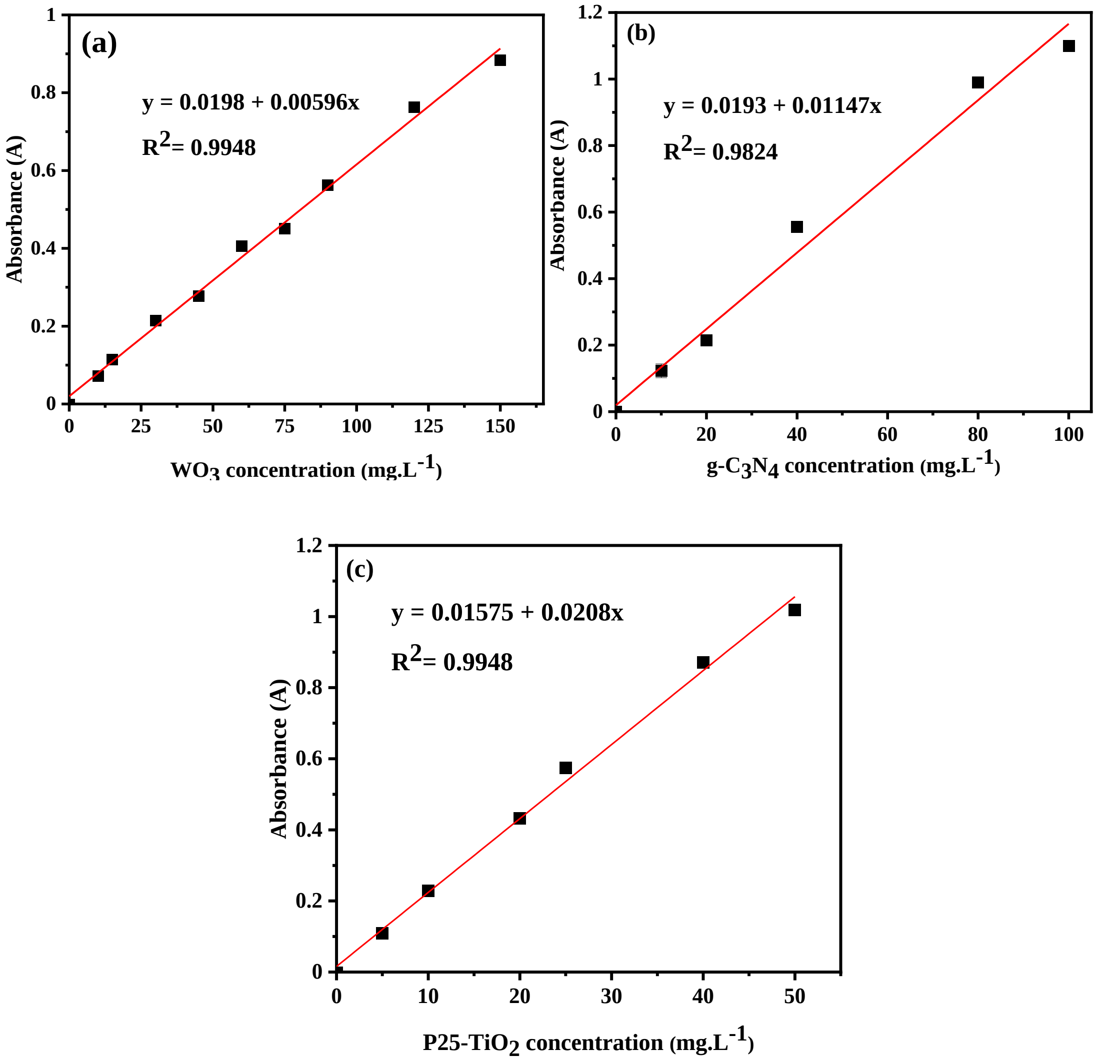

Figure 4.18 Integrated absorbance A(λ) vs calibration plot over the wavelength range of 280-500 nm for determining the optimal loading of photocatalyst (a) WO_3, (b) g-C_3N_4, (c) P25- TiO_2

Table 4.5 Statistical parameters for calculating the optimal loading for photocatalyst

Photocatalyst	**Standard deviation**	**Coefficient of determination (R^2)**	**Absorption coefficient ($L.mg^{-1}.cm^{-1)}$**	**Optimal loading ($mg.L^{-1}$)**
WO_3	±0.001	0.9948	0.0059	55.55
g-C_3N_4	±0.020	0.9824	0.0115	28.98
P25-TiO_2	±0.007	0.9948	0.0208	16.02

4.4.3 Photocatalytic tests

4.4.3.1 Photocatalytic degradation of formic acid

The rate of formic acid degradation was measured as a function of photocatalyst loading using P25-TiO_2. The initial concentration of formic acid used was 1×10^{-2} $mol.L^{-1,}$ and the photocatalytic degradation of formic acid was observed to follow a pseudo zero order kinetics for the entire catalyst loading tested. In Figure 4.19, the formic acid degradation was observed using P25-TiO_2 at $30mg.L^{-1}$, that was analysed in UV-Vis wavelength range of 200-500 nm. At catalyst loading of 30 $mg.L^{-1,}$ the formic acid degradation rate achieved was 2.96×10^{-5} $mol.L^{-1}.min^{-1}$ with a zero order best fit R^2 value = 0.9947 (Figure 4.20). The degradation rate obtained at theoretically estimated loading of 16 $mg.L^{-1}$ was comparable to the rate obtained at 30 $mg.L^{-1}$, i.e. 2.94×10^{-5} $mol.L^{-1}.min^{-1}$. However, the coefficient of determination (R^2) calculated at 16 $mg.L^{-1}$ was 0.8034. An experimental error of $\pm 0.074 \times 10^{-5}$ $mol.L^{-1}$ was associated with all the measurements done in this experiment. At 10x times higher catalyst loading of 330 $mg.L^{-1}$ for P25-TiO_2, the zero order degradation rate for formic acid was determined to be 3.73×10^{-5} $mol.L^{-1}.min^{-1}$ and the corresponding $R^2 = 0.7193$. Only a 1.5x times high pseudo zero order rate of formic acid degradation was observed with 330 $mg.L^{-1}$ P25-TiO_2 as compared to 30 $mg.L^{-1}$ P25-TiO_2. There is no significant difference in rate as compared to the 10x times increased photocatalyst loading. It is probably the case where a well stirred reaction with no mass transport limitation, reaches the optimal photocatalyst loading, with maximum degradation rate and beyond that point no change in rate occurs with increasing concentration.

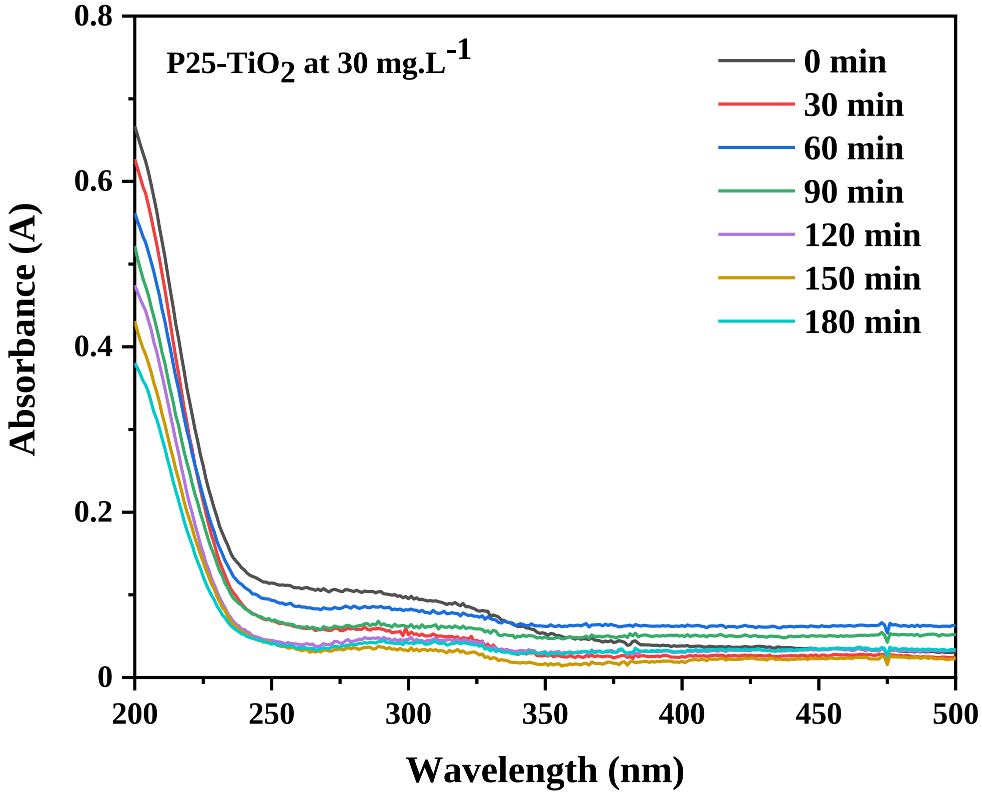

Figure 4.19 Photocatalytic oxidation of formic acid using P25-TiO_2 at 30 mg.L^{-1} analysed at UV-Vis wavelength (200-500 nm)

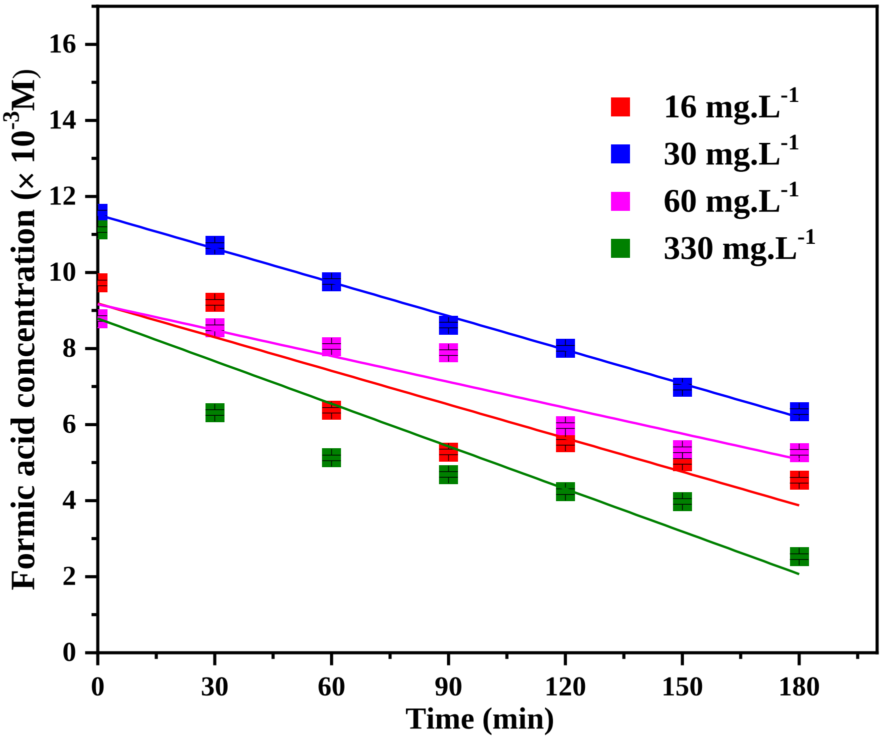

Figure 4.20 Photocatalytic oxidation of formic acid using simulated solar irradiation in the presence of different catalyst loading of P25-TiO_2.

Usually, in most of the photocatalytic systems, the degradation of organic pollutants is described by a Langmuir Hinshelwood (L-H) kinetic mechanism [77]. According to L-H kinetics, organic pollutant degradation mainly follow two types of kinetics, i.e. pseudo zero order kinetics and pseudo first order kinetics.

In the case of photocatalytic degradation of formic acid pseudo zero order rate kinetics was observed for P25-TiO_2 concentrations 16-300 mg.L^{-1}. The rate of formic acid degradation can be explained as shown in equation 4.5 [77]

$$R = -\frac{d[HCOOH]}{dt} = \frac{k_0 K[HCOOH]}{[1+K[HCOOH]]} \qquad 4.5$$

Where R was the initial rate of formic acid degradation, [HCOOH] was the initial concentration, K was the constant for Langmuir adsorption, and k_0 represents the rate constant of the reaction.

The photocatalytic oxidation of formic acid followed pseudo zero order kinetics, which correlates well with the literature [199, 221].

Considering ~50% degradation in initial formic acid concentration (1×10^{-2} mol.L^{-1}) was achievable in 3 h with 30 mg.L^{-1} P25-TiO_2 as the standard photocatalyst. The same catalyst loading was used to test the photocatalytic activity of the as-prepared WO_3 nanoplates (figure 4.21). No substantial degradation in formic acid concentration was observed as a result of photocatalytic reaction with 30 mg.L^{-1} WO_3 nanoplates. The reduction in the initial concentration of formic acid in the first 15 min of reaction was instead the adsorption of formic acid, with no further decrease in concentration up to 3 h of simulated solar irradiation. On comparing the pseudo zero order rate constants, a degradation rate of 9.72 $\times10^{-6}$ mol.L^{-1}·min^{-1} was obtained for WO_3 nanoplates. The achieved rate is unrealistic because hardly any degradation was observed, and the kinetic fit parameters reveal an R^2 = 0.1709. The negligible degradation of formic acid using WO_3 nanoplates is attributed due to a positive CB edge potential that limits the reduction of molecular oxygen to produce ROS, leading to a faster electron-hole pair recombination reaction taking place in case of WO_3.

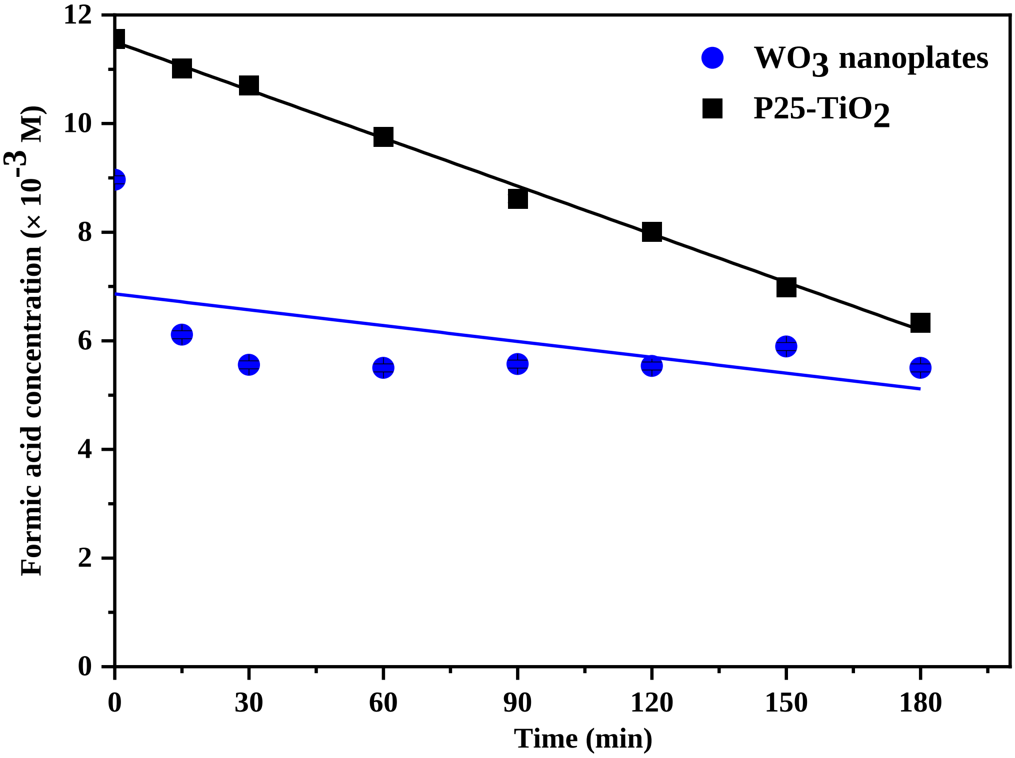

Figure 4.21 Photocatalytic degradation of formic acid with 30 mg.L^{-1} WO_3 nanoplates vs 30 mg.L^{-1} P25-TiO_2

4.4.3.2 Photocatalytic degradation of phenol

The photocatalytic efficiency of WO_3 and the prepared heterostructures were also investigated by studying the photocatalytic degradation of phenol as an organic pollutant under simulated solar irradiation. Phenol degradation was observed to follow pseudo zero order kinetics within the time scale of the experiments for all the photocatalyst tested as shown in figure 4.22. All photocatalysts were tested at a 30 mg.L^{-1} estimated optimal loading for 5 h irradiation time. Only P25-TiO_2 was efficient in photocatalytic degradation of phenol (figure 4.23), with the reaction rate of of 1.2 × 10^{-6} mol.L^{-1}.min^{-1} and 40% degradation in the concentration of phenol was observed in 5 h of irradiation. With g-C_3N_4 only 12% degradation of phenol was observed in 5 h of irradiation. The rate for g-C_3N_4 was 2 × 10^{-7} mol.L^{-1}.min^{-1}.

These results achieved here do not correlate well with those reported previously for g-C_3N_4 and its heterostructures [222, 223]. Considering in the present study, the experimental loading of 30 mg.L^{-1} was equivalent to theoretical calculated loading 28.8 mg.L^{-1} of g-C_3N_4 (through UV-Vis transmission data (refer to table 4.5.)), some photocatalytic degradation was expected with this material, highlighting the effect of catalyst active sites present for photocatalytic degradation to take place.

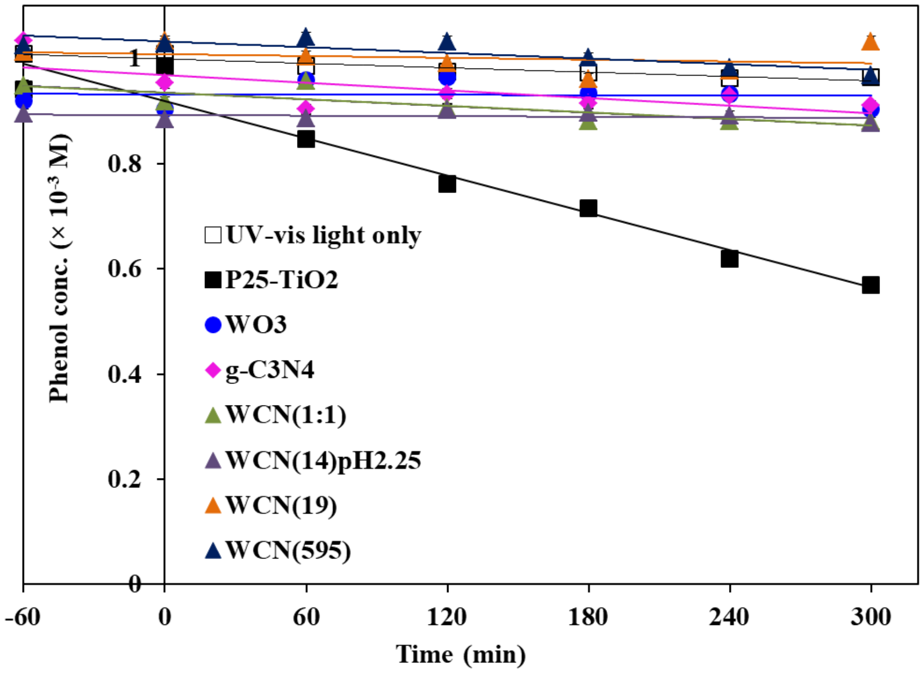

Figure 4.22 Photocatalytic degradation of phenol (10^{-3} M) in the presence of 30 mg.L^{-1} prepared photocatalysts at pH 6.5(distilled water).

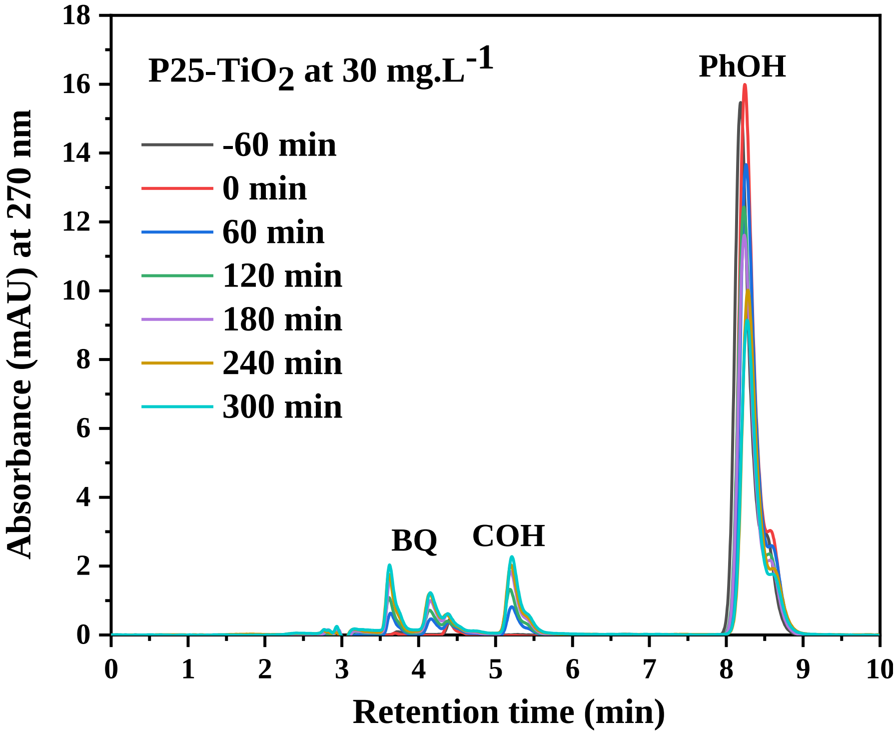

Figure 4.23 Photocatalytic degradation of phenol (10^{-3} M) in the presence of 30 mg.L^{-1} P25-TiO_2

No real photocatalytic degradation of phenol was observed either with WO_3 nanoplates or with any of the WO_3/g-C_3N_4 heterostructures. The obtained results were unexpected, considering if a photocatalytic z-scheme mechanism was in operation with the heterostructures, they should show some phenol degradation.

4.4.3.3 Photocatalytic inactivation of *E. coli*

The efficiency of the photocatalysts was evaluated for photocatalytic disinfection of water using *E. coli* as the model microorganism under simulated solar irradiation, as shown in figure 4.24. The inactivation of *E. coli* was correlated to the UV-dose under both photocatalytic and light only conditions i.e. photo-inactivation. The UV dose was calculated using equation 4.6 [40]

$$\text{UV Dose } \left(\frac{\text{J}}{\text{m}^2}\right) = \int \text{Irradiance } \left(\frac{\text{W}}{\text{m}^2}\right) \times \text{dt(s)} \qquad 4.6$$

A 4.54-log reduction of *E. coli* was observed in 180 min under simulated solar irradiation i.e. the photo-inactivation process. With P25-TiO_2 a 6-log reduction in *E. coli* was observed in 150 min of irradiation, reaching the detection limit of 2 CFU.mL^{-1}. Previously with a similar photocatalyst loading, Curz-Ortiz et al.(2017) observed a 6-log reduction in 120 min of UV-Vis irradiation in the same reactor [40]. When WO_3 nanoplates and g-C_3N_4 were used as photocatalyst, no photocatalytic inactivation of *E. coli* took place. Instead the kill rate due to photo-inactivation was suppressed by the addition of WO_3 and g-C_3N_4 in the individual run. A 0.7-log reduction was observed with both g-C_3N_4 and WO_3 nanoplates in 180 min of irradiation time. The unpredictable response obtained for WO_3 nanoplates was probably due its positive CB edge, making it unable to drive the one electron reduction of oxygen to superoxide radical anion ($^{\bullet}O_2^-$ (-0.16 V (NHE)) and thus leading to electron-hole pair recombination.

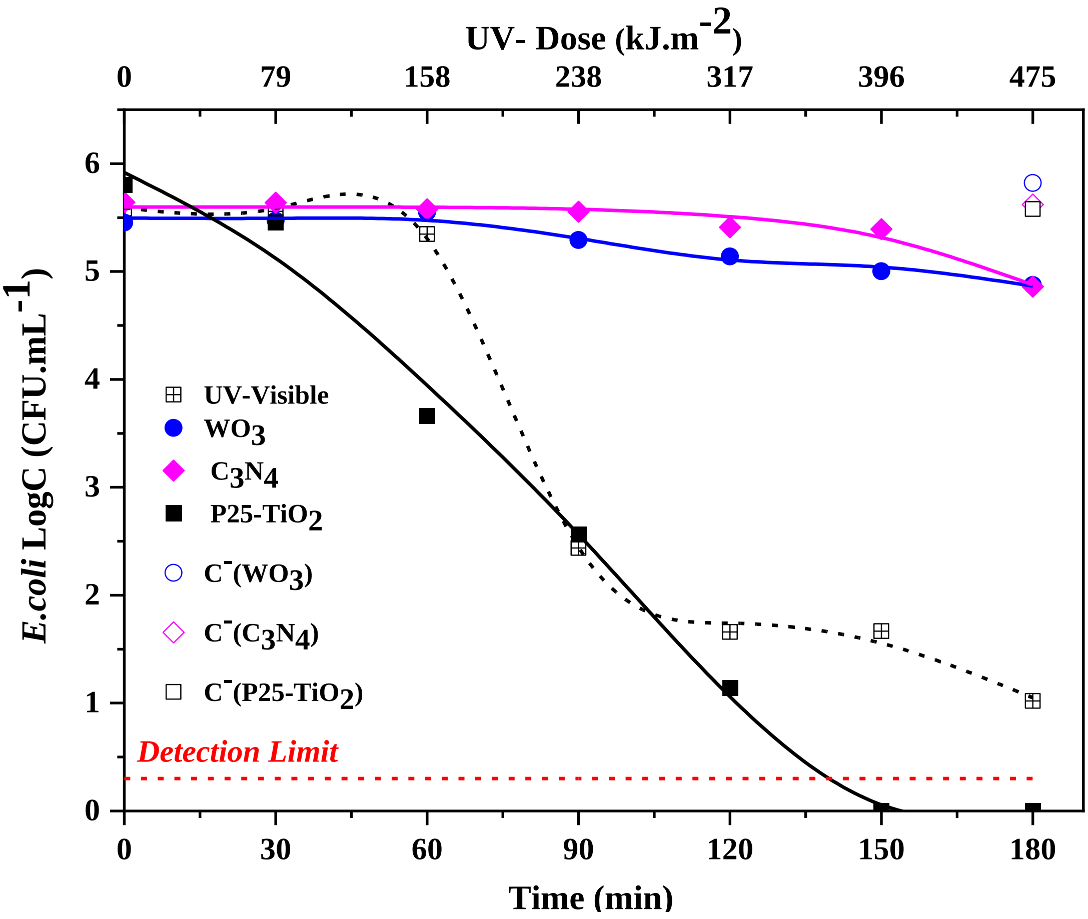

Figure 4.24 *E. coli* inactivation at 20 mg.L^{-1} concentration for 2D-WO_3 and g-C_3N_4 in comparison to P25-TiO_2. C$^-$ refers to dark control. Detection limit = 2 CFU.mL^{-1}. All lines represent the fitted data using GInaFIT models.

Heterostructures of WO_3 and g-C_3N_4 were also tested for the photocatalytic disinfection under the same conditions, and results are shown in figure 4.25. With sample WCN91, a 4.51-log reduction of *E. coli* in 180 min of irradiation was observed, followed by WCN19 showing a reduction of 4.35-log of *E. coli* in 180 min. The heterostructure samples prepared from ultrasonic chemical exfoliation showed a 2.8-log (WCN1:1) and 2.6-log reduction (ex.WCN1:1) of *E. coli* in 180 min. However, no improved activity with any form of heterostructures was observed for photocatalytic activation of *E. coli* as compared to photo-inactivation. The *E. coli* viability in the dark with the photocatalytic suspension was not affected following 180 min in any of the experiments. The temperature in all experiments was controlled at 20 ± 2 °C to avoid any effect of temperature.

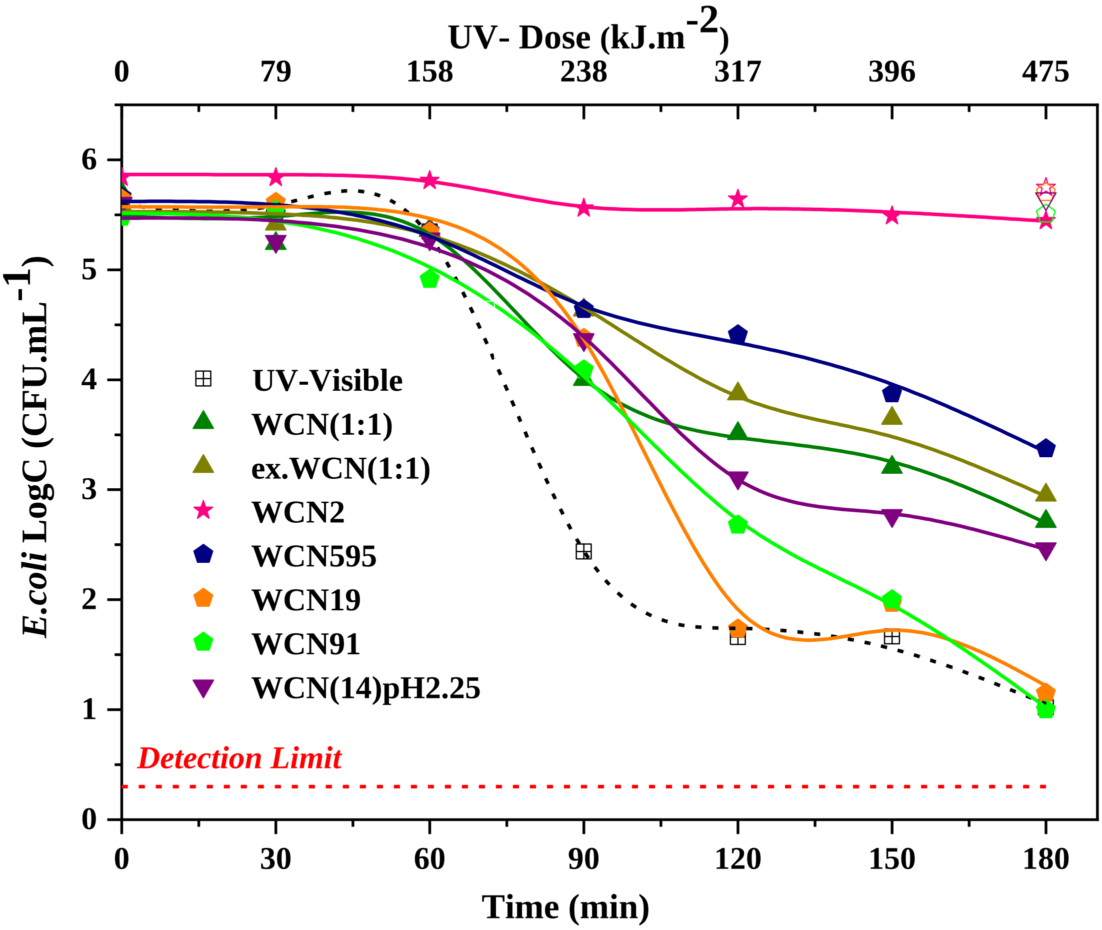

Figure 4.25 *E. coli* inactivation at 20 mg.L^{-1}concentration for several $WO_3/g\text{-}C_3N_4$ heterostructures. Detection limit = 2 CFU.mL^{-1}. All lines represent the fitted data using GInaFIT models.

The results of the inactivation experiments were analysed using the Geeraerd, and Van Impe Inactivation model fitting tool, i.e. GInaFIT, version 1.6 [200, 224]. Weibull, Weibull+ tail or double Weibull fitting models were found to be the genuine fit for the experiments performed in this work (Table 4.6). A basic inactivation mechanism model for *E. coli* has been described in 3 steps: i.e. an initial decay of inactivation referred to as "shoulder". This region is often represented by scale parameter δ in the Weibull model (or δ_1 in double Weibull model), where both refer to the time taken for first log reduction in *E. coli* cells. It is the region where any reactive species generated as a part of the reaction, attack the bacterial cells. The second region is the log-linear process, where rapid destruction of microorganisms takes place due to oxidative attack on the cell wall, leading to cell damage. Sometimes, bacterial cells are more resistant in this region, so a second parameter δ_2 is presented for this region in the double Weibull model, which is the time taken by the more resistant bacterial cells to be inactivated. Third, is the decelerated "tail" region, where a residual population is observed [225].

The kinetic parameters and inactivation rates with irradiation time as an independent variable have been described in table 4.6. Since three different models were shown to provide the lowest possible RMSE values (0.05-0.26) and highest possible R^2 values (0.939-0.999) to get a perfect fit. It is very complicated to give a direct comparison between the disinfection rates for each data set. Above all, the only parameters that could be used to provide a simple comparison here are the scale parameter δ (time taken for the first log reduction) or the $Log_{10}N_{res}$ (residual bacterial population in the end). Using these two kinetic parameters, P25-TiO_2 as a photocatalyst outperformed with $\delta = 35.72 \pm 7.38$ min^{-1} and a total inactivation within 150 min. The light control, i.e. photo-inactivation of *E. coli* was calculated to have the first log reduction of *E. coli* (δ) in 73.91 ± 2.86 min^{-1}, followed by heterostructure WCN91 with a $\delta = 77.29 \pm 4.54$ min^{-1} comparable to the photo-inactivation. The residual population ($Log_{10}Nres$) for photo-inactivation was 1.05 logC ($CFU.mL^{-1}$) and that observed for WCN91 was 1.02 logC ($CFU.mL^{-1}$) after 180 min of irradiation .i.e. identical rate of reduction. The rest of the samples were found to show even poor performance for the photocatalytic inactivation of *E. coli* by suppressing the photo-inactivation rate. *E. coli* K12 is a target microorganism in solar disnfection and shows some resistance to UV. A double Weibull model also shows the inactivation rate for the more resistant bacterial population using scale parameter δ_2. The δ_2 for light only i.e. photo-inactivation was 188.59 ± 6.66 min^{-1} and that for WCN91 was 132.52 ± 11.85 min^{-1}, suggestive a more solar(or UV) resistant *E. coli* population could be inactivated under photocatalytic conditions using WCN91 heterostructure.

Table 4.6 Effect of different photocatalyst on *E. coli* under simulated solar irradiation. Kinetic parameters found by applying the GInaFIT tool.

Catalyst	**Scale parameter (δ), (min^{-1})**	**RMSE**	**R^2**	**Log$_{10}$N$_0$ (CFU.mL^{-1})**	**Log$_{10}$N$_{res}$ (CFU.mL^{-1})**
Light*	δ_1 = 73.91 ± 2.86 δ_2 = 188.59 ± 6.66	0.0873	0.999	5.59±0.08	1.05
P25-TiO$_2$**	δ = 35.72 ± 7.38	0.2674	0.994	5.92±0.21	0.00
WO$_3$*	δ_1 = 104.45 ± 16.55 δ_2 = 224.90 ± 45.79	0.0594	0.973	5.49±0.05	4.87
g-C$_3$N$_4$***	δ = 191.80 ± 5.37	0.0717	0.955	5.60±0.04	4.88
WCN(1:1)*	δ_1 = 82.31 ± 7.06 δ_2 = 184.75 ± 13.99	0.1915	0.987	5.49±0.17	2.70
Ex. WCN(1:1)*	δ_1 = 91.11 ± 3.81 δ_2 = 174.14 ± 9.15	0.0750	0.998	5.53±0.07	2.94
WCN595*	δ_1 = 80.24 ± 7.84 δ_2 = 166.13 ± 11.59	0.0907	0.995	5.69±0.09	3.34
WCN19*	δ_1 = 87.19 ± 4.95 δ_2 = 184.75 ± 13.99	0.1982	0.995	5.57±0.17	1.22
WCN91*	δ_1 = 77.29 ± 4.54 δ_2 = 132.52 ± 11.85	0.1033	0.998	5.51±0.10	1.02
WCN(1:4) pH2.25*	δ_1 = 87.54 ± 5.56 δ_2 = 230.09 ± 36.86	0.1414	0.994	5.47±0.13	2.46
WCN2*	δ_1 = 83.11 ± 22.17 δ_2 = 254.97 ± 86.47	0.0592	0.939	5.87±0.05	5.44

**Double Weibull model;* ** *Weibull + Tail model;* *** *Weibull model*

The WCN91 was the only sample that showed comparable photocatalytic activity against photo-inactivation of *E. coli*. Therefore, the data for this sample was fitted against the parent photocatalyst materials WO_3 and g-C_3N_4 to compare for any enhancement in photocatalytic disinfection activity (figure 4.26). As discussed above a comparable $Log_{10}N_{res}$ was obtained from WCN91 against photo-inactivation. This means no major change on the photo-inactivation rate took place on addition of WCN91 photocatalyst. Moreover, the heterostructure also showed limited photocatalytic disinfection activity as compared to P25-TiO_2.

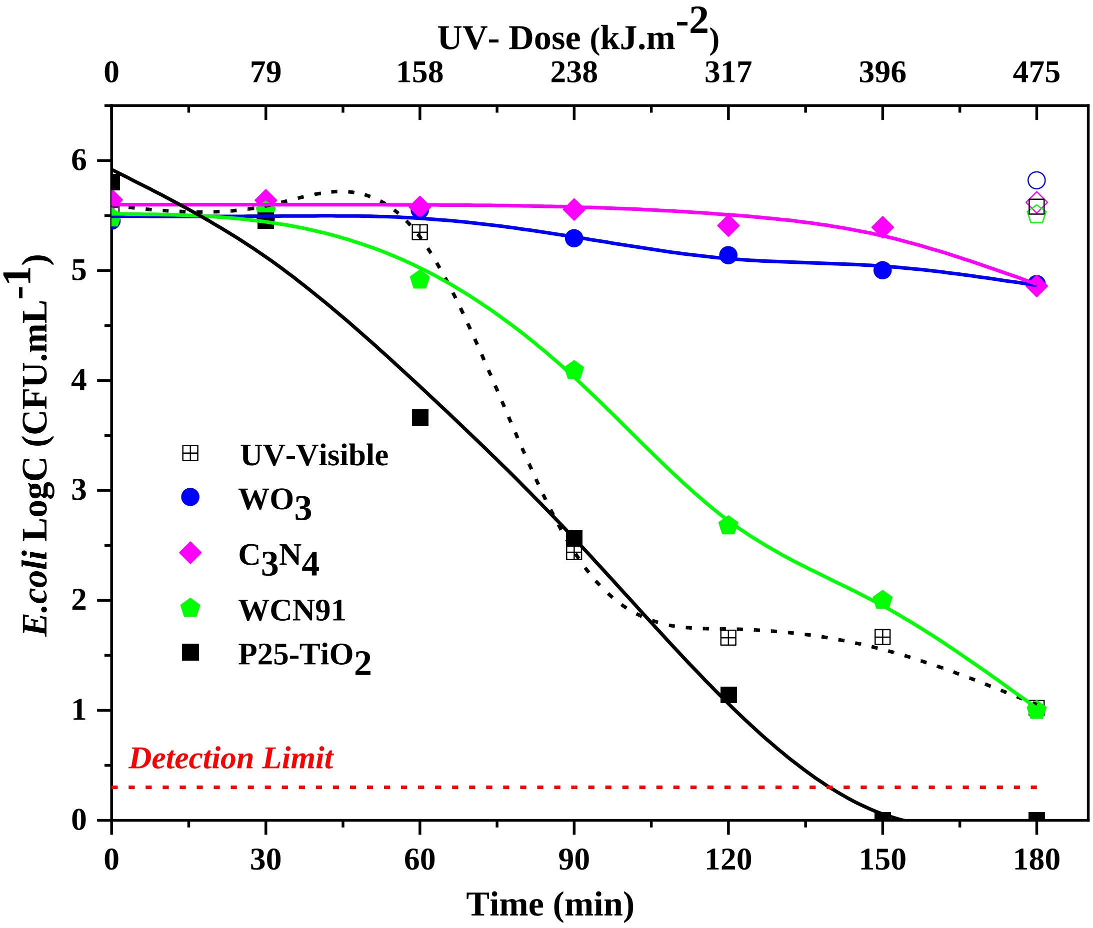

Figure 4.26 *E. coli* inactivation at 20 mg.L^{-1} concentrations for WO_3/g-C_3N_4 heterostructure WCN91 compared to individual WO_3 nanoplates and g-C_3N_4. Detection limit = 2 CFU.mL^{-1}. All lines represent the fitted data using GInaFIT models.

A set of experiments to investigate the photocatalytic disinfection performance for g-C_3N_4 before and after ultrasonic exfoliation is also shown in figure 4.27. No photocatalytic activity was observed with as-synthesized g-C_3N_4, but in case of the exfoliated sample (Ex.g-C_3N_4), 3-log inactivation of *E. coli* was observed in 180 min, still less than the photo-inactivation. However, similar reports on g-C_3N_4 nanosheets as a photocatalyst for *E. coli* inactivation in visible irradiation have been presented in the literature [39, 156, 157, 226]. For instance, in 4 h visible only irradiation, total inactivation (10^7 CFU.mL^{-1}) of *E. coli* was reported by Quan et al.(2014) for a single layer of the g-C_3N_4 sheet with less than 1 nm thickness [157]. According to them, ultrasonic exfoliation of the prepared g-C_3N_4 will improve its performance for photocatalytic disinfection, but results reported do not show any specific argument on why photocatalytic performance will be enhanced. The heterostructure exfoliated WCN(1:1) also was tested for photocatalytic disinfection. However, no increase in photocatalytic activity was observed and in all cases the photocatalytic activity was less than the photo-inactivaton of *E. coli*.

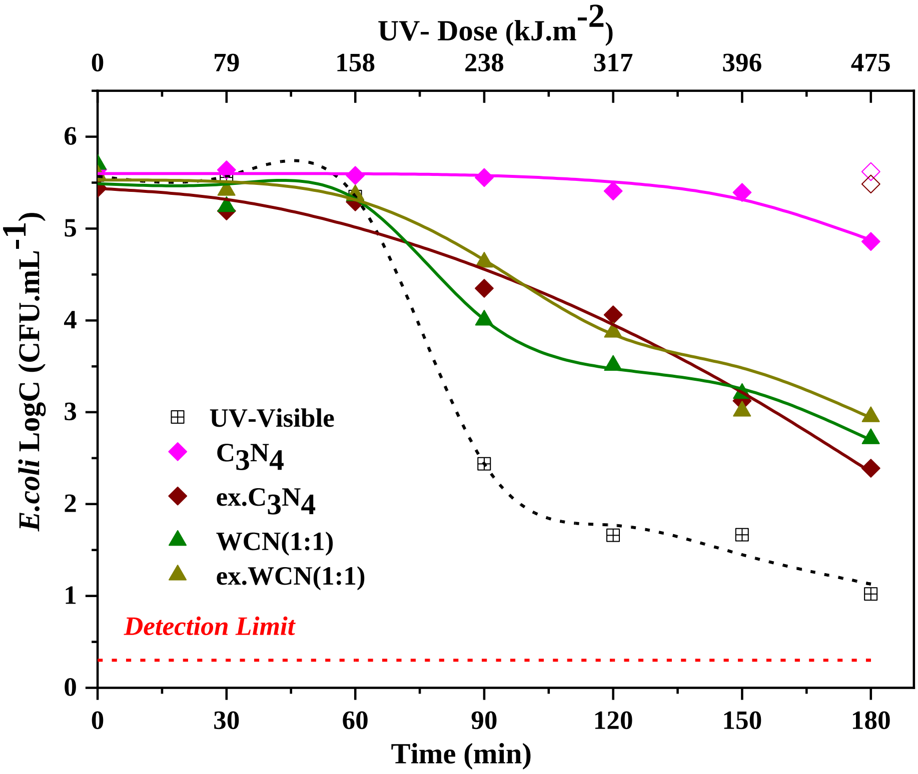

Figure 4.27 *E.coli* inactivation at 20 mg.L^{-1} concentration for ultrasonic exfoliated photocatalysts (ex. C_3N_4 and ex.WCN1:1) in comparison to g-C_3N_4 and WCN1:1 (none exfoliated) materials. Detection limit = 2 CFU.mL^{-1}. All lines represent the fitted data using GInaFIT models.

4.5 Conclusions

Two-dimensional nanoplates of WO_3 were synthesised by a hydrothermal method, and graphitic-C_3N_4 was obtained by a two-step thermal polymerisation process. The 2D nanomaterials were characterised by TEM, SEM and XRD for structural and crystal morphology. Compared to WO_3, g-C_3N_4 in a two-step synthesis had an increased specific surface area, which could also be correlated to an increase in the active sites for photocatalytic reactions. The photocatalytic performance of the WO_3, g-C_3N_4 and WO_3/g-C_3N_4 heterostructures was tested by organic pollutant degradation using formic acid and phenol under simulated solar irradiation. P25-TiO_2 was used as a benchmark photocatalyst. All materials synthesised showed poor (or no) photocatalytic activity for organic pollutant degradation and disinfection. No change in the photocatalytic degradation rate for organic pollutant phenol was observed using the WO_3/g-C_3N_4 heterostructures prepared by a range of methods adapted from the literature. In all cases, P25-TiO_2 showed the best photocatalytic activity for organic degradation. The photocatalytic disinfection activity under simulated solar irradiation was evaluated for WO_3, g-C_3N_4 and WO_3/g-C_3N_4 heterostructures. In comparison to P25-TiO_2, none of the synthesized heterostructures showed evidence of photocatalytic inactivation of *E. coli* in 180 min of irradiation. On comparing the double Weibull model parameters for *E. coli* inactivation, using WCN91 heterostructured photocatalyst (i.e. $\delta_1 = 77.29 \pm 4.54$ min^{-1}, $\delta_2 = 132.52 \pm 11.85$ min^{-1} and $Log_{10}N_{res} = 1.02$ log) against photo-inactivation rates (i.e. $\delta_1 = 73.91 \pm 2.86$ min^{-1}, $\delta_2 = 188.59 \pm 6.66$ min^{-1} and $Log_{10}N_{res} = 1.05$ log), it could be observed WCN91 heterostructure was the only 2D photocatalyst that showed photocatalytic activity comparable to photo-inactivation of *E. coli.* Nevertheless, the WCN91 photocatalyst itself had no major improvement on the overall photo-inactivation rate. Further investigation is necessary to determine why these materials, either individually or combined, did not show any real photocatalytic activity as compared to P25-TiO_2 which is in complete contradiction to the reported literature.

Chapter 5. Investigation of the photogenerated charge transfer processes in WO_3/g-C_3N_4 heterostructures for photocatalysis

5.1 Aim and Objectives

5.1.1 Aim

The aim of this work was to investigate the reason for the poor photocatalytic performance of the synthesised WO_3 nanoplates, g-C_3N_4 and the WO_3/g-C_3N_4 heterostructures and to elucidate the charge transfer mechanism for the heterostructures.

5.1.2 Objectives

i. To study the generation of reactive oxygen species (hydroxyl radicals) using the chemical probe p-nitrosodimethylaniline (RNO).
ii. To investigate the electron transfer processes using the reduction of methyl viologen at different solution pH values.
iii. To determine the optical bandgap and band alignment positions of WO_3 and g-C_3N_4 by Tauc plots and valence band XPS.
iv. To study the photoluminescent properties for the materials and compare the recombination processes in the parent and heterostructured photocatalysts.
v. To perform photoelectrochemical characterisation on WO_3 and g-C_3N_4 photocatalysts and to determine their flat band potential by impedance spectroscopy.
vi. To propose a photocatalytic charge transfer mechanism in WO_3/g-C_3N_4 heterostructures based on the obtained results.

5.2 Introduction

Identifying the charge transfer mechanism is fundamental to understanding the mechanism and efficiency of photocatalytic materials. Similarly, the pathways of production of reactive oxygen species by the photogenerated electrons and holes during the reaction are also important. Researchers have previously focused on reporting the photocatalytic properties of WO_3/g-C_3N_4 heterostructures (Table 5.1). Most of these studies concentrated on the development of heterostructures on the grounds of previously reported values of the band edge potentials. Often the photogenerated charge carriers in WO_3/g-C_3N_4 are presumed to follow a z-scheme or Type-II mechanism based on their reported CB edge and VB edge potentials.

Table 5.1 WO_3/g-C_3N_4 photocatalysts based on z-scheme or Type-II mechanism

Photocatalytic applications		Scheme	Ref.
Photoelectrochemical water splitting		Type-II	[99-101]
Organic pollutant degradation	Dye degradation (Methylene Blue, Rhodamine B, Methyl Orange, Fuchsin)	Z-scheme	[94, 102, 162-164, 167, 194]
		Type-II	[227]
	Antibiotics (Tetracycline, ceftiofur sodium, sulfamethoxazole)	Z-scheme	[102, 166, 169]
	Phenolic compounds (4-chlorophenol)	Type-II	[227]
H_2 production		Z-scheme	[92, 93, 194, 228]
Gas-phase reactions (acetaldehyde degradation, CO_2 reduction)		Z-scheme	[98, 229]
		Type-II	[96]

However, the active centres of the individual material responsible for the photocatalytic activity have not been studied in detail. A prime criterion for selection of materials for ideal solar photocatalysts is the identification of their band edge potentials and a narrow bandgap within 2-3 eV. A critical point overlooked while achieving these two criteria is the presence of any surface states or the effect of these surface states on the photocatalytic activity of the materials. Some interdisciplinary studies have given insights into the existence of surface defects in TiO_2 [230, 231], g-C_3N_4[232, 233] and WO_3 [85] related to their photocatalytic and photoelectrochemical applications. However, a direct measurement to identify such defects in structures is still elusive in terms of experimental methods, especially in the case of novel inorganic/organic semiconductor heterostructure systems such as WO_3/g-C_3N_4. A direct correlation between the theoretical and experimental values for band edge potentials is still missing. The photocatalytic activity of such semiconductors might be possibly affected due to surface charge, pH-dependent behaviour of the band edges of the material by adsorption of H^+/OH^- ions, chemical defect states (or formation of polaron states) and structural deformation. All the above parameters should be equally considered and confirmed by multiple measurements to determine the photocatalytic efficiency of new materials synthesized. Therefore, this work is focused on determining the band energetics of the synthesised 2D-WO_3 and g-C_3N_4 to understand why the results of photocatalysis experiments in this work do not correlate to the published literature.

Hydroxyl radicals ($^\bullet$OH) are considered to be the primary oxidants in any photocatalytic disinfection process. These non-selective ROS species have a short lifetime of 10^{-9} s [234, 235]. However, some recent reports do suggest they can live up to a few micro-seconds (μs) [236, 237]. Their detection and quantification is challenging and usually relies on spin trapping methods such as electron paramagnetic resonance (EPR). An alternative to direct spin trapping is the reaction of $^\bullet$OH present in aqueous solution with a reagent that traps and converts $^\bullet$OH to carbon centred radical species for quantification. The quantification of $^\bullet$OH is either accumulation or loss of reactant. A compound that selectively and directly reacts with $^\bullet$OH without altering any other aspects of the solution should be used for optimal detection of $^\bullet$OH. Colourimetric probe methods for detection of ROS are easy, inexpensive and straightforward techniques. Chemical probes such as p-nitrosodimethylaniline (RNO) have been used to trap $^\bullet$OH present in the solution as a result of photogenerated charge carriers, to form an adduct $RNO^{\bullet}OH$ [238-240]. Using TiO_2 as suspended or immobilised photocatalyst for photocatalytic RNO degradation researchers have reported $^{\bullet}OH$ production rate of up to 10^{10} $mol.L^{-1}.s^{-1}$ [239-241]. Previously Cruz- Ortiz et al.(2017), also analysed $^{\bullet}OH$ production under UV-Vis and visible only irradiation using RNO as a chemical probe for testing the efficiency of TiO_2-P25 and TiO_2-rGO photocatalyst for photocatalytic disinfection [40]. The analysis of Cruz-Ortiz et al.(2017) indicated a higher RNO degradation with TiO_2-rGO as compared to TiO_2-P25 only in UV-Vis irradiation, due to a faster e^--h^+ separation in TiO_2-rGO.

The direct electron reduction and hole oxidation pathway in the photocatalytic transformation of reactants to products is important. The direct electron reduction pathway can be utilised to define the potential for CB edge or flat band potential of semiconductor systems via pH-independent electron mediators such as methyl viologen dichloride (MV^{2+}). MV^{2+} is a pH-independent redox mediator capable of forming a stable blue cation $MV^{+\bullet}$ by 1 electron reduction at $E^0 = -0.445$ V (NHE) [242]. Using laser photolysis, Grätzel and co-workers developed a direct method of determining the flat band potential of semiconductor with the addition of electron acceptor (MV^{2+}) in solution [243]. Watanabe and Honda reported a method to quantify the molar extinction coefficient of reduced methyl viologen (i.e. $MV^{+\bullet}$) via photocatalytic reactions involving TiO_2 and ZnO suspensions in organic solvents in a thin-layer photoelectrochemical cell [244]. Bard et al.(1983), studied the photocurrent response of TiO_2 in the presence of MV^{2+} to determine the shift in the Fermi level energy (or flat band potential E_{fb}) of TiO_2 with pH [245]. Later the same protocol was applied for non-oxide semiconductors such as CdS, where a negative shift of 0.04 V/pH unit in the conduction band potential (E_{fb}) was reported by Bard and White [246], different from a Nernstian response of 0.059 V/pH. A 0.03 V/pH shift in E_{fb} was also reported by Roy et al.(1995) from photovoltage measurements of CdS/MV^{2+} suspension [204]. The use of methyl viologen is now well established in determining the flat band potential or quasi Fermi level of electrons in oxide and non-oxide semiconductor photocatalysts, due to its pH-independent behaviour and a fixed reduction potential of -0.445 V (NHE).

A correlation exists between the Fermi level, optical bandgap and valence band energy of a semiconductor towards elucidating its electronic band structure. In a recent study to asses the limited photocatalytic performance of haematite electrodes, Lohaus et al.(2018) reported the existence and interference of polaron defect states formed under excitation that leads to pinning the Fermi level of hematite [247]. The polaron state was identified through VB XPS measurements and was said to limit the Fermi level at a potentially much lower than H^+/H_2 reduction potential for photocatalytic water splitting. The presence of defect states that are active under optical excitation can limit a material's photocatalytic performance.

The presence of surface defects limiting the photocatalytic performance of g-C_3N_4 has been reported. For instance, Durrant et al.(2017) attempted to study the electron transfer process taking place in different precursors based g-C_3N_4 by solid state photoluminescence spectroscopy and transient absorption spectroscopy[233]. In one of their previous reports, a limited photocatalytic performance was reported by g-C_3N_4 towards H_2 production. Through time-resolved photoluminescence (TRPL) and transient absorption spectroscopy (TAS) measurements, the trapping of free electrons in the picosecond range was reported in their study. They also reported the electrons were trapped in the chemical defect states of g-C_3N_4 situated well below the reduction potential of H^+/H_2 that attributed towards limited photocatalytic half-reactions of g-C_3N_4 for H_2 production[248]. Similarly, some structural deformation and chemical instability of g-C_3N_4 as a photocatalyst have also been reported both in aqueous as well as gas-phase reactions [112, 198].

There are some electrochemical investigations on g-C_3N_4, which report its amphoteric properties with both electrons and holes contributing towards photocurrent generation. For instance, both anodic and cathodic photocurrents were reported by Zhang et al.(2010) [155] and Jing et al.(2019) [185] on sweeping potentials from positive to negative bias. However, no plausible explanation through chemical studies was presented by the authors to justify the dual photocurrent response. Osterloh et al.(2014) reported the limited photocatalytic performance of g-C_3N_4 towards reduction reactions were due to defects arising from the terminal N-atoms of g-C_3N_4, i.e. amino group [232]. The surface defects were identified through photochemical investigation and co-related with their photovoltage signals.

To understand the poor photocatalytic performance of 2D/2D WO_3/g-C_3N_4 heterostructures, the band energies of WO_3 and g-C_3N_4 as individual and heterostructured photocatalyst was investigated. The band potentials of individual materials were studied via chemical probes and corroborated with chemical investigations such as photoluminescence and XPS. The band energy values were correlated with electrochemical band potentials studied using multiple electrochemical techniques. In this work, the chemical and electrochemical investigations were bridged to elucidate the pathway of electron transfer in WO_3/g-C_3N_4 heterostructures by identifying the type of photocatalytic mechanism taking place.

5.3 Experimental Section

5.3.1 Photocatalyst preparation

The synthesis of WO_3 nanoplates and g-C_3N_4 has been discussed previously in chapter 3. The WO_3/g-C_3N_4 heterostructures used in this study were prepared as follows:

5.3.1.1 Heterostructure formation by calcination

WO_3/g-C_3N_4 heterostructures were prepared by one-step calcination route as follows: specific amounts of synthesized WO_3 nanoplates and g-C_3N_4 were mixed and ground in an agate mortar for 20 min and then annealed at 400°C for 1 h in an air muffle furnace. According to this method, WO_3/g-C_3N_4 samples of the weight ratio of 10:90 and 90:10 were prepared and denoted as WCN19 and WCN91, respectively.

5.3.1.2 Heterojunction formation based on surface charge

The synthesis of WO_3/g-C_3N_4 heterostructure prepared by dispersion in citrate buffer has been discussed in section 3.2.3.4. Briefly, the zeta potential for WO_3 nanoplates and g-C_3N_4 was measured under different pH ranges from 2-6 to determine a pH with zero point of charge (pzc). Based on the pzc values estimated, the two materials were dispersed at a pH where they had opposite zeta potential values to facilitate electrostatic attraction. Using this approach, the WO_3/g-C_3N_4 heterostructure was obtained in the weight ratio of 1:4 (WO_3:g-C_3N_4) in a solution of pH 2.25. This sample was named as WCN(14)pH2.25.

Therefore, the photocatalysts investigated in this study were WO_3, g-C_3N_4 and the heterostructures WCN19, WCN91 and WCN(14)pH 2.25.

5.3.2 Photocatalytic RNO degradation

The detection of hydroxyl ($^{\bullet}$OH) radicals was performed using a chemical probe p-nitrosodimethylaniline (RNO). RNO is used as a scavenger of $^{\bullet}$OH radicals generated during the photocatalytic reaction and can be quantified using UV-Vis spectroscopy. Details on the RNO quantification and photocatalytic degradation process have been discussed previously in chapter 3, section 3.4.4.1. In the present study, $^{\bullet}$OH production was also assessed using RNO degradation in the presence of an electron scavenger ($AgNO_3$).

5.3.3 Photocatalytic reduction of methyl viologen dichloride

The electron transfer process in WO_3 and g-C_3N_4 photocatalyst was also analysed using a pH indepedent chemical probe methyl viologen dichloride (MV^{2+}). The single electron reduction of MV^{2+} to its $MV^{+\bullet}$ radical at a pH independent potential, E^0 = -0.445 V (NHE) is a way of determining the flat band potential of semiconductor photocatalyst with changing pH of the suspension under irradiation. A detailed quantification process has been mentioned previously in chapter 3, section 3.4.4.2.

5.3.4 Optical bandgap determination

The optical bandgap of the samples was determined using UV-Vis diffuse reflectance. The samples were spray-coated on borosilicate glass slides, and the transmittance of each sample was analysed in wavelength from 250-800 nm. The optical bandgap of the material was calculated using the Kubelka-Munk function ($F(R_\infty)$) [249], used in the Tauc plot and the slope of the Tauc plot was extrapolated to $y = 0$ on the x-axis, i.e. the corresponding bandgap energy (eV).

5.3.5 XPS analysis

A narrow scan spectrum of the samples was performed using XPS to study the energy difference between the valence band minima and Fermi level of the sample (E_{VBM}- E_{f}) derived from the onset at binding energy scale. The binding energy from the VB XPS for each sample was calibrated to the C 1s peak at 284.8 eV. Core level XPS was performed to study the chemical states in the parent sample and the heterostructures, with respect to their binding energy. The details of the instrument have been described in section 3.3.4.

5.3.6 Photoluminescence studies

The photoluminescence studies of the samples were performed using the fluorescence spectroscopy by excitation of the samples at wavelength 330 nm. The obtained emission peaks were recorded between 300-600 nm for all the samples.

5.3.7 Photoelectrochemical characterisation

The photoelectrochemical measurements were performed to determine the on-set photocurrent potential and the flat band potential of the photocatalysts. The photocatalytic materials were immobilised by spray coating on tungsten foils of dimension 2 × 1 cm^2 according to the method described in section 3.2.4.

5.3.7.1 Current-Potential (I-*E*) measurements

The current versus potential measurements were performed using linear sweep voltammetry at pH 1(0.1M $HClO_4$), 7(0.1M KCl), 13 (0.1M NaOH) electrolytes to study the dependency of on-set photocurrent on changing pH. The measurements were performed under chopped irradiation of 10 s and at a scan rate of 5 $mV.s^{-1}$ in applied potential range 0.0 to +1.0 V for WO_3 and -1.0 to +1.0 V for g-C_3N_4. All potentials were reported against SCE. The current (I) at fixed potential vs time (t in s) was determined at +1.0 V with chopped irradiation at 200 s interval.

5.3.7.2 Mott-Schottky analysis

Mott-Schottky analysis on WO_3, g-C_3N_4 and heterostructure WCN91 was performed in the dark and under irradiation with FRA (frequency response analyser) potential scan to determine the flat band potential of the individual semiconductors. The setup conditions were similar to the I-V curve measurements. The potential scan range was 0.0 to +1.0 V for both WO_3, and g-C_3N_4 with a step potential of +0.1 V. A single sinusoidal AC voltage with root mean square (RMS) value of 10 mV was applied in the frequency range from 0.01 Hz to 100 kHz. In the case of g-C_3N_4 Mott-Schottky analysis was performed in different electrolytes of pH 1, 7 and 13 to determine the pH-dependent shift on the flat band potential of g-C_3N_4 under dark conditions.

5.4 Results and Discussion

5.4.1 Zeta potential measurements of WO_3 and g-C_3N_4

The zeta potential measurements of the synthesised WO_3 and g-C_3N_4 were performed over a range of pH values in sodium citrate buffer. As shown in figure 5.1, between pH 2 and pH 6 WO_3 exhibited a negative zeta potential. The surface of WO_3 nanoplates was negatively charged at pH greater than 2, and its point of zero charge (pzc) lies below pH 2. The pzc for WO_3 was previously reported to be pH 0.43[250]. In another case, a value 0.5 was given as ISEP (isoelectric point) for WO_3 [251]. The negative zeta potential values at higher pH for WO_3 were obtained due to the dissolution of hydroxides (OH^-) to form tungstate ions, thus making WO_3 more stable in the strongly acidic environment [252]. The zeta potential for g-C_3N_4 was variable with pH, and pzc was observed around pH 2.5. The positive charge for g-C_3N_4 has been attributed in literature as the protonation of the terminal amine (-NH_2) groups of g-C_3N_4[253]. Effectively, both WO_3 and g-C_3N_4 exhibit opposite charges around pH 2.25. Therefore, for the formation of heterostructures, a pH of 2.25 was used to facilitate electrostatic attraction between the WO_3 and g-C_3N_4. The schematic presentation for the heterostructure formation is shown in figure 5.2.

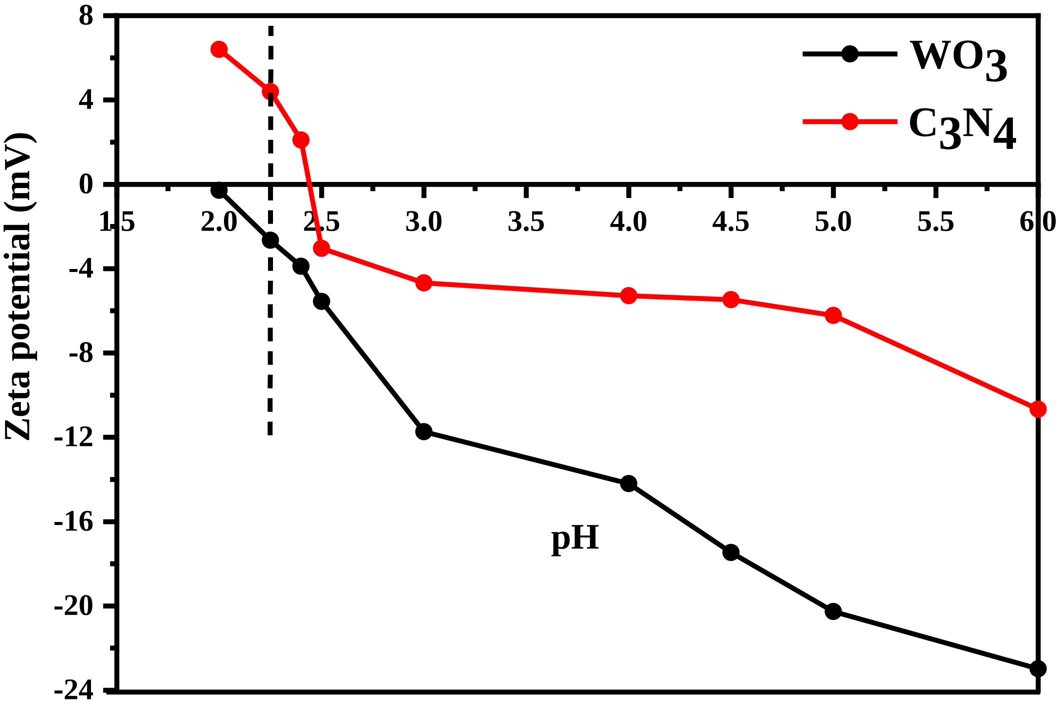

Figure 5.1 Zeta-potential vs pH plot for WO_3 and g-C_3N_4

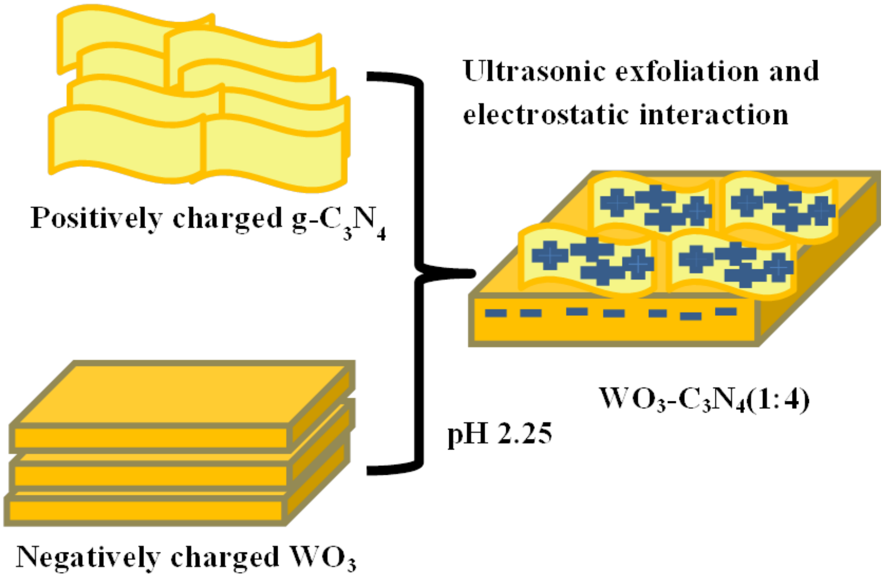

Figure 5.2 Scheme of 2D WO_3/g-C_3N_4 at pH 2.25

5.4.2 Detection of hydroxyl radicals (•OH) using RNO

The determination of RNO was performed by analysing the absorbance in 3 replicates for a set of standard concentrations by UV-visible spectroscopy at a peak wavelength of 440 nm. A line of best fit was obtained, using a regression analysis of $R^2 = 0.998$, as shown in figure 5.3. A standard deviation of ± 0.004 was calculated across the range of 3 data sets with a standard error of ± 0.014. The corresponding molar absorption coefficient for RNO was calculated from the slope (m) of linear fit equivalent to 0.0347×10^{-6} mol.L $^{-1}$cm^{-1}.

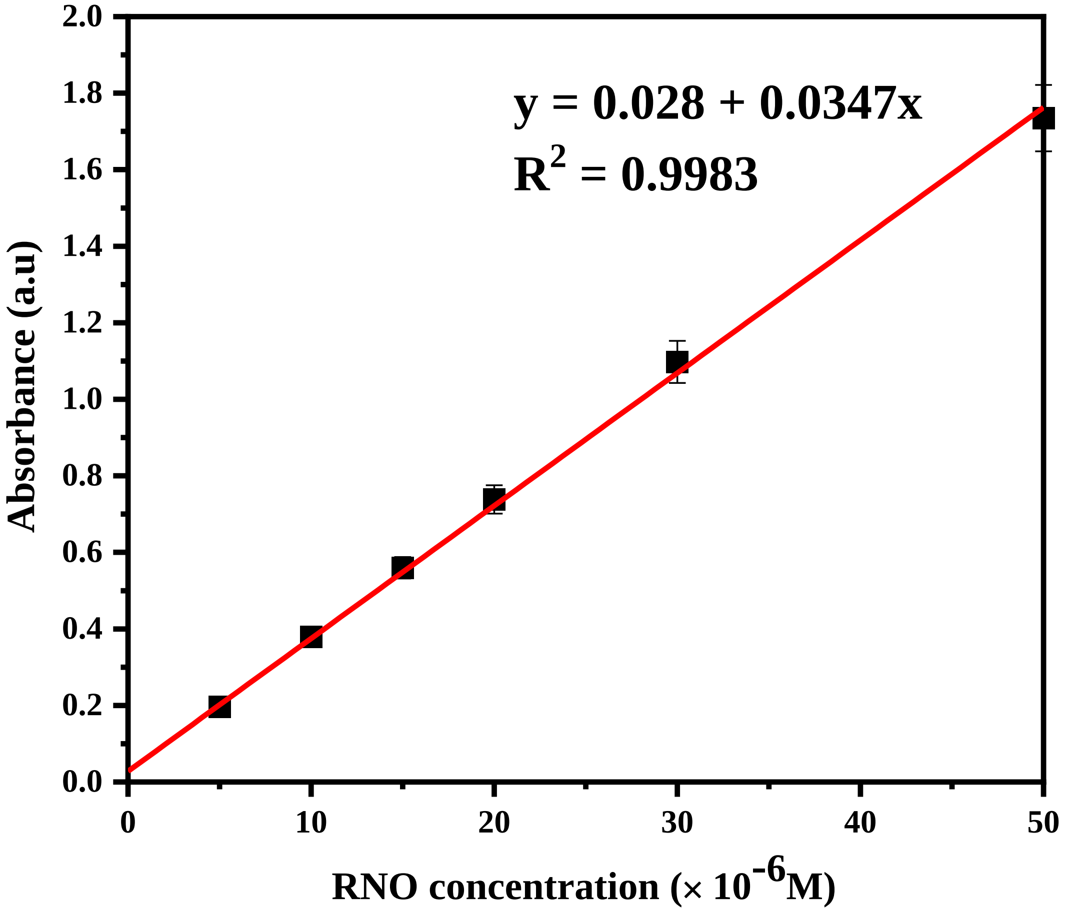

Figure 5.3 Absorbance vs concentration plot for p-nitrosodimethylaniline at λ= 440 nm.

The $^{\bullet}OH$ radical production in semiconductor photocatalysis has been described as direct oxidation of adsorbed surface hydroxyl groups (OH^{-}_{ad}) or water (H_2O) molecules in reaction with photogenerated holes (h^{+}) based on equation 5.1 and 5.2 [44, 46].

$$h^{+} + OH^{-}_{ad} \rightarrow \bullet OH_{ad} \qquad 5.1$$

$$h^{+} + H_2O \rightarrow \bullet OH_{ad} + H^{+} \qquad 5.2$$

The electrochemical potential for production of $^{\bullet}OH$ radicals is +2.73 V (NHE) at pH 0[46], which is theoretically favourable reaction for WO_3 (E_{VB} = + 3.1 V(NHE) at pH 0) and TiO_2 (E_{VB} = +3.0 V(NHE) at pH 0) but unfavourable for g-C_3N_4 whicht has a less favourable HOMO level (or VB) with reported values ranging between +1.4 to +1.7 V(NHE) [109, 111, 151]. With the RNO probe, the $^{\bullet}OH$ radicals generated during the process are trapped and scavenged by the conjugated double-bonded (nitroso) R-N=O group to form R-N=O$^{\bullet}$OH, where the R represents the dimethylaniline ($C_8H_{10}N$) [238, 239] (Figure 5.4).

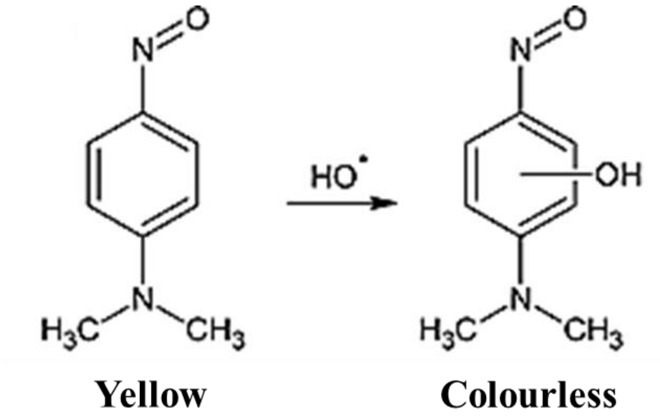

Figure 5.4 RNO oxidation pathway by the attack of hydroxyl radicals. Adapted from Simonsen et al.(2011) J Appl Electrochem 41, 599–607 (2011) [238].

The •OH radical detection was investigated as a mean of photocatalytic degradation of RNO by observing the changes in the absorption spectrum recorded at different irradiation times for photocatalytic suspensions of WO_3, g-C_3N_4 and P25-TiO_2 at 20 mg.L^{-1}. The concentration of RNO was observed to be decreasing with every 10 min interval of irradiation time for TiO_2, and the discolouration of the yellow solution was obtained within 60 min. However, the 2D photocatalysts WO_3 and g-C_3N_4 did not show any degradation of RNO, suggesting negligible production of •OH radicals (Figure 5.5).

The •OH production is thermodynamically favourable for both TiO_2 and WO_3 based on their positive VB potentials. The limited activity observed for WO_3 is probably due to the less negative CB edge potential of WO_3 (+0.4 V (NHE) pH 0), meaning it is less effective at reducing oxygen. Therefore e^--h^+ recombination will dominate. Thus, the RNO experiment was repeated with the addition of an electron scavenger such as $AgNO_3$ with a more positive reduction potential than the CB edge of WO_3 (Figure 5.6).

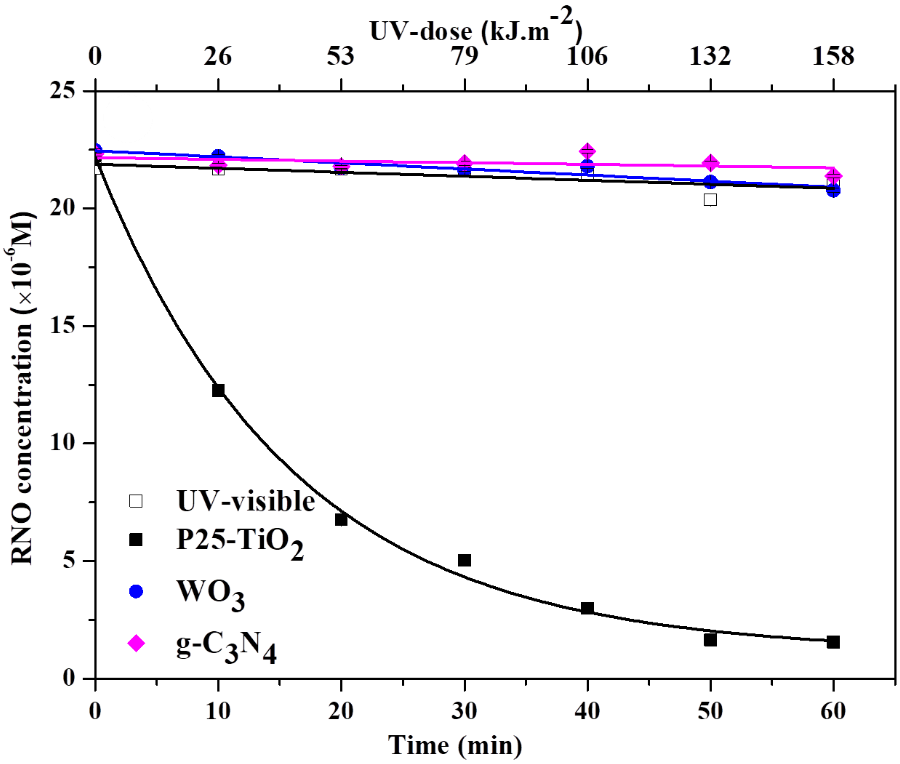

Figure 5.5 RNO concentration vs time for different photocatalysts at 20 mg.L^{-1}; UV-visible is light control, pH 6.5 (distilled water).

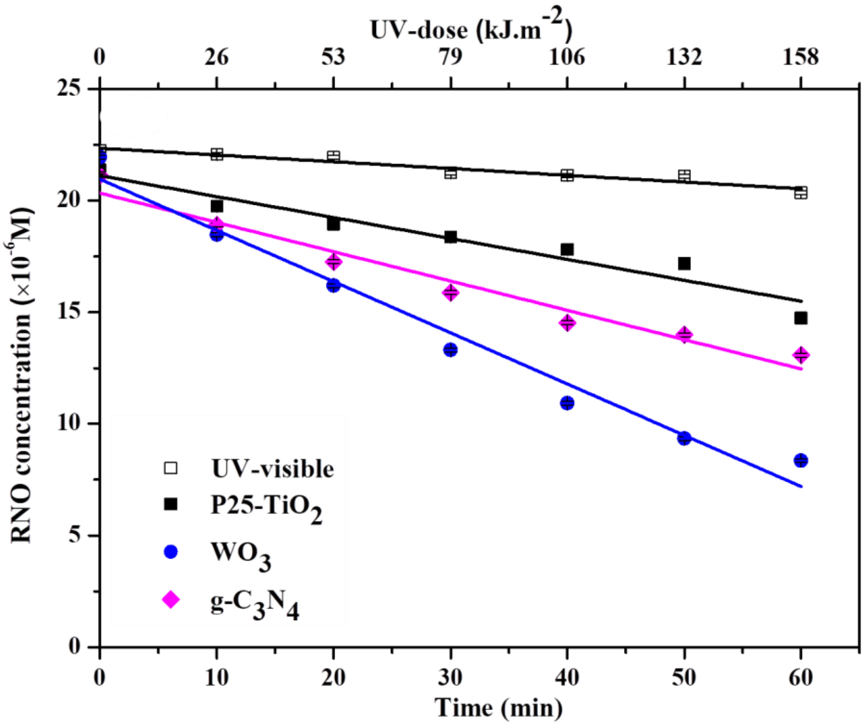

Figure 5.6 RNO concentration vs time for different photocatalysts using at 20 mg.L^{-1}. $AgNO_3$ was added as an electron scavenger; UV-Vis is the light control, pH 6.5 (distilled water).

When $AgNO_3$ was added as an electron scavenger to the RNO, the formation of $^{\bullet}OH$ radicals was detected for WO_3 and g-C_3N_4, as shown in figure 5.6. The photoreduction of Ag^+/Ag^0 takes place at +0.80 V (NHE) [209]. Hence the scavenging of electrons leaves the photogenerated holes behind to react with water molecules for $^{\bullet}OH$ production which then react with the RNO. The improved activity with electron scavenger confirmed the presence of $^{\bullet}OH$ radicals as a reaction of VB holes for WO_3. The addition of Ag^+ with TiO_2 suppressed the photocatalytic degradation of RNO as compared to without any scavenger. This suggests that the RNO bleaching with P25-TiO_2 could be due to $^{\bullet}OH$ radicals being produced both by the oxidation of water and by the reduction of molecular oxygen (equations 5.3 to 5.5).

$$O_2 + e^- \rightarrow O_2^{\bullet -} \qquad 5.3$$

$$O_2^{\bullet -} + 2H^+ + e^- \rightarrow H_2O_2 \qquad 5.4$$

$$H_2O_2 + e^- + H^+ \rightarrow HO^{\bullet} + H_2O \qquad 5.5$$

If Ag^+ utilises the photogenerated electrons in P25-TiO_2 on excitation, the production of $^{\bullet}OH$ through reductive route is suppressed with not enough electrons available to react with molecular oxygen. However, photogenerated holes can react with H_2O/OH^- to form $^{\bullet}OH$ (eq. 5.1 and 5.2). Hydroxyl radical detection by RNO oxidation under aerobic and anaerobic conditions with electron/hole scavengers had already been reported by Simonsen et al.(2011) to be a reductive reaction of CB electrons in case of P25-TiO_2 [239]. P25 and P25-rGO for solar photocatalytic disinfection have been reported in the past to produce $^{\bullet}OH$ radicals and their detection by RNO degradation by Curz-Ortiz et al.(2017) The photocatalytic disinfection activity and production of $^{\bullet}OH$ radicals studied by the same authors was presented to be more in case of P25-rGO, due to the effective charge separation and transport of CB electrons through the rGO [40]. They reported the production of singlet oxygen as the route through consumption of superoxide ions in case of P25-rGO, which means the production of $^{\bullet}OH$ radicals is also possible based on equation 5.3 to 5.5. Perhaps, the lower rate of $^{\bullet}OH$ radical production observed with P25-TiO_2 in the presence of $AgNO_3$ in this work could be due to Ag^+ competing for conduction band electrons with molecular oxygen, so less $^{\bullet}OH$ radicals are produced via a reductive route. Nevertheless, with g-C_3N_4 alone, there was no formation of $^{\bullet}OH$ radicals without scavenger (figure 5.7). This could be predicted as a charge recombination similar to the case of WO_3. Considering the band edge potentials of g-C_3N_4, in the presence of scavengers, the only pathway for $^\bullet OH$ production should be the reduction of molecular oxygen. Therefore, by addition of h^+ scavenger such as potassium iodide, the production of $^\bullet OH$ was studied and still found to be negligible. It is assumed the oxidation of iodide ($2I^-/I_2$) was possible in the photocatalytic process as the $E_{I-/I2}$ = +0.54 V (NHE) is above the VB potential of g-C_3N_4 (+1.75 V (NHE)) making it favourable to scavenge the photogenerated holes and leaving behind free electrons. Nevertheless, no photocatalytic bleaching of RNO was observed through the reductive pathway for g-C_3N_4. Conversely in the presence of $AgNO_3$ as electron scavenger and aerobic conditions, higher photocatalytic bleaching of RNO was obtained for g-C_3N_4, indicating the production of $^\bullet OH$ radicals through the oxidative pathway. The obtained result was unexpected, considering the more positive potential of $^\bullet OH$ generation as compared to HOMO of g-C_3N_4, an 11x times faster photocatalytic RNO degradation activity was achieved with e^- scavenger as compared to without any scavenger. The reason for the increased $^\bullet OH$ production with g-C_3N_4 +Ag^+ was unknown. However, the chemical instability of g-C_3N_4 has been questioned previously in literature towards photocatalytic oxidation reactions due to excessive nitrogen present in solution following photocatalytic reactions [112, 198]. For instance, Xie et al.(2017) reported the decomposition of g-C_3N_4 in aqueous solutions with O_2 and under simulated solar irradiation. In this case, g-C_3N_4 was observed to release nitrate ions (NO_3^-) by self-decomposing into cyameluric acid (detected through ESI mass spectrophotometry) [112]. The decomposition of g-C_3N_4 was attributed due to an oxidative attack of $^\bullet OH$ produced during the reaction, which breaks the heptazine unit through the terminal N- atom and release it as NO_3^- in solution, being replaced by O-atom to form cyameluric acid (observed through XPS in study of Xie et al.(2017)). The study was concluded with the observation of lower decomposition of g-C_3N_4 under solar irradiation when a $^\bullet OH$ scavenger such as tert-butyl alcohol (TBA) was added. During the process, most of the $^\bullet OH$ radicals produced were utilised by TBA with a slower release rate of NO_3^- ions. The reduction potential of NO_3^-/NO_2 is +0.80 V (NHE), similar to Ag^+/Ag^0. In such cases, an oxidative attack of g-C_3N_4 could be predicted by self-decomposition of g-C_3N_4, which might not give reproducible results on the use of the same photocatalyst.

Another report on the instability of g-C_3N_4 was published by Pomilla et al.(2018) in gas phase reactions (CO_2 reduction) where through XPS investigations, the base unit of heptazine of g-C_3N_4 was observed to change by a replacement of N-atom to O-atom [198]. Nevertheless, the reports of Xie et al.(2017) and Pomilla et al.(2018) raised a question over g-C_3N_4's ability to do photocatalytic reactions, indicating a photo-oxidation in g-C_3N_4 taking place during irradiation. To investigate if there was any photo-oxidation of g-C_3N_4 taking place in the present study, core level XPS investigations were performed on g-C_3N_4 and the heteostructures to obtain more information of their chemical and structural configurations which will be discussed in later sections.

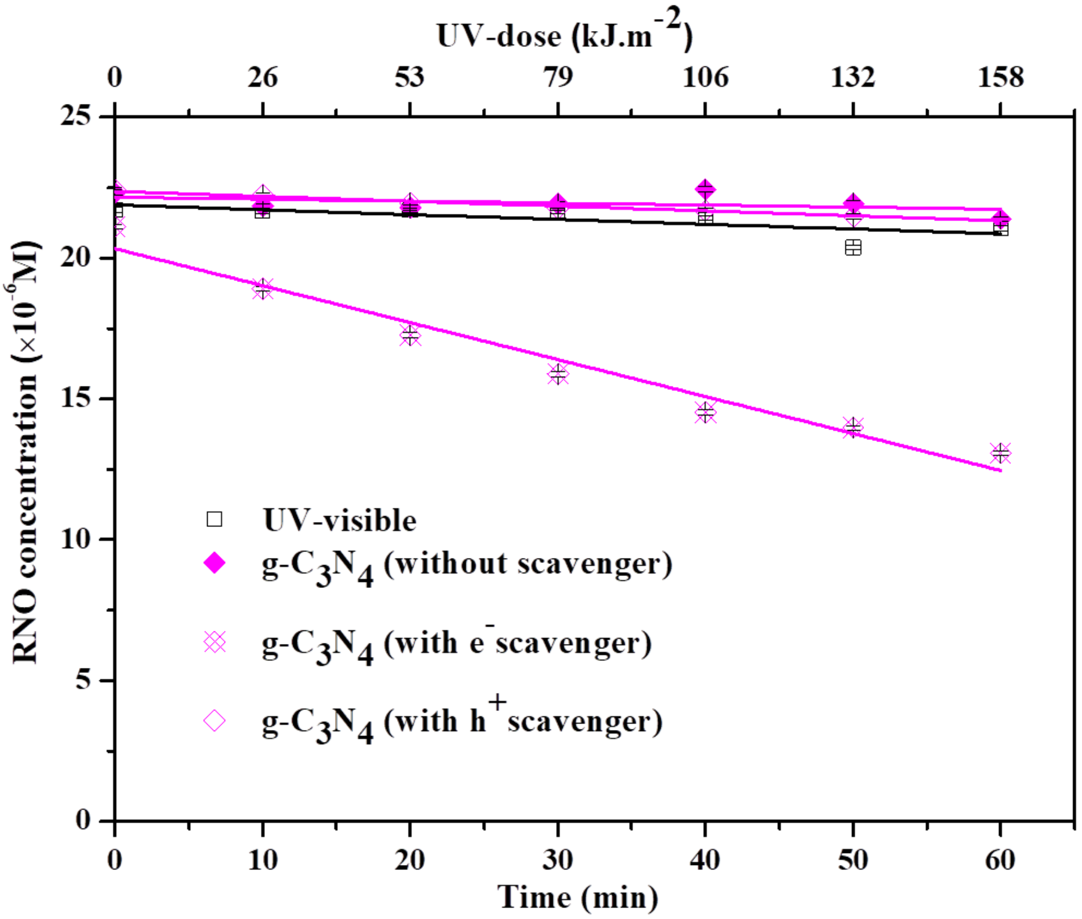

Figure 5.7 RNO concentration vs time with g-C_3N_4 under simulated solar irradiation, with and without scavengers in air saturated solutions (electron scavenger: 200 µM $AgNO_3$; hole scavenger: 10 mM KI), pH 6.5 (distilled water).

The WO_3/g-C_3N_4 heterostructures were also tested for photocatalytic RNO degradation to identify the production of hydroxyl radicals. Without any electron scavenger limited photocatalytic activity was observed for the heterostructures (figure 5.8), although the rate of degradation for WCN91 (6.33×10^{-10} mol.L^{-1}.s^{-1}) was 1.5x times faster than only WO_3 (4.30×10^{-10} mol.L^{-1}.s^{-1}). An increase in the photocatalytic activity was obtained, albeit on the addition of $AgNO_3$ as the scavenger for electrons for WO_3, g-C_3N_4, and the heterostructures WCN19, WCN14 and WCN91 (figure 5.9). A degradation rate of 46.7×10^{-10} mol.L^{-1}.s^{-1}) was achieved for WCN91 on the addition of e^- scavenger that was 7.4x times faster than without any scavenger.

The order of RNO degradation with respect to the zero order rate constant observed in the presence of the Ag^+ electron scavenger was determined to be as follows: WCN91>WO_3>WCN14> WCN19>g-C_3N_4> TiO_2 (table 5.2).

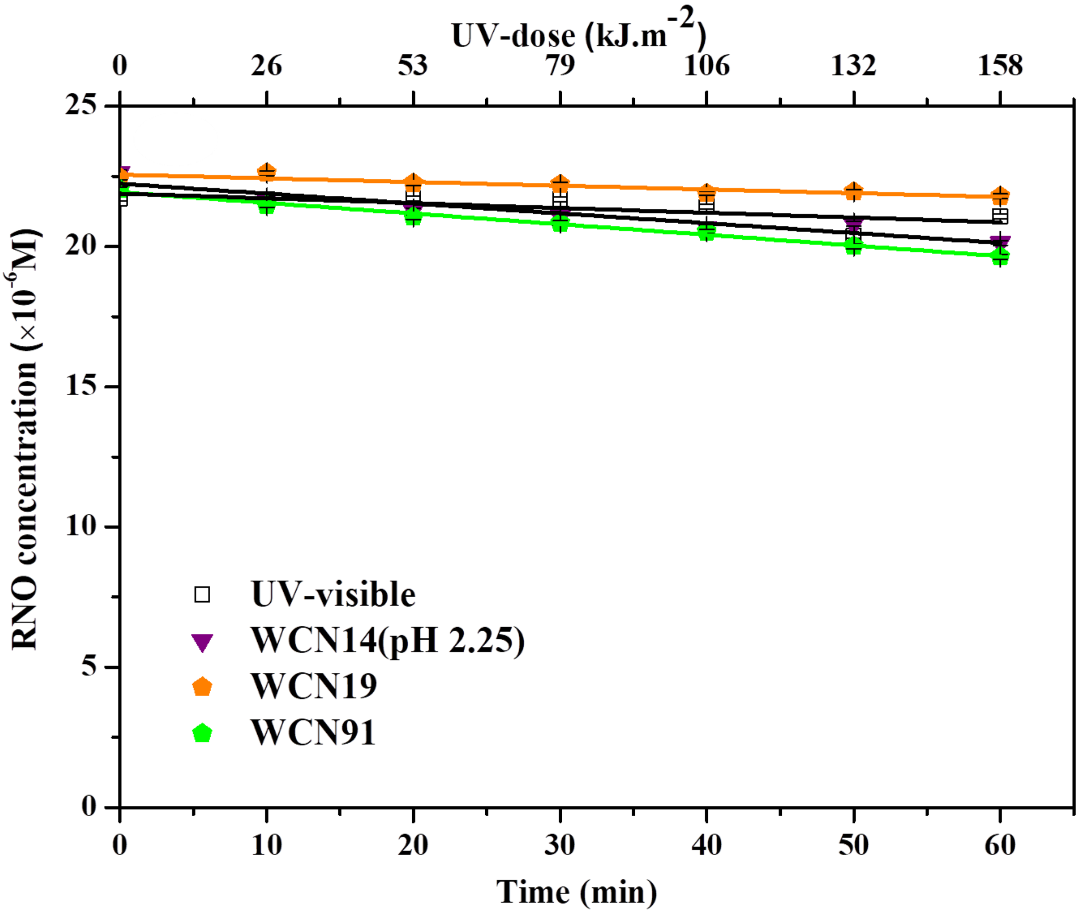

Figure 5.8 RNO concentration vs time using WO_3/g-C_3N_4 samples without any scavenger in pH 6.5 (distilled water).

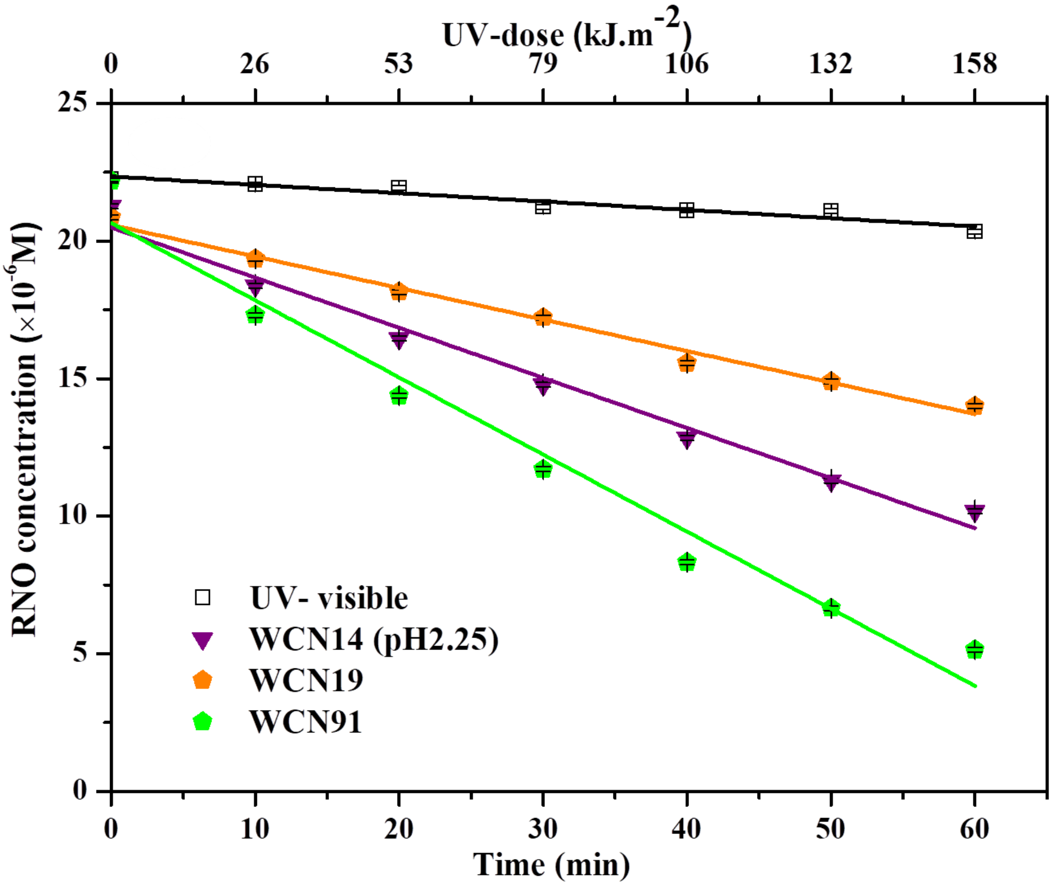

Figure 5.9 RNO concentration vs time using WO_3/g-C_3N_4 with $AgNO_3$ as electron scavenger in pH 6.5 (distilled water).

Table 5.2 Rate of $^{\bullet}OH$ production (detected by RNO degradation)

Catalyst (20 mg.L^{-1})	Rate without e$^-$ scavenger (× 10^{-10} mol.L^{-1}.s^{-1})	Rate with e$^-$ scavenger (× 10^{-10} mol.L^{-1}.s^{-1})
Light	2.83	5.05
P25-TiO_2	7.67	0.83
WO_3	4.30	38.20
g-C_3N_4	1.18	2.87
WCN19	2.22	19.10
WCN14pH2.25	5.87	30.40
WCN91	6.33	46.70

The rate of $^{\bullet}OH$ production in the case of WO_3/g-C_3N_4 heterostructures was relatively low. This could be due to fast electron-hole recombination, or perhaps photo-oxidation of the g-C_3N_4, which has previously been reported by Xie et al.(2017) [112]. Improved $^{\bullet}OH$ radical production was observed in the presence of Ag^+ as an electron scavenger suggesting that transfer of CB electrons from the g-C_3N_4 was rate-limiting (in the absence of electron scavenger). The limited production of $^{\bullet}OH$ from the reductive route of g-C_3N_4 is a question for its applicability in photocatalytic reactions. If the reduction pathway in photocatalysis was based on the transfer of electrons through the negative CB edge of the photocatalyst, then reported CB(or LUMO) (-1.13 V(NHE)) in literature for g-C_3N_4 should have larger overpotential for O_2 reduction, relative to metal oxides such as WO_3. However, if we hypothesize, a presence of an electronic trap lower than the LUMO of g-C_3N_4, with filled (or trapped) electrons, the reduction of O_2 may not occur. To confirm if there was any electron trapping in g-C_3N_4 happening here, it was necessary to study the reductive pathway for these materials against a fixed, known potential. For this reason, the next step was to investigate the electron transfer from the semiconductor's CB (or LUMO) to a redox chemical probe methyl viologen, which undergoes reduction via 1 electron to $MV^{\bullet+}$ at a pH-independent potential of -0.445 V (NHE).

5.4.3 Photocatalytic reduction of methyl viologen dichloride

The electrochemical potential of the photogenerated electrons in a semiconductor's conduction band can be measured using electron acceptors with known and pH-independent electrochemical reduction potentials, e.g. methyl viologen dichloride (MV^{2+}). The band energetics of both metal-oxide (TiO_2)[245], as well as non-oxide (CdS)[246] semiconductors in suspension, have been explored using pH-independent electron acceptor MV^{2+} by Bard et al.(1983) in different pH of the suspension. In most heavily doped semiconductors the distinction between the band edge potential and its Fermi level is rarely made, as the Fermi level lies close to the either CB (n-type SC) or close to VB (p-type SC). This distinction between the doping levels is based on the majority type of charge carrier concentrations, causing the Fermi level to shift negative or positive from the middle of the energy band where dopant density for both electrons and holes is equivalent (i.e. the case of intrinsic semiconductor)[91]. On excitation, the

Fermi level splits into its quasi Fermi levels, i.e. quasi Fermi level for electrons (E_{fn}) and quasi Fermi level for holes (E_{fp}).

The photochemical investigation using $MV^{2+/\bullet+}$ as reported earlier is an accurate chemical probe method to determine the flat band potential (E_{fb}) of a semiconductor by identifying electron transfer from the quasi Fermi level for electrons (E_{fn}) of the semiconductor into the MV^{2+} redox couple as a function of pH [204, 245, 246]. When a semiconductor suspension with MV^{2+} is irradiated, the E_{fn} should equilibrate with Fermi level or redox potential of $MV^{2+,}$ i.e., -0.445 V (NHE) at a certain pH. Hence, the pH at which this equilibrium is achieved can be used to determine the flat band potential (E_{fb}) or the E_{fn} of the semiconductor (Figure 5.10).

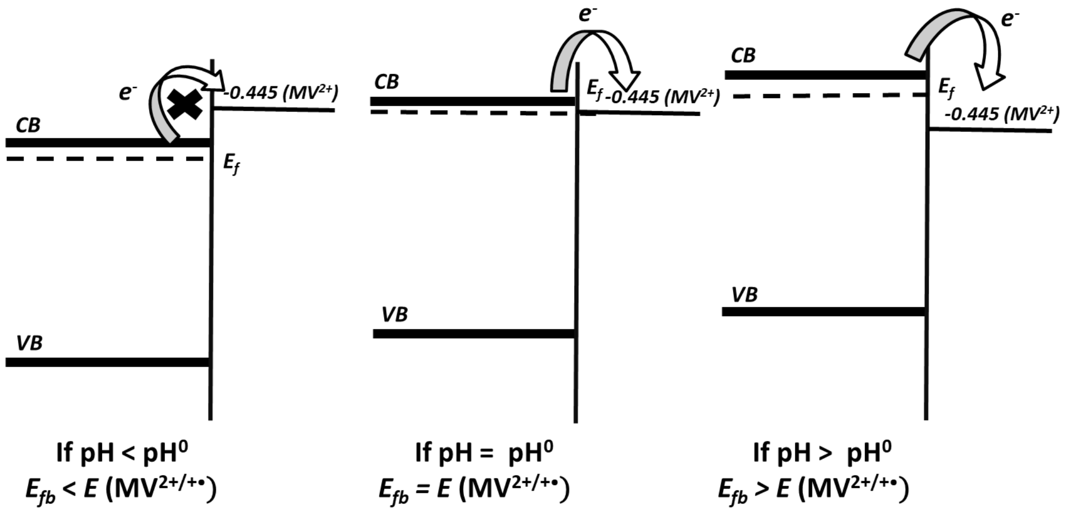

If pH < pH^0
$E_{fb} < E\ (MV^{2+/+\bullet})$

If pH = pH^0
$E_{fb} = E\ (MV^{2+/+\bullet})$

If pH > pH^0
$E_{fb} > E\ (MV^{2+/+\bullet})$

Figure 5.10 Fermi level and band edge potentials as a function of pH for MV^{2+} reduction, (case of typical n-type semiconductor)

The band edges of metal oxide semiconductors negatively shift upwards with the increasing pH, showing a Nernstian response (0.059 V/pH unit). Since the quasi Fermi level of electrons lies close to the CB edge, the E_{fn} is also affected with changing pH. Therefore, at particular pH (pH$^{\mathrm{o}}$) on irradiating the semiconductor in the presence of MV^{2+}, a reduction can take place when $E_{\mathrm{fn}} = E_{\mathrm{fb}} = E_{\mathrm{MV2+/+}} = -0.445$ V (NHE), i.e. when the photogenerated electron in the CB (or in the quasi Fermi level) is scavenged by MV^{2+} to reduce to $MV^{+}\bullet$ This transition can be detected by the characteristic blue colour of the suspension. Beyond this pH$^{\mathrm{o}}$, the E_{fn} (or E_{fb}) becomes more negative than $E_{\mathrm{MV2+/+,}}$ consequently enhancing the overpotential for the reduction reaction, ultimately leading to a faster electron reduction pathway, as desired in heterogeneous photocatalysis.

The value of flat band potential can be derived by equation 5.6 for the case of oxide as well as non-oxide semiconductors, [204, 245, 246] i.e.

$$E_{\mathrm{fn}}\ (\mathrm{pH} = 7) = E_{\mathrm{fb}}\ (\mathrm{pH} = 7) = E_{\mathrm{MV2+/+\bullet}} + 0.059(\mathrm{pH}^{o\,-}\ \mathrm{pH7}) \qquad 5.6$$

Where pH^o is the pH at which the electron transfer from the semiconductor (CB) to MV^{2+} takes place for the transition to $MV^{+\bullet}$ and $E_{\mathrm{MV2+/+\bullet}}$ = -0.445 V (NHE). Based on the above mechanism of $MV^{2+,}$ suspension of g-C_3N_4 and WO_3 nanoplates were tested against P25-TiO_2 (anatase-rutile mixture) and UV Hombikat TiO_2 (pure anatase) to observe the photocatalytic reduction of MV^{2+} to MV^+ under anaerobic conditions with changing pH from 5-14. With WO_3 and g-$C_3N_{4,}$ tested individually at low pH, no reduction of MV^{2+} to $MV^{+\bullet}$ was observed. No colour change was observed at higher pH for both either WO_3 or g-C_3N_4. With P25-TiO_2, initially at pH < 7 no transition to blue colour was observed, but at a $\mathrm{pH}^o = 7.26$ the reduction of MV^{2+} to $MV^{+\bullet}$ was observed, which on further increasing the pH intensified the blue colour of the solution. Similarly, for a pure anatase form of $TiO_{2,}$ i.e. UV Hombikat 100, the $\mathrm{pH}^o = 6.64$ was observed (where the transition to blue colour appeared).

By equation 5.6, the value of E_{fn} or the flat band potential for P25-TiO_2 was calculated to be -0.43 V (NHE) at pH 7.0, and for UV Hombikat-100, it was -0.46 V (NHE) at pH 7.0. An E_{fn} value of -0.01 V (NHE) at pH 0 (or -0.42 V,NHE at pH 7.0) for mixture of anatase:(3-5%) rutile TiO_2 and E_{fn} = -0.05 V(NHE) at pH 0 (or -0.46 V,NHE at pH 7.0) for pure anatase-TiO_2 was reported by Bard et al.(1983) in their study [245]. These values by Bard et al.(1983) are in agreement with the E_{fn} values obtained in the present work. The positive shift in value for P25-TiO_2 is due to the presence of rutile phase with a less negative CB potential. Unlike TiO_2, WO_3 has a relatively positive CB edge potential at pH 7 (-0.03 V (NHE)), and at pH 14 the potential would be close to the $E_{\mathrm{MV2+/+}} =$ -0.445 (NHE) but with no overpotential to drive the reduction, explaining why the methyl viologen system doesn't work with WO_3. The RNO degradation activity observed in the present of Ag^+ as electron acceptor (figure 5.6), was a confirmation of the positive CB edge of WO_3 which was negative enough to drive the reduction of Ag^+/Ag^0 (0.8 V, NHE) via 1 electron reduction at a neutral pH (distilled water pH~6-7) but was not negative enough to reduce MV^{2+} to $MV^{+\bullet}$ (-0.445 V, NHE) at pH 7. Also, based on the pzc of WO_3 at such high pH levels, the dissolution of WO_3 takes place, making it highly unstable for any reaction. While g-C_3N_4 has been widely reported to have a very negative CB potential (-1.13 V (NHE)) for photocatalytic reduction reactions, no reduction of methyl viologen was observed (-0.445 V (NHE)) suggesting that the photoexcited electrons are trapped in states with less negative electrochemical potentials. g-C_3N_4 is a non-oxide semiconductor, and so it's not expected to follow a Nernstian response (0.059 V/pH unit) in negative band shifting. However, a shift in flat band potential with pH for different g-C_3N_4 solids (protonated, regenerated, bulk, etc.) has been reported through electrochemical measurements by Zhang et al.(2010) which do not obey a Nernstian response [155]. Also, the technique of MV^{2+} reduction has been tested with pH shifting for other semiconductors such as CdS. Therefore, it should be a suitable technique to identify the flat band potential for organic semiconductors system such as g-C_3N_4 that show a shift in the flat band by protonation of the surface as per investigation of Zhang et al.(2010) The limited electron transfer from g-C_3N_4 to MV^{2+} at higher pH is counter-intuitive to its reported reduction potential $E > -1.0$ V (NHE) when compared to TiO_2 that has the CB edge lower than g-C_3N_4 and still manages to perform the methyl viologen reduction as shown in figure 5.11.

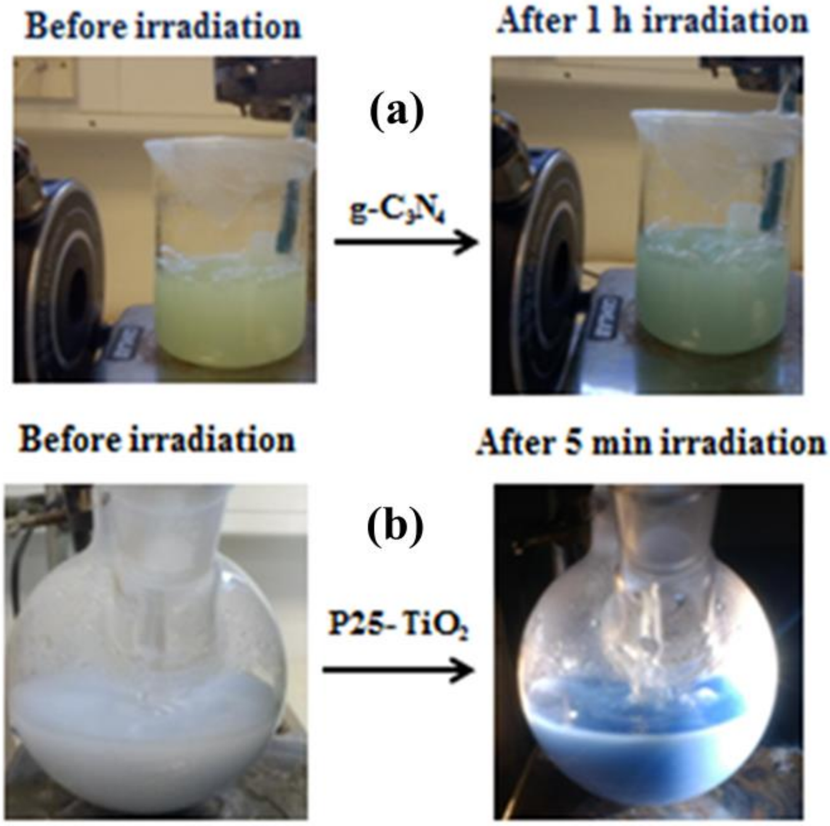

Figure 5.11 Methyl viologen reduction under UV-Vis irradiation using (a) g-C_3N_4 and (b) P25-TiO_2

The methyl viologen system has mainly been reported for investigating heavily doped semiconductors, where there is not much difference between the quasi-Fermi level of electrons (E_{fn}) and the conduction band edge and CB = E_{fn}. However, in systems with lower dopant density, the Fermi level is located in the middle of the forbidden gap. In such cases, this technique can indicate the electrochemical potential of the quasi-Fermi level of electrons with respect to the MV^{2+} reduction potential. In photocatalysis, under irradiation, any transfer of electrons or recombination are thermodynamically downhill processes [254]. Based on this mechanism, the electron transfer from the LUMO of g-C_3N_4 to $MV^{2+/+\bullet}$ should be thermodynamically achievable, but this was not observed. The g-C_3N_4 showed a low rate of reaction for RNO oxidation in the presence of Ag^+ as an electron acceptor and limited MV^{2+} reduction. Therefore, it must be concluded that electron transfer from g-C_3N_4 to the solution is not efficient. Reasons for this might be a short lifetime of electrons in the LUMO or trapping of electrons in a surface state present at a much lower energy in the g-C_3N_4 [232, 233] or an intrinsic type behaviour of g-C_3N_4 with the Fermi level placed in approximately middle of the bandgap [185].

5.4.4 Optical and electronic properties of WO_3 and g-C_3N_4

The energy band diagrams of WO_3 and g-C_3N_4 were determined based on their optical and electronic characterisation.

5.4.4.1 Optical band gap

The apparent UV-Vis absorption of the materials using diffuse reflectance spectrum (DRS) is shown in figure 5.12. The apparent absorption can be calculated from the diffuse reflectance spectrum by applying a logarithmic function to the obtained reflectance (R_∞) i.e. Apparent absorbance = $\log(1/R_\infty)$. The WO_3 nanoplates show the expected absorption range from UV to visible region, with a wide absorption edge around 390 nm extended tail up to 460 nm. In contrast, g-C_3N_4 presented a lower absorption edge around 310 nm in the UV region and second edge around 380 nm arising from the π-π* transition, with an extended tail region from 430 nm to 500 nm. This tail is assigned as the lone pair (n) to π* transitions in g-C_3N_4 [233]. According to Jorge et al.(2013), this lone pair (n) arises from terminal N-atom (NH-) in g-C_3N_4 that are forbidden in perfect symmetrical heptazine units of g-C_3N_4 but become allowed if some distortion develops within the structure [255]. The visible absorption of g-C_3N_4 is suggested to be due to n- π* transitions. It was observed that the absorbance intensity for g-C_3N_4 was lower in the visible region as compared to the sharp intensified absorption for WO_3. By overlapping the spectral emission of the light source used in photocatalytic experiments (blackline is figure 5.12), we can see the optical absorption of both materials extending from UVB to the violet-blue region (300-460 nm) of the visible light spectrum.

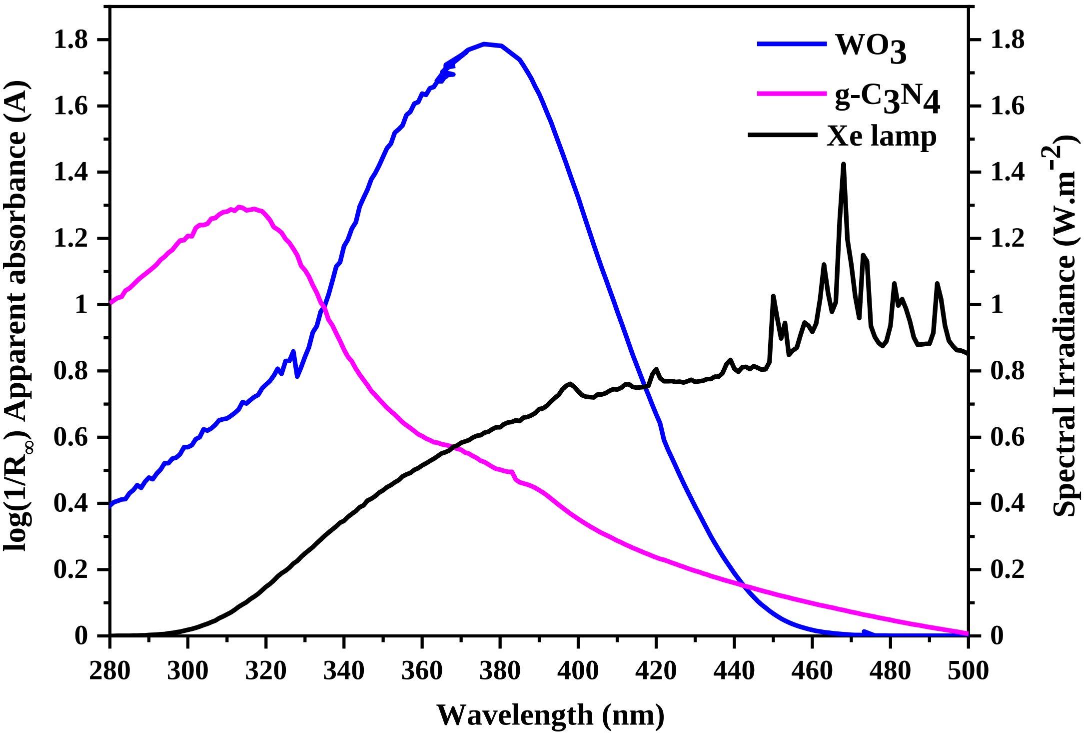

Figure 5.12 Apparent absorbance spectrum for WO_3 and g-C_3N_4 overlapping the spectral intensity of the light source used in the study.

The optical energy band gap for WO_3 nanoplates and the corresponding HOMO-LUMO (H-L) gap for g-C_3N_4 were obtained to be 2.68 eV and 2.72 eV, respectively, as shown in figure 5.13. The bandgap estimation was done based on the Tauc plot following equation 5.7

$$F(R_\infty)=\frac{(1-R_\infty)^2}{2R_\infty} \qquad 5.7$$

Where $F(R_\infty)$ is the Kubelka-Munk function that can be calculated using the reflectance (R_∞) from the diffuse reflectance spectrum. The K-M function is also proportional to the extinction coefficient (α). Following the type of electronic transition (n) occurring within a semiconductor the bandgap energy (eV) can be estimated in proportion to the K-M function ($F(R_\infty)$) as $(F(R_\infty))*h\nu)^{1/n}$ against the energy hν (eV) as per Lopez et al.(2012)[249]. Since, both WO_3 and g-C_3N_4 followed an indirect allowed transition with n = 2. The experimentally obtained optical bandgap in our studies for both WO_3 and g-C_3N_4 has been observed and confirmed equivalent to the theoretical estimations reported in the literature as per the density functional theory calculations. The value of 2.72 eV for g-C_3N_4 is correspondent of its hexagonal g-h heptazine structural unit [151, 153] and 2.68 eV for WO_3 have been referred to as the room temperature monoclinic phase of WO_3 [256].

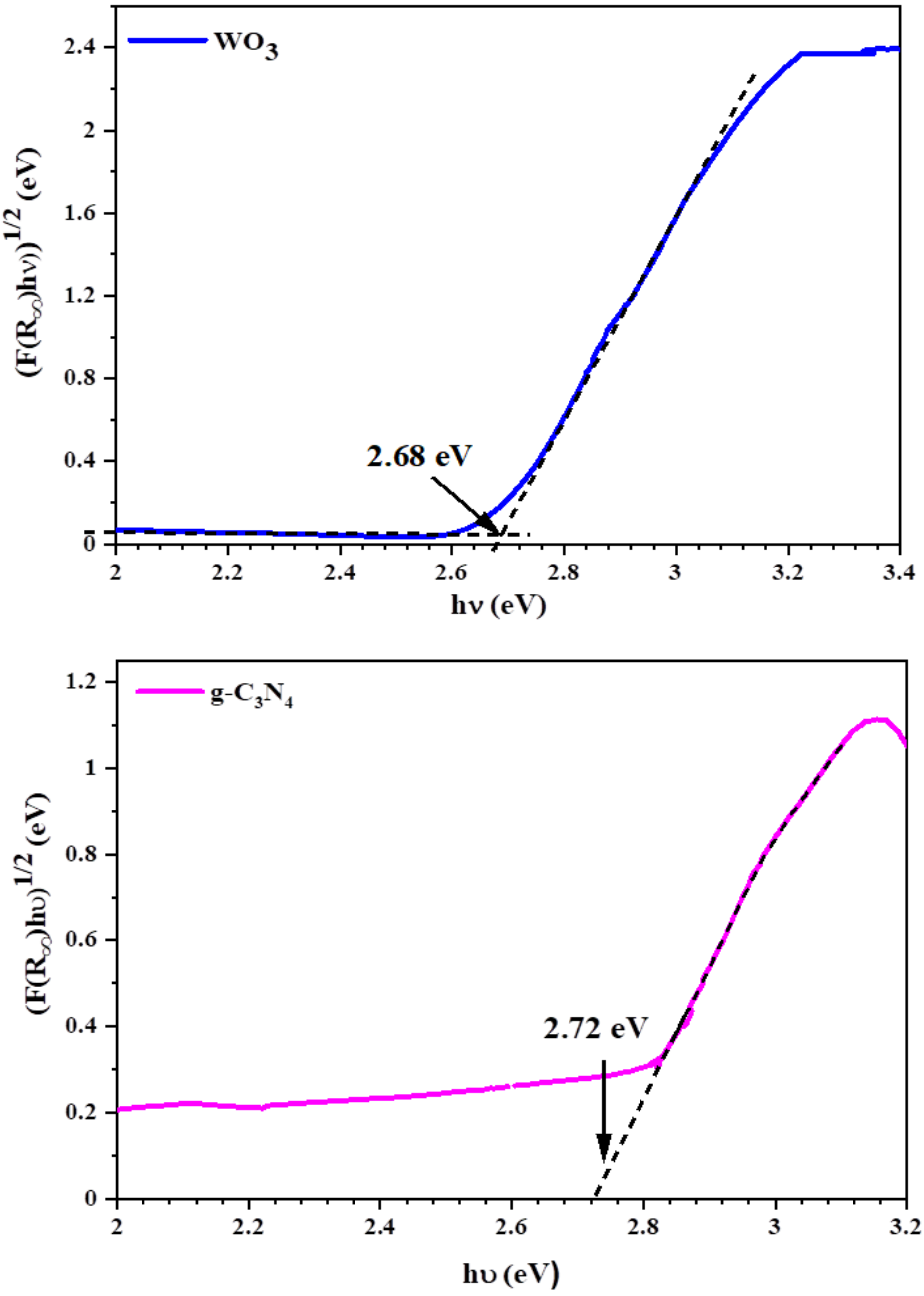

Figure 5.13 Tauc plot for WO_3 and g-C_3N_4

5.4.4.2 XPS analysis

The energy states of semiconductors can be identified by photoelectron spectroscopy such as XPS or UPS. According to Miller et al.(2016) using the XPS or UPS measurements, we can determine the photoelectron intensity onset closest to the Fermi level, by corroborating the photon energy emitted from the electrons in the VBM or the HOMO, i.e. highest occupied molecular orbital [257]. In this case, the valence band maxima position is reported with respect to the Fermi level, i.e. (E_f - E_{VBM}) or in the absolute vacuum scale as the ionisation energy (IE). Lohaus et al.(2017) recently termed the difference of E_{VBM} to E_f measured through VB XPS as an electronic bandgap of the material. They emphasized on using the energy difference obtained through VB XPS to be the true electronic bandgap, instead of the optically determined bandgap [247]. According to them, the electronic bandgap measured through VB XPS is a crucial determinant of the effective band position in any materials where Fermi level can be pinned due to formation of polaron states during optical excitation of the semiconductor. The valence band maxima of the materials were determined through VB XPS and are shown in figure 5.14. An E_{VBM} - E_f value of 2.46 eV for WO_3 and 1.88 eV for g-C_3N_4 was obtained with respect to the intercept at the binding energy scale [165]. A valence band offset of 0.58 eV was calculated between the VBM of WO_3 and g-C_3N_4, with WO_3 having more positive VBM than g-C_3N_4. A redshift of 0.56 eV and 0.16 eV was observed for the E_f - E_{VBM} values of WCN(14) pH2.25 and WCN91 samples with respect to WO_3. Interestingly the experimentally obtained redshift in case of WCN14 sample was equivalent to the calculated energy difference between the valence band offset of WO_3 and g-C_3N_4 before contact, i.e. 0.58 eV, possibly indicating no or limited charge transfer on contact as a heterojunction. Whereas the redshift of 0.16 eV was observed for WCN91 and a less positive VBM than WO_3. This was achievable if the two systems on contact reach a thermodynamic equilibrium by electron transfer from one material to another, and their respective Fermi levels (E_f) are adjusted to each other by bending bands.

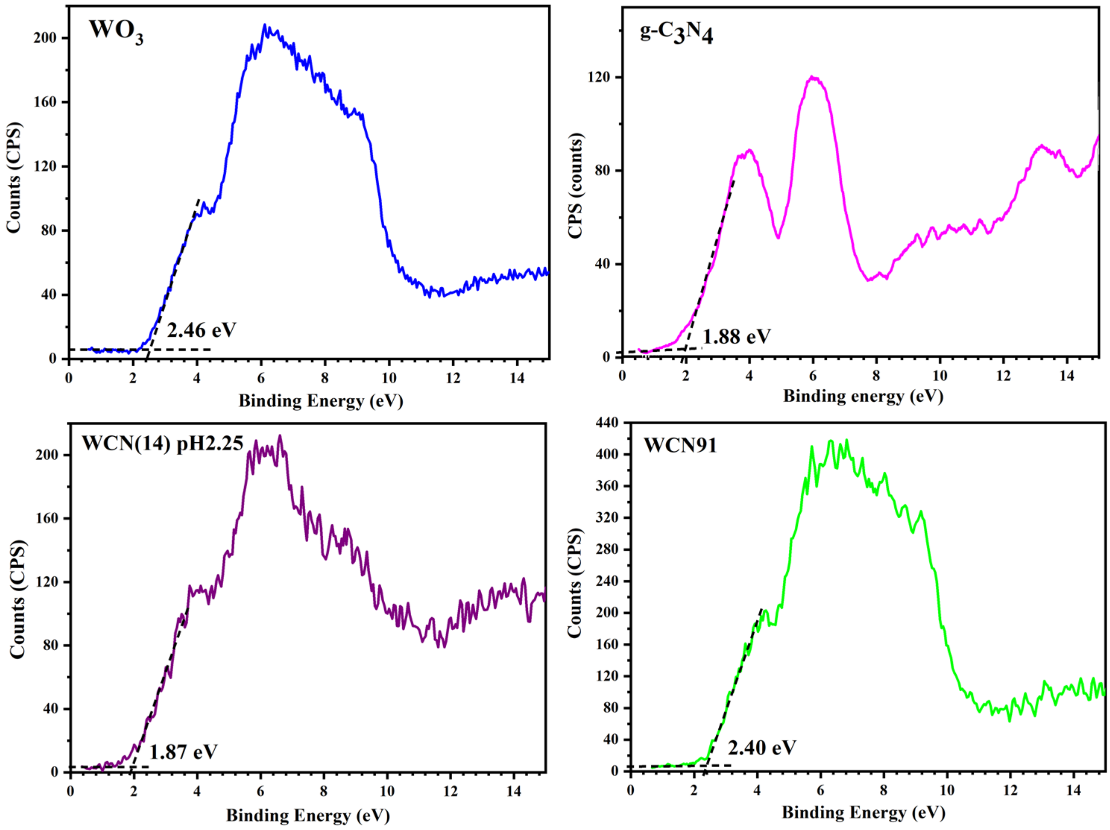

Figure 5.14 VB XPS measurements for WO$_3$, g-C$_3$N$_4$ and WO$_3$/g-C$_3$N$_4$ heterostructures.

An energy band diagram for the individual materials before contact is presented in figure 5.15, displaying the energy difference obtained from the optical bandgap and electronic bandgap. Now, if optical bandgap (E_g) is considered the difference between the top of the E_{VBM} and bottom of E_{CBM} and electronic bandgap as per Lohaus et al.(2017) [247], is determined as E_f - E_{VBM}, then, the difference between E_f - E_{CBM} can also be calculated as per equation 5.8,

$$(E_f - E_{CBM})\,(\text{eV}) = E_g - (E_f - E_{VBM}) \qquad 5.8$$

i.e. (E_f - E_{CBM}) = 0.22 eV for WO$_3$ and (E_f - E_{CBM}) = 0.84 eV for g-C$_3$N$_4$. WO$_3$ is an n-type semiconductor; however, its polarity can be altered by introducing oxygen vacancies. Its Fermi level should be below and practically merging with the bottom of the CB. Therefore, the energy difference value of 0.22 eV is realistic. While, on the other hand, an energy difference of 0.84 eV obtained for g-C$_3$N$_4$, reveals the Fermi level for g-C$_3$N$_4$ to be situated well below the LUMO. To note in case of g-C$_3$N$_4$, the energy difference E_f - E_{CBM} < E_f - E_{VBM}, i.e. 0.84 eV < 1.88 eV suggesting g-C$_3$N$_4$ not to be heavily doped n-type or p-type. The obtained result was contrary to the results of Zhan et al.(2015)[99], Chen et al.(2017) [94] and Zhang et al.(2010)[154] who reported an n-type characteristic of g-C_3N_4 based on the positive slope and a flat band potential value of $E_{fb} > -1.0$ V (NHE) obtained through Mott Schottky plots.

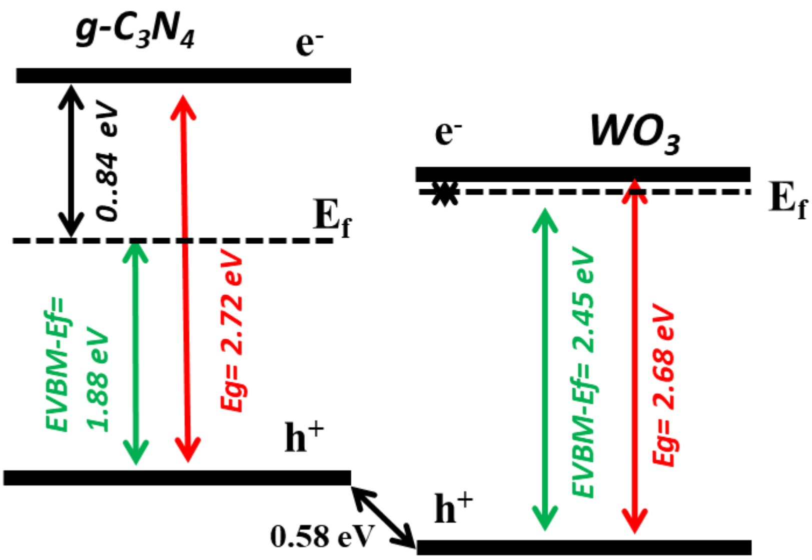

Figure 5.15 Band structure diagram for individual WO_3 and g-C_3N_4 (before contact as heterojunction) based on optical and VB-XPS energy difference

The surface chemical states of the prepared WO_3/g-C_3N_4 heterostructures along with their analogue WO_3 and g-C_3N_4 were studied by X-ray photoelectron spectroscopy (XPS). The binding energies of the elements were calibrated against C1s at 284.8 eV. The XPS survey spectra for all 5 samples reporting W4f, C1s, N1s, and O1s are shown in figure 5.16. In pristine WO_3, only carbon, tungsten and oxygen peaks were identified. For g-C_3N_4 after quantification, the main elements were carbon, nitrogen, and oxygen to some extent. The atomic percentage of each element is shown in table 5.3. The C1s atomic percentage in all samples is inclusive of the adventitious carbon peak at 284.8 eV alongside the various carbon bonding configurations of g-C_3N_4. In sample WCN91, where only 10% weight ratio of g-C_3N_4 is present in the mixture, a low-intensity signal of N1s was observed with an atomic % equivalent to 0.64%. The C1s satellite peak at 284.8 eV in WCN91 comprises of an 85.26% the total atomic %. To understand the contribution of each element towards heterostructure formation, narrow scan spectra for all elements C1s, N1s, W4f, and O1s were also performed.

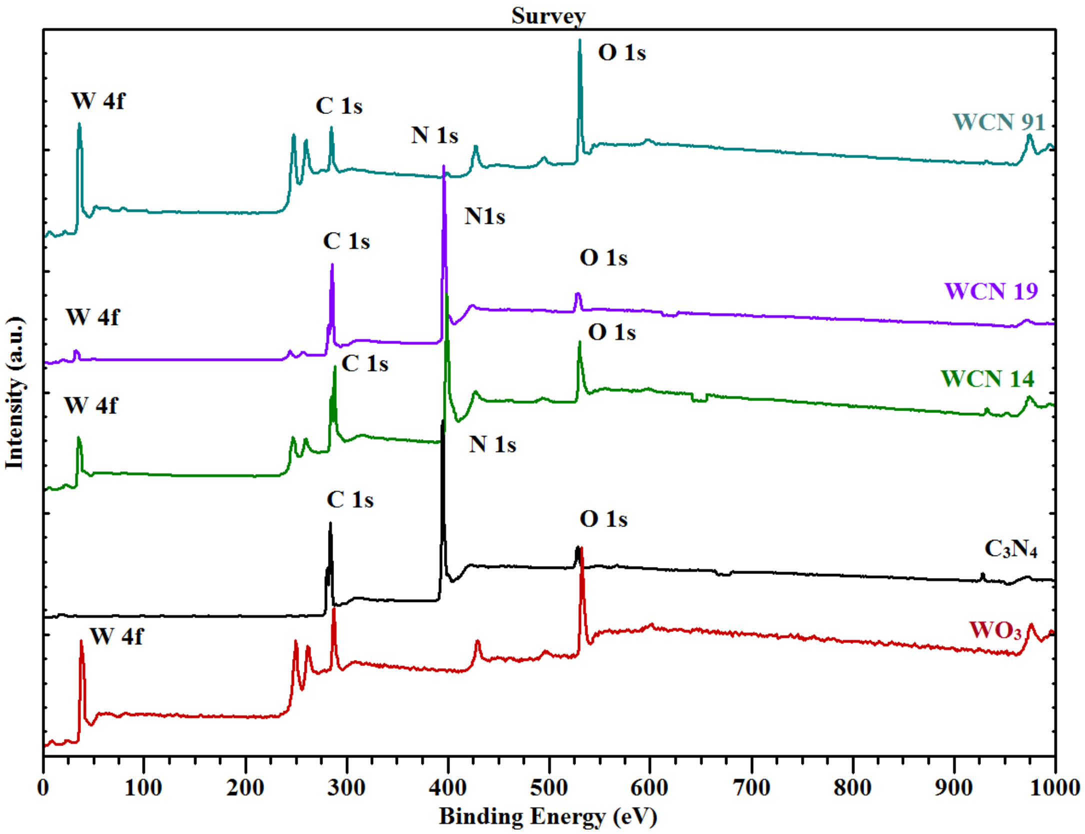

Figure 5.16 XPS survey scan for synthesized photocatalysts.

Table 5.3 Atomic % of each element present in WO_3/g-C_3N_4 heterostructures

	Atomic %			
	C%	**N%**	**O%**	**W%**
WO_3	60.36	-	34.77	4.87
g-C_3N_4	55.15	40.47	4.37	-
WCN(1:9)	49.45	44.45	5.46	0.64
WCN(1:4)	49.14	37.37	11.03	2.45
WCN(9:1)	85.26	0.64	8.87	5.22

The structural configuration of g-C_3N_4 with the simplest dimer formation consists of 2 carbon stoichiometry, i.e. C1, C2 and 4 nitrogens, i.e. N1(sp^2 hybridised; C-N=C), N2 (edge; N-H), N3(sp^3 hybridised central nitrogen; N-C3) and N4 (terminal; NH_2)[198]. The terminal N4 is responsible for linking the infinite chain of polymers in g-C_3N_4 and consists of a lone pair of electrons. The polymerization of g-h heptazine unit takes place by replacing the N4 with N2 in every monomer unit along the polymeric chain axis. Therefore, any change observed in the ratio of N2 to N4 before and after heterostructure will be attributed as a structural change in the parent g-h heptazine unit of g-C_3N_4. On deconvoluting the narrow scan spectrum of N1s for all samples, various atomic % configurations i.e. N1,N2,N3 andN4 were observed as shown in figure 5.17. Changes in the nitrogen bonding percentages of the samples after heterostructure formation has been illustrated in table 5.4. No source of N was found in WO_3. Therefore it is not included in the table. For the synthesized g-C_3N_4, all N1 to N4 signals were observed at the expected positions. In WCN91, the main N signals detected were the edge N2 and bridging/terminal N4. The N1 was not found relative to the parent g-C_3N_4 sample. Only 2.09% of N3 (central nitrogen) percentage was observed as compared to 11.5 % in the parent g-C_3N_4. This significant change was suggestive of damage to the base of the tri-s-triazine unit. The deconvoluted N4% in the heterostructure WCN91 was increased as compared to only g-C_3N_4, suggesting the shortening of the polymeric chain of g-C_3N_4. The unexpected increase in weight percentage of both N2 and N4 in the heterostructures and reduction of N3 and N1 was presumed to be as the destruction in the periodicity of g-C_3N_4, after thermal treatment at 400°C during heterostructure formation. A similar result was reported by Pomilla et al.(2018), where a thermal treatment of pre-synthesized g-C_3N_4 in an oxygen atmosphere, lowered the N1 ratio and increased the N2 and N4 content [198]. Their research concluded as the thermal oxygen treatment of g-C_3N_4 lead to a structural deformation with oxygen replacing the N1. In this case, a small percentage (2.8%) of tungsten nitride (W-N) formation was also observed in WCN91 sample at binding energy 397.4 eV in N1s narrow scan spectrum (figure 5.17). The formation of W-N bonds in literature have been reported as dissociative adsorption of the N-H radicals on the tungsten surface under heat treatment [258].

Table 5.4 Contribution from different nitrogen species based on deconvolution of N1s narrow scan spectrum with respect to the binding energy

	N1s									
	N1(C-N=C)		N2(N-H)		N3(N-C3)		N4(N-H2)		N π-π	
	BE (eV)	Area %	BE (eV)	Area %	BE (eV)	Area %	BE (eV)	Area %	BE (eV)	Area %
g-C_3N_4	398.6	15.5	398.9	55.8	400.1	11.6	401.2	13.0	404.3	4.1
WCN14	398.6	25.9	399.1	27.2	399.8	36.5	401.4	6.5	404.5	3.9
WCN91	-		399.3	63.4	400.6	2.1	401.5	31.7	-	

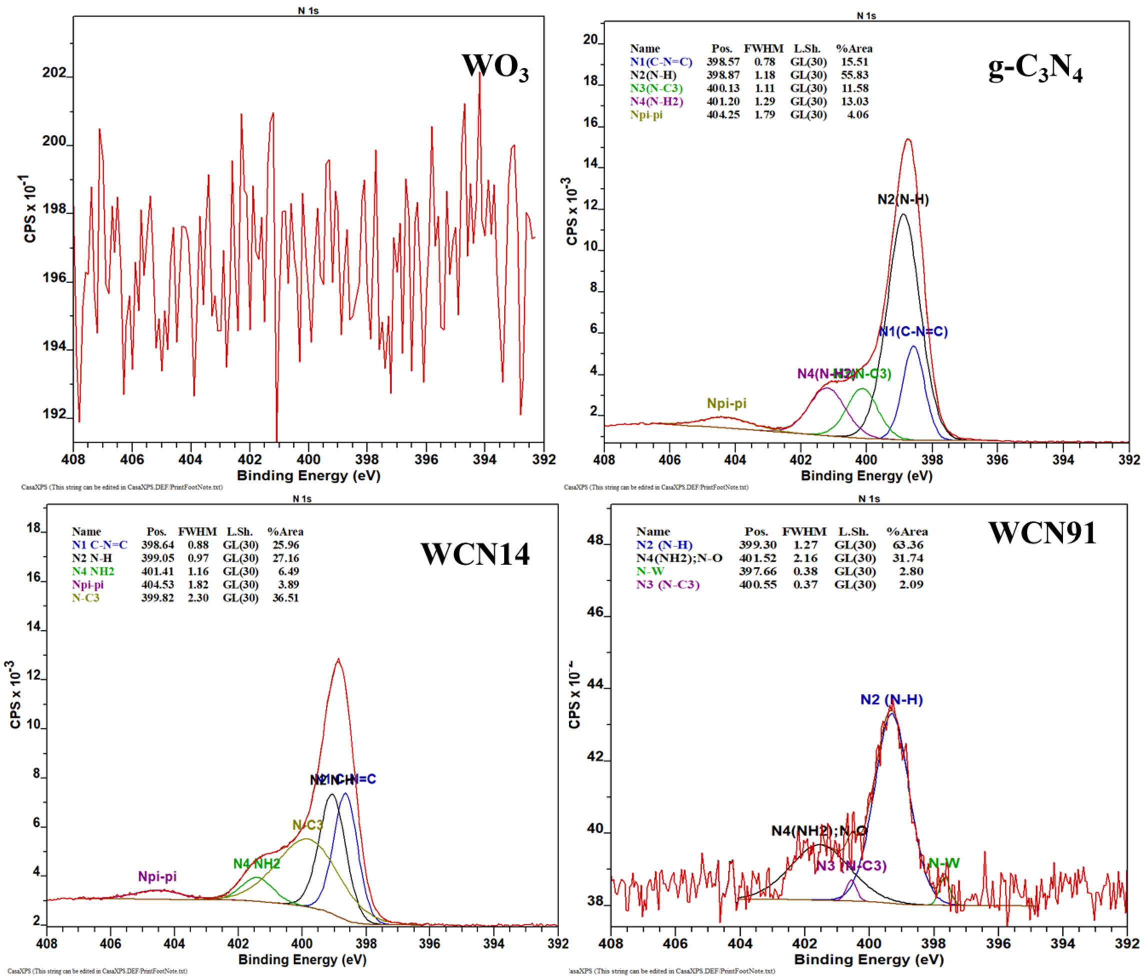

Name	Pos.	FWHM	L.Sh.	%Area
N1(C-N=C)	398.57	0.78	GL(30)	15.51
N2(N-H)	398.87	1.18	GL(30)	55.83
N3(N-C3)	400.13	1.11	GL(30)	11.58
N4(N-H2)	401.20	1.29	GL(30)	13.03
Npi-pi	404.25	1.79	GL(30)	4.06

Name	Pos.	FWHM	L.Sh.	%Area
N1 C-N=C	398.64	0.88	GL(30)	25.96
N2 N-H	399.05	0.97	GL(30)	27.16
N4 NH2	401.41	1.16	GL(30)	6.49
Npi-pi	404.53	1.82	GL(30)	3.89
N-C3	399.82	2.30	GL(30)	36.51

Name	Pos.	FWHM	L.Sh.	%Area
N2 (N-H)	399.30	1.27	GL(30)	63.36
N4(NH2);N-O	401.52	2.16	GL(30)	31.74
N-W	397.66	0.38	GL(30)	2.80
N3 (N-C3)	400.55	0.37	GL(30)	2.09

Figure 5.17 N1s narrow scan XPS spectrum for all the samples

The W4f narrow scan of the synthesized photocatalysts is shown in figure 5.18. The structural configuration of WO_3 consists of W=O bonds, with W^{6+} as primary oxidation state represented by binding energies 35.12 eV ($W4f^{7/2}$) and 37.26 eV ($W4f^{5/2}$). Another doublet peak corresponding to W^{5+} oxidation state was also observed at a percentage of 0.68% at 33.83 eV and 1.59% 35.97 eV. No signals of W4f were observed in g-C_3N_4 apart from impurity peaks due to sampling contamination by consecutive runs along with the other heterostructure samples. For WCN91, W^{6+} doublet was red-shifted by 0.3 eV as compared to only WO_3. A new peak positioned at 34.33 eV appeared in WCN91 sample after heat treatment at 400°C with g-C_3N_4. This peak is referred to as the W^{4+} state formation in the tungsten nitride bond.

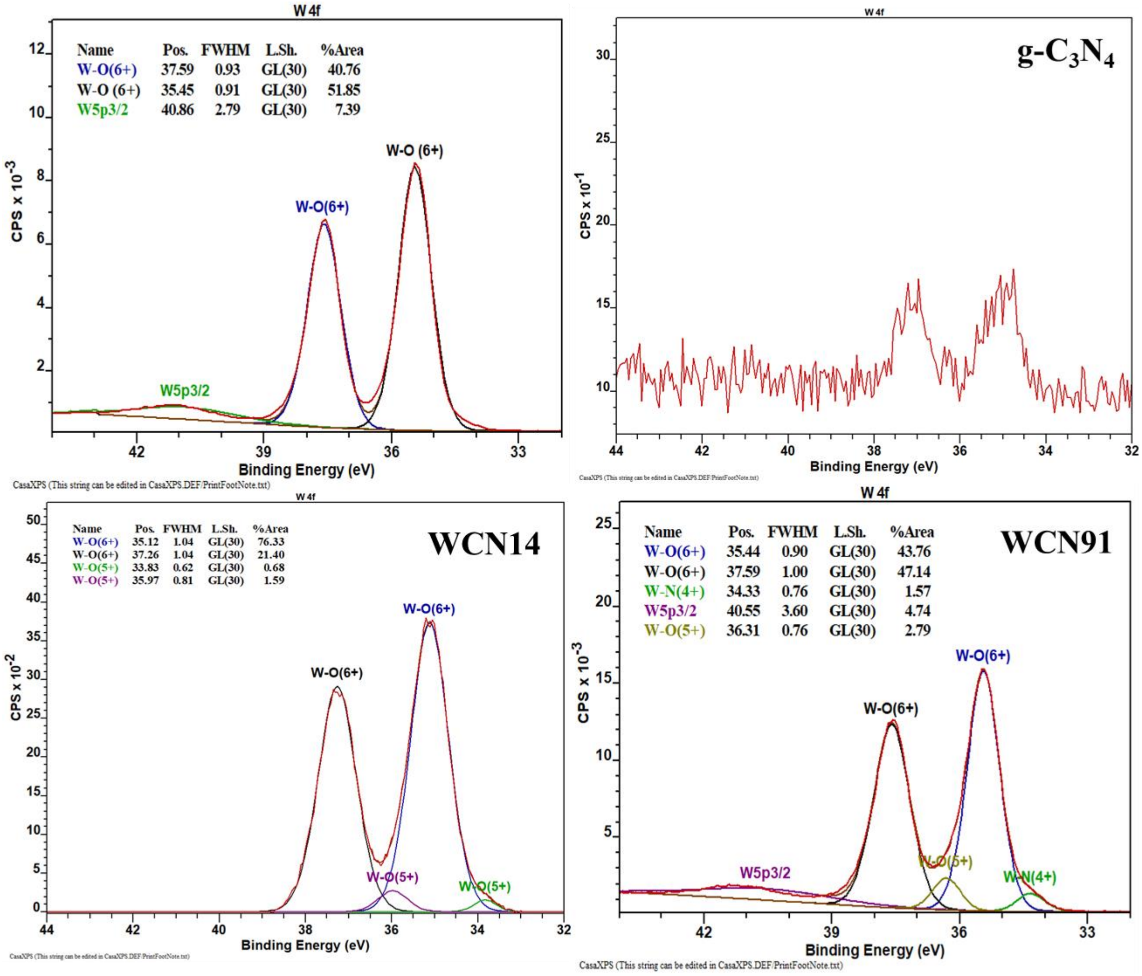

Name	Pos.	FWHM	L.Sh.	%Area
W-O(6+)	37.59	0.93	GL(30)	40.76
W-O (6+)	35.45	0.91	GL(30)	51.85
W5p3/2	40.86	2.79	GL(30)	7.39

WCN14

Name	Pos.	FWHM	L.Sh.	%Area
W-O(6+)	35.12	1.04	GL(30)	76.33
W-O(6+)	37.26	1.04	GL(30)	21.40
W-O(5+)	33.83	0.62	GL(30)	0.68
W-O(5+)	35.97	0.81	GL(30)	1.59

WCN91

Name	Pos.	FWHM	L.Sh.	%Area
W-O(6+)	35.44	0.90	GL(30)	43.76
W-O(6+)	37.59	1.00	GL(30)	47.14
W-N(4+)	34.33	0.76	GL(30)	1.57
W5p3/2	40.55	3.60	GL(30)	4.74
W-O(5+)	36.31	0.76	GL(30)	2.79

Figure 5.18 W4f narrow scan XPS spectrum for all the samples

On deconvoluting the C1s peak for all samples, changes in the carbon region were also observed on heterostructure formation. Figure 5.19 demonstrates a comparison of the deconvoluted C1s peaks of the samples. The changes in the weight percentage of the components are tabulated in table 5.5 for comparison. A noticeable increase in the C-C and C-OH components was observed in WCN91 sample as compared to g-C_3N_4. No sign of C1s peak was found in WCN91.

Table 5.5 Contribution from different carbon species based on deconvolution of C1s narrow scan spectrum with respect to the binding energy

	C 1s							
	C-C		C-OH		C1		C2	
	BE (eV)	Area %	BE (eV)	Area %	BE (eV)	Area %	BE (eV)	Area %
g-C_3N_4	284.8	27.8	286.2	4.9	288.2	49.3	288.7	10.3
WCN14	284.8	28.0	285.5	14.6	288.4	43.6	288.9	11.3
WCN91	284.8	69.7	286.0	21.2	-		288.9	9.1
WO_3	284.8	80.4	286.4	12.3	-		-	

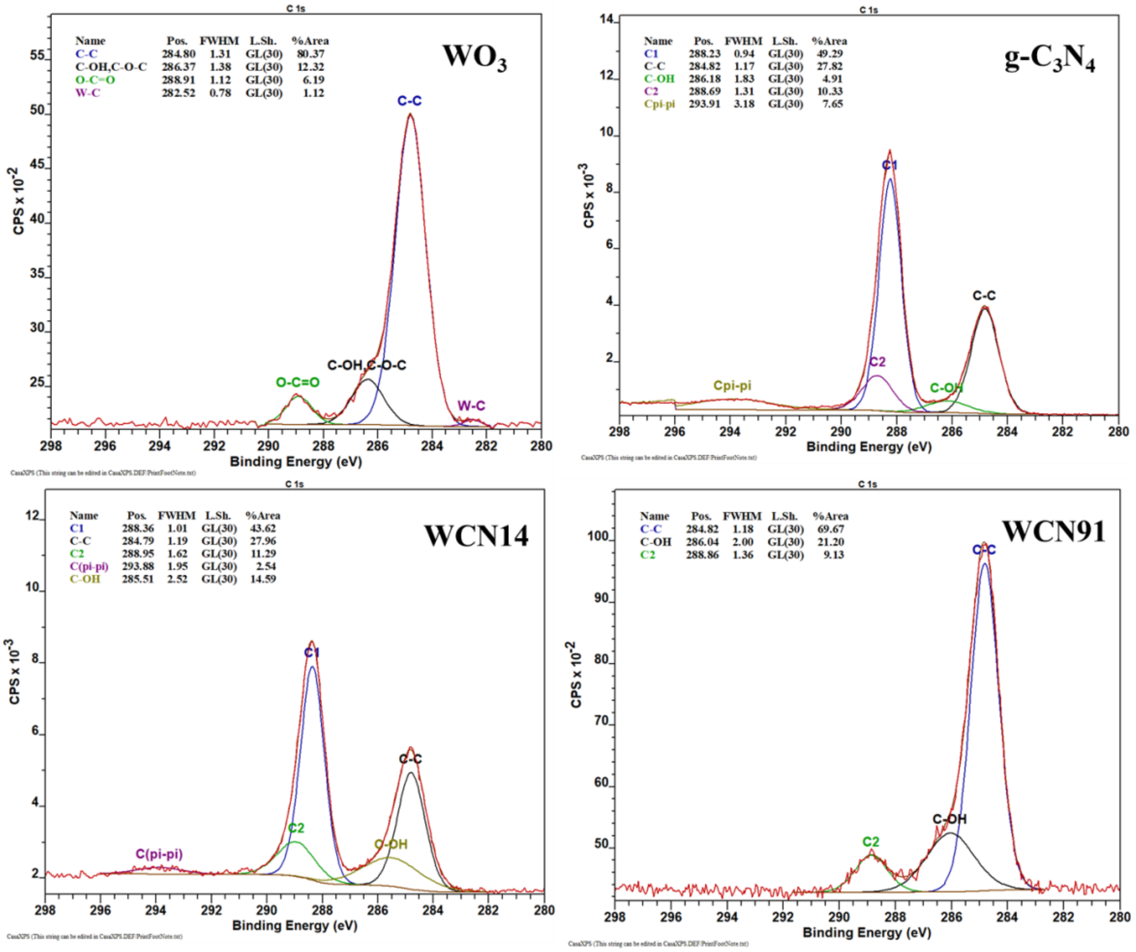

Figure 5.19 C1s narrow scan XPS spectrum for all the samples

However, the oxygen content (O1s) was seen to be equivalent throughout the runs of the individual as well as heterostructures, as shown in figure 5.20. The absorbed water (OH) was observed in all cases around 532.2 ± 0.2 eV. The lattice oxygen (O-C-N) content of 26% was observed in WCN91 sample because of thermal treatment of g-C_3N_4, and no trace of H_2O was found. The content of oxygen bonded with W surface i.e. W-O was similar in both WO_3 and WCN91, i.e. 72.76 % and 73.92 % respectively.

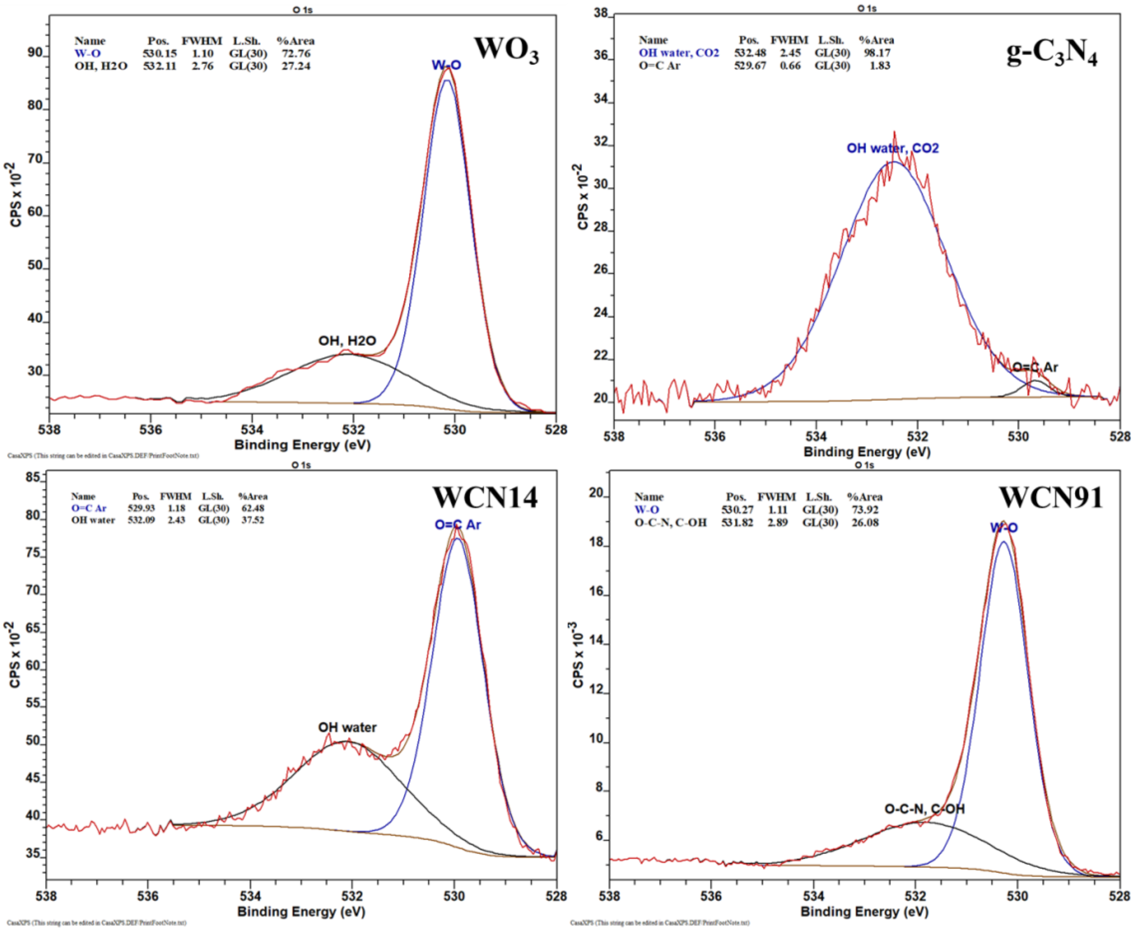

Figure 5.20 O1s narrow scan XPS spectrum for all the samples

The limited photocatalytic activity of g-C_3N_4 for reduction of MV^{2+} and generation of $^{\bullet}OH$ radicals through reductive route could be attributed due to its middle structural deformation during heat treatment and a much lower Fermi level energy as per the energy difference obtained from VB XPS measurements. The photophysical process of g-C_3N_4 has not been explored in detail. We know it is an organic semiconductor and has a structural configuration similar to a conjugated polymer. But what is still unknown is the photoexcitation process, i.e. if on irradiation it generates free excitons like inorganic doped semiconductors such as TiO_2, WO_3 or it generates excitons bound to defects. A further investigation was carried out to observe the excitation of charge carriersand to understand if any trapping of charge carriers takes place on emission that might affect the photocatalytic activity.

5.4.4.3 Photoluminescent properties

The photoluminescence properties of g-C_3N_4, WO_3 and WO_3/g-C_3N_4 heterostructure WCN19 were investigated on excitation of irradiation wavelength of $\lambda = 330$ nm. The corresponding luminescent emission intensities are measured as a result of the electronic excitation and relaxation processes occurring within a semiconductor. They are proportional to the recombination of the photogenerated electron-hole pairs. In the traditional cases of good photogenerated charge separation and migration, a lower PL emission intensity is to be observed.

From figure 5.21, the PL intensity for WCN19 was seen to be stronger than the parent materials g-C_3N_4 and WO_3, indicating several recombinations taking place within the heterostructure system. Both WCN19 and g-C_3N_4 display a sharp emission around 430 nm, whereas with WO_3 negligible emission was observed. The inset graph in figure 5.21 shows an emission for WO_3 with the intensity 1/20th of its counterpart g-C_3N_4 and WCN19.

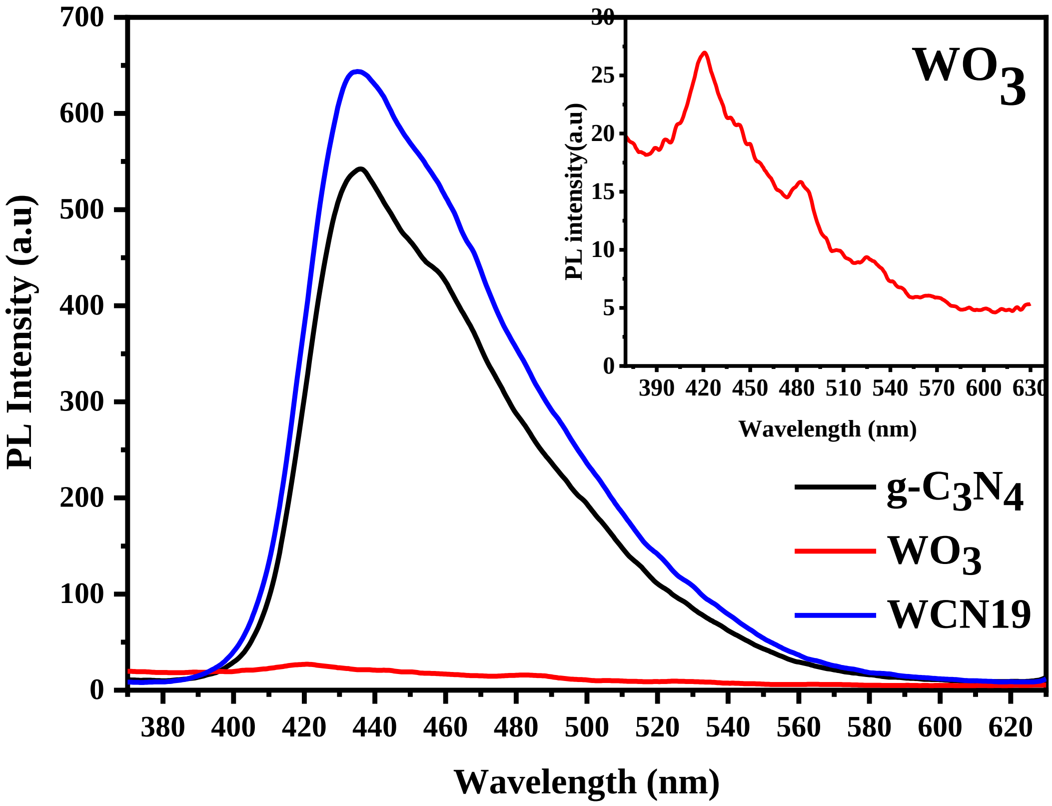

Figure 5.21 Photoluminescence spectra with emission peaks for the tested samples; Inset: scan for WO_3 nanoplates emission spectrum.

On deconvoluting the individual PL intensities of all the samples, strong PL emissions were observed for g-C_3N_4 (figure 5.22) with 3 deconvoluted peak emissions at 430, 453 and 481 nm. These broad emissions correspond to 2.88, 2.73 and 2.57 eV in energy scale. The PL emission peaks observed in g-C_3N_4 are caused by multiple transitions taking place consisting of conjugated states and the lone pair of tertiary N atom, i.e. N-atom bridging two tri-s-triazine units [233, 255, 259]. The broad PL peak observed at 453 nm corresponding to the H-L gap (2.72 eV) of g-C_3N_4 is a result of emission from the band edges of g-C_3N_4. Durrant et al.(2017) also reported the PL peak centred at 2.8 and 2.5 eV [233], by following a deconvolution with 2 Gaussian fitted peaks. The similar peaks were observed in the present study with peak centres at 430 nm (2.88 eV) and 481 nm (2.57 eV). The high PL peak at 430 nm(~2.8 eV) was attributed to as transition between HOMO of g-C_3N_4 and intraband lone pair (LP)of the bridging N atom [233, 260] whereas the peak at 481 nm (2.57 eV) was denoted as an interband lone pair state of the bridging N atom of g-C_3N_4 [260].

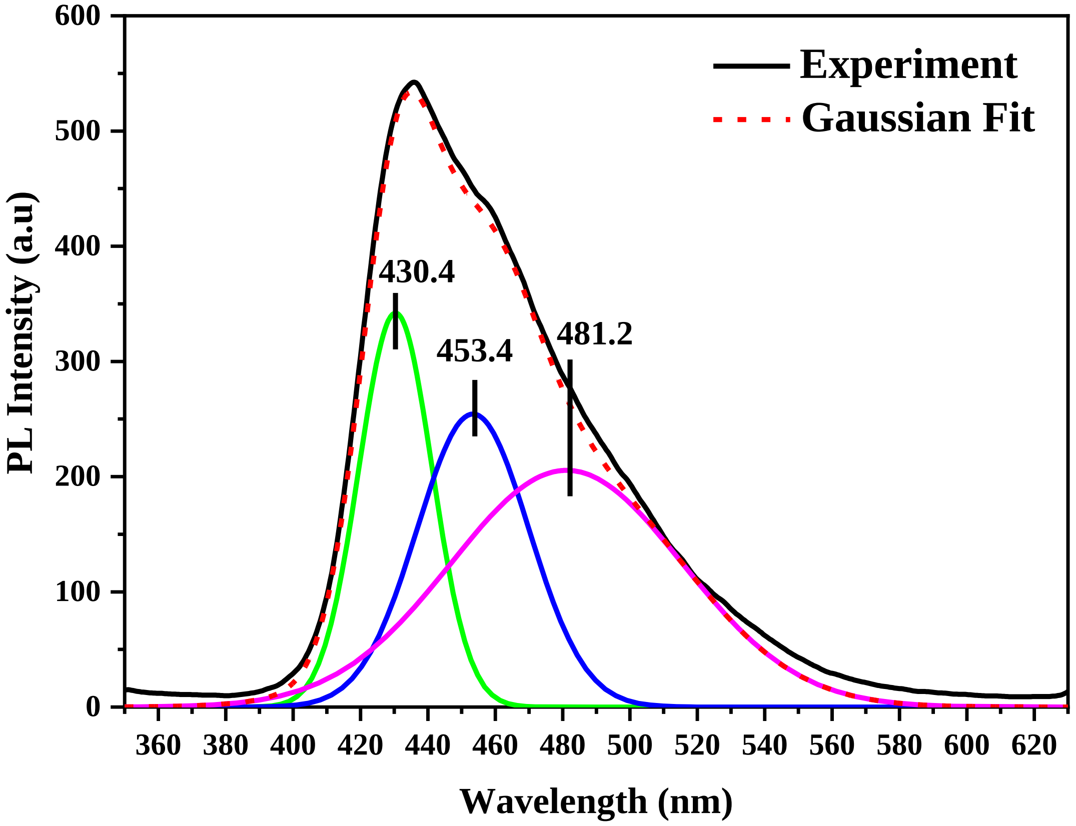

Figure 5.22 Deconvoluted photoluminescence spectrum of g-C_3N_4 with Gaussian fit

A similar emission was observed in the WCN19 sample upon deconvolution (figure 5.23). A shift of 5 nm was observed in WCN19 samples for emission peak that initially appeared at 430 nm. A minor redshift of 0.03 eV (2.88 to 2.85 V) and 19% increase in the deconvulated peak area was observed for the heterostructure as compared to g-C_3N_4. The redshift and increased peak area could be due to charge trapping at the intraband LP state, which is situated below the absorption band edges of g-C_3N_4 [233]. The trapped charges in this state have been reported to have a longer lifetime of microseconds, and they are mostly unreactive trapped electrons limiting the photocatalytic activity of g-C_3N_4.

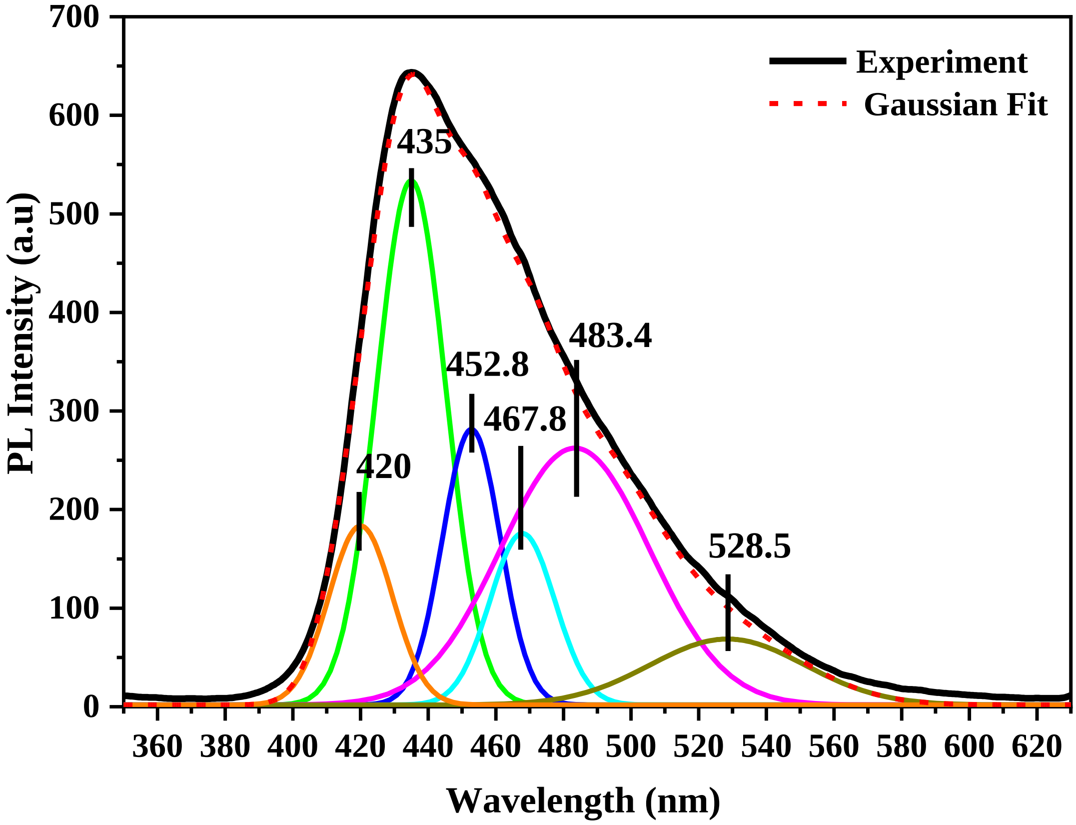

Figure 5.23 Deconvoluted photoluminescence spectrum of WO_3/g-C_3N_4 sample WCN19 with Gaussian fit

As demonstrated in figure 5.24, PL emission (blue emission) peaks at 420 nm and 482 nm can be assigned to measurable bandgap energy range (2.6-2.9 eV) for WO_3, present due to the indirect band-to-band transitions [85, 261]. However, the low PL energy at 525 nm (2.36 eV) has been explained due to the presence of localised vacancy in the bandgap of WO_3 nanosheets [85]. The theoretical investigation of the nature of oxygen vacancies (V_o) in WO_3 by Wang et al.(2011),[262] relate the PL emission at 2.36 eV very closely to the calculated energies for the optical level transitions taking place from an initially relaxed state to an unrelaxed vacancy state of WO_3.

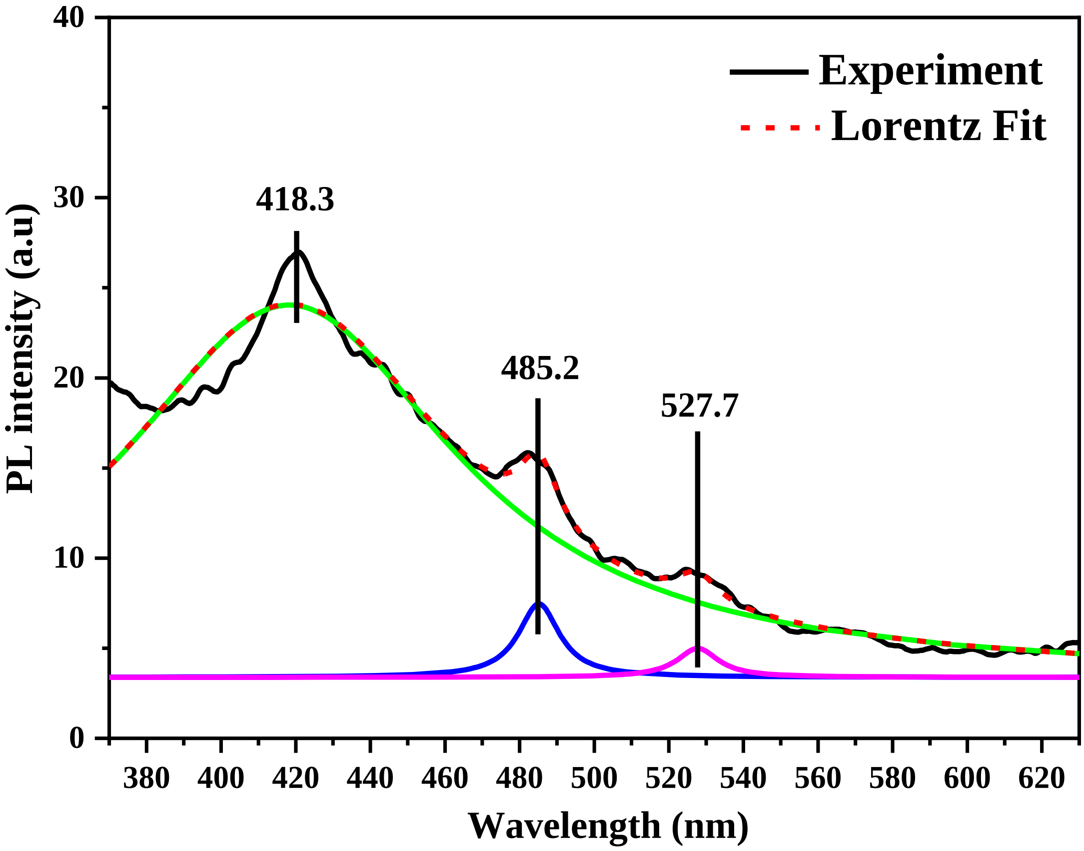

Figure 5.24 Deconvoluted photoluminescence spectrum of WO_3 with Lorentz fit.

5.4.5 Photoelectrochemical characterisation of WO_3 and g-C_3N_4

The presence of trapped states in TiO_2 [230], Fe_2O_4[87] has been studied previously, using photoelectrochemistry. For this reason, electrochemical measurements were carried out for the immobilised photoelectrodes using photocurrent density-potential measurements (*J*-V) and Mott-Schottky plots by measuring the charge transfer capacitance ($1/C_p^2$) against potential in the dark and under irradiation. Both onset photocurrent and M-S plots are a measure of flat band potential of the semiconductors and therefore can give an indirect measurement for CB edge potential.

5.4.5.1 Photocurrent response for WO_3 and g-C_3N_4

Photoelectrochemical studies were performed on WO_3 and g-C_3N_4 photocatalysts synthesised in this work. As per figure 5.25, on applying fixed potential from the range of +0.1 to +1.0 V, the photocurrent was measured for over 800 s under chopped illumination. An anodic photocurrent onset potential of +0.18 V (SCE) (pH 1) was obtained for WO_3, which corresponds to +0.42 V (NHE) (pH 1). A value of +0.41 V (RHE) was reported by Grigioni et al.(2015) [263]. The anodic photocurrent response obtained in the desired potential range typically shows the n-type characteristic of WO_3. Considering the onset for anodic photocurrent is always slightly positive than the flat band potential, their flat band potential for WO_3 nanoplates would be close to +0.4 V (NHE), which is also the reported CB potential for WO_3.

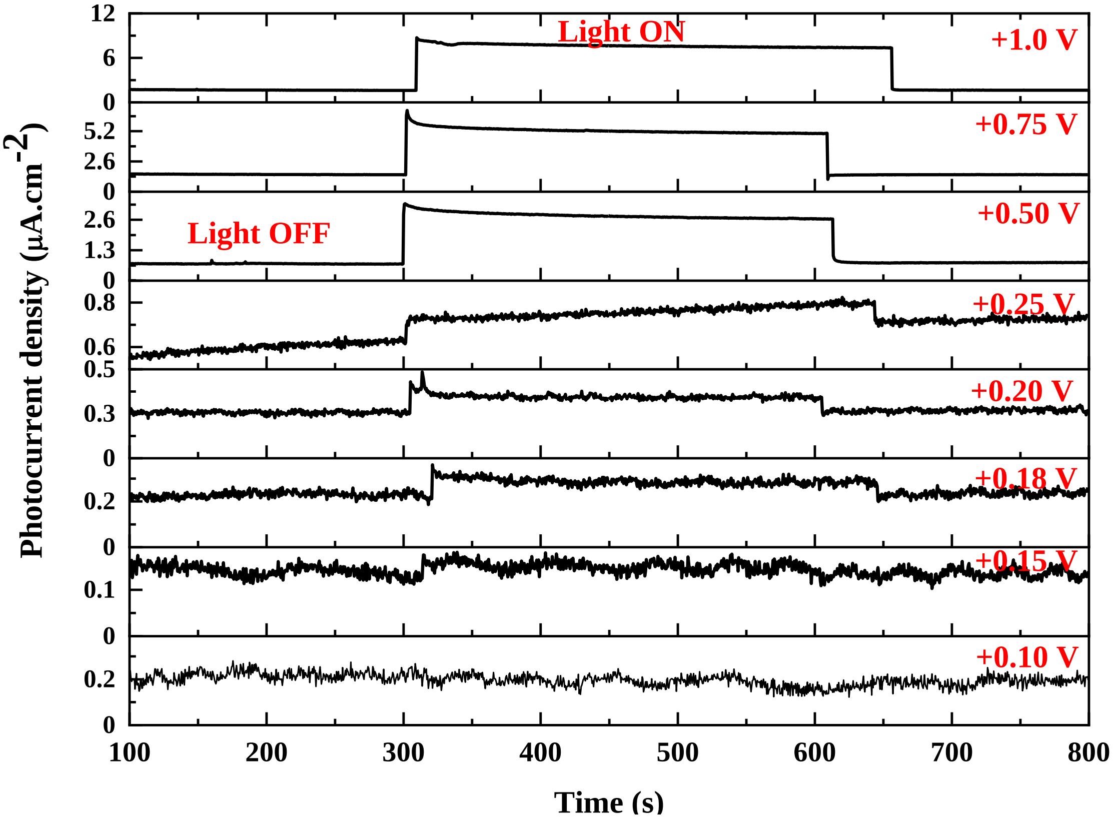

Figure 5.25 Photocurrent measurements for WO_3 nanoplates at the fixed potential from +0.1 to +1.0 V (SCE). Electrolyte = pH 1, 0.1 M $HClO_4$

For g-C_3N_4 very small photocurrent (<2 µA.cm^{-2}) was obtained on applying the potential from 0 to +1.0 V. To study the much smaller photocurrent response in-depth, current values at a fixed potential were observed for g-C_3N_4 over a time interval of 700 s with chopping off light at 300 s. From figure 5.26, the photocurrent density vs fixed potential (+1.0 to -0.4 V) can be seen, wherein g-C_3N_4 inhibits a photocurrent switching property. The polarity of photocurrent was observed to switch from anodic to cathodic between from +1.0 to +0.4 V, and no photocurrent was observed to be generated beyond -0.4 V in the chronoamperometric measurements due to poor adhesion of the film over the substrate.

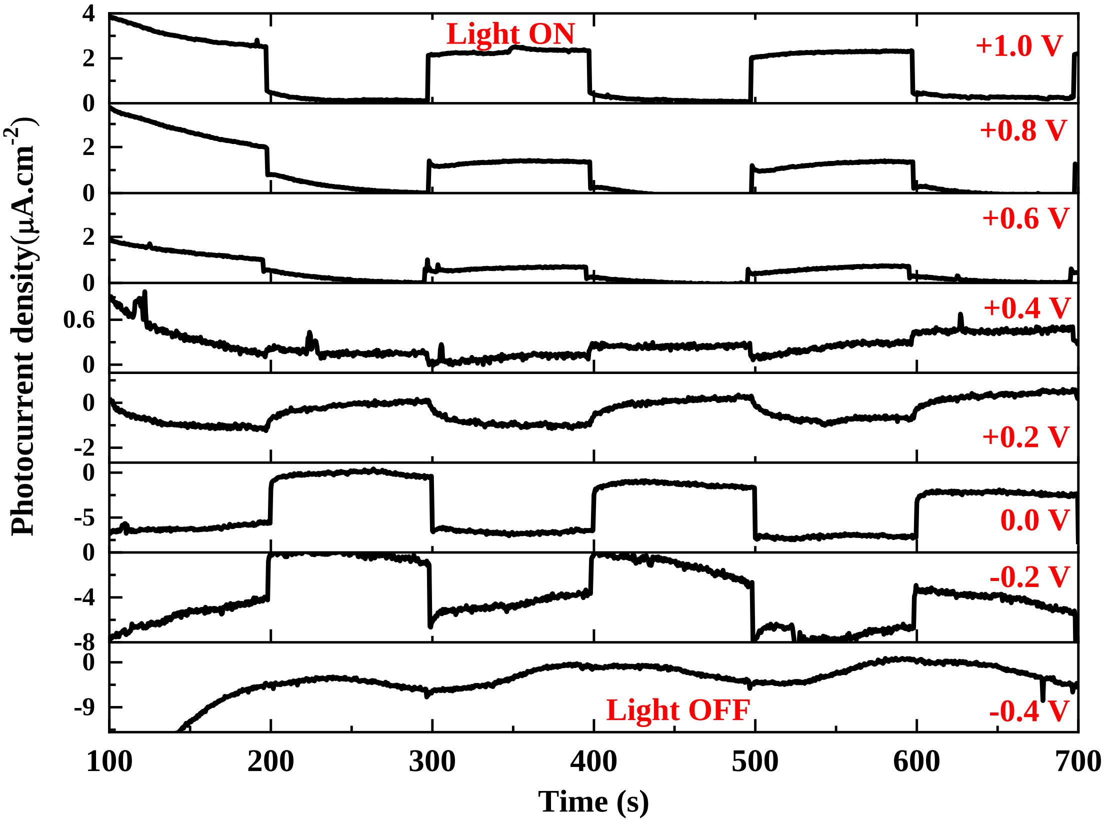

Figure 5.26 Photocurrent measurements for g-C_3N_4 at the fixed potential from -0.4 to +1.0V (SCE). Electrolyte = pH 1 0.1 M $HClO_4$

The transition of anodic to cathodic photocurrent indicated the dual photocurrent behaviour of g-C_3N_4. This dual photocurrent behaviour of g-C_3N_4 was speculated to be a result of unbiased Fermi level of g-C_3N_4 situated approximately in the middle of the forbidden gap by Jing et al.(2019) [185]. Based on the energy diagram previously mentioned in figure 5.15, the energy difference between Fermi level and CBM for g-C_3N_4 was 0.84 eV, albeit the photocurrent switching observed through electrochemical measurements here is real. Jing et al.(2019) mention the switching response to be an unbiased Fermi level. Rather it is a presence of mid-gap surface state of g-C_3N_4 that is causing the surface pinning of Fermi level, with surface state continuously accepting and donating electrons until fully charged or discharged.

5.4.5.2 pH-dependent band edge positions

The photocurrent vs potential measurements for WO_3 and g-C_3N_4 were investigated in 0.1 M electrolytes of pH 1, 7 and 13 to observe the onset photocurrent with respect to pH. As demonstrated in figure 5.27, at pH 1, the photocurrent onset was observed close to +0.20 V (SCE), i.e. +0.44 V (NHE). This onset was a confirmation of the value obtained through transient photocurrent measurements in section 5.4.4.1. At pH 7, the photocurrent increased for WO_3. At pH 13, the photocurrent was very low, and the onset photocurrent potential was difficult to identify for WO_3, mainly due to its instability at such a basic pH.

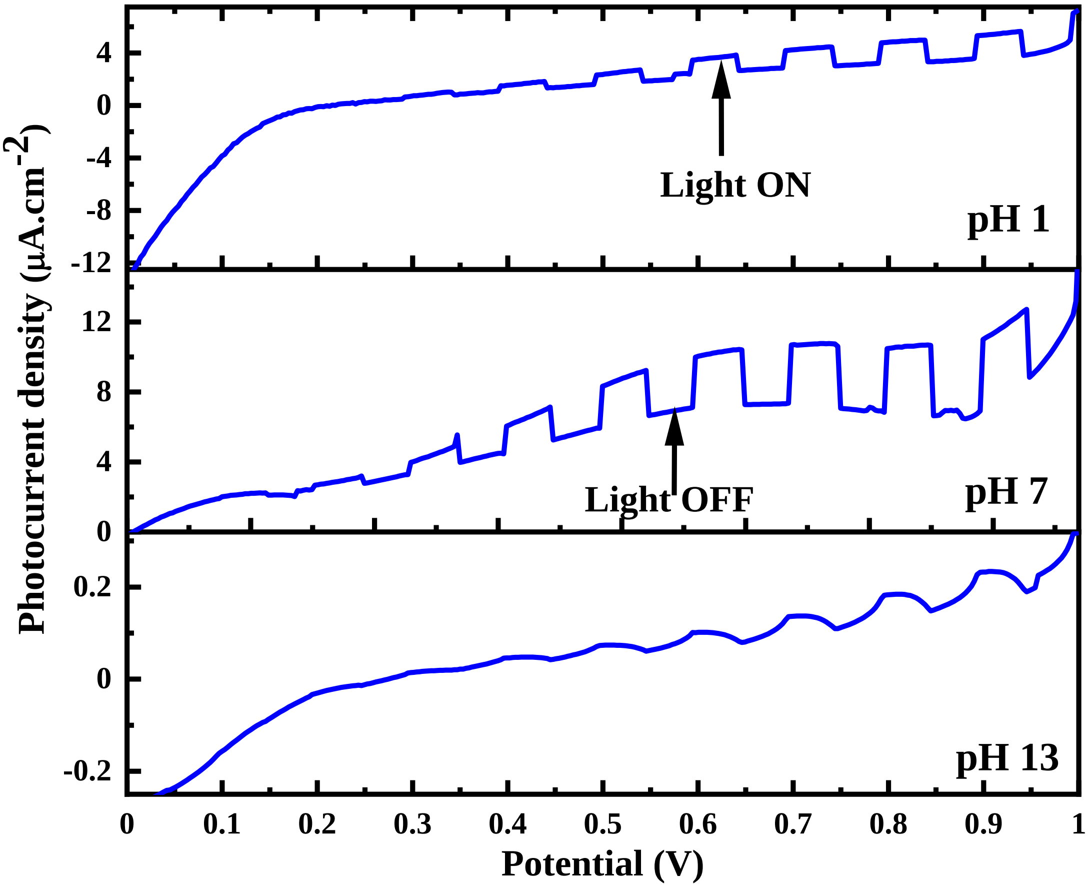

Figure 5.27 LSV measurement under chopped UV-Vis irradiation for WO_3 against applied potential. The variation in on-set can be observed with different pH electrolyte at 0.1 M $HClO_4$ pH 1; 0.1 M KCl pH 7; 0.1 M NaOH pH 13.

The onset photocurrent for g-C_3N_4 was observed to shift towards a negative potential with increasing pH. An estimated shift of ~0.03V/pH was observed through the obtained onset photocurrent (Table 5.26) which does not follow the Nernstian response i.e. shift of 0.059 V/pH unit). This was suggestive that pH-induced bending does not occur in the organic g-C_3N_4 system which makes sense because the organic solids have molecular levels (i.e. HOMO and LUMO). However, the shift in photocurrent onset potential with pH also indicated a surface reaction occurring between the ions (H^+/OH^-) present in the electrolyte and the semiconductor's surface. For example, as shown in figure 5.28 at pH 1, g-C_3N_4 demonstrates an anodic photocurrent in the range of +1.0 to +0.5 V, on reaching a potential beyond +0.49 V, the magnitude of the photocurrent-generated changes to the opposite, i.e. cathodic.

Moreover, the cathodic photocurrent was observed in the range of +0.49 V to -0.63 V beyond which no difference in light or dark could be discerned. A potential difference of 1.12 V was observed between the two onset photocurrent, i.e. -0.63 V (onset of cathodic photocurrent) and +0.49 V (onset of anodic photocurrent). Table 5.6 demonstrates the different values of onset obtained as a result of the change in pH for g-C_3N_4. A similar pH-dependent response was observed by Zhang et al.(2010) through their electrochemical measurements. They reported the onset potential as the flat band potential (E_{fb}) of g-C_3N_4, which is more positive, i.e. +0.45 V (SCE) at pH 2 and +0.25 V (SCE) at pH 6 and +0.01 V(SCE) at pH 13 [155]. These values are comparable to those achieved in this work and shown in table 5.6. A dual photocurrent effect of g-C_3N_4 was also observed in their measurements. However, they did not classify the dual photocurrent characteristic to any surface defect state present in g-C_3N_4. They concluded on a similar argument as per Jing et al.(2019) [185], i.e. E_f for g-C_3N_4 is situated at a positive potential and approximately in the middle of the forbidden gap.

Table 5.6 On-set potential values (SCE) of g-C_3N_4 vs pH

pH	**Onset I_{pa} (V)**	**No net I_{ph} (V)**	**Onset I_{pc} (V)**	**$\Delta V = (I_{pa} - I_{pc})$**
1	+0.53	+0.49 (I)	-0.63	1.16 V
7	+0.33	+0.29 (I)	-0.85	1.18 V
13	+0.02	+0.02 to -0.4 (I)	(> -1.0)	1.14 V

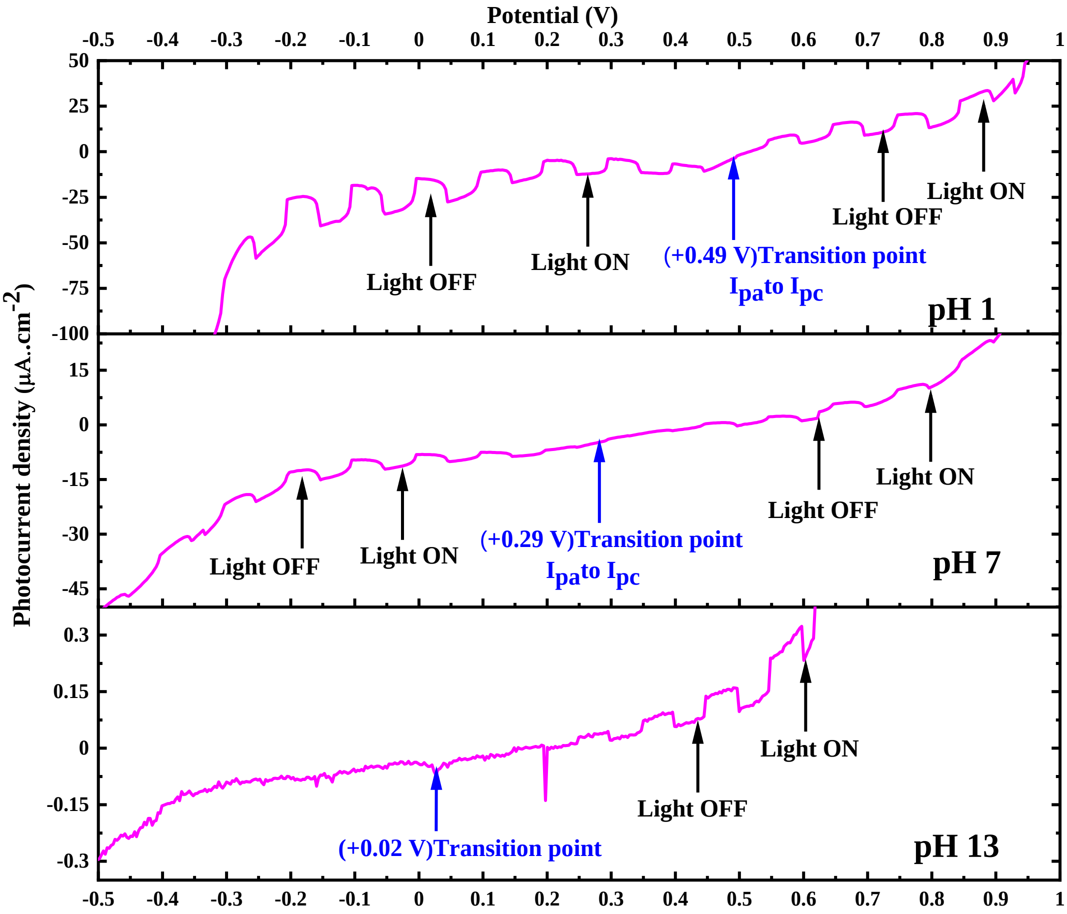

Figure 5.28 LSV measurement under chopped UV-Vis irradiation for g-C_3N_4 against applied potential. The variation in on-set can be observed with different pH electrolyte i.e. 0.1 M $HClO_4$, pH 10.1 M KCl pH 7 and 0.1 M NaOH pH 13.

A study on surface photovoltage measurements by Osterloh et al.(2014) co-related the potential difference obtained with the structural defects of g-C_3N_4 [232]. They observed two CPD signals at +0.97 V (NHE) (pH 0) and -0.38 V (NHE) (pH 0) and denoted these signals as a consequence of structural defects in g-C_3N_4. Roughly a potential difference of 1.3 V is seen between these two signals. They assigned the defects to be from the edge and terminal nitrogen groups of g-C_3N_4 i.e. N2 (NH) and N4 (NH_2). As shown in table 5.6 a potential difference between the anodic and cathodic photocurrent onset for g-C_3N_4 was observed to be 1.14-1.18 V. Also, the values in the present study are comparable to one reported by Osterloh et al.(2014) Henceforth, the photocurrent switching observed for g-C_3N_4 is a result of surface defect state involving the amino groups of g-C_3N_4. The weight ratio of which has been seen to be changing through the XPS investigations.

5.4.5.3 Mott-Schottky plots for WO_3 and g-C_3N_4

The flat band potential of a semiconductor can be determined using Mott-Schottky analysis. Identifying the flat band potential through M-S plots is also a measurement to obtain the true location of the CB edge potential of the semiconductor, especially in the case of heavily doped metal oxides such as n type or p type. However, recent concern over the use of M-S plot as a direct measurement for determination of flat band potential (or CB edge) of semiconductors was raised by Hankin et al.(2019)[264]. The authors reported by using inappropriate electrochemical fittings for M-S plots, very negative values for the flat band potential can be obtained, which may not be realistic. In addition, if only the dark conditions for Mott-Schottky analysis were to be considered, the obtained flat band potential values might not be accurate for all types of semiconductors. For instance, materials like Fe_2O_3 show active polaron states under irradiation, that pin the Fermi level at a much lower potential that the actual flat band potential of Fe_2O_3 obtained through the dark measurements [247]. Therefore, performing the M-S plot under both dark and irradiation should be considered as a standard to identify the presence of any mid-gap surface state hindering the performance of photocatalytic semiconductors.

The Mott-Schottky plots were obtained for WO_3 and g-C_3N_4 in complete darkness and under UV-Vis irradiation as per equation 5.9 [265];

$$\frac{1}{C^2} = \left(\frac{2}{e\varepsilon\varepsilon_0 A^2 N_d}\right)\left(E\text{-}E_{fb}\text{-}\frac{K_B T}{e}\right) \qquad 5.9$$

Where C is charge transfer capacitance, e is the charge of 1 electron (1.6×10^{-19} C), ε is the permittivity of free space, ε_0 is the dielectric constant of the material, A is the area of the electrode, N_d is the dopant (charge carrier) density, K_B is the Boltzmann constant (1.38×10^{-23} J/K), T is absolute temperature (in Kelvin) and E is the applied potential and E_{fb} is the flat band potential.

The x- intercept (at y = 0) of the linear region of the M-S plot determines the value of flat band potential (E_{fb}) and the slope (b) of the linear region (y = a + bx) of the M-S plot is equivalent to $\left(\frac{2}{e\varepsilon\varepsilon_0 A^2 N_d}\right)$ which is an indication of the charge carrier concentration of the semiconductor [264, 265].

The unmodified WO_3 shows a cross over at +0.14 V (SCE), as shown in figure 5.29. No difference in the type of the plot was observed under illumination for WO_3. A typical M-S plot with a positive slope was observed for WO_3 in the dark and under irradiation, confirming its n-type behaviour.

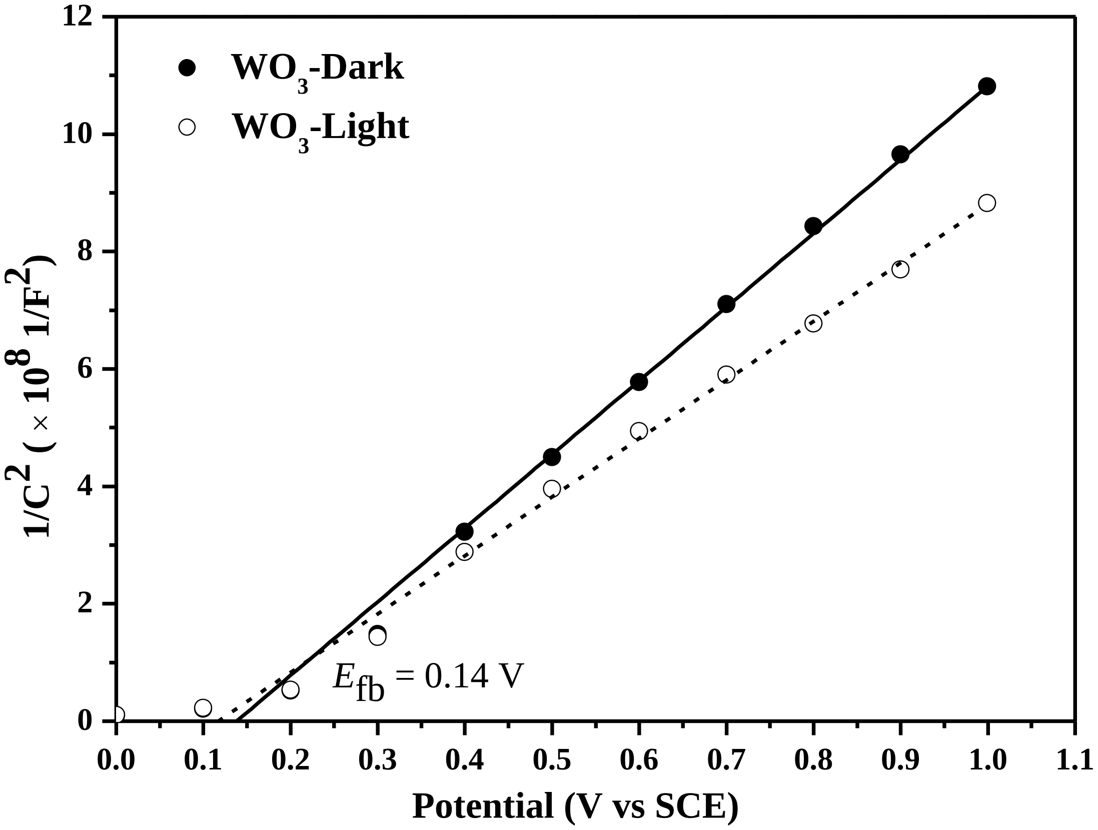

Figure 5.29 Mott-Schottky plot for WO_3 nanoplates at 0.1 M $HClO_4$ pH 1

For g-C_3N_4, the M-S plot obtained in dark displays a positive slope and an n-type semiconductor characteristic with onset potential E_{fb} = 0.012 V. But under UV-Vis irradiation, the plot seems to change, and two different linear regions are observed. Region-1 with x-intercept (E_{fb1}) extending to -0.72 V and region-2 with x-intercept (E_{fb2}) at 0.027 V. A constant capacitance region is observed under irradiation between 0.4 to 0.8 V. Sato has referred this constant region as the surface state capacitance which is zero in range of potential where the Fermi level of the semiconductor is pinned at the surface state[266] as explained from the inset graph of figure 5.30. Around the similar potential range, a photocurrent transition from anodic to cathodic was observed through I-V curve measurements (figure 5.28). Interestingly, this surface state comes into existence under irradiation, and as long as the fermi level of the semiconductor is away from the surface state, a capacitance value is observed.

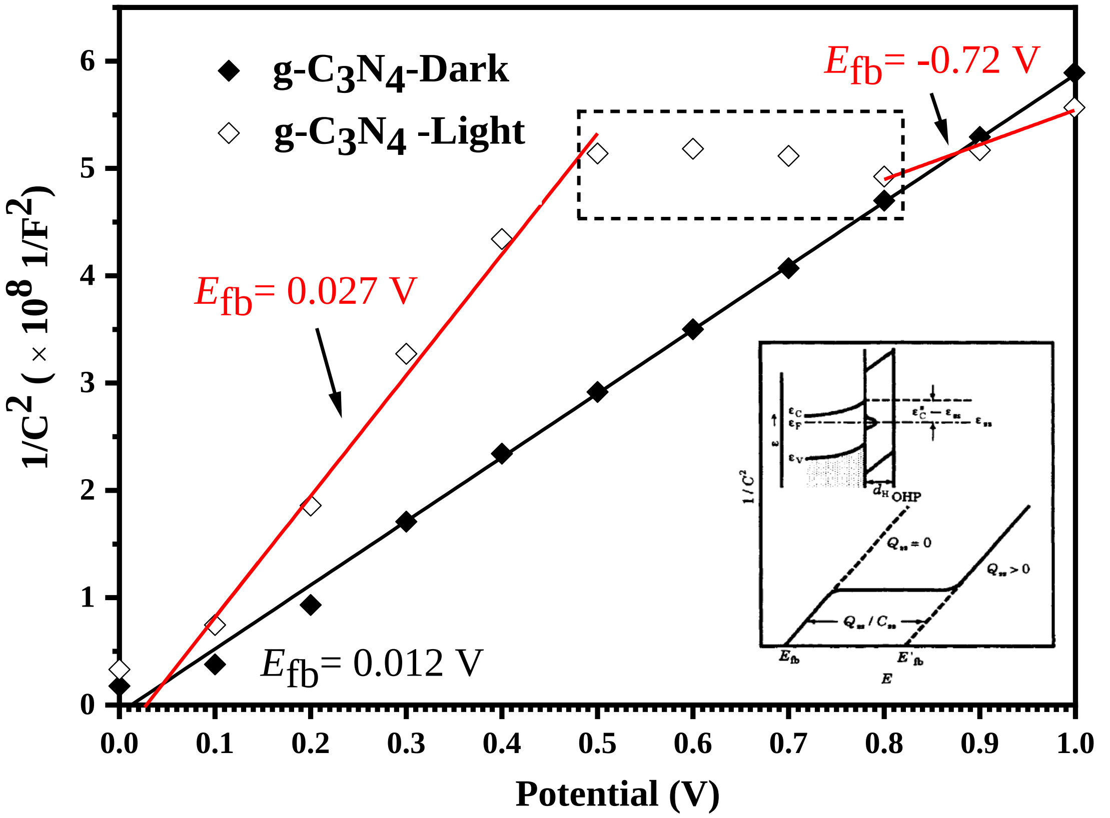

Figure 5.30 Mott-Schottky plot for a g-C_3N_4 sample at 0.1 M $HClO_4$ pH 1. Inset diagram for surface state pinned M-S plot on a semiconductor electrode. Reproduced from the Book: Electrochemistry of Metal and Semiconductor electrodes; N. Sato,(1998)[266].

A pH based Mott Schottky analysis for g-C_3N_4 was also performed in the dark to see the changes in the flat band potential. As shown in figure 5.31, g-C_3N_4 shows a positive slope at pH 1, 7 and 13. A magnified representation of pH 13 M-S plot of g-C_3N_4 is shown in figure 5.32. However, the interesting point was the different values obtained for flat band potential of g-C_3N_4 from onset photocurrent displaying the amphoteric behaviour and total n-type behaviour in M-S plot performed in the dark on varying pH. Hankin et al.(2019), also discussed in their research, to use multiple electrochemical techniques to determine the flat band potential of semiconductor photoelectrodes [264]. A variation in values of the flat band for hematite was observed in their report with 4 different methods.

Interestingly, hematite, just like g-C_3N_4, has some surface defect states that are active under excitation and cause a deviation in the flat band potential upon irradiation. Therefore, for such materials, it is essential to use more than one technique to determine the energetics of semiconductor electrodes for more systematic evidence of their photocatalytic or photoelectrochemical performance. Nevertheless, the difference in M-S plot under dark and irradiation in g-C_3N_4 here reflects the average nature of charge carriers of g-C_3N_4 to be more electrons in the dark, thus an n-type behaviour [154]. The majority of charge carriers in g-C_3N_4 are electrons was also confirmed by the energy difference E_f - E_{CB} = 0.84 eV obtained from the VB XPS and optical band gap, where the $E_f - E_{CB} < E_f - E_{VB}$.

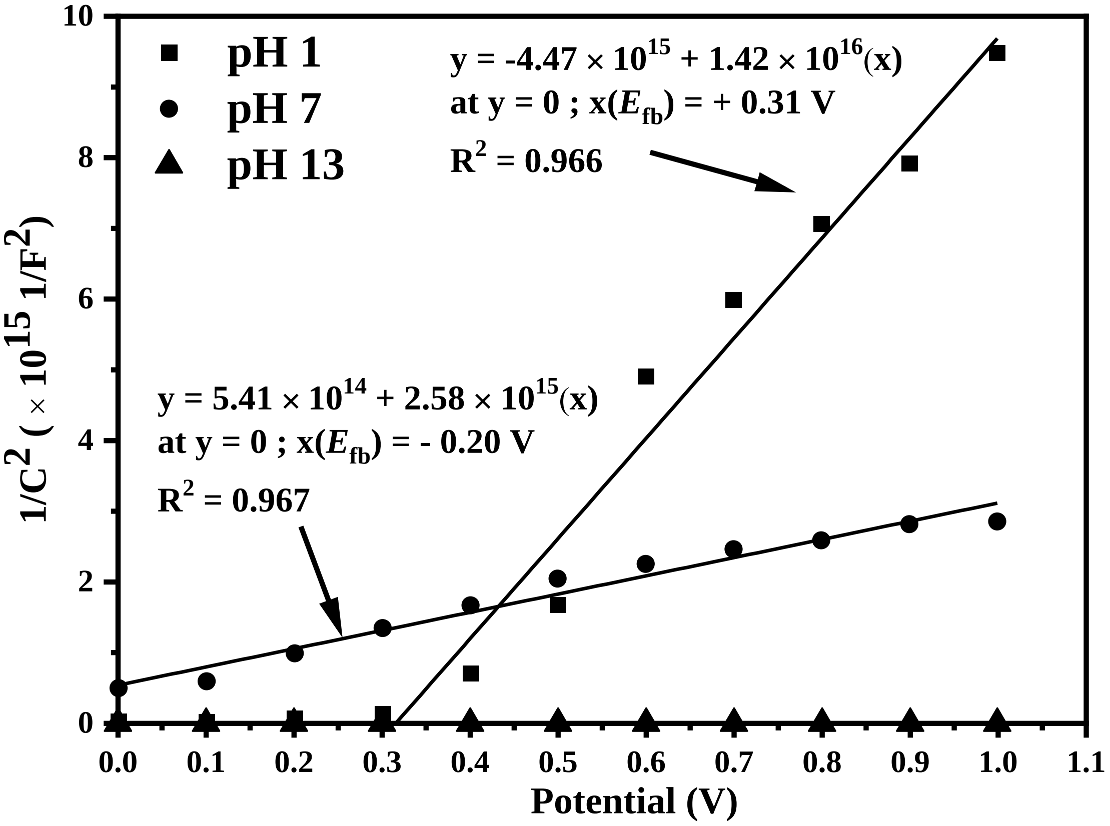

Figure 5.31 Mott-Schottky plot for g-C_3N_4 in the dark at different pH electrolytes.

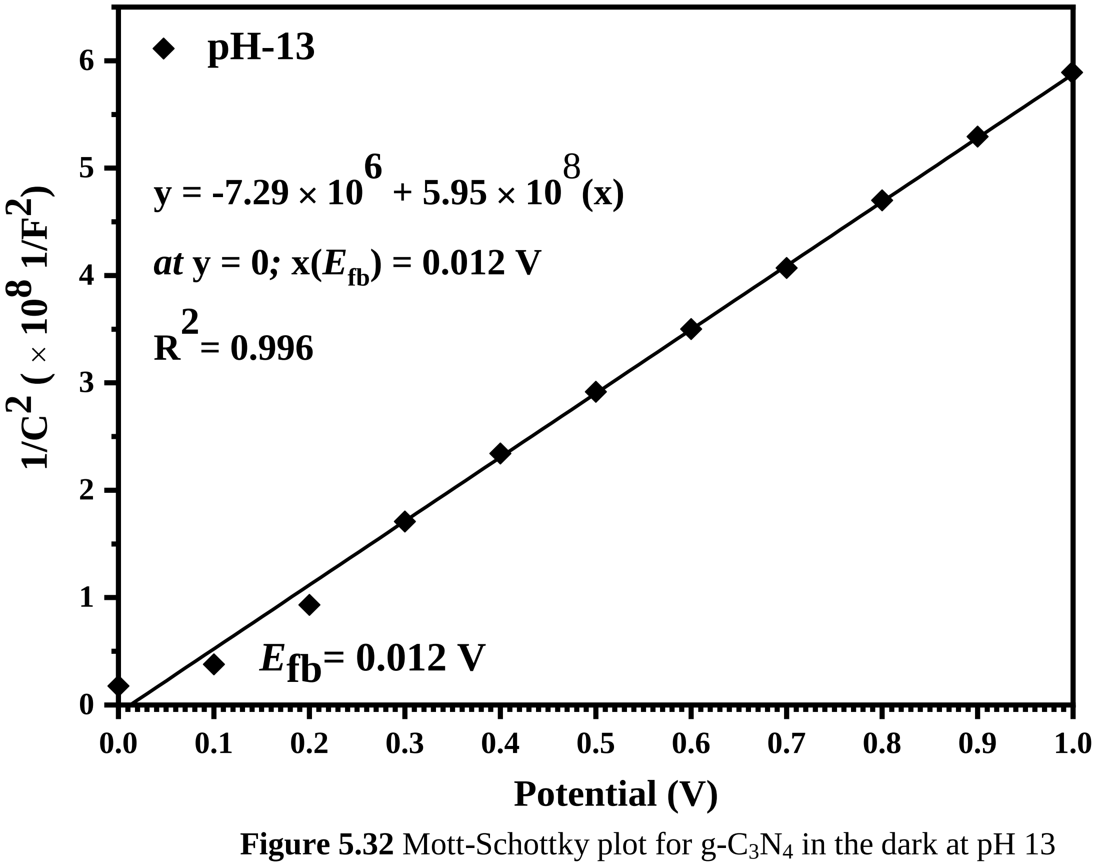

Figure 5.32 Mott-Schottky plot for g-C_3N_4 in the dark at pH 13

The Mott-Schottky measurements on heterostructure WCN91 were also carried out in the dark and under irradiation at pH 1, as shown in figure 5.33. The x-intercept in M-S plot for WCN91 was at +0.10 V (SCE), showing a significant cathodic shift in the flat band potential of WO_3/g-C_3N_4 as compared to unmodified WO_3. Through the obtained cathodic shift, it can be thus suggested a charge separation taking place across the interface of the heterostructures. It is an interesting point, which needs to be studied further in detail. However, comparing the dark and light measurements for WCN91, it may be suggested the surface state of g-C_3N_4 plays a key role in suppressing the activity of the overall heterostructure.

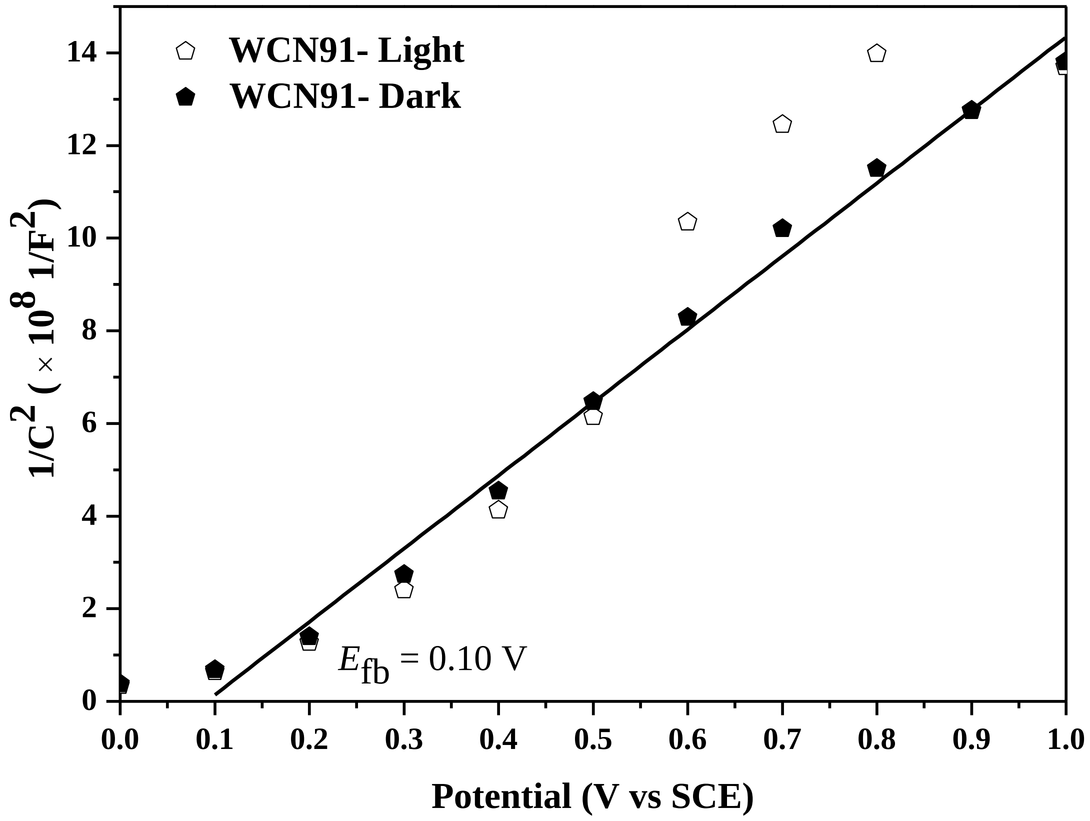

Figure 5.33 Mott-Schottky plot for WCN91 sample in the dark and under irradiation in pH 1 (0.1 M $HClO_4$).

5.5 Conclusions

The limited photocatalytic activity obtained for WO_3, g-C_3N_4 and WO_3/g-C_3N_4 heterostructures was investigated using multiple chemical and electrical measurements. The detection of hydroxyl ($^{\bullet}OH$) radicals generated during the photocatalytic process was done using RNO as the chemical probe. In presence of an electron scavenger, the WO_3/g-C_3N_4 heterostructure (WCN91) showed a 7.4x times increased $^{\bullet}OH$ production rate of 46.70×10^{-10} mol.L^{-1}.s^{-1} as compared to 6.33×10^{-10} mol.L^{-1}.s^{-1} without electron scavenger. The $^{\bullet}OH$ production for WCN91(with scavenger) was also 1.2x times higher to that of WO_3. Suggestive, both WO_3 and WO_3/g-C_3N_4 heterostructure under irradiation do cause an electron-hole pair separation and increase the lifetime of holes to oxidise H_2O or OH^- for $^{\bullet}OH$ generation as observed through RNO degradation. However, the study on the photocatalytic reduction pathway of WO_3 and g-C_3N_4 using methyl viologen (MV^{2+}) indicated the electrons in CB of WO_3 and LUMO of g-C_3N_4 do not have negative enough potential to drive the reduction of MV^{2+} to $MV^{+\bullet}$ even at higher pH. The limited MV^{2+} reduction using g-C_3N_4 was unexpected, indicating the CB(or LUMO) electrons in g-C_3N_4 were trapped at more positive potential than -0.445 V(NHE). The obtained result is not very encouraging as it limits the overall photocatalytic efficiency of the synthesized WO_3/g-C_3N_4 heterostructures for photocatalytic disinfection.

The XPS and electrochemical studies indicated a possible existence of surface state in g-C_3N_4 at potential more positive than the CB edge of WO_3 that is active under irradiation. The presence of the surface state in g-C_3N_4 was possibly due to terminal N-H bonds of g-C_3N_4 and was seen in the heterostructure. This surface state in g-C_3N_4 working as an electron trap under excitation between the potential range +0.5 to +0.8 V (SCE) or +0.74 to + 1.0 V(NHE) causes the Fermi level to pin in this range and makes the charge transfer mechanism downhill from WO_3 into the electron trap of g-C_3N_4. This limits the interfacial electron transfer across the g-C_3N_4 surface into solution, and blocks the photocatalytic reduction pathway in water disinfection. Finally, this work is an instructive for the rational design of heterostructures, taking in consideration the role of trap/defect levels towards photocatalytic charge transfer mechanism across the inorganic/organic semiconductor interfaces, particularly when one of the components of the system display intrinsic semiconductor characteristics.

Chapter 6. Electrochemically Assisted Photocatalytic Disinfection of Water

6.1 Aim and Objectives

6.1.1. Aim

The aim of this work was to study the photoelectrochemical properties of the WO_3/g-C_3N_4 heterostructures and to incorporate the best performing materials as a photoanode for the electrochemically assisted photocatalytic (EAP) inactivation of *E. coli* in water.

6.1.2. Objectives

i. To fabricate photoelectrodes by immobilising the synthesized nanomaterials onto the metal foil and ITO conductive glass.
ii. To analyse the immobilised coatings for film thickness and elemental composition.
iii. To study the photoelectrochemical properties of the electrodes.
iv. To test the different electrodes for the electrochemically assisted photocatalytic (EAP) inactivation of *E. coli*.
v. To compare the obtained results with previous reports from Ulster on P25-TiO_2 and vertically aligned titania nanotube electrodes for EAP inactivation under similar conditions.

6.2 Introduction

The limited performance of semiconductor photocatalysis is an issue for the practical application in water disinfection. Low photocatalytic efficiencies obtained may be due to (i) the rapid recombination of electron-hole pairs, (ii) trapping of electrons in the conduction band or semiconductor’s defect states, (iii) hole trapping at the semiconductor’s surface, (iv) low surface area to volume ratio (v) insufficient bandgap to absorb solar photons,(vi) mismatched band edge potentials to drive redox reactions or ROS generation, (vii) low overpotential to drive the photocatalytic reduction or oxidation reactions (viii) mass transfer limitations or even in some cases (ix) difficult post-treatment filtration or separation of suspended photocatalyst leading to increased cost and complexity of overall treatment. To improve the efficiency, different approaches have been investigated including; surface modification, heterostructure formations and introducing dopants to alter the band structure of the materials.

Immobilisation of photocatalyst onto a solid glass/metal support substrate overcomes the post-treatment filtration steps [31, 267]; however, the issues mentioned from (i) - (viii) still exist. Alternatively, if immobilised on an electrically conducting support, the separation of charge carriers may be assisted by the application of an external electrical bias. The efficiency of the semiconductor photocatalyst(or the photoanode) has been reported to increase the overall photocatalytic rate for water splitting [76], and the degradation of organic pollutants[67, 78, 179, 268, 269] and inactivation of microbial contaminants[50, 65, 270] present in water. The approach of the application of an external anodic potential to the existing photocatalytic systems has been given different names in the literature, which include electrochemically assisted photocatalysis (EAP), photoelectrolysis, or photoelectrocatalysis (PEC).

It is beneficial to use EAP as one can separate the anodic and cathodic reactions for mechanistic analysis. Since the half-reactions occurring are physically and spatially separated, the oxidation takes place at the working electrode (i.e. semiconductor photoanode), and the reduction half-reaction occurs at the counter electrode (usually a metal electrode). A schematic representation of reactive oxygen species generated during the electrochemically assisted photocatalysis is given in figure 6.1. The fundamental mechanism of EAP disinfection is similar to that of photocatalytic disinfection. As illustrated in figure 6.1, upon irradiation of a semiconductor photoanode, the photogenerated electrons move to the cathode under the influence of the external electrical bias and the holes in the VB, react at the semiconductor-electrolyte interface to generate ROS such as hydroxyl radicals ($^{\bullet}OH$), superoxide ions ($^{\bullet}O_2^-$) and hydrogen peroxide (H_2O_2). By using an external electrical bias to separate charge carriers, the rate of charge carrier recombination is reduced, therefore improving the quantum efficiency. Hydroxyl radicals can also be formed by the multiple electron reduction of molecular oxygen at the cathode.

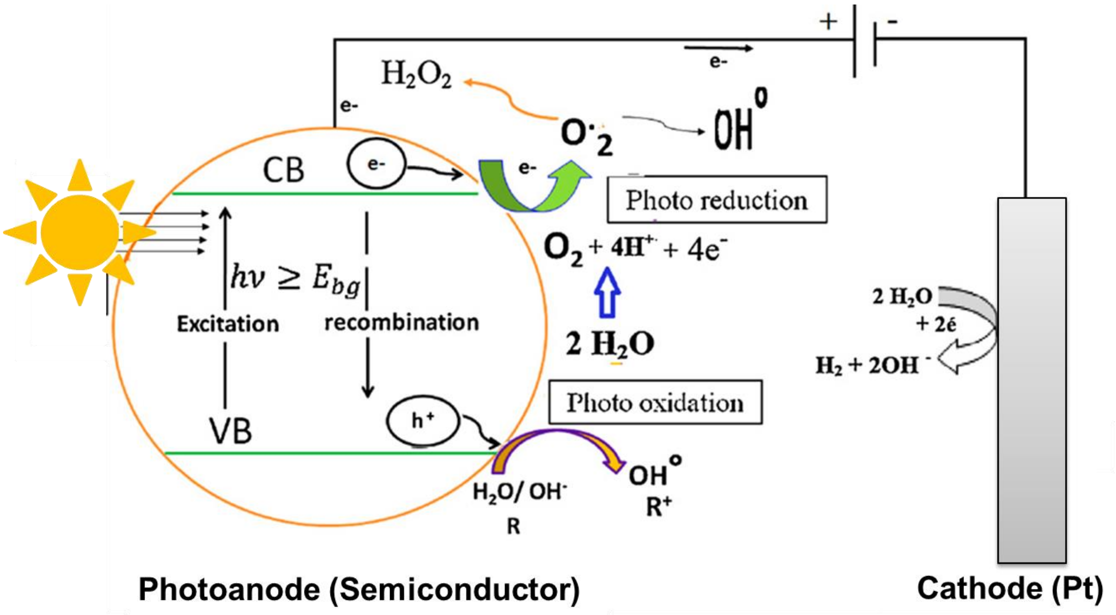

Figure 6.1 Schematic of electrochemically assisted photocatalysis (EAP) mechanism. Adapted from R. Daghrir et al.(2012), Journal of Photochemistry and Photobiology A: Chemistry, 230, 41-52, (2012) [178].

EAP may also enhance the rate of inactivation of microorganisms by improving mass transport through electromigration[270]. Normally, a semiconductor photoanode is used as the working electrode against a metal (cathode) counter electrode to drive photoelectrocatalytic oxidation reactions. But some recent investigations have also employed a functionalised TiO_2 photocathode as the working electrode with a doped semiconductor counter electrode of W: $BiVO_4$ to test photoelectrocatalytic reduction of CO_2 [271]. However, the TiO_2 photocathode used was prepared by a complex method, i.e. functionalising the surface of P25-TiO_2/FTO electrode with amine ligand- 3-aminopropyl-triethoxysilane(APTES) used for CO_2 activation and doped with palladium nanoparticles to absorb H^+ and Eosin Y disodium dye to absorb solar light. Another more challenging approach is the use of photoanode and photocathode together for overall photoelectrocatalytic systems, but the availability of stable p-type materials is limiting [67, 180, 272].

The use of TiO_2 electrode in photoelectrochemical applications gained momentum in 1972, through the work of Fujishma and Honda in photoelectrochemical water splitting [76]. The authors reported that water splitting could be promoted using single crystal rutile TiO_2 as photoanode under UV irradiation with applied electrical bias. TiO_2 as an immobilised photoelectrode for water disinfection was first reported by Butterfield et al. (1997) [270]. They reported a 3-log reduction of *E. coli* and 2-log reduction of *Clostridium perfringens* in 25 min using sol-gel TiO_2 thin film electrode and Ni mesh as counter electrode. Since then a considerable amount of literature is available on the use of TiO_2 as the electrode for photoelectrochemical disinfection of water mainly in removal of bacterial cells [65, 273-279] and toxic microcystins [280]. But the research on alternative materials to TiO_2 for EAP disinfection is limited. Owing to its relatively positive valence band edge at 3.1 V (NHE) and narrow bandgap of 2.68 eV, tungsten oxide (WO_3) is widely reported as photoanode material for photoelectrochemical water splitting [107, 184, 281] and EAP oxidation of organic contaminants [67, 86, 183].

The use of WO_3 nanostructures in electrodes by either direct growth or deposition of preformed WO_3 as nanoplates on the conductive FTO/ITO substrates has been reviewed in the past by Liu et al.(2012) [281]. Augustynski et al.(2014) deposited their pre-synthesized monoclinic WO_3 nanoplates on FTO glass via a doctor blading method to form photoanode for the photoelectrochemical splitting of water under AM 1.5G simulated solar irradiation [184]. They observed O_2 evolution using the WO_3 nanoplate/FTO photoanodes, but the yield obtained was reported to be changing before and after the cathodic polarization of electrodes. The yields were affected by the polarization of electrodes but, independent on the large photocurrent in the range of 1-3 $mA.cm^{-2}$. The formation of WO_3 electrodes by drop-coating of single-crystal WO_3 nanosheets on FTO glass was reported by Osterloh et al.(2012) [107]. They reported an O_2 evolution rate with a yield of 35.5 $\mu mol.h^{-1}$ using WO_3 nanosheet/FTO electrodes. However, these were predominantly photocatalytic water oxidation to O_2 evolution reactions performed in the presence of 8.3 mM of $AgNO_3$ solution as the sacrificial electron acceptor.

A photoelectrocatalytic fuel cell configuration was constructed by Emuakpor et al.(2012) to study the efficacy of WO_3 as photoanode for visible light degradation of organic contaminants such as 2,4-dichlorophenol [67]. The cell configuration was similar to a proton exchange membrane fuel cell. A 5 layer membrane electrode assembly was fabricated, consisting of Pt contact, gas diffusion layer, nafion proton exchange membrane between the photoanode (WO_3) and the cathode (i.e. teflon/carbon loaded with Pt). The current configuration of photoanode-cathode assembly used by Emuakpor et al.(2012) is one of the rational designs of photoelectrocatalytic reactor assemblies reported to date for water treatment applications using visible light active material like WO_3. The rational design of photoreactor assemblies is very much dependent on utilising the appropriate electrode material, shape and geometry of the cell. The overall quantum efficiency of the PEC cells can be improved by exploring new stable photoelectrocatalysts, which are good solar light absorbers. The ideal configuration of a PEC reactor should be the one, where on applying minimal electrical energy, the maximum rate of disinfection (or organic pollutant degradation) is achieved under the real sun. Practical applications of such PEC reactors are yet to be explored.

Electrochemically anodized WO_3 nanosheet electrodes for photoelectrocatalytic degradation of atrazine were also reported by Antón et al.(2018) and showed complete mineralisation of 20 $mg.L^{-1}$ atrazine concentration in 3 h, at an applied potential of +1.0 V (Ag/AgCl) under 360 nm monochromatic irradiation using a 1 kW Xe light source[183]. Recently Choi et al.(2019) also reported the use of WO_3 photoanode in a photoelectrocatalytic system for degradation of organic contaminants and *E. coli* inactivation, based on reactive chlorine species generation (RCS) [66]. A 3.7-log reduction in *E. coli* cells was observed in 4 h of visible light irradiation ($\lambda > 420$ nm) with WO_3 as photoanode under EAP conditions of potential +0.5 V (Ag/AgCl), Pt wire as a counter electrode and 0.1 M Na_2SO_4(pH 4) as the electrolyte. When 50 mM of NaCl (as a source of Cl^- ions) was added to the electrolyte with the other reaction parameters unchanged, a 7-log reduction in *E. coli* was observed in 4 h. The increased disinfection rate in the presence of chloride ions under EAP conditions was attributed to the formation of reactive chlorine spieces such as ClO_3^-. The authors detected the generation of ClO_3^- as an indirect pathway of reaction between ($^{\bullet}OH$) radicals (generated during the oxidation of water) and HOCl. Choi et al.(2019) also reported the production of H_2 under visible light irradiation as the simultaneous reductive half-reaction under EAP conditions.

There are no reports of the use of g-C_3N_4 as a photoelectrocatalyst for water disinfection. One reason can be the chemical instability of the materials towards reactive oxygen species like hydroxyl radicals generated as a result of photocatalytic organic pollutant degradation as reported by Xiao et al.(2012) [112]. Another reason could be the presence of mid-gap defect states in the g-C_3N_4, at potential lower than the reduction potential of molecular oxygen (-0.33 V (NHE)), that limit the electrons to take part in any reduction reactions as seen in chapter 4 and chapter 5. Considering the electrons are trapped at much positive potential than the LUMO of g-C_3N_4, the availability of electrons for any photoelectrocatalytic reduction reaction using g-C_3N_4 will be limited. This is also in agreement with the negligible photocurrent response obtained from g-C_3N_4 under irradiation with the applied anodic potential of +1.0 V. Recently, g-C_3N_4 in the presence of metal dopants such as Pd, Ag as photoanodes was reported to show improved photocurrent density of 79.2 $\mu A.cm^{-2}$ (Pd-gC_3N_4) and 40.6 $\mu A.cm^{-2}$ (Ag-gC_3N_4) by Nazarabad et al.(2019)[186]. However, there was no real evidence for water oxidation to O_2. There are some reports of g-C_3N_4 behaving as an electrocatalyst for the reduction of oxygen [282-284]. However, most of these studies are on conjugated g-C_3N_4-metal co-catalysts that show the improved response for oxygen reduction.

g-C_3N_4 based heterostructures such as TiO_2/g-C_3N_4 [104] or WO_3/g-C_3N_4 as a photoanode for photoelectrochemical water splitting have been reported recently. Feng et al.(2014) fabricated 3D arrays of WO_3 nanosheets with g-C_3N_4 layers and co-doped with CoO_x nanoparticles on W foil as hybrid photoanodes to study the photoelectrochemical water oxidation [285]. The 2D/2D heterostructure fabricated electrodes of WO_3/g-C_3N_4 displayed a high faradaic efficiency close to 82.8%, based on the EAP mechanism of type-II heterostructures. In another report, 2D/2D WO_3/g-C_3N_4 photoanodes constructed on FTO glass were reported to be effective for photoelectrochemical seawater splitting [101]. The authors used saline seawater as the electrolyte with pH 6.4 from a natural source in Huanghai, China. The splitting of natural seawater was explained as a mechanism of oxidation of chloride ions (Cl^-) to generate chlorine (Cl_2) at the photoanode. Likewise, the cathodic reaction was said to be the production of H_2 from H^+ ions. However, the authors did not measure any generation of Cl_2 or H_2 during the splitting of seawater.

In all the studies discussed above for heterostructured electrodes, the authors report the increased performance of WO_3 or TiO_2 as a photoelectrocatalyst incorporated with g-C_3N_4. The EAP activity is compared to their parent material, i.e. WO_3 or TiO_2. Still, none of the reports shows any evidence of comparing the performance of g-C_3N_4 as a standalone photoelectrocatalyst for water oxidation or water splitting.

Photoelectrochemical water splitting using WO_3/g-C_3N_4 does give an insight into the increased electron-hole separation in the heterostructures upon the application of an external electrical bias. Therefore, use of two-dimensional heterostructures of WO_3/g-C_3N_4 as photoanodes for electrochemically assisted photocatalytic disinfection of water should increase the lifetime of photogenerated charge carriers and avoid recombination. Along with the longer lifetime of charge carriers, the external electrical bias will provide overpotential to drive simultaneous reduction and oxidation reactions for generation of reactive oxygen species.

In this work, the EAP inactivation of *E. coli* was investigated using two-dimensional heterostructure photoanodes of WO_3/g-C_3N_4.

6.3 Experimental Section

6.3.1 Electrode preparation

The electrodes used in this study were prepared following protocols previously discussed in detail in chapter 3 section 3.2.4. Following the preparation steps, the 2D powder samples of WO_3, g-C_3N_4 and WO_3/g-C_3N_4 heterostructures, i.e. WCN19, WCN91 and WCN1:4 pH2.25 were immobilised on W-foil by spray coating and annealing at 400°C for 1 h (please see section 3.2.4.2). Annealing of WO_3 samples at 400°C has been reported by Ng et al.(2013) to provide a stable electron transport in photoelectrochemical water splitting and proper adhesion of the materials without causing any crystalline changes in the structure of γ-WO_3 [286]. In some cases, where difficulty was faced with spraying g-C_3N_4 on W foil, a simple doctor blading method was adapted to coat the nanomaterials (WO_3, g-C_3N_4 and WCN91) on conductive ITO glass using an organic polymeric blend poly(3,4-ethylene dioxythiophene)-

poly(styrenesulfonate) (PEDOT:PSS). PEDOT:PSS was used to provide a well-hydrated binding of the nanomaterials to the ITO, especially g-C_3N_4. For more details on doctor blading procedure, please refer to section 3.4.2.3. All samples made as photoelectrodes by spray coating were named as nanomaterial/W electrodes, and those prepared by doctor blading were named as nanomaterial/PEDOT/ITO electrodes.

6.3.2 Electrode material characterization

The prepared electrodes were characterized via scanning electron microscopy equipped with energy dispersive X-ray accessory. For more details please refer to section 3.3.2.

6.3.3 Photoelectrochemical measurements

Photoelectrochemical measurements were performed using a PC controlled electrochemical workstation AUTO LAB PGSTAT30 equipped with an optical shutter for monochromatic chopped irradiations. A three-electrode cell was used as a photoelectrochemical set up with coated nanomaterial/W or nanomaterial/PEDOT/ITO electrode as the working electrode, a Pt mesh as the counter electrode and saturated calomel as the reference electrode. The electrolyte was 0.1 M $HClO_4$ (pH 1). The irradiation light source was a 450 W xenon lamp. The cell was placed 4 cm away from the irradiation source with UV-visible light spectral dose of 185 $W.m^{-2}$ between 280-800 nm determined using a spectral radiometer. The spectral output was displayed in figure 3.4. The UV spectral dose output was calculated to 13.86 $W.m^{-2}$ between 280-400 nm, which is equivalent to 1/3rd UV output of the AM1.5 G solar spectrum. For more details, please refer to section 3.5.1 and 3.5.2. The current densities of the electrodes were determined using linear sweep voltammetry (LSV) under chopped irradiation of 10 s. The I-V measurements were recorded under a scan rate of 5 $mV.s^{-1}$ and sweep potentials of 0.0 to +1.0 V. The current vs time at a fixed potential of +1.0 V was also performed under chopped irradiation. All potentials are reported against SCE. The spectral response measurements of the samples were performed at a fixed potential of +1.0 V under monochromatic irradiation at 10 nm intervals in the range 250-500 nm. The incident photon to current conversion efficiency (IPCE%) was calculated from spectral photocurrent response obtained in the wavelength range of 250-500 nm following equation 3.1 and 3.2 (section 3.5.2.3) or as reported in [180, 205].

6.3.4 Electrochemically assisted photocatalytic (EAP) disinfection.

For EAP disinfection, a quartz water jacket reactor of total volume 35 mL was used as the photoreactor as described in section 3.5.4. The electrolyte was quarter (¼) strength of Ringer's solution (pH 7) (2.25×10^3 mg.L^{-1} NaCl, 1.2×10^2 mg.L^{-1} $CaCl_2$, 1.05×10^2 mg.L^{-1} KCl and 50 mg.L^{-1} $NaHCO_3$ prepared in deionized water [65]). A working volume of 15 µL of *E. coli* K12 (CTEC 4624) was diluted in 15 mL sterile Ringer's solution and added to the reactor, giving an initial *E. coli* concentration of ~10^6 CFU.mL^{-1}. The *E. coli* culture protocol was discussed in section 3.4.2.2, and for detailed EAP disinfection set up, please refer section to 3.5.4. The EAP disinfection was performed at a fixed potential of +1.0 V applied to the photoanode. The current-time characteristics were also recorded.

6.3.5 Quantification

During all experiments, samples were taken every 30 min, and colony-forming units were enumerated using a standard plate count method by serial dilution in Ringer's solution. Every time 6 drops of each 10 µL volume were plated on Luria Bertani agar plates and colonies counted after 24 h incubation at 37°C. At higher irradiation time when the colony-forming units were expected to be low, 100 µL samples were spread over LB agar plates to obtain the viable counts with a detection limit of 2 CFU.mL^{-1}.

6.3.6 GInaFIT modelling tool

The disinfection kinetics were assessed using the Gerraerd and Van Impe Inactivation Model Fitting Tool, i.e. GInaFiT v1.6 [200]. The kinetic parameters and different type of models used are described in section 3.4.3. The model has been previously used for fitting kinetic data in solar disinfection [201, 202] and photocatalytic disinfection experiments [40, 41, 203]. Different models were applied for comparison on each data set to determine the best fit. The selection of the best fit model is based on the lowest possible root mean sum of squared errors (RMSE) value (close to 0) and a maximum regression(or the coefficient of determination) close to unity, i.e. $R^2 = 1$. Most of the data presented in this work had the best fit using log-linear + shoulder, Weibull or Weibull+ tail model. Their respective kinetic fit parameters have also been discussed.

6.4 Results and Discussion

6.4.1 Electrode characterization

The analysis of the films was performed using a scanning electron microscope to estimate the film thickness. The heterostructure WCN91 was analysed in comparison to WO_3 nanoplates. The elemental mapping of the samples was also performed using energy dispersive analysis of X-rays. The samples are thereby denoted in SEM images based on the conductive substrate used, i.e. WO_3/W, WCN91/W for spray coated samples on W-foil and WO_3/PEDOT/ITO, WCN91/PEDOT/ITO for samples mixed as a slurry paste in PEDOT and deposited on ITO glass. Figure 6.2(a) shows the cross-sectional image of WO_3/W electrode. As illustrated, the thickness of the conductive W-foil was measured ~120 µm, in agreement to the thickness provided by the supplier (Sigma-Aldrich) in the data specification sheet, which is 0.127 mm. The thickness of the 2D-WO_3 nanoplates spray-coated on W-foil was measured in the range of 1.5-4 µm across the different area of analysis on the electrode. The maximum thickness area obtained was between 3.5-4 µm, as shown in figure 6.2(b). The thickness and roughness of the film deposited by the spray coating were relatively uniform throughout (figure 6.2(c)). The inset of the graph displayed the sharp nanoplates and 2D surface of WO_3. The EDS analysis is shown in figure 6.2(d) and a specific region of WO_3/W electrode (inset graph), show the peak signals from W, which is found across the entire region confirmed through element maps also. Through element maps, it is clear the O signal is mainly from the WO_3 nanoplates.

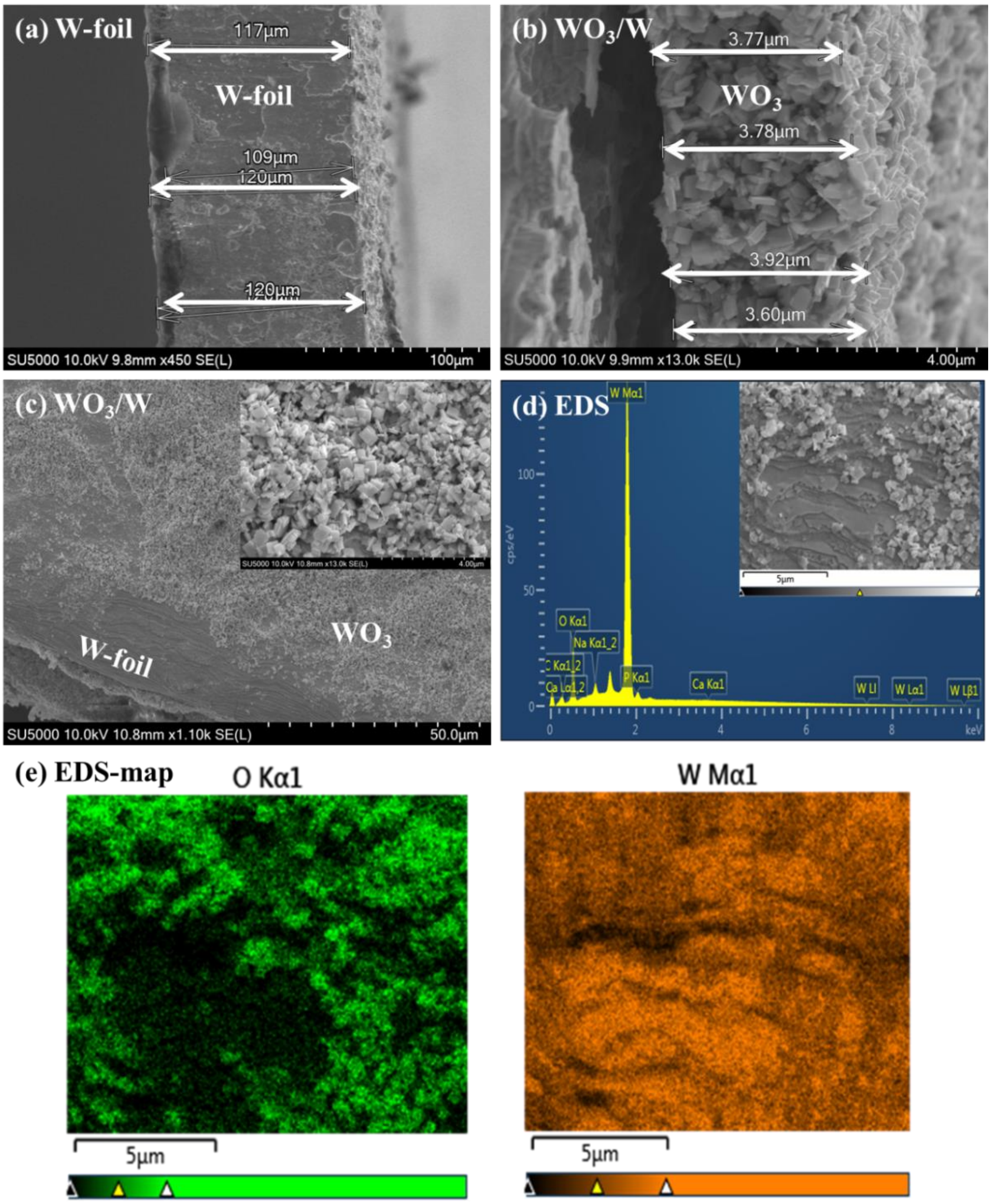

Figure 6.2 SEM images of WO_3 nanoplates immobilised on W-foil electrode (a) cross-section SEM of W-foil, (b) cross-section SEM of WO_3/W electrode, (c) top-view of WO_3/W electrode surface; inset: WO_3 nanoplates deposited on the surface, (d) EDS spectrum of WO_3/W surface and (e) elemental mapping of the WO_3 deposition on W-foil. The inset shown in the EDS spectrum is also the corresponding area analysed for the maps.

The high-resolution SEM scan of heterostructure WCN91 immobilised on W as the electrode is displayed in figure 6.3. The flake-like structures of g-C_3N_4 are visible across the WO_3 nanoplates.

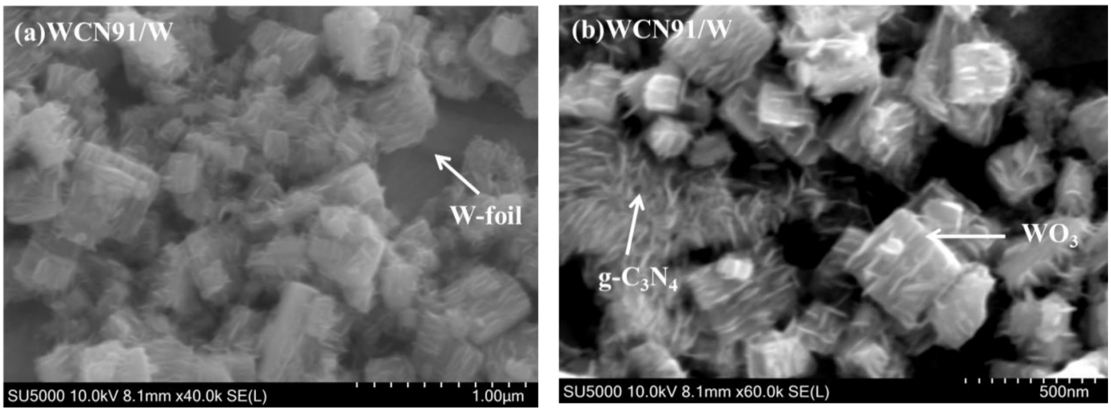

Figure 6.3 SEM images of WCN91/W electrodes. (a) Top-view SEM of sample deposited on W-foil, (b) zoomed image of grafting of g-C_3N_4 flake around WO_3 nanoplates.

An EDS analysis of a section of the electrode surface confirmed the presence of g-C_3N_4 in mixture with WO_3, as shown in figure 6.4. The EDS electron image shown in figure 6.4 was taken as the area of interest, where a distinction between the substrate W foil and the deposited sample WCN91 could be made. The corresponding maps of elements C, N, O and W are also shown. From the EDS analysis, it was clear the W signal of 33.0% was attributed from the substrate and the samples found across the entire area of investigation. However, a maximum signal of O was obtained with 55.4% in regions where the sample (WCN91) was deposited, albeit the O was due to WO_3. Similarly, the maps of C (10.1%) and N (<1%) were seen as a result of g-C_3N_4 content in the WCN91. Negligible signals of C or N could be found in regions of empty W foil.

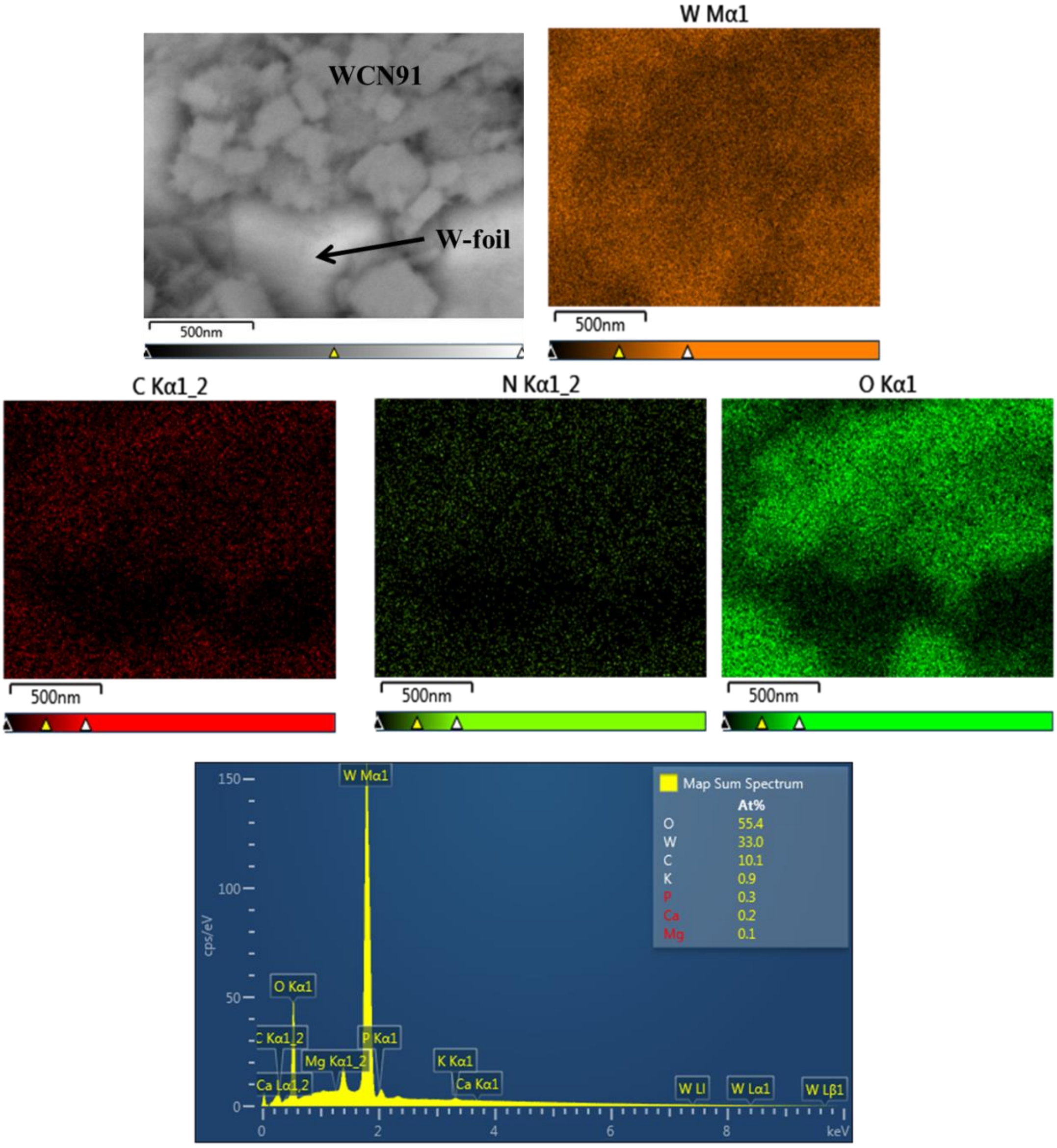

Figure 6.4 EDS analysis of WCN91/W electrodes with the corresponding elemental mapping and EDS spectrum.

A second region where only g-C_3N_4 could be observed by scanning the surface of the electrode was selected. This area was analysed by line scan EDS. The electron image of the area of interest is shown in figure 6.5, constituting mainly of g-C_3N_4 flakes and less WO_3 nanoplates. The W counts (cps) were decreasing at the centre of the material, i.e. from 12000 cps (entire region) to 9000 (on the top of the featured material). On the contrary, the oxygen signal counts were increased around the centre material, i.e. from 0 to ~ 3000 cps. The counts per second (cps) of N and C are similar (~300 cps) at the centre of the material. The total content of oxygen across the entire line scanned was found to be 42% as compared to that of 43.3% of W (the majority of the W signal was from substrate W foil), 14.8% of C and N(<1%). The atomic % of N signal was found below the limit of detection of the line scan, i.e. < 1 %. The 10x times higher counts (~3000 cps) were measured for oxygen at the centre of the material analysed, indicated about the oxidation of sample, precisely oxidation of g-C_3N_4 in the mixture. As illustrated before, no significant W signals from WO_3 were observed in the featured area. Therefore, any oxygen present was associated with g-C_3N_4. The increment of O and possible reduction on N in the centre of the sample was in agreement to the changes in the O and N content observed in sample WCN91 through XPS investigations described in chapter 5. Pomilla et al.(2018) have also reported the decreasing of N-content in g-C_3N_4 on undergoing an oxidative treatment [198]. This leads to a higher photocatalytic activity but chemical instability and non-reproducibility of results using g-C_3N_4 in their study. The electrode WCN91 was annealed at 400°C in the air to form stable adhesion to the conductive substrate before analysing through SEM. It can be assumed a similar oxidative treatment was given to g-C_3N_4 content in this sample during the annealing step. Therefore, the changes in oxygen content observed in the present sample can be possibly the replacement of N with O in g-C_3N_4 as a result of annealing.

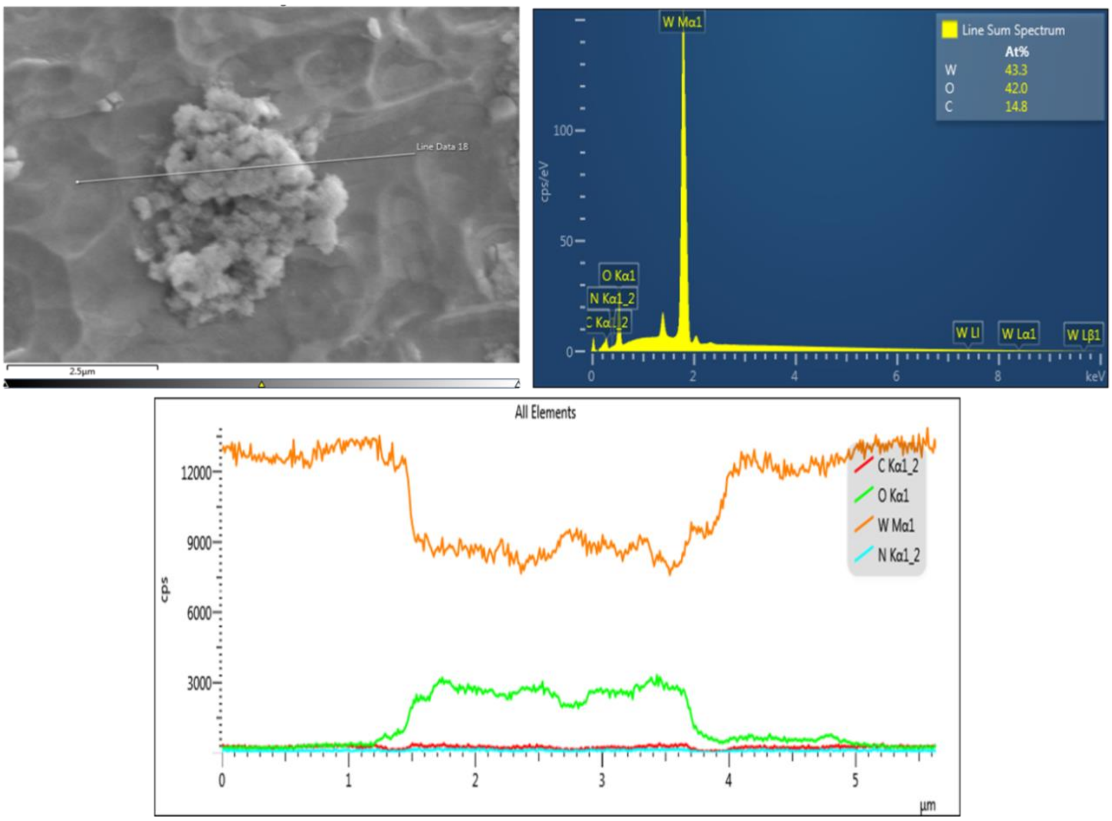

Figure 6.5 EDS analysis of WCN91/W electrode in region-2.

The electrodes depositing using PEDOT:PSS on conductive ITO glass were also characterized through SEM. In figure 6.6, cross-sectional SEM of WO_3 nanoplates deposited on PEDOT/ITO has been demonstrated. The thickness of WO_3/PEDOT on ITO was measured to be ~1 μm. The film deposited as seen from figure 6.6(a) and (b) are relative of equal thickness. A 200 nm (0.2 μm) thick layer of ITO was coated on the glass substrate, and it was in agreement with the information provided by the supplier (Diamond Coating, Ltd.). A line EDS spectrum of the cross-section of WO_3/PEDOT/ITO electrode was performed as per the selected electron image in figure 6.6(c). In the EDS spectrum (Figure 6.6(d)), atomic percentage (at %) of O was 38.7% that was the highest. The sources of O are all the components of this electrode, i.e. WO_3, PEDOT: PSS, ITO and glass (mainly SiO). A carbon atomic percentage of 37.8% was present in the cross-section area analysed. The source of carbon across the cross-section was PEDOT:PSS. PEDOT:PSS is a polymeric mixture of sulfonated polystyrene and 3,4- ethylene dioxythiophene. Therefore, the presence of carbon (C) and sulphur (S) in the EDS spectrum is a confirmation of the PEDOT:PSS. The sharp peak of Si is a result of SiO, i.e. glass and In (2.1%) and Sn (0.4%) were detected around the ITO coating. W (3.6%) was attributed to WO_3 nanoplates.

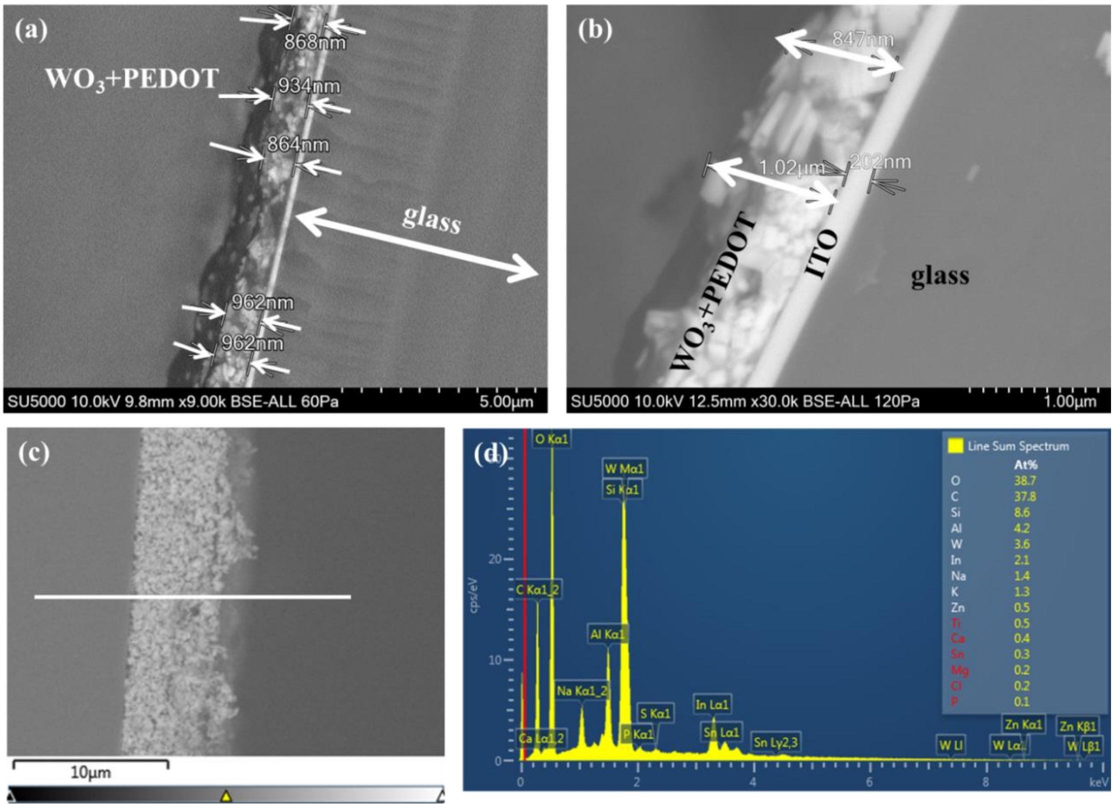

Figure 6.6 (a) Cross-sectional SEM of WO_3 nanoplates deposited on PEDOT/ITO with film thickness measurements (b) higher magnification for WO_3/PEDOT/ITO at the interface, (c) electron map image of the line scan performed at WO_3/PEDOT/ITO and (d) the corresponding EDS spectrum

The cross-sectional SEM image for WO_3/g-C_3N_4 heterostructure WCN91 deposited on ITO glass is illustrated in figure 6.7. A thick layer of ~2 μm was measured for WCN91/PEDOT deposited on ITO. The thickness observed was 2x times to WO_3/PEDOT deposition on ITO, although the method of slurry deposition was the same in both cases. The increased thickness could be due to the presence of g-C_3N_4 flakes, that are always found in the agglomerated form. The EDS map of the electron image shown in figure 6.7(b) reveals the presence of g-C_3N_4 across the entire surface with N signals highlighted in the maps. g-C_3N_4 is the only source of N present in the sample; hence signals of N are due to g-C_3N_4. The content of C was found to be distributed across the entire region, and a total of 51.8% of C was observed in the spectrum. The presence of N and increase in C% from 37.8% in WO_3/PEDOT/ITO to 51.8% in WCN91/PEDOT/ITO is a confirmation of g-C_3N_4 in the mixture. The W and O signals distributed equally across the entire surface were a result of WO_3, with oxygen being a composition in WO_3, PEDOT, ITO and SiO (glass). The glass substrate showed a background signal of Si (7.8%).

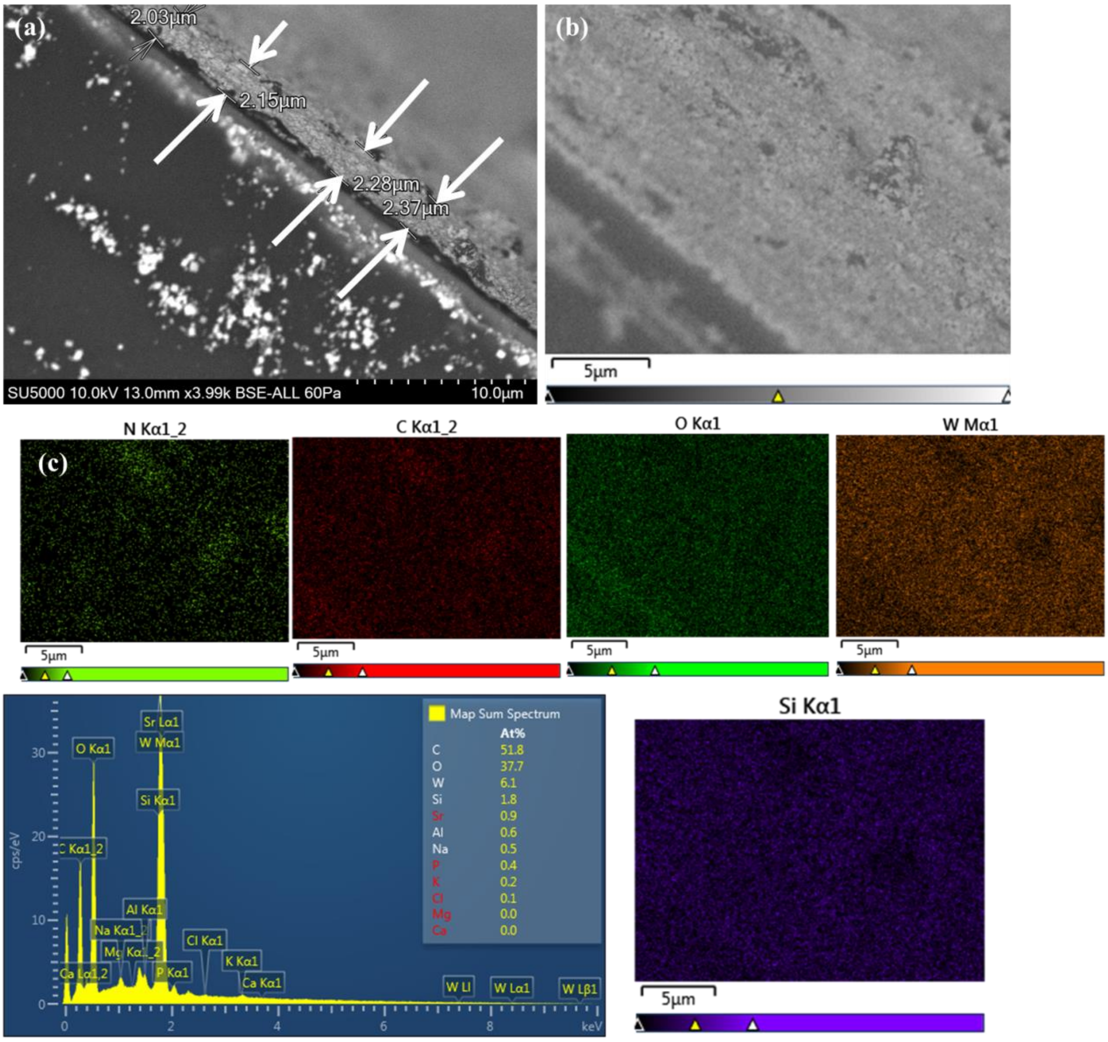

Map Sum Spectrum

	At%
C	51.8
O	37.7
W	6.1
Si	1.8
Sr	0.9
Al	0.6
Na	0.5
P	0.4
K	0.2
Cl	0.1
Mg	0.0
Ca	0.0

Figure 6.7 (a) Cross-sectional SEM of WCN91 deposited on PEDOT/ITO with film thickness measurements of the deposited heterostructure (b) electron map image of the surface of WCN91/PEDOT/ITO (c) the corresponding EDS element maps and EDS spectrum for WCN91/PEDOT/ITO.

6.4.2 Photoelectrochemical studies

6.4.2.1 Photoelectrochemical studies in pH 1 electrolyte

The photoelectrochemical response of the WO_3/g-C_3N_4, WO_3 and g-C_3N_4 electrodes were determined using linear sweep voltammetry and current-time response at fixed potential under chopped irradiation. The materials tested in this chapter were selected based on their photocatalytic performance for RNO bleaching from chapter 5.

The linear sweep voltammograms for samples WO_3, g-C_3N_4 and WO_3/g-C_3N_4 were recorded by sweeping potential from 0 to +1.0 V under chopped polychromatic UV-visible irradiation at every 10 s (figure 6.8). It is observed that WO_3 and WO_3/g-C_3N_4 heterostructures showed typical n-type semiconductor behaviour. Since these experiments were done in supporting electrolyte of pH 1 (0.1 M $HClO_4$), it is assumed that water oxidation is the reaction driven by the holes. The WO_3/g-C_3N_4 samples exhibit a higher photocurrent density compared to WO_3 alone over the entire potential range. A photocurrent density of ~ 12 $\mu A.cm^{-2}$ was observed for WCN91 at +1.0 V through LSV measurements. On applying a bias, the photogenerated electrons from the semiconductor are collected at the supporting Pt electrode as a photocurrent, and the holes react with the electrolyte solution. From figure 6.9, it is clear no evident photocurrent was observed through g-C_3N_4 across the potential range of 0 to +1.0 V.

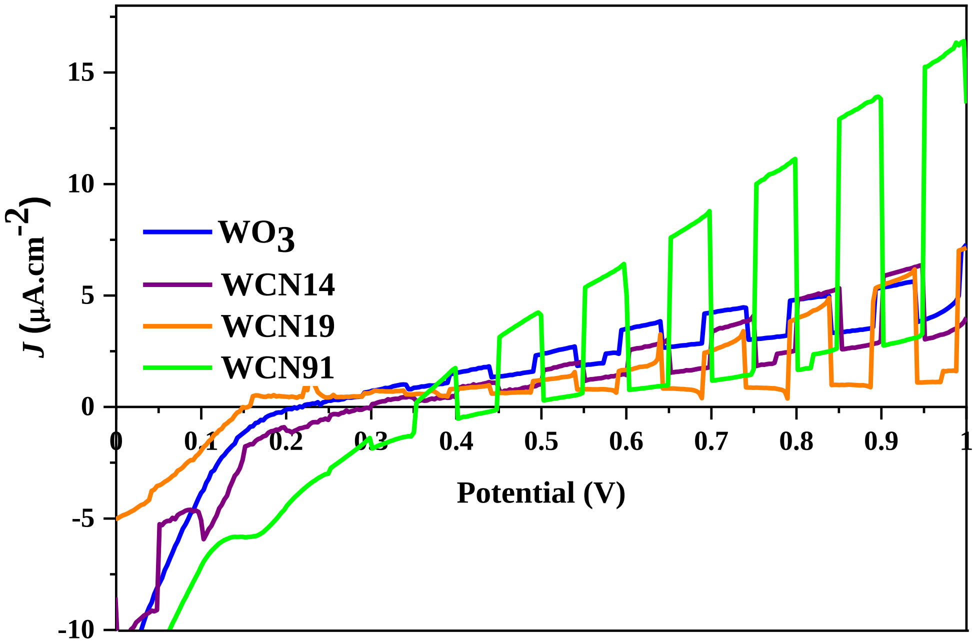

Figure 6.8 LSV for different electrodes with W foil as the conducting support (sweeping potential positive from 0.0 to +1.0 V at scan rate = 5 mV.s^{-1}; electrolyte = 0.1 M $HClO_4$ pH 1, UV-Vis irradiation chopped every 10 s)

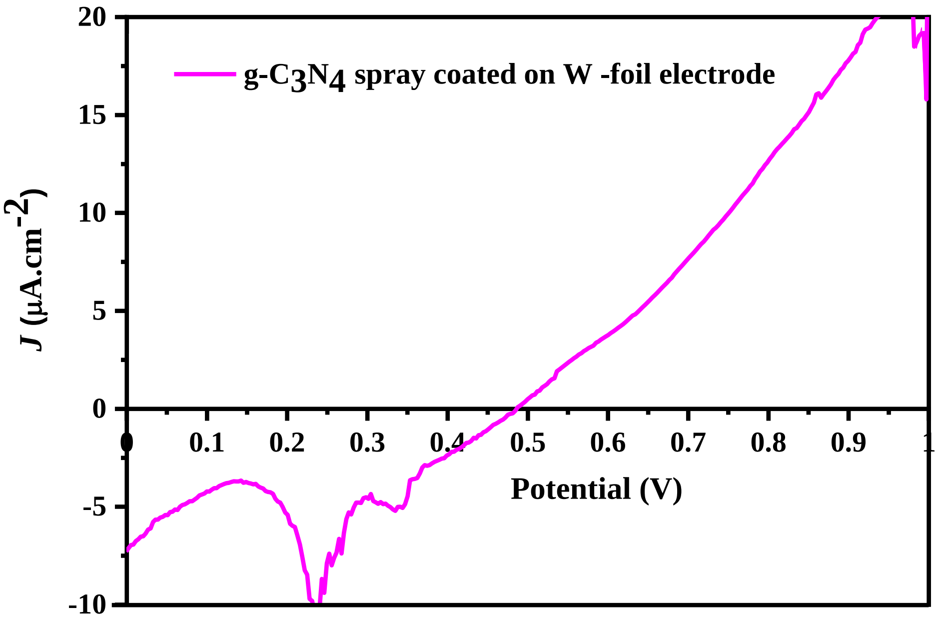

Figure 6.9 LSV for g-C_3N_4 electrode on W foil as the conducting support (sweeping potential positive from 0.0 to +1.0 V at scan rate = 5 mV.s^{-1}; electrolyte = 0.1 M $HClO_4$ pH 1; UV-Vis irradiation chopped every 10 s).

A blank W-foil electrode was also analysed to see the effect of the substrate on the current density of the immobilised electrodes. As shown in figure 6.10, no difference in the light and dark current was observed for W-foil under irradiation.

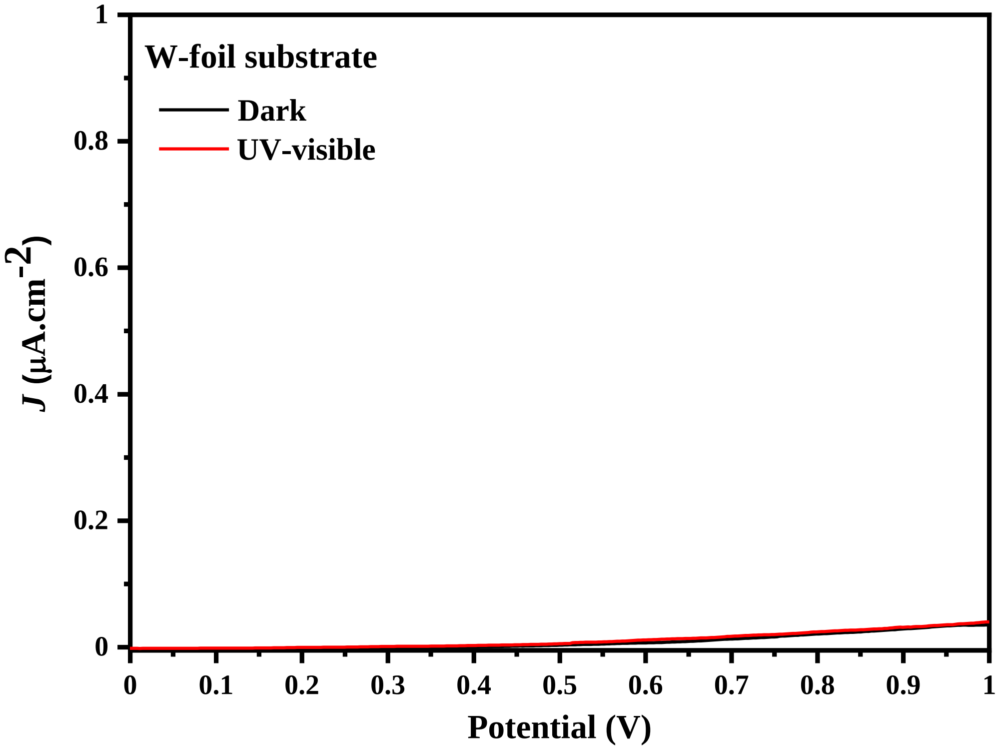

Figure 6.10 I-V curve for blank W-foil electrode in UV-Vis irradiation (sweeping potential positive from 0.0 to +1.0 V at scan rate = 5 mV.s^{-1}; electrolyte = 0.1 M $HClO_4$ pH 1)

The current at fixed potential versus irradiation time was also analysed for the WO_3, WO_3/g-C_3N_4 and g-C_3N_4 electrodes at the fixed potential of +1.0 V (SCE). The applied potential of +1.0 V was selected on observation of saturated photocurrent received at this potential through LSV investigations. As shown in figure 6.11, the photocurrent density of the electrodes was recorded with UV-visible irradiation chopped ON and OFF at every 200 s. The electrode WCN91 exhibits a steady-state photocurrent density of 12.14 µA.cm^{-2} at an applied potential +1.0 V, which was in agreement to photocurrent observed through LSV measurements (shown in figure 6.8). WCN19 was observed to have a steady-state photocurrent density of 5.64 µA.cm^{-2}. The WO_3 electrode showed a steady-state photocurrent density of 1.82 µA.cm^{-2} at +1.0 V applied potential.

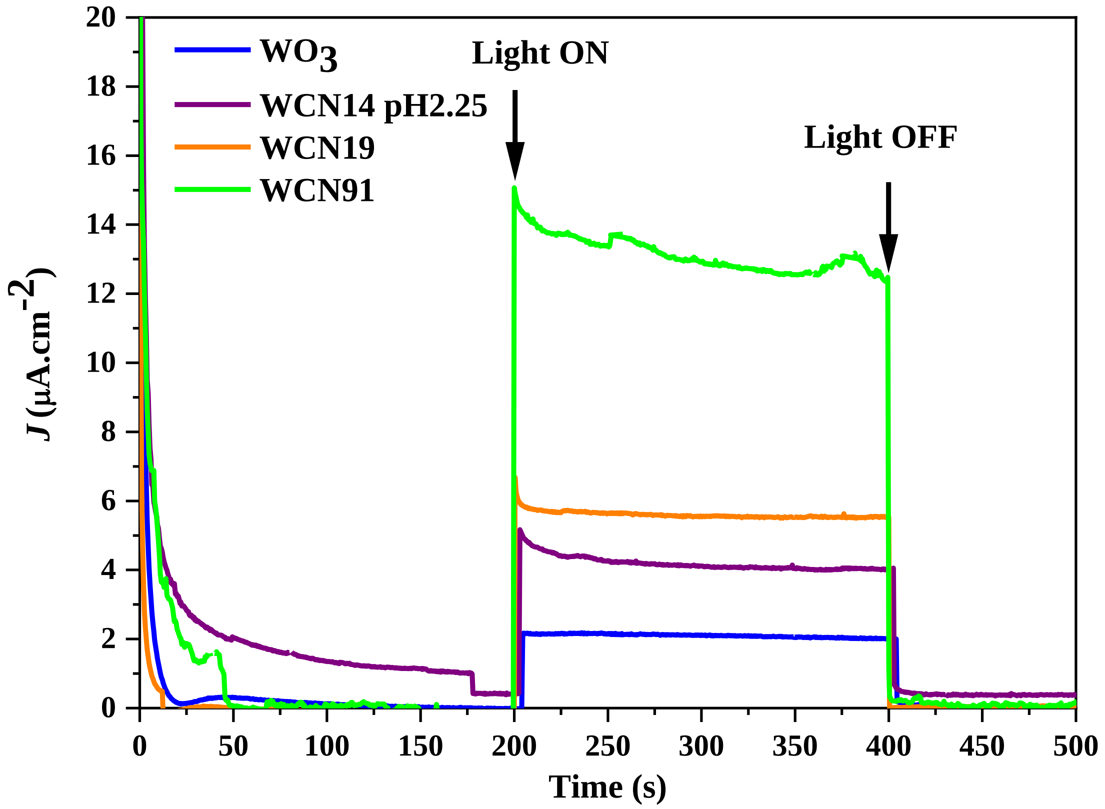

Figure 6.11 Current density vs time at fixed potential (+1.0 V) for different electrodes under chopped irradiation (electrolyte = 0.1 M $HClO_4$ pH 1)

No significant photocurrent was generated by g-C_3N_4 at +1.0 V under irradiation in the same conditions. The lack of photocurrent response exhibited by g-C_3N_4 (Figure 6.12) may also have been due to the film instability. Though, the material was spray-coated and annealed at similar conditions to WO_3. Some detachment of the film from the W foil was observed when in contact with the electrolyte under bias. With the g-C_3N_4/WO_3 heterostructure, a significant increase in the photocurrent density was observed with 7x times higher photocurrent in WCN91 as compared to WO_3 alone.

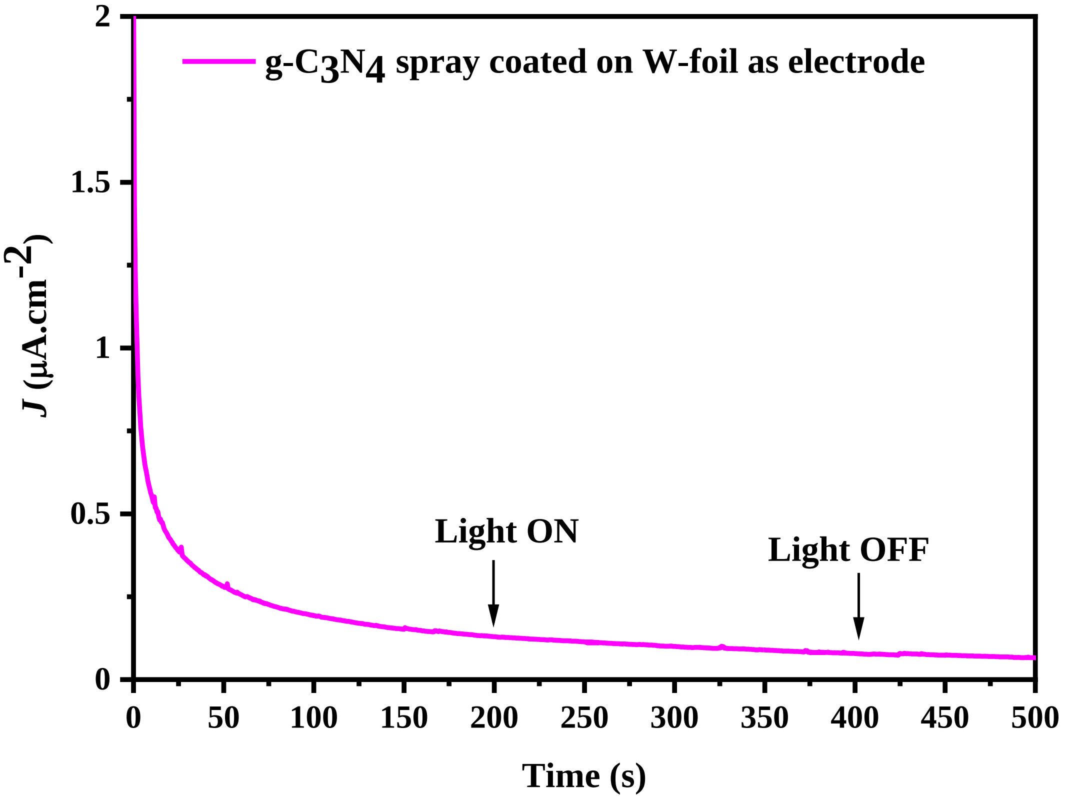

Figure 6.12 Current density vs time at fixed potential (+1.0 V) for g-C_3N_4 on W foil prepared by spray-coating (electrolyte = 0.1 M $HClO_4$ pH 1)

The spectral photocurrent response was measured at a fixed potential of +1.0 V for all the samples (figure 6.13-6.16). All electrodes show a measurable photocurrent response up to 450 nm. The WO_3 (figure 6.13) and WCN91 (figure 6.16) electrodes gave photocurrent response up to 460 nm. The WCN91 gave the highest photocurrent density through the spectral range from 250-500 nm. WO_3 shows the highest peak range between 310-350 nm. For g-C_3N_4, the photocurrent response was low, (<0.5µA) from 260-450 nm, (figure 6.14). The WO_3/g-C_3N_4 heterostructures WCN14 (figure 6.15) and WCN91 (figure 6.16) have higher photocurrent density as compared to WO_3 (figure 6.13) and g-C_3N_4 (figure 6.14) in the spectral range 250-500 nm.

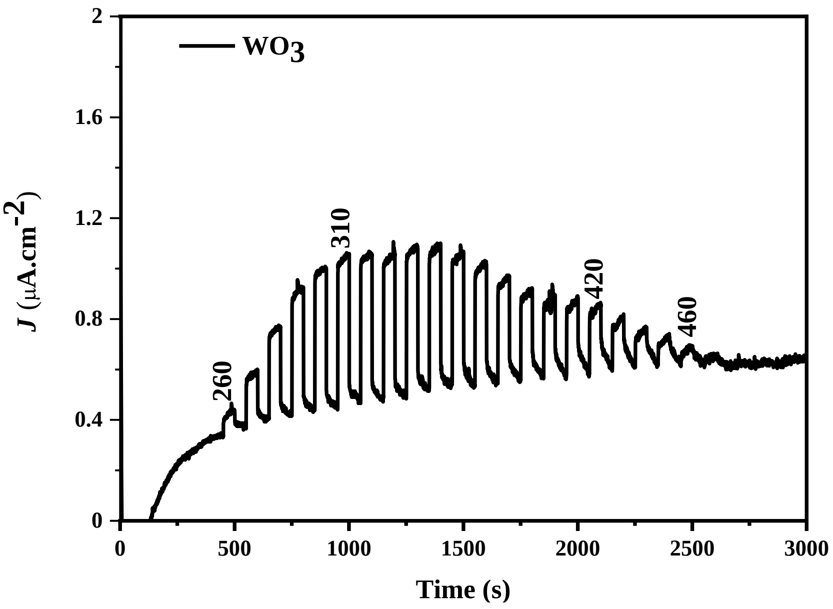

Figure 6.13 Spectral current density for WO_3. The number indicates the peak wavelength where photocurrent was observed with 10 nm increments from 250-500 nm. Electrolyte = 0.1 M $HClO_4$ (pH 1), applied potential = +1.0 V, exposure delay cycle = 50 s, irradiation = monochromatic 450 W Xe light source.

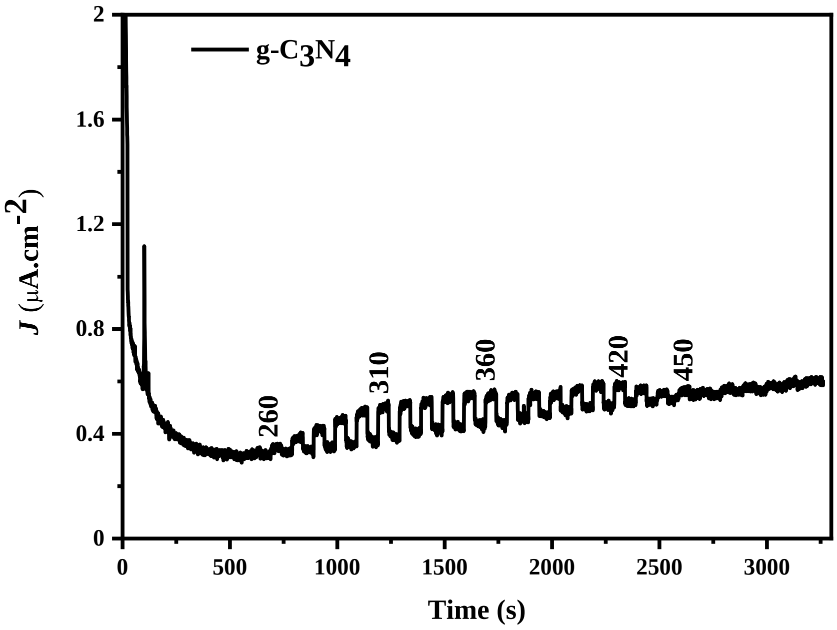

Figure 6.14 Spectral current density for g-C_3N_4.The number indicates the peak wavelength where photocurrent was observed with 10 nm increments from 250-500 nm. Electrolyte = 0.1 M $HClO_4$ (pH 1), applied potential = +1.0 V, exposure delay cycle = 50 s, irradiation = monochromatic 450 W Xe light source.

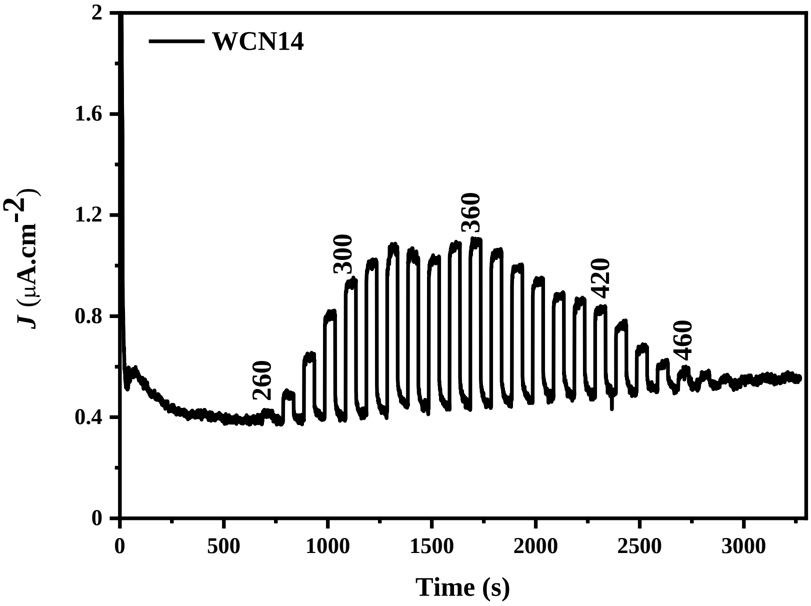

Figure 6.15 Spectral current density for WCN14. The number indicates the peak wavelength where photocurrent was observed with 10 nm increments from 250-500 nm. Electrolyte = 0.1 M $HClO_4$ (pH 1), applied potential = +1.0 V, exposure delay cycle = 50 s, irradiation = monochromatic 450 W Xe light source.

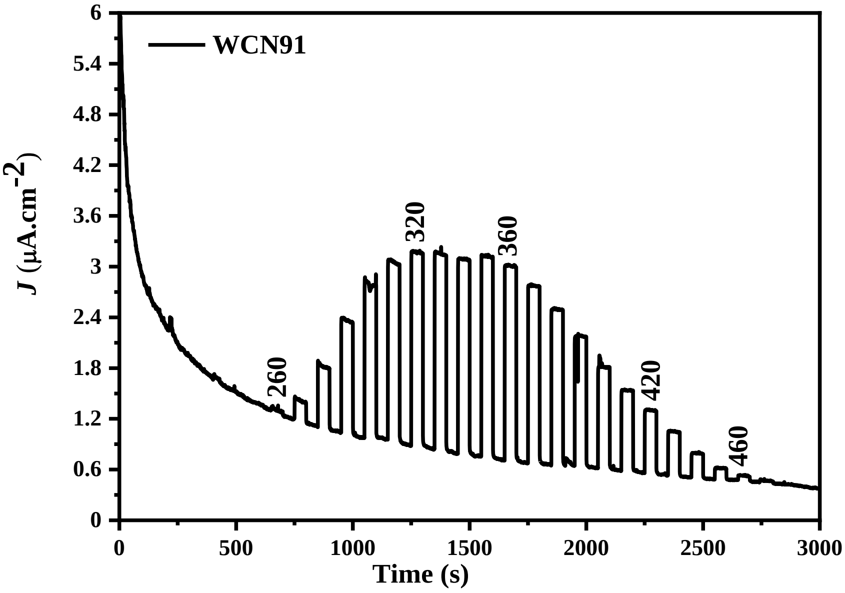

Figure 6.16 Spectral current density for WCN91. The number indicates the peak wavelength where photocurrent was observed with 10 nm increments from 250-500 nm. Electrolyte = 0.1 M $HClO_4$ (pH 1), applied potential = +1.0 V, exposure delay cycle = 50 s, irradiation = monochromatic 450 W Xe light source.

The spectral photocurrent response of WO_3, g-C_3N_4, heterostructures WCN19, WCN(14)pH2.25 and WCN91, along with the monochromatic photon flux were used to calculate the incident photon to current conversion efficiency (IPCE %). The IPCE % data for all the WO_3/g-C_3N_4 samples is given in figure 6.17. WCN19 showed the highest peak efficiency of 2.5% at wavelength 290 nm. Whereas, WCN91 demonstrated a peak efficiency of 2% around 320 nm compared to only 0.52 % for WO_3. The IPCE % was observed to be higher with WCN91 for a broader range of wavelengths compared to WO_3 or WCN19.

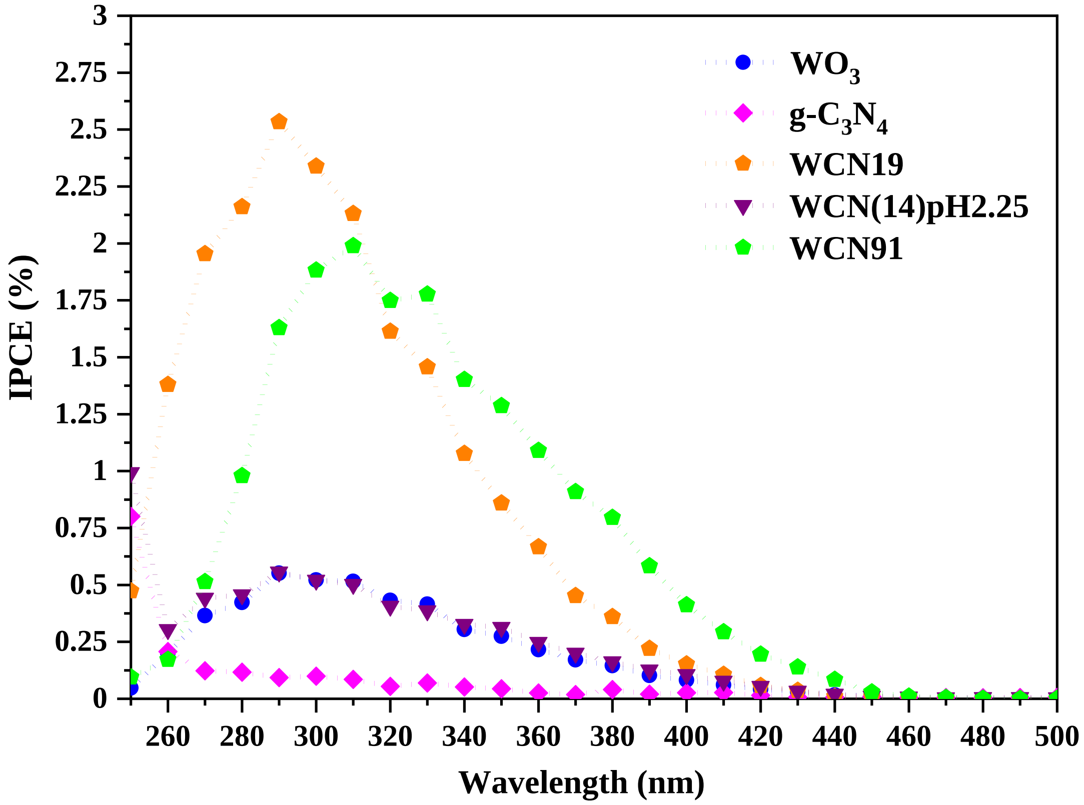

Figure 6.17 IPCE % vs wavelength for WO_3 nanoplates, g-C_3N_4 and heterostructures WCN19, WCN14 (pH2.25) and WCN91.

The WCN91 electrode was also tested for its stability over prolonged irradiation time to determine if there was any decay in the response. As seen in figure 6.18, the current density for WCN91 was maintained over 3 h of irradiation.

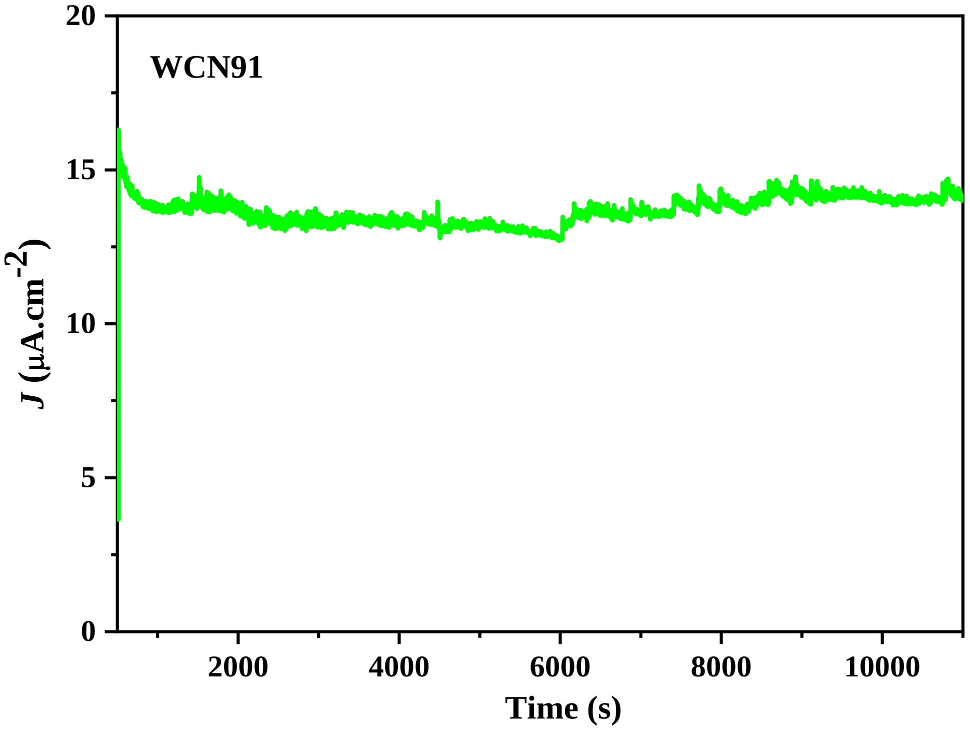

Figure 6.18 Current density vs time for WCN91 electrode. (Applied potential = +1.0 V; electrolyte = 0.1 M $HClO_4$ (pH 1) in 3 h OFN spurging).

The increase in the anodic photocurrent in WCN91 electrode correlated to the improved $^{\bullet}OH$ production observed using WCN91 (+ $AgNO_3$ as an electron acceptor) as a suspended photocatalyst for RNO degradation in chapter 5. Although the $^{\bullet}OH$ production under EAP conditions was not investigated in the present work, assuming anodic photocurrent is a measure of water oxidation and hydroxyl radical production is also a result of water oxidation. A better charge separation of electron-hole pair was attainable for sample WCN91 making it a potential candidate for water splitting. On comparing the photoelectrochemical studies of WO_3, g-C_3N_4 and WO_3/g-C_3N_4 heterostructures, WCN91 showed the maximum photocurrent density in all the measurements and stability over prolonged UV-Vis irradiation (> 3 h). Further experiments to determine the efficiency for disinfection were undertaken with the WCN91 electrode.

6.4.2.2 Photoelectrochemical studies in pH 7 Ringer's solution

Ringer's solution is normally used as the electrolyte for electrochemically assisted photocatalytic (EAP) disinfection tests to maintain an osmotic balance for the bacterial cells. Therefore, before testing the EAP disinfection activity of prepared electrodes, measurements of current at a fixed potential of +1.0 V were performed in pH 7 Ringer's solution. The spray-coated WO_3/ W foil electrode was investigated in pH 7 electrolyte and is shown in figure 6.19. A photocurrent density of 4.78 µA.cm^{-2} was observed for WO_3 on applying a fixed potential of +1.0 V. Previously, the photocurrent density obtained at pH 1 was 1.82 µA.cm^{-2} for the same electrode. Therefore, an increase in photocurrent density which is 2.6x times higher in pH 7 than pH 1 was observed for WO_3 electrodes. However, on comparing the decay of photocurrent, it was observed that the photocurrent decay (initial J_{ph} - steady-state J_{ph}) was slower at pH 1(0.30 µA) than at pH 7 (0.95 µA) for WO_3. At pH 7, the increased photocurrent density and faster decay of photocurrent can be due to the interaction of ions with electrode surface [66, 287]. A direct effect of cations such as Na^+, K^+, Li^+ and also anions such as Cl^-, ClO_4^- on the photocurrent density and water oxidation (ca. O_2 evolution) has been reported by Choi et al.(2012) with WO_3 electrodes [287]. The same authors also reported that the dominant photo-oxidation reaction is the oxidation of chloride ions instead of water oxidation. The oxidation potential for Cl^- is +1.36 V (NHE) as compared to +1.23 V (NHE) for water oxidation. Although the potential of chloride oxidation is more positive than water oxidation, it is still an alternative reaction occurring due to poor kinetics of O_2 evolution on the WO_3 surface. The oxidation of chloride to chlorine/hypochlorite is a 2-electron reaction (eq. 6.1) as compared to water oxidation that requires 4 electrons (eq. 6.2).

$$2Cl^- \rightarrow Cl_2 + 2e^- \qquad E^0 = 1.36 \text{ V (NHE)} \qquad 6.1$$

$$2H_2O \rightarrow 4H^+ + O_2 + 4e^- \quad E^0 = 1.23 \text{ V (NHE)} \qquad 6.2$$

The Ringer's solution mostly consists of chloride ions (NaCl (2.25 g.L^{-1}) + $CaCl_2$ (0.12 g.L^{-1}) + KCl (0.11 g.L^{-1})). The negatively charged anions can adsorb on the positively charged WO_3 anode and consume the majority of photogenerated holes from the VB of WO_3, thus lowering the overpotential required to drive the chloride oxidation reaction. Therefore, it is expected that Cl^- oxidation will compete with water oxidation and lower the photocurrent over time.

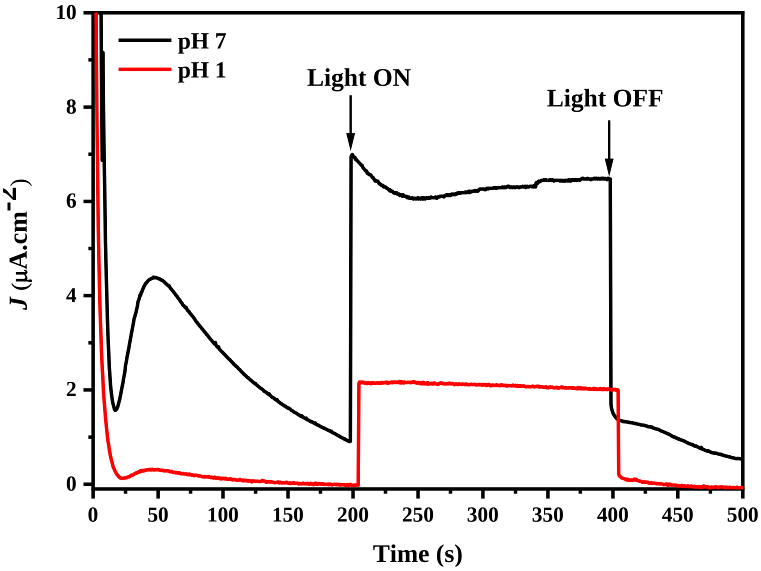

Figure 6.19 Comparison of current density at a fixed potential (+1.0 V) with WO_3/W electrodes in pH 1 and pH 7 electrolyte, delay exposure cycle = 200 s.

The heterostructure WCN91 was also studied further in terms of its photoelectrochemical performance in Ringer's solution at pH 7. However, the response obtained at pH 7 and applied potential +1.0 V was unexpected. The photocurrent density of ~ 16 µA.cm^{--2} was observed for WCN91/W foil electrode, as shown in figure 6.20. However, the initial photocurrent at light ON (200 s) was ~ 2.5 µA.cm^{--2}; thereby a continuous increase was observed until a steady state was reached before the light was chopped OFF at 400 s.

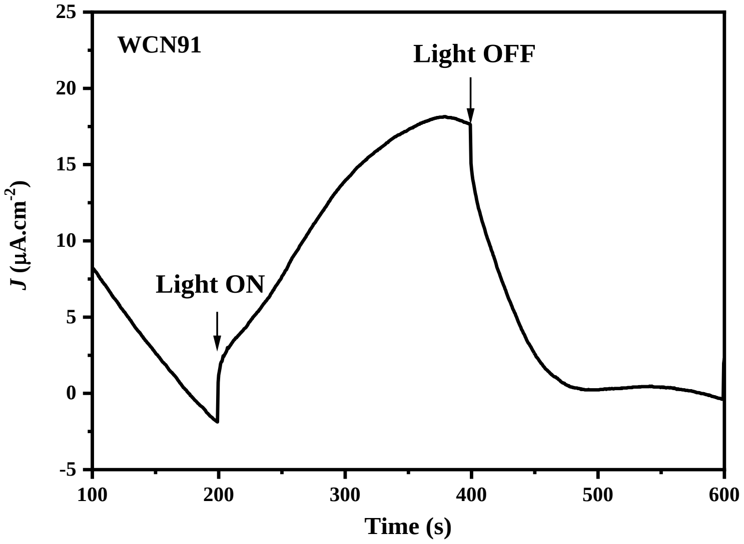

Figure 6.20 Current density at a fixed potential (+1.0 V) with WCN91/W electrodes, (electrolyte = 1/4th strength Ringer's solution pH 7; delay exposure cycle = 200 s).

$g\text{-}C_3N_4$ was deposited on the ITO conductive glass using the organic binder PEDOT:PSS. The latter is used as a hole transport agent in organic photovoltaic cells [155]. No photocurrent response was found with PEDOT:PSS alone. The photocurrent at a fixed potential (+1.0 V) obtained at pH 7 for WO_3, $g\text{-}C_3N_4$ and heterostructure WCN91 prepared on PEDOT/ITO electrodes is illustrated in figure 6.21. As shown, an apparent enhancement of photocurrent density was observed for WCN91/PEDOT/ITO electrode over its parent materials WO_3/PEDOT/ITO and $g\text{-}C_3N_4$/PEDOT/ITO electrode. Roughly, a photocurrent density of 10 $\mu A.cm^{-2}$ was observed for WCN91, whereas the photocurrent density was < 1 $\mu A.\ cm^{-2}$ in both WO_3 and $g\text{-}C_3N_4$ deposited on PEDOT/ITO. Considering the photocurrent obtained at both pH 1 and pH 7 and with different conductive substrates was always higher for the heterostructure WCN91 over WO_3, this sample was tested for photoelectrochemical inactivation of *E. coli* K12 in the following sections.

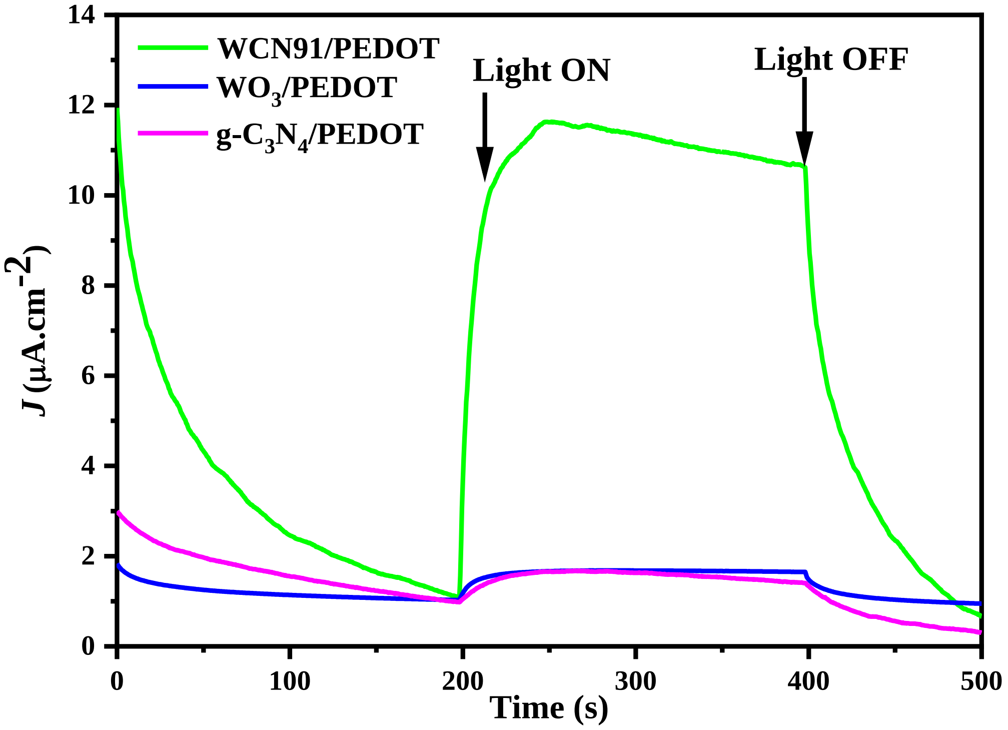

Figure 6.21 Current density at a fixed potential (+1.0 V) with PEDOT/ITO electrodes, (electrolyte = 1/4th strength Ringer's solution pH 7; delay exposure cycle = 200 s).

6.4.3 Electrochemically assisted photocatalytic (EAP) disinfection

6.4.3.1 EAP with spray-coated W-foil electrodes

The WO_3/g-C_3N_4 heterostructure sample WCN91 was studied as the photoanode for EAP inactivation of *E. coli*. For comparison, the WO_3 photoelectrode was also tested. For each set of electrodes, experiments in dark at +1.0 V as electrocatalysis (EC), electrodes under irradiation at open circuit, i.e. photocatalysis (PC), and EAP at +1.0 V were performed.

Initial control experiments were performed to assess the *E. coli* inactivation due to photolysis and osmotic stress. No reduction in *E. coli* was observed in the dark with electrolyte Ringer's solution (figure 6.22). Irradiation of the photoelectrochemical reactor with UV-visible photons alone (no photocatalyst) resulted in a 2-log reduction of *E. coli* over 4 h of irradiation. The photo-inactivation obtained in this experiment is approximately 33% lower than those reported under real sun conditions (solar disinfection). Considering the spectral dose obtained from the light source in the present study is 1/3rd of the AM1.5 G spectrum, these results correlate well to real sun experiments for solar water disinfection [17, 201, 202].

The *E. coli* inactivation using WCN91 as the photoanode is also shown in figure 6.22. For photocatalysis a 3.5-log reduction of *E. coli* in 4 h was observed using WCN91, which is a greater reduction than photo-inactivation (irradiation but no catalyst). On applying a potential of +1.0 V (SCE) to the anode under UV-Vis irradiation (EAP), a 6-log reduction (~10^6 CFU.mL^{-1}) of *E. coli* was observed in 150 min reaching the detection limit of 2 CFU mL^{-1}. The faster disinfection observed with EAP (+1.0 V) over PC can be attributed to the enhanced charge carrier separation due to the electric field. Interestingly, with an applied potential but no irradiation of the electrode (+1.0 V, electrolysis), a 2-log reduction in *E. coli* was observed in 4 h. The inactivation of *E.coli* under electrocatalytic conditions (i.e. +1V, dark) can also be due to potential formation of some reactive chlorine species (RCS)/reactive oxygen species from the dissolved chlorides/oxygen in the water. Due to the use of Ringer's solution that consists of high concentration of chloride ions, these Cl^- ions can potentially react at the anode surface leading to chloride oxidation to RCS formation at such positive anodic potential and contribute towards electrolytic disinfection.

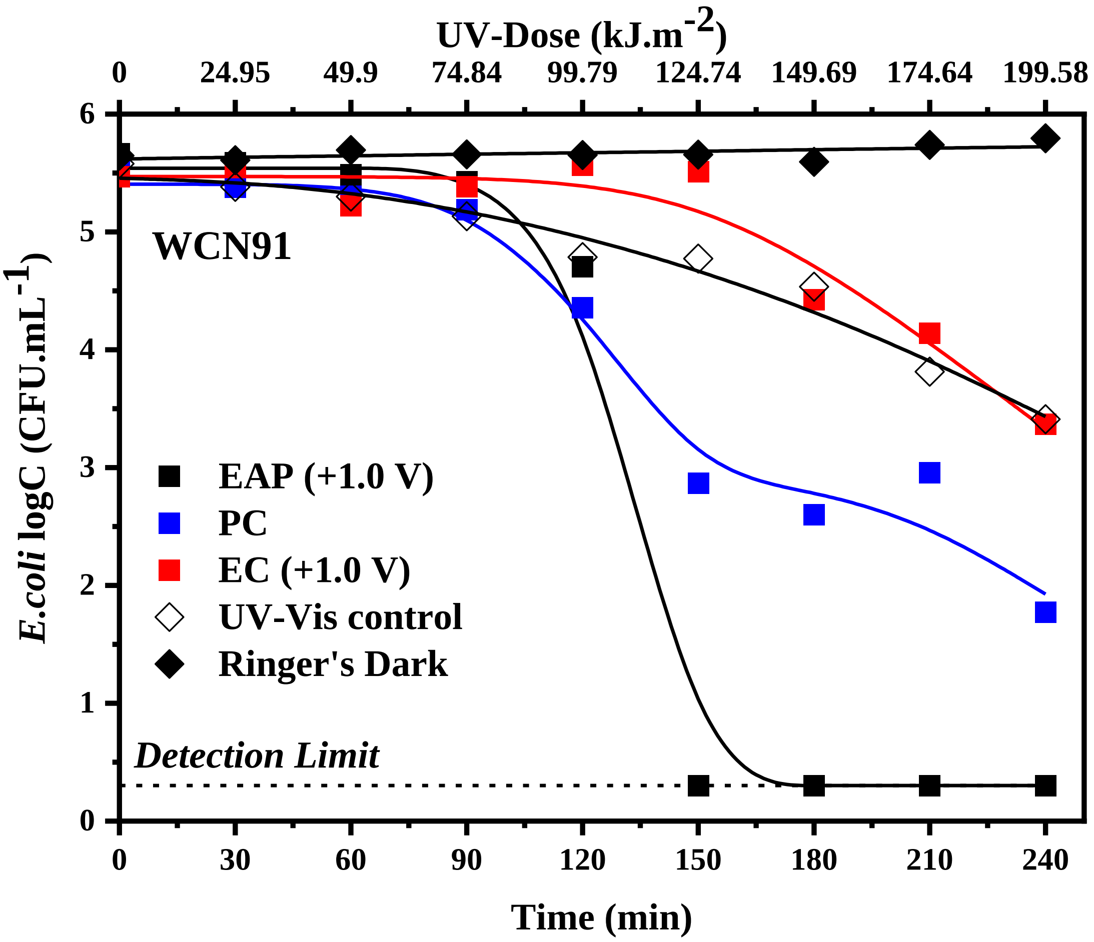

Figure 6.22 *E. coli* logC vs time for WCN91/W electrode under UV-visible irradiation; where EAP (+1.0 V) = electrochemically assisted photocatalysis; PC = photocatalysis under open-circuit conditions; EC (+1.0 V) = electrocatalysis. The solid lines represent the fitted data using GInaFIT models.

The EAP disinfection was also assessed using the WO_3 as the photoanode and is shown in figure 6.23. A 5.1-log reduction of *E. coli* was obtained in 4 h at +1.0 V applied potential. For photocatalysis (open circuit), WO_3 showed a 3.2-log reduction in the *E. coli* colonies forming units in 4 h, slightly less than that observed with the WCN91 electrode. However, no inactivation of *E. coli* was observed in dark electrocatalysis (+1.0 V) for WO_3. Recently, the photoelectrocatalytic inactivation of ~10^7 CFU.mL^{-1} of *E. coli* was reported using WO_3 photoelectrode in 4 h visible light irradiation (UV cut off filter $\lambda >$ 420 nm) by Choi et al.(2019) [66]. This result reported by the authors illustrates the inactivation in the presence of addition of 50 mM chloride ions (NaCl + NaOCl) to the electrolyte (pH 4 0.1M Na_2SO_4). In contrast, they achieved only 3.7-log reduction in *E. coli* cells without the chloride ions. However, it must be highlighted the results obtained in the present work cannot be directly compared to Choi et al.(2019), due to differences in operational parameters such as light intensity and applied potential (+0.5 V vs Ag/AgCl). Nevertheless, no other reports of using WO_3 as photoelectrode for microbial disinfection have been found.

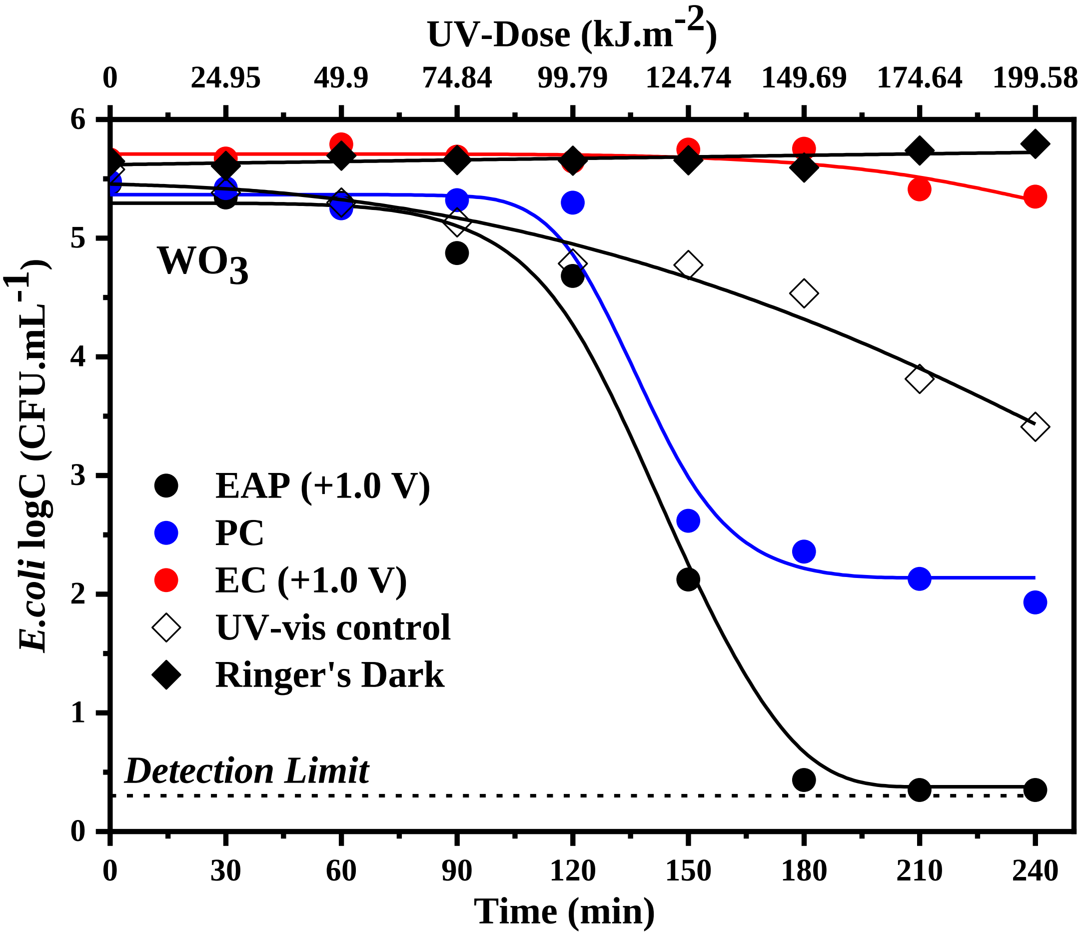

Figure 6.23 *E. coli* logC vs time for WO_3/W electrode under UV-visible irradiation, where EAP (+1.0 V) = electrochemically assisted photocatalysis; PC = photocatalysis under open-circuit conditions; EC (+1.0 V) = electrocatalysis. The solid lines represent the fitted data using GInaFIT models.

It is essential to model the disinfection kinetics using appropriate fitting models. GInaFIT modelling tool was utilised to fit the data obtained for each experiment to find a model with a line of best fit. Different types of GInaFIT model were explained in chapter 3 section 3.4.3.3 (and in figure 3.4). Briefly, a genuine fit is determined by applying the tool that gives the closest possible value for RMSE = 0 and $R^2 = 1$. In the present study, the *E. coli* inactivation data was modelled using different GInaFIT models with an obtained RMSE value for all data sets between 0.05-0.24. The kinetic parameters are displayed in table 6.1. In case, of photo-inactivation of *E. coli*, the best fit obtained was using Weibull model. In this model, the time taken to achieve first log reduction is denoted by δ, the scale parameter. The shape parameter, p represents the fit of the curve, i.e. $p<1$ concave curve is observed and if $p>1$ a convex curve is obtained. For the light control experiment, $p>1$ was seen, i.e. a convex fit. The electrocatalysis with WO_3 (+1.0 V) also followed a Weibull model with the convex fit. A Weibull + tail model with $p>1$ was followed by EAP-WO_3 and PC-WO_3 samples. However, a log-linear shoulder was observed as the best fit for EAP-WCN91 with a next to unity R^2 value and low RMS value of 0.082, representing the goodness of this model on the data set. The first order rate constant (k_{max}) observed for EAP-WCN91 was 0.61 ± 0.2 min^{-1}. The electrocatalysis with WCN91 followed a log-linear + shoulder fit, with 10x times slower k_{max} of 0.06 ± 0.01 min^{-1} as compared to EAP with WCN91 electrode. A clear comparison between all the samples analysed is difficult due to the complexity of the different models fitted based on giving the lowest possible RMSE and highest possible R^2 values. Still, the samples could be compared based on the Log of residual bacterial left after the 4 h irradiation time i.e. $Log_{10}N_{res}$. According to this kinetic parameter (also shown in table 6.1), the fastest degradation was achieved using EAP-WCN91 with $Log_{10}N_{res} = 0.30$ in 150 min, i.e. reaching the detection limit, followed by EAP-WO_3 with $Log_{10}N_{res} = 0.38$ in 240 min. Interestingly, the photocatalytic open-circuit conditions for both WCN91 and WO_3 showed faster inactivation kinetics as compared to photo-inactivation. The $Log_{10}N_{res}$ for PC-WCN91 was 1.93, and that of PC-WO_3 was 2.14, as compared to $Log_{10}N_{res} = 3.43$ for photolysis after 240 min.

Table 6.1 Kinetic fit parameters using the GInaFiT tool for nanomaterial/W electrodes

Sample	**Shoulder length (SI)**	**Rate (k_{max})**	**Scale parameter (δ)**	**Shape parameter (p)**	**Log$_{10}$ Nres**	**RMSE**	**R^2**
Light*	-	-	169.7±11.3	2.03±0.3	3.43	0.138	0.973
Dark	-	0.00	-	-	5.72	0.055	0.319
EAP-WCN91‡	117.1±1.0	0.61	-	-	0.30	0.082	0.999
PC-WCN91	-	-	118.5±6.2 237.6±15.0	6.00±3.8	1.93	0.241	0.983
EC-WCN91‡	154±13.9	0.06	-	-	3.33	0.219	0.943
EAP-WO_3**	-	-	126.1±4.2	6.64±1.2	0.38	0.169	0.997
PC-WO_3**	-	-	140.6±6.1	16.6±1.1	2.14	0.156	0.994
EC-WO_3*	-	-	281.7±29.2	5.85±3.3	5.32	0.088	0.751

**Weibull model, **Weibull + tail model, ‡Log-linear + shoulder*

The results obtained in this work were compared to the results of previous work done at Ulster and published by Pablos et al.(2017). They used P25-TiO_2 electrode (electrophoretic deposition of P25-TiO_2 nanoparticles on Ti foil) and electrochemically anodised aligned titania nanotubes (Ti-NT) for electrochemically assisted photocatalytic disinfection [50]. The reaction conditions in the present work were kept the same as the ones reported by Pablos et al.(2017). Except, a slight difference in the irradiance was observed in the work of Pablos and the present work. For instance, the UV-visible light intensity in the present work was 185 $W.m^{-2}$ measured between 280-800 nm and Pablos et al.(2017), reported a light intensity of 197 $W.m^{-2}$ in UV-Vis region (250-800 nm). Pablos et al.(2017) reported a 5-log inactivation of *E. coli* K12(~10^6 $CFU.mL^{-1}$ as start concentration) in 120 min for Ti-NT under UV- Vis irradiation in EAP conditions of +1.0 V (SCE) [50]. However, the result reported by Pablos et al.(2017) for P25-TiO_2 electrodes was only ~4-log reduction in *E. coli* over irradiation time of 4 h under the same EAP conditions. A comparison of results from the present work and results from Pablos et al.(2017) is illustrated in table 6.2.

Table 6.2 Comparison of present EAP disinfection work with previous work at Ulster

Photoanode	***E. coli* reduction ($CFU.mL^{-1}$) (initial conc = 10^6 $CFU.mL^{-1}$)**	**UV-Vis irradiation time (min)**	**Detection limit ($CFU.mL^{-1}$)**	**Ref.**
P25-TiO_2	~ 10^4	240	10	[50]
Ti-NT	~ 10^5	120	10	
WO_3/W	~ 10^5	240	2	This work
WCN91/W	~10^6	150	2	

P25-TiO_2 *= electrophoretic deposition of P25-TiO_2 nanoparticles on Ti foil;* ***Ti-NT*** *= aligned anodised nanotubes on Ti foil;* ***WO_3/W*** *= 2D WO_3 nanoplates spray coated on W foil;* ***WCN91/W*** *= 2D WO_3/g-C_3N_4 heterostructure spray coated on W foil.*

As seen from table 6.2, the 2D photoelectrodes (WO_3/W and WCN91/W) prepared in the present work display a faster inactivation of *E. coli* in electrochemically assisted photocatalysis as compared to P25-TiO_2 electrodes, potentially due to their capability of absorbing more visible photons. When compared to Ti-NT, which was reported to show 5-log reduction in 120 min, a 6-log reduction of *E. coli* cells in 150 min was observed for WCN91/W electrodes. However, WO_3/W electrodes displayed a 5-log reduction in 240 min, (2x irradiation times as compared to Ti-NT). Considering the detection limit set by Pablos et al.(2017) was 10 CFU.mL^{-1} and detection limit in the present work was 2 CFU.mL^{-1}. A comparable activity for electrochemically assisted photocatalytic disinfection was obtained using the 2D photoelectrodes WO_3/W and WCN91/W against anodised titania nanotubes, i.e. Ti-NT. The observed results instead are very positive, indicating the potential for WO_3 and its heterostructures as photoanodes for photoelectrochemical disinfection of water under solar irradiation.

6.4.3.2 EAP with doctor bladed PEDOT/ITO electrodes

The photoelectrodes prepared by slurry deposition of nanomaterials mixed in PEDOT:PSS on ITO glass were also tested for EAP inactivation of *E. coli* in water under UV-Vis irradiation for 4 h. On applying an external potential +1.0 V (SCE) on PEDOT/ITO as the photoanode, a 1.2-log reduction in *E. coli* cells was observed in 4 h. The reduction observed was slower to the 2-log reduction observed for *E. coli* earlier as the photo-inactivation effect, also shown in figure 6.25. PEDOT:PSS had no effect of its own on the inactivation of *E. coli*. A 3-log reduction in *E. coli* was observed with g-C_3N_4/PEDOT/ITO as the photoanode in 4 h. However, the photocurrent density observed for the sample at +1.0 V was negligible (<1 µA.cm^{-2}). PEDOT:PSS acts as a hole conductor and transports the photogenerated holes to the semiconductor-electrolyte interface, thus, reducing the electron-hole pair recombination in g-C_3N_4. The EAP *E. coli* inactivation observed for WO_3/PEDOT/ITO reached the detection limit in 90 min with a 5.6-log total reduction. However, only 3.25-log reduction in *E. coli* was observed under EAP conditions for WCN91/PEDOT deposited on ITO electrodes, comparable to g-C_3N_4/PEDOT electrode but slower to WO_3/PEDOT electrode.

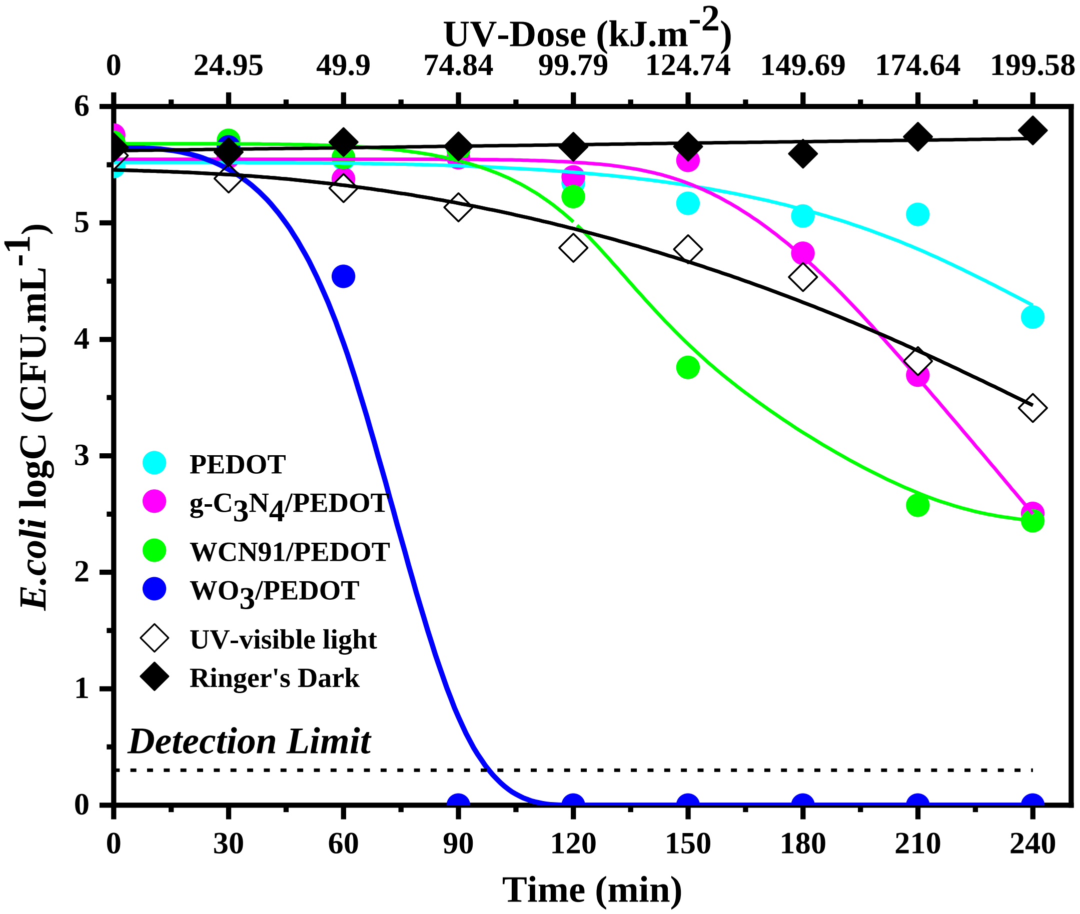

Figure 6.24 EAP inactivation of *E. coli* using PEDOT coated ITO electrodes over a 4 hour UV- visible irradiation time under an applied potential of +1.0 V. The solid lines represent the fitted data using GInaFiT models.

The increased photocatalytic inactivation of *E. coli* observed with WO_3/PEDOT/ITO over WCN91/PEDOT/ITO was rather interesting and needs further investigation in future work to explore the effect of PEDOT in charge transport across the semiconductor-electrolyte interface. The corresponding current observed for all the tested samples during the EAP disinfection is reported in figure 6.26.

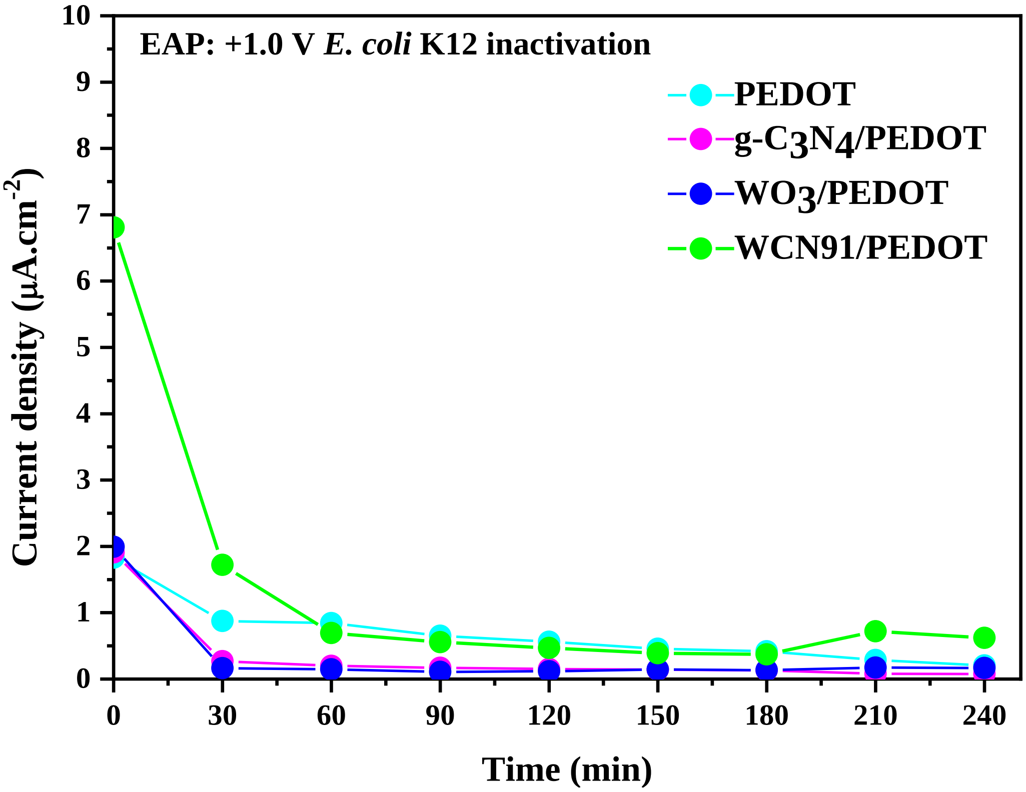

Figure 6.25 Current density vs. time plot for PEDOT coated ITO electrodes during EAP *E. coli* inactivation over a 4 h UV- visible irradiation time under an applied potential of +1.0 V.

The overall rate kinetics and fitting data parameters for all the samples tested under EAP conditions have been tabulated in table 6.3 based on GInAFiT modelling tool. A log-linear + shoulder + tail model was fitted for WO_3/PEDOT with a first order rate constant of 0.63 ± 2.1 min^{-1} whereas samples PEDOT and g-C_3N_4/PEDOT followed a Weibull model, with a convex fit ($p>1$). A double Weibull model was observed to be the best fit for WCN91/PEDOT/ITO electrode with decay rate δ_1 and δ_2. The δ_1 represents the time taken for 1 log reduction in *E. coli* cells from its initial concentration, and δ_2 is referred to as the decay rate for more resistant bacteria. Because two different models were fitted here, the actual comparison of each result is rather complicated and to simplify, a comparison based on Log of the residual bacterias ($Log_{10}N_{res}$) left in the solution after 240 min irradiation was made. A lower $Log_{10}N_{res}$ value represents faster inactivation. Based on the $Log_{10}N_{res}$ values, WO_3/PEDOT was the most efficient electrode with a value of 0 within 90 min, followed by g-C_3N_4/PEDOT and WCN91/PEDOT that show $Log_{10}N_{res}$ ~2.43-2.44 in 240 min. The photo-inactivation of *E. coli* showed a $Log_{10}N_{res} = 3.43$ in 240 min.

Table 6.3 Kinetic parameters using the GInaFIT tool for PEDOT/ITO electrodes.

Sample	**Shoulder length (SI)**	**Rate (k_{max})**	**Scale parameter (δ)**	**Shape parameter (p)**	**Log_{10} N_{res}**	**RMSE**	**R^2**
Lightǂ	-	-	169.7±11.3	2.0±0.3	3.43	0.138	0.973
PEDOTǂ	-	-	228.2±7.8	4.1±1.3	4.29	0.158	0.906
g-C_3N_4 PEDOTǂ	-	-	186.3±6.8	4.6±0.7	2.43	0.188	0.978
WO_3 PEDOT*	56.1±13.1	0.63	-	-	0.00	0.005	1
WCN91 PEDOTǂǂ	-	-	134.3±2.2 304.7±42.2	6.0±0.8	2.44	0.066	0.999

**log-linear + shoulder model; ǂWeibull model; ǂǂ double Weibull model*

6.4.4 Photoelectrochemical charge separation mechanism in WO_3/g-C_3N_4

The EAP disinfection rate for both WO_3 and WO_3/g-C_3N_4 (WCN91) heterostructure electrodes was increased under applied potential. The increased rate is the result of reduced recombination of photogenerated electron-hole pairs within the semiconductor. In WO_3 on applying a positive potential reduces the photogenerated charge recombination and therefore, an increase in disinfection activity is achieved. The application of an external potential also increases the electromigration of negatively charged *E. coli* towards the positively biased photoanode, thus improving the mass transfer. Comparing WO_3 with its heterostructure WCN91, the EAP disinfection is further increased, with g-C_3N_4 possibly acting as an electron sink or conductor. However, an electron trapping has known to be occurred within the g-C_3N_4, due to a possible defect state active under irradiation. The electron trapping and accumulation in g-C_3N_4 has lowered its use as photocatalyst on its own. Nevertheless, as shown in figure 6.26, in case of WCN91, g-C_3N_4 plays a significant role in the interfacial electron transport. Wherein, on applying a positive potential to the heterostructure, the Fermi level of the conductive substrate is lowered, and overpotential to transfer the electrons from the WCN91 film's surface to the conductive substrate is achieved. The electrons, therefore, can be transferred from the WO_3 to the g-C_3N_4. Please note: figure 6.26 is an oversimplied model of a complex 2D/2D system, which does not take in account the nature of the coating of one material onto another material's surface. It is only used to identify the charge transfer mechanism in EAP systems.

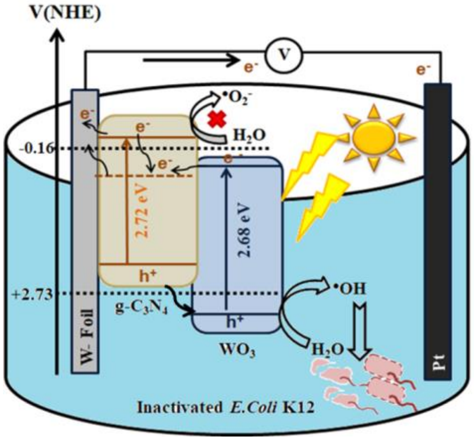

Figure 6.26 Simplified schematic of EAP inactivation of *E. coli* in a 2D heterostructured WO_3/g-C_3N_4 system.

6.5 Conclusions

The synthesized 2D heterostructure of WO_3/g-C_3N_4 and WO_3 nanoplates were immobilised onto electrically conducting supports and used as electrodes for electrochemically assisted photocatalytic inactivation of *E. coli*. The 2D heterostructure WCN91 electrode as compared to other electrodes outperformed in the photoelectrochemical applications. A 6-log reduction of *E. coli* was achieved within 150 min using the WCN91/W electrode compared to a 5-log reduction in 240 min for WO_3/W electrode. The photocurrent density response of the electrodes obtained under the fixed potential of +1.0 V correlated to their disinfection activity under the same reaction conditions. However, on comparing the use of different substrate for deposition, i.e. metal (W-foil) versus conductive ITO glass, the rate of disinfection was varied. In case of nanomaterial/PEDOT/ITO electrodes, a 6-log reduction was obtained in 90 min for *E. coli* inactivation using WO_3/PEDOT/ITO electrode under EAP conditions. This faster inactivation as compared to other PEDOT/ITO and W-foil electrodes was unexpected, but an encouraging result that needs to be further explored. It was suggestive that the PEDOT:PSS was an active hole transport medium and increased the electron-hole separation in WO_3 to achieve a faster log reduction. Overall, this study demonstrated the use an electrochemically assisted photocatalysis as a strategy to avoid the charge recombination process in semiconductor photocatalysis and achieve an improved *E. coli* inactivation rate using two-dimensional heterostructures of WO_3/g-C_3N_4.

Chapter 7. Conclusions and Future recommendations

7.1 Conclusions

The aim of the present work was to investigate the use of two-dimensional nanomaterials as either individual or combined heterostructured photocatalysts towards solar photocatalytic disinfection of water. The 2D heterostructures gave limited activity for the photocatalytic disinfection of water and degradation of organic pollutants. Therefore, the research was extended to investigate the reasons why the materials did not perform as expected based on the literature reports. Some evidence of improved photocurrent response led to the use of the materials in a photoelectrochemical cell for the electrochemically assisted photocatalytic inactivation of *E. coli*.

To achieve the aim, the objectives set at the beginning of this research where accomplished. The objectives are stated below and were addressed in detail in chapters 4 to 6.

i. Synthesis of 2D nanostructures of tungsten trioxide (WO_3) and graphitic carbon nitride ($g\text{-}C_3N_4$) and their combination as heterostructured photocatalysts.
ii. Investigation of the photocatalytic performance of 2D $WO_3/g\text{-}C_3N_4$ heterostructures for the degradation of organic pollutants and inactivation of *E. coli* under simulated solar irradiation.
iii. Comparison of the photocatalytic efficiency of the 2D photocatalyst with a known research bench mark photocatalyst, i.e. *Evonik Aeroxide* P25-TiO_2.
iv. Investigation of the photocatalytic charge transfer mechanism taking place between $WO_3/g\text{-}C_3N_4$ heterostructures.
v. Determination of the photoelectrochemical properties of WO_3 and $g\text{-}C_3N_4$ as photoanodes and comparison of their incident photon to current conversion efficiency.
vi. Investigation of the efficacy of 2D/2D heterostructures of WO_3 & $g\text{-}C_3N_4$ as photoanodes for the electrochemically assisted photocatalytic disinfection of water.

As described in chapter 4, 2D-WO_3 and g-C_3N_4 were synthesised. The morphology of the prepared 2D semiconductors was studied using TEM, SEM and XRD to understand the structural and crystalline properties of the materials. Through TEM and SEM, WO_3 nanoplates of dimensions 225 × 150 nm and thickness 25 nm were observed. The surface area analysis indicated an increase in specific surface area in WO_3 and g-C_3N_4 because of the annealing process. The increased specific surface area can also be correlated to an increase in the active sites of both materials for photocatalytic reactions. The specific surface area of WO_3 nanoplates was observed to increase from 10.87 $m^2.g^{-1}$ to 25.59 $m^{2.}g^{-1}$ after annealing at 400°C. Similarly, g-C_3N_4 prepared in a two-step heat treatment had an increased surface area from 8.25 $m^{2.}g^{-1}$ in cycle-1 (520°C) to 91.27 $m^{2.}g^{-1}$ in cycle-2 (500°C).

A range of heterostructures were synthesised by routes such as ultrasonic exfoliation, calcination, in-situ hydrothermal synthesis and dispersion in citrate buffer. The photocatalytic performance of the prepared 2D photocatalysts, i.e. WO_3 nanoplates, g-C_3N_4 and 2D/2D WO_3/g-C_3N_4 heterostructures, was assessed by the degradation of organic pollutants (formic acid and phenol) and inactivation of *E. coli*. The obtained photocatalytic activities of the materials were compared to a benchmark photocatalyst, i.e. *Evonik Aeroxide* P25-TiO_2. The 2D materials show relatively poor photocatalytic efficiency as compared to P25-TiO_2. The limited photocatalytic activity was expected from the individual materials, i.e. WO_3 nanoplates and g-C_3N_4 due to the unfavourable band edge potentials for the formation of ROS. However, it was expected that the materials, when combined in a heterostructure, should be able to generate ROS under simulated solar irradiation. Although the WO_3/g-C_3N_4 heterostructures were fabricated by adapting different methods well reported in the literature with potential z-scheme charge transfer mechanism, TiO_2 in comparison was still observed to outperform in both photocatalytic degradations of formic acid and phenol. Using P25-TiO_2 (30 $mg.L^{-1}$), a 50% degradation in formic acid (start conc. = 10 mM) was achieved in 3 h of simulated solar irradiation, and 40% degradation of phenol (start conc. = 1 mM) was achieved in 5 h of simulated solar irradiation. The photocatalytic disinfection activity for the parent and heterostructured 2D photocatalyst was also examined against P25-TiO_2 under simulated solar irradiation. The parent photocatalysts WO_3 and g-C_3N_4 made no significant contribution towards the *E. coli* inactivation and instead the photo-inactivation rate was suppressed by using them in suspension. The most important finding that emerged from these experiments was the outperformance of P25-TiO_2 as photocatalyst for solar disinfection of water with a total *E. coli* kill rate (10^6 CFU.mL^{-1}) within 150 min. The inactivation rate was compared using fit parameters, scale parameter δ (time taken to inactivate 1-log of *E .coli*), and $Log_{10}N_{res}$ (residual bacterial population in the end). The WO_3/g-C_3N_4 heterostructures prepared by physical mixture and calcination method were able to show inactivation of *E. coli* comparable only to photo-inactivation. A 4.35-log and 4.51-log reduction in *E. coli* was obtained with heterostructures WCN19 and WCN91 against 4.54-log photo-inactivation of *E. coli* in 3 h simulated solar irradiation. Therefore, no major improvement in inactivation rate was seen with heterostructures. The inactivation rate for the heterostructures was also ~2-2.5 times slower to than that of P25-TiO_2. The poor performance of the g-C_3N_4, WO_3 and WO_3/g-C_3N_4 heterostructures raised an important question as to why they were unable to generate reactive oxygen species (ROS) for the photocatalytic disinfection of water. In general, a further investigation of the charge transfer process occurring between WO_3 and g-C_3N_4 as heterojunction had to be performed to understand why the materials did not perform as indicated by the prior art.

In chapter 5, studies on elucidating the photogenerated charge transfer mechanism in WO_3/g-C_3N_4 heterostructures were performed. Based on the results obtained from chapter 4, heterostructures prepared by calcination process (WCN19, WCN91) and dispersion in citrate buffer (WCN(1:4)pH 2.25) against WO_3 and g-C_3N_4 were further investigated for detection of reactive oxygen species, such as hydroxyl radicals. Using RNO as the probe indicator, some evidence of $^{\bullet}OH$ production was observed with WO_3/g-C_3N_4 heterostructured photocatalysts and WO_3 itself, albeit in the presence of electron acceptor ($AgNO_3$). The heterostructured photocatalyst WCN91, showed an increased production rate of 46.7×10^{-10} mol.L^{-1}.s^{-1} with the presence of e^- scavenger, as compared to the rate of 6.33×10^{-10} mol.L^{-1}.s^{-1} without e^- scavenger. However, on exploring the photocatalytic reductive half-reaction using pH-independent probe methyl viologen under UV-Vis excitation, no 1 e^- reduction of MV^{2+} to $MV^{+\bullet}$ ($E_{MV2+/+\bullet}$ -0.445 V(NHE)) was achieved by varying the pH of the solution using both WO_3 and g-C_3N_4. The no observed reduction of MV^{2+} using g-C_3N_4 at higher pH (7-14) with predicted E_{fb} values >-1.0 V (NHE) was undesirable and contrary to the literature where it is reported that the CB potential (or LUMO) of g-C_3N_4 is more negative than -1.0 V (NHE). A further investigation in detail about the band energetics of individual materials WO_3 and g-C_3N_4 through optical bandgap, XPS and photoluminescence measurements was performed to identify the cause for the poor performance of the materials. Through optical band gap and VB XPS, an energy band diagram of each material was determined, revealing an energy difference (E_f - E_{CBM}) of 0.84 eV existing for g-C_3N_4 as compared to 0.22 eV for WO_3. The greater difference for g-C_3N_4 was suggestive for its Fermi energy level to be situated well below its reported LUMO (or CB). The core-level XPS separately determined the changes in the chemical composition of g-C_3N_4 taking place before and after heterostructure formation with WO_3. The atomic % of the N groups in g-C_3N_4 was changed in the heterostructured photocatalysts. The central N3 and N1(C-N=C) at% was reduced in WCN91, however, the at% of N-H groups, i.e. edge N2 (N-H) and terminal N4 (N-H_2) of g-C_3N_4 was increased in heterostructured samples as observed through core level XPS. This was possibly indicating the photo-corrosion of g-C_3N_4 as compared to its original tri-s-triazine formation in the heterostructured samples. The terminal N4 (i.e. NH_2 group) is the bridge between each monomeric C_3N_4 unit and consist of a lone pair of electrons. The increase of N4% in WCN91 indicated a possible increase in the electron trapping sites. To study further about the existence of possible electron traps in g-C_3N_4, PL studies were performed. The deconvoluted PL peaks of g-C_3N_4 showed broad emission at 481 nm representative of the inter-band state consisting of the lone pair of electrons in the bridging N atom, i.e. terminal N4 of g-C_3N_4. Both XPS and PL investigations were in agreement towards a possible existence of electronic trap in g-C_3N_4 arising from the NH_2 group (terminal-N4). These chemical data investigations suggested the NH_2 group of g-C_3N_4 was behaving as the surface defect state leading to electron trapping in g-C_3N_4 upon excitation and emission. Also, the greater energy difference obtained (E_f - E_{CBM}) justifies the electrons to be trapped at a much lower potential than LUMO of g-C_3N_4. If this to be true a possible Fermi level pinning of g-C_3N_4 could be a reason for its poor performance in photocatalytic applications. However, the actual electrochemical potential for the trap state was still unknown. To support the chemical studies, the electrochemical investigations were carried out on WO_3 and g-C_3N_4, which gave an insight into the flat band potential of the individual materials. The flat band potential of each material was determined by multiple electrochemical techniques to confirm the electron transfer process in heterostructures. The flat band potential for WO_3 was obtained at +0.42 V (NHE), showing an anodic photocurrent response in positive bias.

However, in the case of g-C_3N_4, the electrochemical measurements, revealed a dual photocurrent response of g-C_3N_4, switching its polarity with changing bias. The dual photocurrent obtained upon excitation of g-C_3N_4 was in agreement to the larger energy difference (0.84 eV) between the E_f and E_{CBM} determined through the optical and VB XPS measurements. Taken together, the results obtained in electrochemical investigations mainly the dark and light excitation in Mott Schottky analysis confirmed the presence of the electronic trap state arising due to NH_2 group of g-C_3N_4 in a potential range between 0.5 to 0.8 V (SCE) or 0.74 to 1.0 V (NHE), causing the Fermi level to pin in this range. It is due to the existence of this electron trap and the Fermi level pinning, a poor photocatalytic performance was observed with g-C_3N_4 in the present work both as individual and as heterostructured photocatalyst with WO_3. Overall, the multiple measurements are done to confirm this active electron trap, strengthen the studies to accomplish the main aim of this work towards elucidating the charge transfer process in WO_3/g-C_3N_4 heterostructures.

The present work contributed towards determining the existence of g-C_3N_4 trapped state bridging both chemical and electrochemical investigations together to identify the limited photocatalytic performance of this material. Due to the active trap state in g-C_3N_4 situated approximately in the middle of its bandgap, the electron transfer process was energetically downhill from CB of WO_3 into the trap state of g-C_3N_4. This energetically downhill transfer of electrons and possible accumulation in the trap state limits the interfacial electron transfer from the g-C_3N_4 to solution for the formation of ROS or photocatalytic reduction reactions. However, the electrons trapped in the surface state of g-C_3N_4, could be possibly scavenged using an electron scavenger such as $AgNO_3$ (+0.8 V, NHE) and this was observable through photocatalytic RNO degradation. The WO_3/g-C_3N_4 heterostructures in the presence of electron scavenger showing improved photocatalytic oxidation reactions such as RNO degradation was possible due to an enhanced electron-hole pair separation, which was encouraging.

In chapter 6, the 2D WO_3/g-C_3N_4 heterostructures and the parent photocatalysts WO_3 nanoplates and g-C_3N_4 were studied further for their photoelectrochemical response. The fabricated electrodes WO_3 and WCN91 were characterised by SEM-EDS to measure the thickness of the nanomaterial deposited on the conductive substrates. A thickness in the range of 1.5-4 µm was measured from WO_3 nanoplates, and WCN91 spray-coated on W foil electrodes. However, EDS analysis of a region of WCN91 revealed increased oxygen counts in the sample indicating the oxidation of sample after heat treatment which was in agreement with the XPS investigations performed in the powdered samples in chapter 5. The photoelectrochemical performance for WCN91 heterostructure was the most compelling, and a maximum photocurrent density of 12.14 $\mu A.cm^{-2}$ under the fixed potential of +1.0 V was observed. Whereas, the WO_3 nanoplates as photoanode displayed only a steady-state photocurrent density of 1.82 $\mu A.cm^{-2}$ at +1.0 V (pH 1). No measurable photocurrent density under the fixed potential of +1.0 V for g-C_3N_4 electrode was obtained. The IPCE% calculated was 2% for WCN91 at 320 nm compared to 0.52% of WO_3. The IPCE % observed for g-C_3N_4 was below 0.1%.

The spray-coated g-C_3N_4 electrode was unstable in the electrolyte solution. Therefore, another method to deposit g-C_3N_4 on the conductive substrate was utilized. The electrodes prepared in a mixture of PEDOT:PSS as the hole transport layer were deposited on ITO conductive glass by doctor blading method. The photoelectrochemical response of the ITO electrodes in Ringer's solution pH 7 were analysed, and a photocurrent density of 4.78 $\mu A.cm^{-2}$ for WO_3 at +1.0 V was obtained. The photocurrent density for WCN91/PEDOT/ITO at pH 7 was ~16 $\mu A.cm^{-2}$ that was 4x times to WO_3/PEDOT/ITO, indicating an enhanced electron-hole pair separation upon bias. All performed studies in this work have shown the suitability of WCN91 as photo(+electro)catalytic material. Therefore, the final work of this thesis was to investigate the use of the WCN91 electrode for the electrochemically assisted photocatalytic disinfection of water. The WCN91 electrode gave a 6-log reduction of *E. coli* (10^6 $CFU.mL^{-1}$) in 150 min of irradiation at +1.0V, whereas the $WO_{3,}$ electrode gave only a 5-log reduction of *E. coli* in 240 min. The disinfection results obtained were correlating with photocurrent density observed for the electrodes at the fixed potential of +1.0 V under the same conditions. The obtained results were comparable to previously reported results for titania nanotubes and P25-TiO_2 electrodes under similar conditions. However, the aligned nanotubes (Ti-NT) were reported to show faster disinfection of 5.1-log reduction (initial *E. coli* conc. = 10^6 $CFU.mL^{-1}$) in 120 min. Nevertheless, the WO_3 single and heterostructured electrode demonstrated a faster disinfection rate as compared to P25-TiO_2 electrodes (4-log reduction in 240 min).

The EAP disinfection using ITO electrodes were also examined here, and the rate of disinfection as a result of substrate varied. The EAP disinfection observed with WO_3/PEDOT/ITO was 5.6-log reduction in 90 min. However, the heterostructure WCN91/PEDOT/ITO electrode displayed only a 3.25-log reduction in 180 min. The increased rate based on kinetic fit parameter δ and $Log_{10}N_{res}$, observed with WO_3/PEDOT/ITO as compared to WCN91/PEDOT/ITO was interesting and needs further investigation as future work to study the effect of PEDOT:PSS as a hole conductor in photocatalytic as well as electrochemically assisted photocatalytic *E. coli* inactivation.

Nevertheless, the interesting finding from the EAP disinfection work was the potential use of WO_3 and WO_3/g-C_3N_4 as photoanodes for photoelectrocatalytic applications. This is the first reported study of the use of 2D heterostructures as photocatalyst for enhanced solar disinfection of water. The approach used here, of applying an externally applied potential to the existing materials to overcome the limitation of charge carrier recombination, was successful in achieving an improved *E. coli* inactivation rate. This work makes a significant contribution to our knowledge concerning methods that can be used to investigate and understand the photocatalytic behaviour of novel materials and their further development as photoelectrocatalyst for water treatment and disinfection.

7.2 Future work

The use of two-dimensional materials in photocatalysis has been gaining interest recently with the development of many new 2D semiconductor photocatalysts. This work was mainly focused on the fabrication of 2D heterostructures from narrow bandgap semiconductors to enhance the photocatalytic efficiency by absorption of more solar photons. The fabricated WO_3/g-C_3N_4 heterostructures with extended solar absorption and narrow bandgap of 2.7 eV, showed their limited performance towards photocatalytic disinfection of water. This limited performance was due to the presence of an electron trap state in g-C_3N_4, which made the charge transfer process thermodynamically less energetic and downhill. However, previous reports in the literature using WO_3/g-C_3N_4 heterostructures never explored the presence of the trap state. Although few reports present the limited performance of this combination as a type-II heterostructure mechanism with charge transfer from band to band, the influence of any trap state remained unexplored. This work provides an investigative insight for the future work to be done in the development of new heterostructured photocatalyst. Few recommendations based on the investigations performed in this research are as follows:

7.2.1 Material selection criteria

Selection of materials for fabricating heterostructures should not be entirely based on their band positions and bandgap. Instead, additional tests should be performed on individual semiconductors before combination as a heterostructure, to identify all possibilities of the limited charge transfer including the existence any active surface defect or electron trap state that can hinder the performance of the material. For instance, the electron trap in g-C_3N_4 was indicated through chemical investigations using PL, and transient absorption spectroscopy wherein trapping of electrons in surface states was reported within picosecond of photogeneration and excitation [233]. The trapped electrons were unreactive towards any reduction reaction and were found to have long lifetime from microseconds to up to a few milliseconds. The trapping of electrons in these N-defect states was also reported to affect the photocatalytic performance of g-C_3N_4 towards photocatalytic H_2 production. However, the effect on this electron trap of g-C_3N_4 in heterostructure systems of WO_3/g-C_3N_4 was never explored until now. This defect was associated with N-H groups and possibly came from either oxidative treatment or photo-induced self-oxidation of g-C_3N_4[198]. One solution to avoid the thermal defects can be the synthesis of g-C_3N_4 under nitrogen atmosphere to reduce the possibility of the oxidation of the material and increase its thermal and chemical stability as a photocatalyst.

7.2.2 Multiple technique approach to determine band energetics of semiconductors

Another recommendation for future work on developing heterostructures is to carry out a detailed analysis of the flat band potential and electrochemical potential of the materials by multiple techniques[264]. To use chemical probes such as methyl viologen or other redox couples with redox potential below and above the reported band positions of the materials to identify the exact electron transfer process. These chemical probe analysis should be backed with electrochemical measurements such as onset-photo potential, photocurrent and flat band potential performed both in dark and irradiation to bridge the gap between the chemical and electrochemical values of the band potential of semiconductors [247].

7.2.3 EAP disinfection using 2D materials

Finally, the present work provides a first comprehensive use of 2D heterostructures of WO_3 and g-C_3N_4 as potential photoelectrocatalysts towards enhanced solar disinfection of water. Therefore, further work is to study the different 2D electrode configurations such as;

i. A single photoanode (WO_3/g-C_3N_4) with a metal counter electrode (Pt).
ii. A photocathode (exploring possibilities of g-C_3N_4 as photocathode) with a metal anode.
iii. A dual-electrode set up with photoanode (WO_3) and photocathode (g-C_3N_4) with or without metal co-catalyst such as Pt.

Recent studies also debate over the production of reactive chlorine species (RCS) such as HOCl, or free chlorine (Cl_2) as a cause of EAP disinfection instead of ROS generation [66]. Therefore, further research is required to examine the EAP disinfection mediated both via ROS generation and via chloride oxidation to RCS generation.

Appendix I

Calculation of spectral intensity (P), supporting the IPCE derivation

The following steps were undertaken to calculate the value of P i.e. spectral power intensity for 450 W Xe lamp at monochromatic chopped wavelength from 250-500 nm to derive the incident photon to current conversion efficiency (IPCE %) as stated in equations 3.1 and 3.2.

1. The spectral intensity of 450 W Xe lamp was measured using the spectral radiometer for every monochromatic wavelength from 250-500 nm at a 10 nm interval. The monochromatic wavelengths were controlled by the uniblitz chopper equipped with the photoelectrochemical workstation. Using this, the spectral radiometer gave a spectral intensity in $\mu W.cm^{-2}$ vs wavelength range i.e. (250-700 nm).
2. The obtained spectral intensity (P) at each monochromatic wavelength λ = 250 to 500 nm, was converted to $W.cm^{-2}$ by a division factor of 10^6.
3. The photon energy (E) for every wavelength was calculated following Plank-Einstein equation i.e.

$$E=\frac{hc}{\lambda}$$

$$E = \frac{6.63 \times 10^{-34}\ (J.s) \times 3 \times 10^{8}\left(\frac{m}{s}\right)}{\lambda \times 10^{-9}(m)}$$

$$E = \frac{19.89 \times 10^{-17}\ (J)}{\lambda}$$

4. The numbers of incident photons (N) were calculated using value of E from step 3 for each wavelength i.e.

$$N = \frac{\text{(Spectral intensity at each wavelength i.e. P)}}{\text{(Photon energy at each wavelength i.e. E)}}$$

$$N=\frac{P\left(\frac{W}{cm2}\right)\times \lambda \times 10^{-9}(m)}{6.63 \times 10^{-34}\ (J.s) \times 3 \times 10^{8}\left(\frac{m}{s}\right)}$$

$$\mathrm{N} = \frac{\mathrm{P}\left(\frac{\mathrm{W}}{\mathrm{cm2}}\right) \times \lambda \times 10^{17}}{19.89}$$

Then at every monochromatic wavelength from 250 - 500 nm the integral sum of incident photons was determined, that was used to derive the IPCE for each sample.

5. Next, the spectral photocurrent density at every monochromatic wavelength was measured as J_{ph} (A.cm^{-2}).
6. The number of charge carriers generated (n) i.e. number of electrons on applying a positive fixed potential of +1.0 V were calculated by

$$\mathrm{n} = \frac{\mathrm{J_{ph}}\left(\frac{\mathrm{A}}{\mathrm{cm2}}\right)}{\text{charge of 1e-}}$$

$$\mathrm{n} = \frac{J_{\mathrm{ph}}\left(\frac{\mathrm{A}}{\mathrm{cm2}}\right)}{1.6 \times 10^{-19}}$$

7. Therefore the IPCE for every monochromtic wavelength from 250-500 nm was calculated as

$$IPCE = \frac{n}{N}$$

$$\mathrm{IPCE} = \frac{\frac{J_{\mathrm{ph}}\left(\frac{\mathrm{A}}{\mathrm{cm2}}\right)}{\mathrm{e-}}}{\frac{\mathrm{P}\left(\frac{\mathrm{W}}{\mathrm{cm2}}\right) \times \lambda \times 10^{-9}(\mathrm{m})}{6.63 \times 10^{-34}\ (\mathrm{J.s}) \times 3 \times 10^{8}\left(\frac{\mathrm{m}}{\mathrm{s}}\right)}}$$

$$\mathrm{IPCE}\ \% = \frac{\mathrm{hc} \times \mathrm{J_{ph}}\left(\frac{\mathrm{A}}{\mathrm{cm2}}\right)}{\mathrm{P}\left(\frac{\mathrm{W}}{\mathrm{cm2}}\right) \times \lambda\ (\mathrm{nm}) \times \mathrm{e-}} \times 100$$

Appendix II

Determination of optimal photocatalyst loading

1. UV-Vis spectrum for each concentration of semiconductor was obtained from 280-700 nm using UV-Vis spectrophotometer. Therefore, an absorbance vs wavelength curve for each concentration overlaying the Xe lamp emission spectrum was obtained. For better understanding spectrum of P25-TiO_2 is used as an example as shown in figure A1.

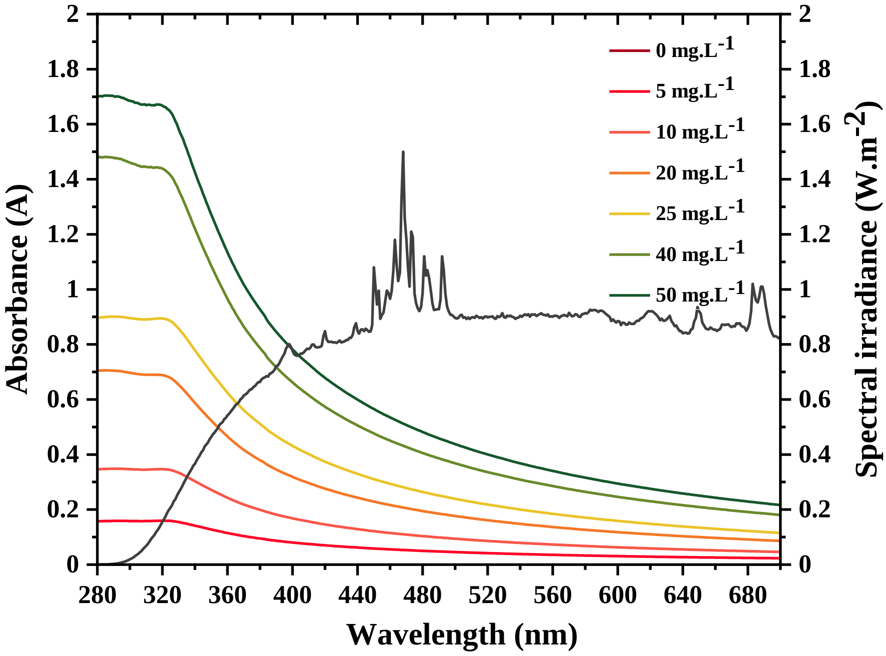

Figure A.1 Absorbance Vs wavelength (280-700 nm) spectrum for P25-TiO_2 with overlaying 1000 W Xe lamp emission spectrum.

2. Absorbance has a logarithmic relationship to the incident light intensity (I_o) entering the cuvette with path length 1 cm and the transmittance light intensity (I) out of the cuvette. Absorbance can be represented as follows:

$$A=\log(\frac{I_0}{I})$$

Therefore, from the absorbance vs wavelength curve, I_o and I can be calculated as

$$\frac{I_0}{I}=10\text{^}A$$

i.e. power 10 of absorbance is equivalent to I_o/I.

3. Transmittance is the ratio of transmitted intensity to incident light intensity i.e.

$$T=\frac{I}{I_0}$$

In addition, reciprocal of T can be denoted as

$$\frac{1}{T}=\frac{I_0}{I}$$

4. Using the spectral irradiance of the Xe lamp, total no. of incident photons (N) from 280- 500 nm can be calculated as

$$N=\frac{\text{Incident irradiance at each wavelength i.e. P}}{\text{Energy of 1 photon at each wavelength i.e. h}\vartheta}$$

5. Therefore no. of incident photons obtained at each wavelength from 280-500 nm can be used to calculated the transmitted photons (n) out of the cell with optical path length = 1 cm.

$$n=(\text{Incident photons at each wavelength, N})\times(\text{Transmitted intensity, T})$$

$$n=N\times\frac{I}{I_0}$$

6. Integrating the total incident photons and transmitted photons between 280-500 nm, gives integrated transmittance (T) i.e.

$$\int_{280}^{500} T=\int_{280}^{500}\frac{I}{I_o}=\int_{280}^{500}\left(\frac{n}{N}\right)$$

Hence, the integrated absorbance between 280-500 nm for each concentration can be obtained by

$$\int_{280}^{500} A=\log\int_{280}^{500}\frac{1}{T}=\log\int_{280}^{500}\frac{I_0}{I}$$

In this way absorbance A(λ) vs concentration for 3 replicate sets was obtained and average absorbance plotted against the concentration to obtain a linear curve as shown previously in figure 4.18 (a-c) in chapter 4.

References

[1] M.M. Mekonnen, A.Y. Hoekstra, Four billion people facing severe water scarcity, Science Advances, 2 (2016) e1500323.

[2] UN-Water, Coping with water scarcity-Challenge of the twenty-first century, FAO, 2007.

[3] M. Emma, Water scarcity affects four billion people each year, Nature, (February 2016).

[4] W. UNICEF, 1 in 3 people globally do not have access to safe drinking water – UNICEF, WHO, 2019.

[5] Progress on Drinking Water, Sanitation and Hygiene: 2017 Update and SDG Baselines. Geneva: World Health Organization (WHO) and the United Nations Children's Fund (UNICEF), 2017.

[6] UNICEF, Estimates of child cause of Death- Dairrhoea 2018, February 2018.

[7] Arsenic in drinking-water: background document for development of WHO guidelines for drinking-water quality, World Health Organization, Geneva, 2011.

[8] Lead in Drinking-water, World Health Organization, Geneva, 2011.

[9] Exposure to inadequate or excess fluoride: a major public health concern, World Health Organization, Geneva, 2010.

[10] Progress on Safe Treatment and Use of Wastewater- Piloting the monitoring methodology and initial findings for SDG indicator 6.3.1, 2018.

[11] Guidelines for drinking-water quality: fourth edition incorporating the first addendum. Geneva: World Health Organization, Geneva, 2017.

[12] WHO, World Health Organization. Regional Office for the Western Pacific (2013). Household water treatment and safe storage : manual for the participant, 2013.

[13] R. Nassar, S. Mokh, A. Rifai, F. Chamas, M. Hoteit, M. Al Iskandarani, Transformation of sulfaquinoxaline by chlorine and UV light in water: kinetics and by-product identification, Environmental Science and Pollution Research, 25 (2018) 34863-34872.

[14] S. Malato, P. Fernández-Ibáñez, M.I. Maldonado, J. Blanco, W. Gernjak, Decontamination and disinfection of water by solar photocatalysis: Recent overview and trends, Catalysis Today, 147 (2009) 1-59.

[15] Standard Tables for Reference Solar Spectral Irradiance: Air Mass 1.5 (ASTM G-173-03)-American Society for Testing and Materials, United States of America (U.S.A.), 1976.

[16] McGuigan, Joyce, Conroy, Gillespie, M. Elmore, Solar disinfection of drinking water contained in transparent plastic bottles: characterizing the bacterial inactivation process, Journal of Applied Microbiology, 84 (1998) 1138-1148.

[17] K.G. McGuigan, R.M. Conroy, H.-J. Mosler, M.d. Preez, E. Ubomba-Jaswa, P. Fernandez-Ibañez, Solar water disinfection (SODIS): A review from bench-top to roof-top, Journal of Hazardous Materials, 235-236 (2012) 29-46.

[18] Evaluating household water treatment options: health-based targets and microbiological performance specifications., World Health Organisation, July 2011.

[19] T.F. Clasen, I.G. Roberts, T. Rabie, W.P. Schmidt, S. Cairncross, Interventions to improve water quality for preventing diarrhoea, Cochrane Database of Systematic Reviews, (2006).

[20] T. Clasen, L. Haller, D. Walker, J. Bartram, S. Cairncross, Cost-effectiveness of water quality interventions for preventing diarrhoeal disease in developing countries, Journal of Water and Health, 5 (2007) 599-608.

[21] T.F. Clasen, L. Haller, Water Quality Interventions to Prevent Diarrhoea: Cost and Cost-Effectiveness, World Health Organization, Geneva, Switzerland, 2008.

[22] S. Luzi, M. Tobler, F. Suter, R. Meierhofer, SODIS manual: Guidance on solar water disinfection, Eawag, the Swiss Federal Institute of Aquatic Science and Technology, Switzerland, 2016.

[23] D.M.A. Alrousan, M.I. Polo-López, P.S.M. Dunlop, P. Fernández-Ibáñez, J.A. Byrne, Solar photocatalytic disinfection of water with immobilised titanium dioxide in re-circulating flow CPC reactors, Applied Catalysis B: Environmental, 128 (2012) 126-134.

[24] K. Lawrie, A. Mills, M. Figueredo-Fernández, S. Gutiérrez-Alfaro, M. Manzano, M. Saladin, UV dosimetry for solar water disinfection (SODIS) carried out in different plastic bottles and bags, Sensors and Actuators B: Chemical, 208 (2015) 608-615.

[25] A. Mills, R.H. Davies, D. Worsley, Water purification by semiconductor photocatalysis, Chemical Society Reviews, 22 (1993) 417-425.

[26] J.A. Byrne, P.S.M. Dunlop, J.W.J. Hamilton, P. Fernández-Ibáñez, I. Polo-López, P.K. Sharma, A.S.M. Vennard, A Review of Heterogeneous Photocatalysis for Water and Surface Disinfection, Molecules, 20 (2015) 5574-5615.

[27] M.R. Hoffmann, S.T. Martin, W. Choi, D.W. Bahnemann, Environmental Applications of Semiconductor Photocatalysis, Chemical Reviews, 95 (1995) 69-96.

[28] J.A. Byrne, P.A. Fernandez-Ibañez, P.S.M. Dunlop, D.M.A. Alrousan, J.W.J. Hamilton, Photocatalytic Enhancement for Solar Disinfection of Water: A Review, International Journal of Photoenergy, 2011 (2011) 798051.

[29] J.S. Zogorski, Carter, J.M., Ivahnenko, Tamara, Lapham, W.W., Moran, M.J., Rowe, B.L., Squillace, P.J., and, P.L. Toccalino, The quality of our Nation's waters—Volatile organic compounds in the Nation's ground water and drinking-water supply wells:, U.S. Geological Survey Circular, 2006, pp. 101.

[30] A. Mills, J. Wang, Photomineralisation of 4-chlorophenol sensitised by TiO_2 thin films, Journal of Photochemistry and Photobiology A: Chemistry, 118 (1998) 53-63.

[31] J.A. Byrne, B.R. Eggins, N.M.D. Brown, B. McKinney, M. Rouse, Immobilisation of TiO_2 powder for the treatment of polluted water, Applied Catalysis B: Environmental, 17 (1998) 25-36.

[32] S. Bougarrani, P.K. Sharma, J.W.J. Hamilton, A. Singh, M. Canle, M. El Azzouzi, J.A. Byrne, Enhanced Photocatalytic Degradation of the Imidazolinone Herbicide Imazapyr upon UV/Vis Irradiation in the Presence of Ca_xMnO_y-TiO_2 Hetero-Nanostructures: Degradation Pathways and Reaction Intermediate, Nanomaterials, *10* (2020).

[33] A.D. McNaught, A. Wilkinson, IUPAC. Compendium of Chemical Terminology, 2nd ed. (the "Gold Book"). Blackwell Scientific Publications, Oxford, 1997.

[34] J.A. Rengifo-Herrera, C. Pulgarin, Photocatalytic activity of N, S co-doped and N-doped commercial anatase TiO_2 powders towards phenol oxidation and *E. coli* inactivation under simulated solar light irradiation, Solar Energy, 84 (2010) 37-43.

[35] J.M. Burns, W.J. Cooper, J.L. Ferry, D.W. King, B.P. DiMento, K. McNeill, C.J. Miller, W.L. Miller, B.M. Peake, S.A. Rusak, A.L. Rose, T.D. Waite, Methods for reactive oxygen species (ROS) detection in aqueous environments, Aquatic Sciences, 74 (2012) 683-734.

[36] P. Ganguly, C. Byrne, A. Breen, S.C. Pillai, Antimicrobial activity of photocatalysts: Fundamentals, mechanisms, kinetics and recent advances, Applied Catalysis B: Environmental, 225 (2018) 51-75.

[37] M. Cho, H. Chung, W. Choi, J. Yoon, Linear correlation between inactivation of *E. coli* and OH radical concentration in TiO_2 photocatalytic disinfection, Water Research, 38 (2004) 1069-1077.

[38] Y. Nosaka, A. Nosaka, Understanding Hydroxyl Radical ($^{\bullet}OH$) Generation Processes in Photocatalysis, ACS Energy Letters, 1 (2016) 356-359.

[39] J. Xu, Z. Wang, Y. Zhu, Enhanced Visible-Light-Driven Photocatalytic Disinfection Performance and Organic Pollutant Degradation Activity of Porous g-C_3N_4 Nanosheets, ACS Applied Materials & Interfaces, 9 (2017) 27727-27735.

[40] B.R. Cruz-Ortiz, J.W.J. Hamilton, C. Pablos, L. Díaz-Jiménez, D.A. Cortés-Hernández, P.K. Sharma, M. Castro-Alférez, P. Fernández-Ibañez, P.S.M. Dunlop, J.A. Byrne, Mechanism of photocatalytic disinfection using titania-graphene composites under UV and visible irradiation, Chemical Engineering Journal, 316 (2017) 179-186.

[41] P. Fernández-Ibáñez, M.I. Polo-López, S. Malato, S. Wadhwa, J.W.J. Hamilton, P.S.M. Dunlop, R. D'Sa, E. Magee, K. O'Shea, D.D. Dionysiou, J.A. Byrne, Solar photocatalytic disinfection of water using titanium dioxide graphene composites, Chemical Engineering Journal, 261 (2015) 36-44.

[42] D.T. Sawyer, J.S. Valentine, How super is superoxide?, Accounts of Chemical Research, 14 (1981) 393-400.

[43] A.A. David, E.H. Robert, L. Sergei, H.K. Willem, M. Gabor, N. Pedatsur, M.S. David, S. Sten, W. Peter, Standard electrode potentials involving radicals in aqueous solution: inorganic radicals, BioInorganic Reaction Mechanisms, 9 (2013) 59-61.

[44] A. Mills, S. Le Hunte, An overview of semiconductor photocatalysis, Journal of Photochemistry and Photobiology A: Chemistry, 108 (1997) 1-35.

[45] M. Pelaez, N.T. Nolan, S.C. Pillai, M.K. Seery, P. Falaras, A.G. Kontos, P.S.M. Dunlop, J.W.J. Hamilton, J.A. Byrne, K. O'Shea, M.H. Entezari, D.D. Dionysiou, A review on the visible light active titanium dioxide photocatalysts for environmental applications, Applied Catalysis B: Environmental, 125 (2012) 331-349.

[46] A. Fujishima, Rao, T.N. and Tryk, D.A., Titanium Dioxide Photocatalysis, Journal of Photochemistry and Photobiology C: Photochemistry Reviews, 1 (2000) 1-21.

[47] K. Nakata, A. Fujishima, TiO_2 photocatalysis: Design and applications, Journal of Photochemistry and Photobiology C: Photochemistry Reviews, 13 (2012) 169-189.

[48] R. Fagan, D. E. McCormack, D. Dionysiou, S. Pillai, A Review of Solar and Visible Light Active TiO_2 Photocatalysis for Treating Bacteria, Cyanotoxins and Contaminants of Emerging Concern, 2015.

[49] D.M.A. Alrousan, P.S.M. Dunlop, T.A. McMurray, J.A. Byrne, Photocatalytic inactivation of *E. coli* in surface water using immobilised nanoparticle TiO_2 films, Water Research, 43 (2009) 47-54.

[50] C. Pablos, J. Marugán, R. Van Grieken, P.S.M. Dunlop, J.W.J. Hamilton, D.D. Dionysiou, J.A. Byrne, Electrochemical Enhancement of Photocatalytic Disinfection on Aligned TiO_2 and Nitrogen Doped TiO_2 Nanotubes, Molecules, 22 (2017) 704.

[51] W. Yossy, L. Sanly, S. Jason, A. Rose, Tungsten Trioxide as a Visible Light Photocatalyst for Volatile Organic Carbon Removal, Molecules, 19 (2014) 17747-17762.

[52] S. Wadhwa, J. Hamilton, P. Dunlop, C. Dickinson, J. Byrne, Effect of Post-annealing on the Photocatalytic Activity of Hydrothermally Synthesised Titania Nanotubes, Journal of Advanced Oxidation Technologies, 14 (2011) 1203-8407.

[53] A.D. Yoffe, Low-dimensional systems: quantum size effects and electronic properties of semiconductor microcrystallites (zero-dimensional systems) and some quasi-two-dimensional systems, Advances in Physics, 42 (1993) 173-262.

[54] D. Beydoun, R. Amal, G. Low, S. McEvoy, Role of Nanoparticles in Photocatalysis, Journal of Nanoparticle Research, 1 (1999) 439-458.

[55] C.N.R. Rao, A.K. Cheetham, Science and technology of nanomaterials: current status and future prospects, Journal of Materials Chemistry, 11 (2001) 2887-2894.

[56] S. Bayda, M. Adeel, T. Tuccinardi, M. Cordani, F. Rizzolio, The History of Nanoscience and Nanotechnology: From Chemical-Physical Applications to Nanomedicine, Molecules (Basel, Switzerland), 25 (2019) 112.

[57] B.D. Malhotra, M.A. Ali, Chapter 1 - Nanomaterials in Biosensors: Fundamentals and Applications, in: B.D. Malhotra, M.A. Ali (Eds.) Nanomaterials for Biosensors, William Andrew Publishing2018, pp. 1-74.

[58] J.E. Hulla, S.C. Sahu, A.W. Hayes, Nanotechnology: History and future, Human & Experimental Toxicology, 34 (2015) 1318-1321.

[59] M.F. Ashby, P.J. Ferreira, D.L. Schodek, Chapter 6 - Nanomaterials: Classes and Fundamentals, Nanomaterials, Nanotechnologies and Design, Butterworth-Heinemann, Boston, 2009, pp. 177-197.

[60] A.K. Singh, K. Mathew, H.L. Zhuang, R.G. Hennig, Computational Screening of 2D Materials for Photocatalysis, The Journal of Physical Chemistry Letters, 6 (2015) 1087-1098.

[61] D. Chen, L. Gao, A. Yasumori, K. Kuroda, Y. Sugahara, Size- and Shape-Controlled Conversion of Tungstate-Based Inorganic–Organic Hybrid Belts to WO_3 Nanoplates with High Specific Surface Areas, Small, 4 (2008) 1813-1822.

[62] Y. Jia, S. Zhan, S. Ma, Q. Zhou, Fabrication of TiO_2–Bi_2WO_6 Binanosheet for Enhanced Solar Photocatalytic Disinfection of *E. coli*: Insights on the Mechanism, ACS Applied Materials & Interfaces, 8 (2016) 6841-6851.

[63] C. Liu, D. Kong, P.-C. Hsu, H. Yuan, H.-W. Lee, Y. Liu, H. Wang, S. Wang, K. Yan, D. Lin, P.A. Maraccini, K.M. Parker, A.B. Boehm, Y. Cui, Rapid water disinfection using vertically aligned MoS_2 nanofilms and visible light, Nature Nanotechnology, 11 (2016) 1098.

[64] G.G. Bessegato, T.T. Guaraldo, J.F. de Brito, M.F. Brugnera, M.V.B. Zanoni, Achievements and Trends in Photoelectrocatalysis: from Environmental to Energy Applications, Electrocatalysis, 6 (2015) 415-441.

[65] P.S.M. Dunlop, J.A. Byrne, N. Manga, B.R. Eggins, The photocatalytic removal of bacterial pollutants from drinking water, Journal of Photochemistry and Photobiology A: Chemistry, 148 (2002) 355-363.

[66] M.S. Koo, X. Chen, K. Cho, T. An, W. Choi, In Situ Photoelectrochemical Chloride Activation Using a WO_3 Electrode for Oxidative Treatment with Simultaneous H_2 Evolution under Visible Light, Environmental Science & Technology, 53 (2019) 9926-9936.

[67] E.O. Scott-Emuakpor, A. Kruth, M.J. Todd, A. Raab, G.I. Paton, D.E. Macphee, Remediation of 2,4-dichlorophenol contaminated water by visible light-enhanced WO_3 photoelectrocatalysis, Applied Catalysis B: Environmental, 123-124 (2012) 433-439.

[68] Key Facts on Drinking-water- World Health Organisation, UNICEF, in: U. Water (Ed.), 2019.

[69] M. Waso, S. Khan, A. Singh, S. McMichael, W. Ahmed, P. Fernández-Ibáñez, J.A. Byrne, W. Khan, Predatory bacteria in combination with solar disinfection and solar photocatalysis for the treatment of rainwater, Water Research, 169 (2020) 115281.

[70] M.E. Borges, Hernández, T. & Esparza, P., Photocatalysis as a potential tertiary treatment of urban wastewater: new photocatalytic materials, Clean Techn Environ Policy, 16 (2014) 431.

[71] Y. Aguas, M. Hincapie, P. Fernández-Ibáñez, M.I. Polo-López, Solar photocatalytic disinfection of agricultural pathogenic fungi (Curvularia sp.) in real urban wastewater, Science of The Total Environment, 607-608 (2017) 1213-1224.

[72] W.Y. Teoh, J.A. Scott, R. Amal, Progress in Heterogeneous Photocatalysis: From Classical Radical Chemistry to Engineering Nanomaterials and Solar Reactors, The Journal of Physical Chemistry Letters, 3 (2012) 629-639.

[73] J. Lasek, Y.-H. Yu, J.C.S. Wu, Removal of NO_x by photocatalytic processes, Journal of Photochemistry and Photobiology C: Photochemistry Reviews, 14 (2013) 29-52.

[74] A. Mills, S. Elouali, The nitric oxide ISO photocatalytic reactor system: Measurement of NO_x removal activity and capacity, Journal of Photochemistry and Photobiology A: Chemistry, 305 (2015) 29-36.

[75] M.A.L.R.M. Cortes, J.W.J. Hamilton, P.K. Sharma, A. Brown, M. Nolan, K.A. Gray, J.A. Byrne, Formal quantum efficiencies for the photocatalytic reduction of CO_2 in a gas phase batch reactor, Catalysis Today, 326 (2019) 75-81.

[76] A. Fujishima, K. Honda, Electrochemical photolysis of water at a semiconductor electrode, Nature, 238 (1972) 37-38.

[77] M.A. Fox, M.T. Dulay, Heterogeneous photocatalysis, Chemical Reviews, 93 (1993) 341-357.

[78] K. Vinodgopal, P.V. Kamat, Electrochemically assisted photocatalysis using nanocrystalline semiconductor thin films, Solar Energy Materials and Solar Cells, 38 (1995) 401-410.

[79] J.A. Byrne, B.R. Eggins, Photoelectrochemistry of oxalate on particulate TiO_2 electrodes, Journal of Electroanalytical Chemistry, 457 (1998) 61-72.

[80] B.R. Eggins, F.L. Palmer, J.A. Byrne, Photocatalytic treatment of humic substances in drinking water, Water Research, 31 (1997) 1223-1226.

[81] E. Grabowska, Selected perovskite oxides: Characterization, preparation and photocatalytic properties—A review, Applied Catalysis B: Environmental, 186 (2016) 97-126.

[82] C.J. Heard, J. Čejka, M. Opanasenko, P. Nachtigall, G. Centi, S. Perathoner, 2D Oxide Nanomaterials to Address the Energy Transition and Catalysis, Advanced Materials, 31 (2019) 1801712.

[83] F. Haque, T. Daeneke, K. Kalantar-zadeh, J.Z. Ou, Two-Dimensional Transition Metal Oxide and Chalcogenide-Based Photocatalysts, Nano-Micro Letters, 10 (2017) 23.

[84] B.V. Zeghbroeck, Principles of semiconductor devices, Colorado, 2011.

[85] I.M. Szilágyi, B. Fórizs, O. Rosseler, Á. Szegedi, P. Németh, P. Király, G. Tárkányi, B. Vajna, K. Varga-Josepovits, K. László, A.L. Tóth, P. Baranyai, M. Leskelä, WO_3 photocatalysts: Influence of structure and composition, Journal of Catalysis, 294 (2012) 119-127.

[86] Y. Park, K.J. McDonald, K.-S. Choi, Progress in bismuth vanadate photoanodes for use in solar water oxidation, Chemical Society Reviews, 42 (2013) 2321-2337.

[87] B. Klahr, S. Gimenez, F. Fabregat-Santiago, J. Bisquert, T.W. Hamann, Electrochemical and photoelectrochemical investigation of water oxidation with hematite electrodes, Energy & Environmental Science, 5 (2012) 7626-7636.

[88] S. Sun, Recent advances in hybrid Cu_2O-based heterogeneous nanostructures, Nanoscale, 7 (2015) 10850-10882.

[89] J. Low, C. Jiang, B. Cheng, S. Wageh, A.A. Al-Ghamdi, J. Yu, A Review of Direct Z-Scheme Photocatalysts, Small Methods, 1 (2017) 1700080.

[90] W.R. Frensley, Chapter 1 - Heterostructure and Quantum Well Physics, in: N.G. Einspruch, W.R. Frensley (Eds.) VLSI Electronics Microstructure Science, Elsevier1994, pp. 1-24.

[91] A.J. Bard, Photoelectrochemistry and heterogeneous photo-catalysis at semiconductors, Journal of Photochemistry, 10 (1979) 59-75.

[92] J. Fu, Q. Xu, J. Low, C. Jiang, J. Yu, Ultrathin 2D/2D WO_3/g-C_3N_4 step-scheme H_2-production photocatalyst, Applied Catalysis B: Environmental, 243 (2019) 556-565.

[93] X. Han, D. Xu, L. An, C. Hou, Y. Li, Q. Zhang, H. Wang, WO_3/g-C_3N_4 two-dimensional composites for visible-light driven photocatalytic hydrogen production, International Journal of Hydrogen Energy, 43 (2018) 4845-4855.

[94] X. Liu, A. Jin, Y. Jia, T. Xia, C. Deng, M. Zhu, C. Chen, X. Chen, Synergy of adsorption and visible-light photocatalytic degradation of methylene blue by a bifunctional Z-scheme heterojunction of WO_3/g-C_3N_4, Applied Surface Science, 405 (2017) 359-371.

[95] S. Chen, Y. Hu, S. Meng, X. Fu, Study on the separation mechanisms of photogenerated electrons and holes for composite photocatalysts g-C_3N_4-WO_3, Applied Catalysis B: Environmental, 150-151 (2014) 564-573.

[96] K.-i. Katsumata, R. Motoyoshi, N. Matsushita, K. Okada, Preparation of graphitic carbon nitride (g-C_3N_4)/WO_3 composites and enhanced visible-light-driven photodegradation of acetaldehyde gas, Journal of Hazardous Materials, 260 (2013) 475-482.

[97] H. Zhang, Z. Feng, Y. Zhu, Y. Wu, T. Wu, Photocatalytic selective oxidation of biomass-derived 5-hydroxymethylfurfural to 2,5-diformylfuran on WO_3/g-C_3N_4 composite under irradiation of visible light, Journal of Photochemistry and Photobiology A: Chemistry, 371 (2019) 1-9.

[98] T. Ohno, N. Murakami, T. Koyanagi, Y. Yang, Photocatalytic reduction of CO_2 over a hybrid photocatalyst composed of WO_3 and graphitic carbon nitride (g-C_3N_4) under visible light, Journal of CO_2 Utilization, 6 (2014) 17-25.

[99] F. Zhan, R. Xie, W. Li, J. Li, Y. Yang, Y. Li, Q. Chen, In situ synthesis of g-C_3N_4/WO_3 heterojunction plates array films with enhanced photoelectrochemical performance, RSC Advances, 5 (2015) 69753-69760.

[100] Y. Hou, F. Zuo, A.P. Dagg, J. Liu, P. Feng, Branched WO_3 nanosheet array with layered C_3N_4 heterojunctions and CoO_x nanoparticles as a flexible photoanode for efficient photoelectrochemical water oxidation, Advanced materials (Deerfield Beach, Fla.), 26 (2014) 5043-5049.

[101] Y. Li, X. Wei, X. Yan, J. Cai, A. Zhou, M. Yang, K. Liu, Construction of inorganic–organic 2D/2D WO_3/g-C_3N_4 nanosheet arrays toward efficient photoelectrochemical splitting of natural seawater, Physical Chemistry Chemical Physics, 18 (2016) 10255-10261.

[102] J. Chen, X. Xiao, Y. Wang, Z. Ye, Ag nanoparticles decorated WO_3/g-C_3N_4 2D/2D heterostructure with enhanced photocatalytic activity for organic pollutants degradation, Applied Surface Science, 467-468 (2019) 1000-1010.

[103] S. Meng, W. Sun, S. Zhang, X. Zheng, X. Fu, S. Chen, Insight into the Transfer Mechanism of Photogenerated Carriers for WO_3/TiO_2 Heterojunction Photocatalysts: Is It the Transfer of Band–Band or Z-Scheme? Why?, The Journal of Physical Chemistry C, 122 (2018) 26326-26336.

[104] Y. Li, R. Wang, H. Li, X. Wei, J. Feng, K. Liu, Y. Dang, A. Zhou, Efficient and Stable Photoelectrochemical Seawater Splitting with TiO_2@g-C_3N_4 Nanorod Arrays Decorated by Co-Pi, The Journal of Physical Chemistry C, 119 (2015) 20283-20292.

[105] G. Li, X. Nie, J. Chen, Q. Jiang, T. An, P.K. Wong, H. Zhang, H. Zhao, H. Yamashita, Enhanced visible-light-driven photocatalytic inactivation of *Escherichia coli* using g-C_3N_4/TiO_2 hybrid photocatalyst synthesized using a hydrothermal-calcination approach, Water Research, 86 (2015) 17-24.

[106] D.J. Martin, P.J.T. Reardon, S.J.A. Moniz, J. Tang, Visible Light-Driven Pure Water Splitting by a Nature-Inspired Organic Semiconductor-Based System, Journal of the American Chemical Society, 136 (2014) 12568-12571.

[107] M.R. Waller, T.K. Townsend, J. Zhao, E.M. Sabio, R.L. Chamousis, N.D. Browning, F.E. Osterloh, Single-Crystal Tungsten Oxide Nanosheets: Photochemical Water Oxidation in the Quantum Confinement Regime, Chemistry of Materials, 24 (2012) 698-704.

[108] J. Kim, C.W. Lee, W. Choi, Platinized WO_3 as an Environmental Photocatalyst that Generates OH Radicals under Visible Light, Environmental Science & Technology, 44 (2010) 6849-6854.

[109] X. Wang, K. Maeda, A. Thomas, K. Takanabe, G. Xin, J.M. Carlsson, K. Domen, M. Antonietti, A metal-free polymeric photocatalyst for hydrogen production from water under visible light, Nature Materials, 8 (2008) 76.

[110] Y. Li, C. Zhang, D. Shuai, S. Naraginti, D. Wang, W. Zhang, Visible-light-driven photocatalytic inactivation of MS2 by metal-free g-C_3N_4: Virucidal performance and mechanism, Water Research, 106 (2016) 249-258.

[111] Y. Cui, Z. Ding, P. Liu, M. Antonietti, X. Fu, X. Wang, Metal-free activation of H_2O_2 by g-C_3N_4 under visible light irradiation for the degradation of organic pollutants, Physical Chemistry Chemical Physics, 14 (2012) 1455-1462.

[112] J. Xiao, Q. Han, Y. Xie, J. Yang, Q. Su, Y. Chen, H. Cao, Is C_3N_4 Chemically Stable toward Reactive Oxygen Species in Sunlight-Driven Water Treatment?, Environmental Science & Technology, 51 (2017) 13380-13387.

[113] K.S. Novoselov, A.K. Geim, S.V. Morozov, D. Jiang, Y. Zhang, S.V. Dubonos, I.V. Grigorieva, A.A. Firsov, Electric Field Effect in Atomically Thin Carbon Films, Science, 306 (2004) 666.

[114] K.S. Novoselov, A. Mishchenko, A. Carvalho, A.H. Castro Neto, 2D materials and van der Waals heterostructures, Science, 353 (2016) aac9439.

[115] D. Deng, K.S. Novoselov, Q. Fu, N. Zheng, Z. Tian, X. Bao, Catalysis with two-dimensional materials and their heterostructures, Nature Nanotechnology, 11 (2016) 218.

[116] A.K. Geim, I.V. Grigorieva, Van der Waals heterostructures, Nature, 499 (2013) 419-425.

[117] J. Yu, G. Dai, Q. Xiang, M. Jaroniec, Fabrication and enhanced visible-light photocatalytic activity of carbon self-doped TiO_2 sheets with exposed {001} facets, Journal of Materials Chemistry, 21 (2011) 1049-1057.

[118] Q. Xiang, J. Yu, W. Wang, M. Jaroniec, Nitrogen self-doped nanosized TiO_2 sheets with exposed {001} facets for enhanced visible-light photocatalytic activity, Chemical Communications, 47 (2011) 6906-6908.

[119] B. Wang, M.K.H. Leung, X.-Y. Lu, S.-Y. Chen, Synthesis and photocatalytic activity of boron and fluorine codoped TiO_2 nanosheets with reactive facets, Applied Energy, 112 (2013) 1190-1197.

[120] G. Wang, Z. Xing, X. Zeng, C. Feng, D.T. McCarthy, A. Deletic, X. Zhang, Ultrathin titanium oxide nanosheets film with memory bactericidal activity, Nanoscale, 8 (2016) 18050-18056.

[121] K. Kamaraj, R.P. George, B. Anandkumar, N. Parvathavarthini, U. Kamachi Mudali, A silver nanoparticle loaded TiO_2 nanoporous layer for visible light induced antimicrobial applications, Bioelectrochemistry, 106 (2015) 290-297.

[122] S. Ma, S. Zhan, Y. Jia, Q. Zhou, Superior Antibacterial Activity of Fe_3O_4-TiO_2 Nanosheets under Solar Light, ACS Applied Materials & Interfaces, 7 (2015) 21875-21883.

[123] J.A.B. J. W. J. Hamilton, P. S. M. Dunlop, N. M. D. Brown, Photo-Oxidation of Water Using Nanocrystalline Tungsten Oxide under Visible Light, International Journal of Photoenergy, 2008 (2008) 5.

[124] C. Di Valentin, F. Wang, G. Pacchioni, Tungsten Oxide in Catalysis and Photocatalysis: Hints from DFT, Topics in Catalysis, 56 (2013) 1404-1419.

[125] K. Kalantar-zadeh, A. Vijayaraghavan, M.-H. Ham, H. Zheng, M. Breedon, M.S. Strano, Synthesis of Atomically Thin WO_3 Sheets from Hydrated Tungsten Trioxide, Chemistry of Materials, 22 (2010) 5660-5666.

[126] X. Chen, Y. Zhou, Q. Liu, Z. Li, J. Liu, Z. Zou, Ultrathin, Single-Crystal WO_3 Nanosheets by Two-Dimensional Oriented Attachment toward Enhanced Photocatalystic Reduction of CO_2 into Hydrocarbon Fuels under Visible Light, ACS Applied Materials & Interfaces, 4 (2012) 3372-3377.

[127] H. Zhang, J. Yang, D. Li, W. Guo, Q. Qin, L. Zhu, W. Zheng, Template-free facile preparation of monoclinic WO_3 nanoplates and their high photocatalytic activities, Applied Surface Science, 305 (2014) 274-280.

[128] X. Gao, X. Su, C. Yang, F. Xiao, J. Wang, X. Cao, S. Wang, L. Zhang, Hydrothermal synthesis of WO_3 nanoplates as highly sensitive cyclohexene sensor and high-efficiency MB photocatalyst, Sensors and Actuators B: Chemical, 181 (2013) 537-543.

[129] J. Yan, T. Wang, G. Wu, W. Dai, N. Guan, L. Li, J. Gong, Tungsten Oxide Single Crystal Nanosheets for Enhanced Multichannel Solar Light Harvesting, Advanced Materials, 27 (2015) 1580-1586.

[130] W. Li, P. Da, Y. Zhang, Y. Wang, X. Lin, X. Gong, G. Zheng, WO_3 Nanoflakes for Enhanced Photoelectrochemical Conversion, ACS Nano, 8 (2014) 11770-11777.

[131] Y.P. Xie, G. Liu, L. Yin, H.-M. Cheng, Crystal facet-dependent photocatalytic oxidation and reduction reactivity of monoclinic WO_3 for solar energy conversion, Journal of Materials Chemistry, 22 (2012) 6746-6751.

[132] X. Su, F. Xiao, Y. Li, J. Jian, Q. Sun, J. Wang, Synthesis of uniform WO_3 square nanoplates via an organic acid-assisted hydrothermal process, Materials Letters, 64 (2010) 1232-1234.

[133] G. Zhang, W. Guan, H. Shen, X. Zhang, W. Fan, C. Lu, H. Bai, L. Xiao, W. Gu, W. Shi, Organic Additives-Free Hydrothermal Synthesis and Visible-Light-Driven Photodegradation of Tetracycline of WO_3 Nanosheets, Industrial & Engineering Chemistry Research, 53 (2014) 5443-5450.

[134] N. Li, H. Teng, L. Zhang, J. Zhou, M. Liu, Synthesis of Mo-doped WO_3 nanosheets with enhanced visible-light-driven photocatalytic properties, RSC Advances, 5 (2015) 95394-95400.

[135] C. Feng, S. Wang, B. Geng, Ti(iv) doped WO_3 nanocuboids: fabrication and enhanced visible-light-driven photocatalytic performance, Nanoscale, 3 (2011) 3695-3699.

[136] Y.-H. Xiao, C.-Q. Xu, W.-D. Zhang, Facile synthesis of Ni-doped WO_3 nanoplate arrays for effective photoelectrochemical water splitting, Journal of Solid State Electrochemistry, 21 (2017) 3355-3364.

[137] W. Zhu, J. Liu, S. Yu, Y. Zhou, X. Yan, Ag loaded WO_3 nanoplates for efficient photocatalytic degradation of sulfanilamide and their bactericidal effect under visible light irradiation, Journal of Hazardous Materials, 318 (2016) 407-416.

[138] P. Wang, B. Huang, X. Qin, X. Zhang, Y. Dai, M.-H. Whangbo, $Ag/AgBr/WO_3{\cdot}H_2O$: Visible-Light Photocatalyst for Bacteria Destruction, Inorganic Chemistry, 48 (2009) 10697-10702.

[139] J. Schneider, D.W. Bahnemann, Undesired Role of Sacrificial Reagents in Photocatalysis, The Journal of Physical Chemistry Letters, 4 (2013) 3479-3483.

[140] S. Dervin, D.D. Dionysiou, S.C. Pillai, 2D nanostructures for water purification: graphene and beyond, Nanoscale, 8 (2016) 15115-15131.

[141] D. Xia, T. An, G. Li, W. Wang, H. Zhao, P.K. Wong, Synergistic photocatalytic inactivation mechanisms of bacteria by graphene sheets grafted plasmonic AgAgX (X = Cl, Br, I) composite photocatalyst under visible light irradiation, Water Research, 99 (2016) 149-161.

[142] N. Khadgi, A.R. Upreti, Y. Li, Simultaneous bacterial inactivation and degradation of an emerging pollutant under visible light by $ZnFe_2O_4$ co-modified with Ag and rGO, RSC Advances, 7 (2017) 27007-27016.

[143] R. Rahimi, S. Zargari, A. Yousefi, M. Yaghoubi Berijani, A. Ghaffarinejad, A. Morsali, Visible light photocatalytic disinfection of *E. coli* with TiO_2–graphene nanocomposite sensitized with tetrakis(4-carboxyphenyl)porphyrin, Applied Surface Science, 355 (2015) 1098-1106.

[144] C.-H. Deng, J.-L. Gong, G.-M. Zeng, Y. Jiang, C. Zhang, H.-Y. Liu, S.-Y. Huan, Graphene–CdS nanocomposite inactivation performance toward *Escherichia coli* in the presence of humic acid under visible light irradiation, Chemical Engineering Journal, 284 (2016) 41-53.

[145] D. Wu, T. An, G. Li, W. Wang, Y. Cai, H.Y. Yip, H. Zhao, P.K. Wong, Mechanistic study of the visible-light-driven photocatalytic inactivation of bacteria by graphene oxide–zinc oxide composite, Applied Surface Science, 358 (2015) 137-145.

[146] P. Gao, K. Ng, D.D. Sun, Sulfonated graphene oxide–ZnO–Ag photocatalyst for fast photodegradation and disinfection under visible light, Journal of Hazardous Materials, 262 (2013) 826-835.

[147] X. Zeng, Z. Wang, G. Wang, T.R. Gengenbach, D.T. McCarthy, A. Deletic, J. Yu, X. Zhang, Highly dispersed TiO_2 nanocrystals and WO_3 nanorods on reduced graphene oxide: Z-scheme photocatalysis system for accelerated photocatalytic water disinfection, Applied Catalysis B: Environmental, 218 (2017) 163-173.

[148] L. Sun, T. Du, C. Hu, J. Chen, J. Lu, Z. Lu, H. Han, Antibacterial Activity of Graphene Oxide/g-C_3N_4 Composite through Photocatalytic Disinfection under Visible Light, ACS Sustainable Chemistry & Engineering, 5 (2017) 8693-8701.

[149] W. Wang, J.C. Yu, D. Xia, P.K. Wong, Y. Li, Graphene and g-C_3N_4 Nanosheets Cowrapped Elemental α-Sulfur As a Novel Metal-Free Heterojunction Photocatalyst for Bacterial Inactivation under Visible-Light, Environmental Science & Technology, 47 (2013) 8724-8732.

[150] A. Thomas, A. Fischer, F. Goettmann, M. Antonietti, J.-O. Müller, R. Schlögl, J.M. Carlsson, Graphitic carbon nitride materials: variation of structure and morphology and their use as metal-free catalysts, Journal of Materials Chemistry, 18 (2008) 4893-4908.

[151] Y. Wang, Y. Tian, L. Yan, Z. Su, DFT Study on Sulfur-Doped g-C_3N_4 Nanosheets as a Photocatalyst for CO_2 Reduction Reaction, The Journal of Physical Chemistry C, 122 (2018) 7712-7719.

[152] X. Wang, S. Blechert, M. Antonietti, Polymeric Graphitic Carbon Nitride for Heterogeneous Photocatalysis, ACS Catalysis, 2 (2012) 1596-1606.

[153] Y. Xu, S.-P. Gao, Band gap of C_3N_4 in the GW approximation, International Journal of Hydrogen Energy, 37 (2012) 11072-11080.

[154] J. Zhang, X. Chen, K. Takanabe, K. Maeda, K. Domen, J.D. Epping, X. Fu, M. Antonietti, X. Wang, Synthesis of a carbon nitride structure for visible-light catalysis by copolymerization, Angew Chem Int Ed Engl, 49 (2010) 441-444.

[155] Y. Zhang, M. Antonietti, Photocurrent Generation by Polymeric Carbon Nitride Solids: An Initial Step towards a Novel Photovoltaic System, Chemistry – An Asian Journal, 5 (2010) 1307-1311.

[156] J. Huang, W. Ho, X. Wang, Metal-free disinfection effects induced by graphitic carbon nitride polymers under visible light illumination, Chemical Communications, 50 (2014) 4338-4340.

[157] H. Zhao, H. Yu, X. Quan, S. Chen, Y. Zhang, H. Zhao, H. Wang, Fabrication of atomic single layer graphitic-C_3N_4 and its high performance of photocatalytic disinfection under visible light irradiation, Applied Catalysis B: Environmental, 152-153 (2014) 46-50.

[158] J. Deng, J. Liang, M. Li, M. Tong, Enhanced visible-light-driven photocatalytic bacteria disinfection by g-C_3N_4-AgBr, Colloids and Surfaces B: Biointerfaces, 152 (2017) 49-57.

[159] M.J. Muñoz-Batista, O. Fontelles-Carceller, M. Ferrer, M. Fernández-García, A. Kubacka, Disinfection capability of Ag/g-C_3N_4 composite photocatalysts under UV and visible light illumination, Applied Catalysis B: Environmental, 183 (2016) 86-95.

[160] J. Low, S. Cao, J. Yu, S. Wageh, Two-dimensional layered composite photocatalysts, Chemical Communications, 50 (2014) 10768-10777.

[161] D. Liu, S. Zhang, J. Wang, T. Peng, R. Li, Direct Z-Scheme 2D/2D Photocatalyst Based on Ultrathin g-C_3N_4 and WO_3 Nanosheets for Efficient Visible-Light-Driven H_2 Generation, ACS Applied Materials & Interfaces, 11 (2019) 27913-27923.

[162] S. Chen, Y. Hu, X. Jiang, S. Meng, X. Fu, Fabrication and characterization of novel Z-scheme photocatalyst WO_3/g-C_3N_4 with high efficient visible light photocatalytic activity, Materials Chemistry and Physics, 149-150 (2015) 512-521.

[163] G. Chen, S. Bian, C.-Y. Guo, X. Wu, Insight into the Z-scheme heterostructure WO_3/g-C_3N_4 for enhanced photocatalytic degradation of methyl orange, Materials Letters, 236 (2019) 596-599.

[164] J. Chen, X. Xiao, Y. Wang, Z. Ye, Fabrication of hierarchical sheet-on-sheet WO_3/g-C_3N_4 composites with enhanced photocatalytic activity, Journal of Alloys and Compounds, 777 (2019) 325-334.

[165] H. Li, H. Yu, X. Quan, S. Chen, Y. Zhang, Uncovering the Key Role of the Fermi Level of the Electron Mediator in a Z-Scheme Photocatalyst by Detecting the Charge

Transfer Process of WO_3-metal-gC_3N_4 (Metal = Cu, Ag, Au), ACS Applied Materials & Interfaces, 8 (2016) 2111-2119.

[166] T. Xiao, Z. Tang, Y. Yang, L. Tang, Y. Zhou, Z. Zou, In situ construction of hierarchical WO_3/g-C_3N_4 composite hollow microspheres as a Z-scheme photocatalyst for the degradation of antibiotics, Applied Catalysis B: Environmental, 220 (2018) 417-428.

[167] K.E. Ahmed, D.-H. Kuo, M.A. Zeleke, O.A. Zelekew, A.K. Abay, Synthesis of Sn-WO_3/g-C_3N_4 composites with surface activated oxygen for visible light degradation of dyes, Journal of Photochemistry and Photobiology A: Chemistry, 369 (2019) 133-141.

[168] Z. Jin, N. Murakami, T. Tsubota, T. Ohno, Complete oxidation of acetaldehyde over a composite photocatalyst of graphitic carbon nitride and tungsten(VI) oxide under visible-light irradiation, Applied Catalysis B: Environmental, 150-151 (2014) 479-485.

[169] W. Zhu, F. Sun, R. Goei, Y. Zhou, Construction of WO_3–g-C_3N_4 composites as efficient photocatalysts for pharmaceutical degradation under visible light, Catalysis Science & Technology, 7 (2017) 2591-2600.

[170] D. Wu, B. Wang, W. Wang, T. An, G. Li, T.W. Ng, H.Y. Yip, C. Xiong, H.K. Lee, P.K. Wong, Visible-light-driven BiOBr nanosheets for highly facet-dependent photocatalytic inactivation of *Escherichia coli*, Journal of Materials Chemistry A, 3 (2015) 15148-15155.

[171] D. Wu, S. Yue, W. Wang, T. An, G. Li, H.Y. Yip, H. Zhao, P.K. Wong, Boron doped BiOBr nanosheets with enhanced photocatalytic inactivation of *Escherichia coli*, Applied Catalysis B: Environmental, 192 (2016) 35-45.

[172] D. Wu, L. Ye, S. Yue, B. Wang, W. Wang, H.Y. Yip, P.K. Wong, Alkali-Induced in Situ Fabrication of Bi_2O_4-Decorated BiOBr Nanosheets with Excellent Photocatalytic Performance, The Journal of Physical Chemistry C, 120 (2016) 7715-7727.

[173] P. Cheng, Q. Zhou, X. Hu, S. Su, X. Wang, M. Jin, L. Shui, X. Gao, Y. Guan, R. Nözel, G. Zhou, Z. Zhang, J. Liu, Transparent Glass with the Growth of Pyramid-Type MoS_2 for Highly Efficient Water Disinfection under Visible-Light Irradiation, ACS Applied Materials & Interfaces, 10 (2018) 23444-23450.

[174] B. Zhang, S. Zou, R. Cai, M. Li, Z. He, Highly-efficient photocatalytic disinfection of *Escherichia coli* under visible light using carbon supported Vanadium Tetrasulfide nanocomposites, Applied Catalysis B: Environmental, 224 (2018) 383-393.

[175] X. Liu, G. Duan, W. Li, Z. Zhou, R. Zhou, Membrane destruction-mediated antibacterial activity of tungsten disulfide (WS_2), RSC Advances, 7 (2017) 37873-37880.

[176] G.S. Bang, S. Cho, N. Son, G.W. Shim, B.-K. Cho, S.-Y. Choi, DNA-Assisted Exfoliation of Tungsten Dichalcogenides and Their Antibacterial Effect, ACS Applied Materials & Interfaces, 8 (2016) 1943-1950.

[177] H. Uk Lee, S.C. Lee, J. Won, B.-C. Son, S. Choi, Y. Kim, S.Y. Park, H.-S. Kim, Y.-C. Lee, J. Lee, Stable semiconductor black phosphorus (BP)@titanium dioxide (TiO_2) hybrid photocatalysts, Scientific Reports, 5 (2015) 8691.

[178] R. Daghrir, P. Drogui, D. Robert, Photoelectrocatalytic technologies for environmental applications, Journal of Photochemistry and Photobiology A: Chemistry, 238 (2012) 41-52.

[179] J.A. Byrne, A. Davidson, P.S.M. Dunlop, B.R. Eggins, Water treatment using nano-crystalline TiO_2 electrodes, Journal of Photochemistry and Photobiology A: Chemistry, 148 (2002) 365-374.

[180] M.A.L.R.M. Cortes, S. McMichael, J.W.J. Hamilton, P.K. Sharma, A. Brown, J.A. Byrne, Photoelectrochemical reduction of CO_2 with TiNT, Materials Science in Semiconductor Processing, 108 (2020) 104900.

[181] G. Hodes, D. Cahen, J. Manassen, Tungsten trioxide as a photoanode for a photoelectrochemical cell (PEC), Nature, 260 (1976) 312-313.

[182] Z. Jiao, J. Wang, L. Ke, X.W. Sun, H.V. Demir, Morphology-Tailored Synthesis of Tungsten Trioxide (Hydrate) Thin Films and Their Photocatalytic Properties, ACS Applied Materials & Interfaces, 3 (2011) 229-236.

[183] R.M. Fernández-Domene, R. Sánchez-Tovar, B. Lucas-granados, M.J. Muñoz-Portero, J. García-Antón, Elimination of pesticide atrazine by photoelectrocatalysis using a photoanode based on WO_3 nanosheets, Chemical Engineering Journal, 350 (2018) 1114-1124.

[184] S. Hilaire, M.J. Süess, N. Kränzlin, K. Bieńkowski, R. Solarska, J. Augustyński, M. Niederberger, Microwave-assisted nonaqueous synthesis of WO_3 nanoparticles for crystallographically oriented photoanodes for water splitting, Journal of Materials Chemistry A, 2 (2014) 20530-20537.

[185] J. Jing, Z. Chen, C. Feng, Dramatically enhanced photoelectrochemical properties and transformed p/n type of g-C_3N_4 caused by K and I co-doping, Electrochimica Acta, 297 (2019) 488-496.

[186] M. Karimi-Nazarabad, E.K. Goharshadi, S.J. Mahdizadeh, Efficient Photoelectrocatalytic Water Oxidation by Palladium Doped g-C_3N_4 Electrodeposited Thin Film, The Journal of Physical Chemistry C, 123 (2019) 26106-26115.

[187] Y. Zhang, Z. Schnepp, J. Cao, S. Ouyang, Y. Li, J. Ye, S. Liu, Biopolymer-activated graphitic carbon nitride towards a sustainable photocathode material, Scientific reports, 3 (2013) 2163-2163.

[188] M. Karimi-Nazarabad, E.K. Goharshadi, Highly efficient photocatalytic and photoelectrocatalytic activity of solar light driven WO_3/g-C_3N_4 nanocomposite, Solar Energy Materials and Solar Cells, 160 (2017) 484-493.

[189] K. Byrappa, T. Adschiri, Hydrothermal technology for nanotechnology, Progress in Crystal Growth and Characterization of Materials, 53 (2007) 117-166.

[190] P.W. Dunne, E. Lester, C. Starkey, I. Clark, Y. Chen, A.S. Munn, CHAPTER 15 The Chemistry of Continuous Hydrothermal/Solvothermal Synthesis of Nanomaterials, Supercritical and Other High-pressure Solvent Systems: For Extraction, Reaction and Material Processing, The Royal Society of Chemistry2018, pp. 449-475.

[191] Y. Mao, T.-J. Park, F. Zhang, H. Zhou, S.S. Wong, Environmentally Friendly Methodologies of Nanostructure Synthesis, Small, 3 (2007) 1122-1139.

[192] I. Krivtsov, E.I. García-López, G. Marcì, L. Palmisano, Z. Amghouz, J.R. García, S. Ordóñez, E. Díaz, Selective photocatalytic oxidation of 5-hydroxymethyl-2-furfural to 2,5-furandicarboxyaldehyde in aqueous suspension of g-C_3N_4, Applied Catalysis B: Environmental, 204 (2017) 430-439.

[193] S. Yang, Y. Gong, J. Zhang, L. Zhan, L. Ma, Z. Fang, R. Vajtai, X. Wang, P.M. Ajayan, Exfoliated Graphitic Carbon Nitride Nanosheets as Efficient Catalysts for Hydrogen Evolution Under Visible Light, Advanced Materials, 25 (2013) 2452-2456.

[194] M. Yang, S. Hu, F. Li, Z. Fan, F. Wang, D. Liu, J. Gui, The influence of preparation method on the photocatalytic performance of g-C_3N_4/WO_3 composite photocatalyst, Ceramics International, 40 (2014) 11963-11969.

[195] G.P. Smestad, M. Gratzel, Demonstrating Electron Transfer and Nanotechnology: A Natural Dye-Sensitized Nanocrystalline Energy Converter, Journal of Chemical Education, 75 (1998) 752.

[196] *X-ray Photoelectron Spectroscopy (XPS) Reference Pages,* Surface Science Western laboratories, University of Western Ontario,.

[197] NIST X-ray Photoelectron Spectroscopy Database, National Institute of Standards and Technology, Gaithersburg MD, 20899, 2000.

[198] F.R. Pomilla, M.A.L.R.M. Cortes, J.W.J. Hamilton, R. Molinari, G. Barbieri, G. Marci, L. Palmisano, P.K. Sharma, A. Brown, J.A. Byrne, An Investigation into the Stability of Graphitic C_3N_4 as a Photocatalyst for CO_2 Reduction, The Journal of Physical Chemistry C, (2018).

[199] T.A. McMurray, J.A. Byrne, P.S.M. Dunlop, J.G.M. Winkelman, B.R. Eggins, E.T. McAdams, Intrinsic kinetics of photocatalytic oxidation of formic and oxalic acid on immobilised TiO_2 films, Applied Catalysis A: General, 262 (2004) 105-110.

[200] A.H. Geeraerd, V.P. Valdramidis, J.F. Van Impe, GInaFiT, a freeware tool to assess non-log-linear microbial survivor curves, International Journal of Food Microbiology, 102 (2005) 95-105.

[201] M. Boyle, C. Sichel, P. Fernández-Ibáñez, G.B. Arias-Quiroz, M. Iriarte-Puña, A. Mercado, E. Ubomba-Jaswa, K.G. McGuigan, Bactericidal Effect of Solar Water Disinfection under Real Sunlight Conditions, Applied and Environmental Microbiology, 74 (2008) 2997.

[202] E. Ubomba-Jaswa, C. Navntoft, M.I. Polo-López, P. Fernandez-Ibáñez, K.G. McGuigan, Solar disinfection of drinking water (SODIS): an investigation of the effect of UV-A dose on inactivation efficiency, Photochemical & Photobiological Sciences, 8 (2009) 587-595.

[203] N.M. Makwana, R. Hazael, P.F. McMillan, J.A. Darr, Photocatalytic water disinfection by simple and low-cost monolithic and heterojunction ceramic wafers, Photochemical & Photobiological Sciences, 14 (2015) 1190-1196.

[204] A.M. Roy, G.C. De, N. Sasmal, S.S. Bhattacharyya, Determination of the flatband potential of semiconductor particles in suspension by photovoltage measurement, International Journal of Hydrogen Energy, 20 (1995) 627-630.

[205] P.V. Kamat, IPCE derivation, University of Notre Dame, USA.

[206] S. Banerjee, New Insights into the Mechanism of Visible Light Photocatalysis, in: P.F. Suresh C. Pillai, Kevin E. O'Shea, John A. Byrne , Dionysios D. Dionysiou (Ed.), ACS, The Journal of Physical Chemistry Letters, 2014, pp. 2543-2544.

[207] J.Y. Zheng, Z. Haider, T.K. Van, A.U. Pawar, M.J. Kang, C.W. Kim, Y.S. Kang, Tuning of the crystal engineering and photoelectrochemical properties of crystalline tungsten oxide for optoelectronic device applications, CrystEngComm, 17 (2015) 6070-6093.

[208] Z.-F. Huang, J. Song, L. Pan, X. Zhang, L. Wang, J.-J. Zou, Tungsten Oxides for Photocatalysis, Electrochemistry, and Phototherapy, Advanced Materials, 27 (2015) 5309-5327.

[209] N. Zhang, C. Chen, Z. Mei, X. Liu, X. Qu, Y. Li, S. Li, W. Qi, Y. Zhang, J. Ye, V.A.L. Roy, R. Ma, Monoclinic Tungsten Oxide with {100} Facet Orientation and Tuned Electronic Band Structure for Enhanced Photocatalytic Oxidations, ACS Applied Materials & Interfaces, 8 (2016) 10367-10374.

[210] X. Ma, D. Jiang, P. Xiao, Y. Jin, S. Meng, M. Chen, 2D/2D heterojunctions of WO_3 nanosheet/$K^+Ca_2Nb_3O_{10}^-$ ultrathin nanosheet with improved charge separation efficiency for significantly boosting photocatalysis, Catalysis Science & Technology, 7 (2017) 3481-3491.

[211] S.K. Gullapalli, R.S. Vemuri, C.V. Ramana, Structural transformation induced changes in the optical properties of nanocrystalline tungsten oxide thin films, Applied Physics Letters, 96 (2010) 171903.

[212] Z. Dechun, 4 - Chemical and photophysical properties of materials for OLEDs, in: A. Buckley (Ed.) Organic Light-Emitting Diodes (OLEDs), Woodhead Publishing2013, pp. 114-142.

[213] M. Bellardita, E.I. García-López, G. Marcì, I. Krivtsov, J.R. García, L. Palmisano, Selective photocatalytic oxidation of aromatic alcohols in water by using P-doped g-C_3N_4, Applied Catalysis B: Environmental, 220 (2018) 222-233.

[214] F. Riboni, L.G. Bettini, D.W. Bahnemann, E. Selli, WO_3–TiO_2 vs. TiO_2 photocatalysts: effect of the W precursor and amount on the photocatalytic activity of mixed oxides, Catalysis Today, 209 (2013) 28-34.

[215] Medical Management Guidelines for Phenol, in: D.o.H.a.H. Services. (Ed.), *Agency for Toxic Substances and Disease Registry*- Department of Health and Human Services., United States of America, October 21, 2014.

[216] W.H. Organization, Guidelines for drinking-water quality: fourth edition incorporating the first addendum, Geneva, 2017.

[217] J.A. Byrne, Photocatalytic Enhancement for Solar Disinfection of Water: A Review, in: P.S.M.D. Pilar A. Fernandez-Ibañez, Dheaya M. A. Alrousan, and Jeremy W. J. Hamilton (Ed.) International Journal of Photoenergy, 2011, pp. 12.

[218] W.H. Bragg, W.L. Bragg, The reflection of X-rays by crystals, Proceedings of the Royal Society of London. Series A, Containing Papers of a Mathematical and Physical Character, 88 (1913) 428-438.

[219] F. Fina, S.K. Callear, G.M. Carins, J.T.S. Irvine, Structural Investigation of Graphitic Carbon Nitride via XRD and Neutron Diffraction, Chemistry of Materials, 27 (2015) 2612-2618.

[220] G. Leofanti, M. Padovan, G. Tozzola, B. Venturelli, Surface area and pore texture of catalysts, Catalysis Today, 41 (1998) 207-219.

[221] S.M. Dunlop Patrick, A. Galdi, A. McMurray Trudy, W.J. Hamilton Jeremy, L. Rizzo, J.A. Byrne, Comparison of Photocatalytic Activities of Commercial Titanium Dioxide Powders Immobilised on Glass Substrates, Journal of Advanced Oxidation Technologies, 2010, pp. 99.

[222] P. Xia, B. Zhu, B. Cheng, J. Yu, J. Xu, 2D/2D g-C_3N_4/MnO_2 Nanocomposite as a Direct Z-Scheme Photocatalyst for Enhanced Photocatalytic Activity, ACS Sustainable Chemistry & Engineering, 6 (2018) 965-973.

[223] H. Ji, F. Chang, X. Hu, W. Qin, J. Shen, Photocatalytic degradation of 2,4,6-trichlorophenol over g-C_3N_4 under visible light irradiation, Chemical Engineering Journal, 218 (2013) 183-190.

[224] A.H. Geeraerd, C.H. Herremans, J.F. Van Impe, Structural model requirements to describe microbial inactivation during a mild heat treatment, International Journal of Food Microbiology, 59 (2000) 185-209.

[225] J. Marugán, R. van Grieken, C. Sordo, C. Cruz, Kinetics of the photocatalytic disinfection of *Escherichia coli* suspensions, Applied Catalysis B: Environmental, 82 (2008) 27-36.

[226] J. Li, Y. Yin, E. Liu, Y. Ma, J. Wan, J. Fan, X. Hu, In situ growing Bi_2MoO_6 on g-C_3N_4 nanosheets with enhanced photocatalytic hydrogen evolution and disinfection of bacteria under visible light irradiation, Journal of Hazardous Materials, 321 (2017) 183-192.

[227] L. Huang, H. Xu, Y. Li, H. Li, X. Cheng, J. Xia, Y. Xu, G. Cai, Visible-light-induced WO_3/g-C_3N_4 composites with enhanced photocatalytic activity, Dalton Transactions, 42 (2013) 8606-8616.

[228] H. Katsumata, Y. Tachi, T. Suzuki, S. Kaneco, Z-scheme photocatalytic hydrogen production over WO_3/g-C_3N_4 composite photocatalysts, RSC Advances, 4 (2014) 21405-21409.

[229] J. Ding, Q. Liu, Z. Zhang, X. Liu, J. Zhao, S. Cheng, B. Zong, W.-L. Dai, Carbon nitride nanosheets decorated with WO_3 nanorods: Ultrasonic-assisted facile synthesis and catalytic application in the green manufacture of dialdehydes, Applied Catalysis B: Environmental, 165 (2015) 511-518.

[230] J.W.J. Hamilton, J.A. Byrne, P.S.M. Dunlop, D.D. Dionysiou, M. Pelaez, K. O'Shea, D. Synnott, S.C. Pillai, Evaluating the Mechanism of Visible Light Activity for N,F-TiO_2 Using Photoelectrochemistry, The Journal of Physical Chemistry C, 118 (2014) 12206-12215.

[231] B. Moss, K.K. Lim, A. Beltram, S. Moniz, J. Tang, P. Fornasiero, P. Barnes, J. Durrant, A. Kafizas, Comparing photoelectrochemical water oxidation, recombination kinetics and charge trapping in the three polymorphs of TiO_2, Scientific Reports, 7 (2017) 2938.

[232] P. Wu, J. Wang, J. Zhao, L. Guo, F.E. Osterloh, Structure defects in g-C_3N_4 limit visible light driven hydrogen evolution and photovoltage, Journal of Materials Chemistry A, 2 (2014) 20338-20344.

[233] R. Godin, Y. Wang, M.A. Zwijnenburg, J. Tang, J.R. Durrant, Time-Resolved Spectroscopic Investigation of Charge Trapping in Carbon Nitrides Photocatalysts for Hydrogen Generation, Journal of the American Chemical Society, 139 (2017) 5216-5224.

[234] H. Kaur, B. Halliwell, [6] Detection of hydroxyl radicals by aromatic hydroxylation, Methods in Enzymology, Academic Press1994, pp. 67-82.

[235] L.M. Dorfman, G.E. Adams, Reactivity of the Hydroxyl Radical in Aqueous Solutions, NATIONAL BUREAU OF STANDARDS, Washington D.C., United States, 1973, pp. 72.

[236] F. Collin, Chemical Basis of Reactive Oxygen Species Reactivity and Involvement in Neurodegenerative Diseases, International journal of molecular sciences, 20 (2019) 2407.

[237] P. Attri, Y.H. Kim, D.H. Park, J.H. Park, Y.J. Hong, H.S. Uhm, K.-N. Kim, A. Fridman, E.H. Choi, Generation mechanism of hydroxyl radical species and its lifetime prediction during the plasma-initiated ultraviolet (UV) photolysis, Scientific Reports, 5 (2015) 9332.

[238] J. Muff, L.R. Bennedsen, E.G. Søgaard, Study of electrochemical bleaching of p-nitrosodimethylaniline and its role as hydroxyl radical probe compound, Journal of Applied Electrochemistry, 41 (2011) 599-607.

[239] M.E. Simonsen, J. Muff, L.R. Bennedsen, K.P. Kowalski, E.G. Søgaard, Photocatalytic bleaching of p-nitrosodimethylaniline and a comparison to the performance of other AOP technologies, Journal of Photochemistry and Photobiology A: Chemistry, 216 (2010) 244-249.

[240] C. Kim, H.-j. Park, S. Cha, J. Yoon, Facile detection of photogenerated reactive oxygen species in TiO_2 nanoparticles suspension using colorimetric probe-assisted spectrometric method, Chemosphere, 93 (2013) 2011-2015.

[241] L. Zang, P. Qu, J. Zhao, T. Shen, H. Hidaka, Photocatalytic bleaching of p-nitrosodimethylaniline in TiO_2 aqueous suspensions: A kinetic treatment involving some primary events photoinduced on the particle surface, Journal of Molecular Catalysis A: Chemical, 120 (1997) 235-245.

[242] P.A. Trudiatger, On the absorbancy of reduced methyl viologen, Analytical Biochemistry, 36 (1970) 222-225.

[243] D. Dung, J. Ramsden, M. Graetzel, Dynamics of interfacial electron-transfer processes in colloidal semiconductor systems, Journal of the American Chemical Society, 104 (1982) 2977-2985.

[244] T. Watanabe, K. Honda, Measurement of the extinction coefficient of the methyl viologen cation radical and the efficiency of its formation by semiconductor photocatalysis, The Journal of Physical Chemistry, 86 (1982) 2617-2619.

[245] M.D. Ward, J.R. White, A.J. Bard, Electrochemical investigation of the energetics of particulate titanium dioxide photocatalysts. The methyl viologen-acetate system, Journal of the American Chemical Society, 105 (1983) 27-31.

[246] W.J. R, B.A. J, Electrochemical Investigation of Photocatalysis at CdS Suspensions in the Presence of Methylviologen, The Journal of Physical Chemistry, 1985.

[247] C. Lohaus, A. Klein, W. Jaegermann, Limitation of Fermi level shifts by polaron defect states in hematite photoelectrodes, Nature Communications, 9 (2018).

[248] J.J. Walsh, C. Jiang, J. Tang, A.J. Cowan, Photochemical CO_2 reduction using structurally controlled g-C_3N_4, Physical Chemistry Chemical Physics, 18 (2016) 24825-24829.

[249] R. López, R. Gómez, Band-gap energy estimation from diffuse reflectance measurements on sol–gel and commercial TiO_2: a comparative study, Journal of Sol-Gel Science and Technology, 61 (2012) 1-7.

[250] B. M.A, G. D.S, Prediction of Flatband Potentials at Semiconductor-Electrolyte Interfaces from Atomic Electronegativities, J. Electrochem. Soc, 125 (1978) 228-232.

[251] G.A. Parks, The Isoelectric Points of Solid Oxides, Solid Hydroxides, and Aqueous Hydroxo Complex Systems, Chemical Reviews, 65 (1965) 177-198.

[252] M. Anik, T. Cansizoglu, Dissolution kinetics of WO_3 in acidic solutions, Journal of Applied Electrochemistry, 36 (2006) 603-608.

[253] P. Praus, L. Svoboda, R. Dvorský, M. Reli, M. Kormunda, P. Mančík, Synthesis and properties of nanocomposites of WO_3 and exfoliated g-C_3N_4, Ceramics International, 43 (2017) 13581-13591.

[254] B. Ohtani, Revisiting the fundamental physical chemistry in heterogeneous photocatalysis: its thermodynamics and kinetics, Physical Chemistry Chemical Physics, 16 (2014) 1788-1797.

[255] A.B. Jorge, D.J. Martin, M.T.S. Dhanoa, A.S. Rahman, N. Makwana, J. Tang, A. Sella, F. Corà, S. Firth, J.A. Darr, P.F. McMillan, H_2 and O_2 Evolution from Water Half-Splitting Reactions by Graphitic Carbon Nitride Materials, The Journal of Physical Chemistry C, 117 (2013) 7178-7185.

[256] F. Wang, C. Di Valentin, G. Pacchioni, Electronic and Structural Properties of WO3: A Systematic Hybrid DFT Study, The Journal of Physical Chemistry C, 115 (2011) 8345-8353.

[257] E.M. Miller, D.M. Kroupa, J. Zhang, P. Schulz, A.R. Marshall, A. Kahn, S. Lany, J.M. Luther, M.C. Beard, C.L. Perkins, J. van de Lagemaat, Revisiting the Valence and Conduction Band Size Dependence of PbS Quantum Dot Thin Films, ACS Nano, 10 (2016) 3302-3311.

[258] T. Varga, H. Haspel, A. Kormányos, C. Janáky, Á. Kukovecz, Z. Kónya, Nitridation of one-dimensional tungsten oxide nanostructures: Changes in structure and photoactivity, Electrochimica Acta, 256 (2017) 299-306.

[259] L. He, M. Fei, J. Chen, Y. Tian, Y. Jiang, Y. Huang, K. Xu, J. Hu, Z. Zhao, Q. Zhang, H. Ni, L. Chen, Graphitic C_3N_4 quantum dots for next-generation QLED displays, Materials Today, 22 (2019) 76-84.

[260] Z. Gan, Y. Shan, J. Chen, Q. Gui, Q. Zhang, S. Nie, X. Wu, The origins of the broadband photoluminescence from carbon nitrides and applications to white light emitting, Nano Research, 9 (2016) 1801-1812.

[261] J. Wang, P.S. Lee, J. Ma, Synthesis, growth mechanism and room-temperature blue luminescence emission of uniform WO_3 nanosheets with W as starting material, Journal of Crystal Growth, 311 (2009) 316-319.

[262] F. Wang, C. Di Valentin, G. Pacchioni, Semiconductor-to-metal transition in WO_{3-x}: Nature of the oxygen vacancy, Physical Review B, 84 (2011) 073103.

[263] I. Grigioni, K.G. Stamplecoskie, E. Selli, P.V. Kamat, Dynamics of Photogenerated Charge Carriers in $WO_3/BiVO_4$ Heterojunction Photoanodes, The Journal of Physical Chemistry C, 119 (2015) 20792-20800.

[264] A. Hankin, F.E. Bedoya-Lora, J.C. Alexander, A. Regoutz, G.H. Kelsall, Flat band potential determination: avoiding the pitfalls, Journal of Materials Chemistry A, 7 (2019) 26162-26176.

[265] K. Gelderman, L. Lee, S.W. Donne, Flat-Band Potential of a Semiconductor: Using the Mott–Schottky Equation, Journal of Chemical Education, 84 (2007) 685.

[266] N. Sato, Electrochemistry at Metal and Semiconductor Electrodes, ELSEVffiR SCIENCE B.V., Amsterdam, The Netherlands, 1998.

[267] M.F.J. Dijkstra, A. Michorius, H. Buwalda, H.J. Panneman, J.G.M. Winkelman, A.A.C.M. Beenackers, Comparison of the efficiency of immobilized and suspended systems in photocatalytic degradation, Catalysis Today, 66 (2001) 487-494.

[268] K. Vinodgopal, U. Stafford, K.A. Gray, P.V. Kamat, Electrochemically Assisted Photocatalysis. 2. The Role of Oxygen and Reaction Intermediates in the Degradation of 4-Chlorophenol on Immobilized TiO_2 Particulate Films, The Journal of Physical Chemistry, 98 (1994) 6797-6803.

[269] Z. Liu, X. Zhang, S. Nishimoto, M. Jin, D.A. Tryk, T. Murakami, A. Fujishima, Highly Ordered TiO_2 Nanotube Arrays with Controllable Length for

Photoelectrocatalytic Degradation of Phenol, The Journal of Physical Chemistry C, 112 (2008) 253-259.

[270] I.M. Butterfield, P.A. Christensen, T.P. Curtis, J. Gunlazuardi, Water disinfection using an immobilised titanium dioxide film in a photochemical reactor with electric field enhancement, Water Research, 31 (1997) 675-677.

[271] Y. Xu, Y. Jia, Y. Zhang, R. Nie, Z. Zhu, J. Wang, H. Jing, Photoelectrocatalytic reduction of CO_2 to methanol over the multi-functionalized TiO_2 photocathodes, Applied Catalysis B: Environmental, 205 (2017) 254-261.

[272] Q. Wang, J. Shang, T. Zhu, F. Zhao, Efficient photoelectrocatalytic reduction of Cr(VI) using TiO_2 nanotube arrays as the photoanode and a large-area titanium mesh as the photocathode, Journal of Molecular Catalysis A: Chemical, 335 (2011) 242-247.

[273] N. Baram, D. Starosvetsky, J. Starosvetsky, M. Epshtein, R. Armon, Y. Ein-Eli, Enhanced Inactivation of *E. coli* Bacteria Using Immobilized Porous TiO_2 Photoelectrocatalysis, Electrochimica Acta - ELECTROCHIM ACTA, 54 (2009) 3381-3386.

[274] Q. Kang, Q.Z. Lu, S.H. Liu, L.X. Yang, L.F. Wen, S.L. Luo, Q.Y. Cai, A ternary hybrid CdS/Pt–TiO_2 nanotube structure for photoelectrocatalytic bactericidal effects on Escherichia Coli, Biomaterials, 31 (2010) 3317-3326.

[275] H. Selcuk, Disinfection and formation of disinfection by-products in a photoelectrocatalytic system, Water Research, 44 (2010) 3966-3972.

[276] M.F. Brugnera, M. Miyata, G.J. Zocolo, C.Q.F. Leite, M.V.B. Zanoni, Inactivation and disposal of by-products from Mycobacterium smegmatis by photoelectrocatalytic oxidation using Ti/TiO_2-Ag nanotube electrodes, Electrochimica Acta, 85 (2012) 33-41.

[277] M.F. Brugnera, M. Miyata, G.J. Zocolo, C.Q. Fujimura Leite, M.V. Boldrin Zanoni, A photoelectrocatalytic process that disinfects water contaminated with Mycobacterium kansasii and Mycobacterium avium, Water Research, 47 (2013) 6596-6605.

[278] X. Liu, Y. Han, H. Zhang, H. Zhao, Instant inactivation and rapid decomposition of Escherichia coli using a high efficiency TiO_2 nanotube array photoelectrode, RSC Advances, 3 (2013) 20824.

[279] C. Pablos, J. Marugán, R. van Grieken, P.S.M. Dunlop, J.W.J. Hamilton, D.D. Dionysiou, J.A. Byrne, Electrochemical Enhancement of Photocatalytic Disinfection on

Aligned TiO_2 and Nitrogen Doped TiO_2 Nanotubes, Molecules (Basel, Switzerland), 22 (2017) 704.

[280] L.E. Fraga, M.A. Anderson, M.L.P.M.A. Beatriz, F.M.M. Paschoal, L.P. Romão, M.V.B. Zanoni, Evaluation of the photoelectrocatalytic method for oxidizing chloride and simultaneous removal of microcystin toxins in surface waters, Electrochimica Acta, 54 (2009) 2069-2076.

[281] X. Liu, F. Wang, Q. Wang, Nanostructure-based WO_3 photoanodes for photoelectrochemical water splitting, Physical Chemistry Chemical Physics, 14 (2012) 7894-7911.

[282] S.M. Lyth, Y. Nabae, S. Moriya, S. Kuroki, M.-a. Kakimoto, J.-i. Ozaki, S. Miyata, Carbon Nitride as a Nonprecious Catalyst for Electrochemical Oxygen Reduction, The Journal of Physical Chemistry C, 113 (2009) 20148-20151.

[283] J. Tian, R. Ning, Q. Liu, A.M. Asiri, A.O. Al-Youbi, X. Sun, Three-Dimensional Porous Supramolecular Architecture from Ultrathin g-C_3N_4 Nanosheets and Reduced Graphene Oxide: Solution Self-Assembly Construction and Application as a Highly Efficient Metal-Free Electrocatalyst for Oxygen Reduction Reaction, ACS Applied Materials & Interfaces, 6 (2014) 1011-1017.

[284] Y. Zheng, Y. Jiao, Y. Zhu, Q. Cai, A. Vasileff, L.H. Li, Y. Han, Y. Chen, S.-Z. Qiao, Molecule-Level g-C_3N_4 Coordinated Transition Metals as a New Class of Electrocatalysts for Oxygen Electrode Reactions, Journal of the American Chemical Society, 139 (2017) 3336-3339.

[285] Y. Hou, F. Zuo, A.P. Dagg, J. Liu, P. Feng, Branched WO_3 Nanosheet Array with Layered C_3N_4 Heterojunctions and CoO_x Nanoparticles as a Flexible Photoanode for Efficient Photoelectrochemical Water Oxidation, Advanced Materials, 26 (2014) 5043-5049.

[286] C. Ng, Y.H. Ng, A. Iwase, R. Amal, Influence of Annealing Temperature of WO_3 in Photoelectrochemical Conversion and Energy Storage for Water Splitting, ACS Applied Materials & Interfaces, 5 (2013) 5269-5275.

[287] J.C. Hill, K.-S. Choi, Effect of Electrolytes on the Selectivity and Stability of n-type WO_3 Photoelectrodes for Use in Solar Water Oxidation, The Journal of Physical Chemistry C, 116 (2012) 7612-7620.